Electrically Driven Light Emission from Carbon Nanotubes with Quantum Defects

TECHNISCHE
UNIVERSITÄT
DARMSTADT

Zur Erlangung des akademischen Grades eines
Doktor der Naturwissenschaften (Dr. rer. nat.)
vom Fachbereich Material und Geowissenschaften
der Technischen Universität Darmstadt

genehmigte

Dissertation

von

Min-Ken Li

aus Taiwan

Referent:	Prof. Dr. Ralph Krupke
Korreferent:	Prof. Dr. Wolfram Pernice
Prüfer:	Prof. Dr. Wolfgang Ensinger
Prüfer:	Prof. Dr. Jan Philipp Hofmann

Darmstadt 2024

Electrically Driven Light Emission from Carbon Nanotubes with Quantum Defects
submitted doctoral thesis by Min-Ken Li

Date of submission: 25.01.2024
Date of thesis defense: 27.03.2024

Darmstadt, Technische Universität Darmstadt

Year of thesis published in TUprints: 2024
URN: urn:nbn:de:tuda-tuprints-269739

This thesis is dedicated to

my beloved family in Germany and in Taiwan

– this page left intentionally blank –

Declaration

I, hereby declare that this thesis is an outcome of my work. Contents from collaborations are acknowledged. I confirm that this thesis has not been submitted elsewhere. Additionally, care has been taken to ensure that the work is original and material included in the thesis previously published is cited congruously. I certify that the electronic version of my thesis corresponds to the written version.

Darmstadt,

(Min-Ken Li)

– this page left intentionally blank –

Table of Contents

Table of Contents .... **i**

Abstract .... **v**

List of Publications and Conference .... **vii**

Curriculum Vitae .... **ix**

1 Introduction **1**

1.1 Scope of thesis 1

1.2 Outline of thesis 3

2 Theoretical Background and Literature **5**

2.1 Carbon-based nanomaterials 5

2.1.1 Single-walled carbon nanotubes 7

2.1.2 Synthesis and functionalization of carbon nanotubes 10

2.2 Optical properties of carbon nanotubes 15

2.2.1 Electronic structure of carbon nanotubes 16

2.2.2 Absorption and photoluminescence 18

2.2.3 Electroluminescence 26

2.3 Carbon nanotubes as non-classical light sources 31

2.3.1 Photon statistics and correlation measurement. 32

2.3.2 Single-photon emission 34

2.3.3 Functionalized carbon nanotubes in nanophotonics 35

3 Experimental Methods **39**

3.1 Device fabrication 39

3.1.1 Dispersion preparation and functionalization 39

3.1.2 Electron beam lithography 40

3.1.3 Dielectrophoresis deposition 43

3.2 Device characterization 44

3.2.1 Electrical transport measurement 44

3.2.2 Electroluminescence spectroscopy 45

3.2.3 Scanning electron microscopy 46

3.3 Photon correlation measurement 47

3.3.1 Measurement setup description 47

3.3.2 Setup alignment and data analysis 48

4 Electroluminescence from Carbon Nanotubes with Quantum Defects 51
4.1 Introduction 52
4.2 Electroluminescence of functionalized (7, 5) carbon nanotubes 53
4.2.1 Functionalized carbon nanotube and device fabrication 53
4.2.2 Electroluminescence from functionalized (7, 5) 56
4.2.3 Influence of gating and doping 59
4.2.4 Comparative electroluminescence data from functionalized (6, 5) 63
4.2.5 Emission lines at very low-temperature 65
4.2.6 Hot-exciton electroluminescence 67
4.3 Photoluminescence from chemically doped nanotubes 71
4.4 Summary 74

5 Photon Correlation Measurements for Carbon Nanotubes with Quantum Defects 75
5.1 Introduction 76
5.2 Characterization of Fiber-coupled superconducting nanowire single-photon detectors 78
5.2.1 Performance metrics 79
5.2.2 Experimental setup 82
5.2.3 Current-voltage characteristics measurement 84
5.2.4 Dark count rates and electrical pulses 88
5.2.5 Detection efficiency 91
5.2.6 Photon number resolution 92
5.3 Photon correlation measurement setup characterization 93
5.3.1 System jitter determination with pulsed laser 93
5.3.2 Photon bunching from sub-threshold laser diode 94
5.4 Photon correlation measurements for carbon nanotubes with quantum defects at 77 K 96
5.4.1 Device fabrication 96
5.4.2 Electroluminescence spectroscopy and intensity correlation measurement 99
5.4.3 Second-order correlation function measurement without spectral filter 104
5.4.4 Photon count rate and applied electrical power 105
5.5 Summary 107

6 Cavity-Enhanced Electroluminescence of Carbon Nanotubes in the Telecom Band 109
6.1 Introduction 109
6.2 Hybrid cross-bar photonic crystal cavity device 110
6.2.1 NCG-based incandescent nanoemitter in the telecom band 113
6.2.2 Electrically controlled electroluminescence from a SWCNT 116
6.3 Summary 121

7 Conclusion and Outlook 123
7.1 Conclusion 123
7.2 Outlook 124

Appendix 131
Calculations of normal-mode frequencies 131
Redox-chemical doping of SWCNT suspensions 131
Supplementary results of the photon correlation measurement at 77 K 132
Low-loss cavity-compatible nanocrystalline graphene electrodes 133
Electron temperature of a NCG-based incandescent nanoemitter 135

List of Figures 137

List of Abbreviations 141

Bibliography 143

Acknowledgements 161

– this page left intentionally blank –

Abstract

In the modern era, with the high demand for energy-efficient, high-speed, and secure data transmission and information processing, photonic technology has emerged as one of the key players. To further advance in the realm of photonic quantum technologies, single-photon sources are one of the indispensable building blocks. Naturally, single-walled carbon nanotubes (SWCNTs) with sp^3 quantum defects, which have attracted great attention in sensing and imaging applications, are of particular interest due to their potential realization as quantum light emitters owing to the superior emission efficiency and the single-photon emission nature in the near-infrared regime. This thesis delves into the exploration of electroluminescence characteristics and the development of an on-chip electrical-driven quantum-light source in the telecom band. The central focus involves the integration of SWCNTs with sp^3 quantum defects in a field-effect transistor configuration.

At first, the electrical-driven defect-induced light emission of SWCNTs functionalized with dichlorobenzene molecules is presented. The introduction of sp^3 quantum defects forms deep potential traps that facilitate the localization of excitons and govern the optical properties. Gate-dependent defect-state emission lines are assigned as localized excitons/trions based on the correlation of electrical transport and electroluminescence measurements. The unconventional equidistant satellite peaks between intrinsic and defect-state emission lines at cryogenic temperatures can be associated with phonon-mediated hot-exciton electroluminescence. The comparison between the electrostatic gating electroluminescence and the chemical doping photoluminescence of SWCNTs reveals the potential complexity of optical transition identification.

Before photon correlation measurements of defect-state electroluminescence, the superconducting single-photon detectors, a crucial component in the Hanbury Brown and Twiss (HBT) experimental setup, are characterized, and the time resolution limitation and internal time delay of the system are determined. Subsequently, the first demonstration of single-photon emission by coupling either excitonic or trionic defect-state electroluminescence from functionalized (7, 5) SWCNTs into the HBT setup at 77 K is achieved. The interplay between the electrical power and the emission wavelength with the photon antibunching behavior is explored, and limitations of the current system from advancing into more controllable and accessible single-photon emitters, even for room temperature operation, are emphasized.

Finally, the proposed resolutions of low-loss heterogeneous integration of electrical control on-chip nanoemitters for the development of hybrid integrated photonic circuits are discussed. Full dynamic control of electroluminescent (9, 8) SWCNTs as a result of the site-selective coupling into a cross-bar Si_3N_4 photonic crystal cavity device nanocrystalline graphene (NCG) electrodes, which avoids compromising on the optical loss, is presented. Additionally, the NCG strip device within the cavity region functions as an incandescent emitter and is exhibited as a candidate for effective Local Density of States probing. The study provides a versatile and scalable approach for photonic applications in the telecom band.

– this page left intentionally blank –

List of Publications and Conference

Publications in the course of this work

- **Li, M.-K.***; Dehm, S.; Kappes, M. M.; Hennrich, F.; Krupke, R. "Correlation Measurements for Carbon Nanotubes with Quantum Defects" *ACS Nano* **2024**, *18*, 13, 9525–9534.
- Ovvyan, A. P.; **Li, M.-K.**; Gehring, H.; Beutel, F.; Kumar, S.; Hennrich, F.; Wei, L.; Chen, Y.; Pyatkov, F.; Krupke, R.; Pernice, W. H. P. "An electroluminescent and tunable cavity-enhanced carbon-nanotube-emitter in the telecom band" *Nature Communications* **2023**, *14*, 3933.
- **Li, M.-K.***; Riaz, A.; Wederhake, M.; Fink, K.; Saha, A.; Dehm, S.; He, X.; Schöppler, F.; Kappes, M. M.; Htoon, H.; Popov, V. N.; Doorn, S. K.; Hertel, T.; Hennrich, F.; Krupke, R. "Electroluminescence from Single-Walled Carbon Nanotubes with Quantum Defects" *ACS Nano* **2022**, *16*, 8, 11742–11754.
- Peyyety, N. A.; Kumar, S.; **Li, M.-K.**; Dehm, S.; Krupke, R. "Tailoring Spectrally Flat Infrared Photodetection with Thickness-Controlled Nanocrystalline Graphite" *ACS Appl. Mater. Interfaces* **2022**, *14*, 7, 9525–9534.

Other publications

- **Li, M.-K.***; Chen, T.*; Lin, Y.; Raghavan, C. M.; Chen, W.; Yang, S.; Sankar, R.; Luo, C.; Chang, Y.; Chen, C. "Intrinsic Carrier Transport of Phase-Pure Homologous 2D Organolead Halide Hybrid Perovskite Single Crystals" *Small* **2018**, *14*, 52, 1803763.
- Ho, P.-H.*; **Li, M.-K.***; Sankar, R.; Shih, F.-Y.; Li, S.-S.; Chang, Y.-R.; Wang, W.-H.; Chou, F.-C.; Chen, C.-W. "Tunable Photoinduced Carrier Transport of a Black Phosphorus Transistor with Extended Stability Using a Light-Sensitized Encapsulated Layer" *ACS Photonics* **2016**, *3*, 6, 1102–1108.
- Other 6 co-authored publications (* co-first authors contributed equally to this work).

Conferences contributions

- 243rd ECS Meeting, Boston (USA), May-June 2023, (Invited) Oral presentation "Electroluminescence from single-walled carbon nanotubes with quantum defects"
- Workshop on NanoMaterials & Optics, (virtual), September 2020, Poster presentation "Low-temperature electroluminescence of monochiral SWCNT devices with metal and graphene electrodes"

– this page left intentionally blank –

Curriculum Vitae

Personal Information

Name	**Min-Ken Li**

Education

06/2019 – Current	Doctor of Philosophy in Materials Science *Technische Universität Darmstadt*, Darmstadt, Germany,
09/2013 – 06/2015	Master of Science in Materials Science and Engineering *National Taiwan University*, Taipei, Taiwan,
09/2009 – 06/2013	Bachelor of Science in Materials Science and Engineering *National Taiwan University*, Taipei, Taiwan

Professional Experience

06/2019 –	Research Associate, Institute for Quantum Materials and Technologies (IQMT) *Karlsruhe Institute of Technology (KIT)*, Karlsruhe, Germany
10/2017 – 06/2019	Research Associate, Chair of Experimental Physics *Friedrich-Alexander-Universität Erlangen-Nürnberg (FAU)*, Erlangen, Germany
08/2016 – 09/2017	Research Assistant, Nano-Materials and Devices Lab *National Taiwan University*, Taipei, Taiwan
08/2015 – 07/2016	Mandatory Military Service, Substitute military service *Dulan Elementary School*, Taitung County, Taiwan

– this page left intentionally blank –

1 Introduction

1.1 Scope of thesis

In the era of modern society with the increasing dominance of data-driven applications, the demand for high-speed, energy-efficient, and secure information processing has propelled the innovation of advanced technologies. Photonic information processing has emerged as a key player in meeting these demands, and indeed the widespread use of fiber optic networks, replacing the electrical communication media, for mid- and long-distance communication stands for an example[1]. Bridging the gap for short-distance on-chip data transfer has been a driving force behind the progress of photonic integrated circuits, exemplified by the utilization of optical waveguides over electrical connections[2]. However, the realization of chip-scale information processing requires the integration of both passive and active optical components, and the conventional approach of coupling light into photonic circuits relies on an external light source with fiber-coupling techniques, inevitably enlarging the system footprint and sophistication. Meanwhile, photonic quantum technology[3] has shown promise in addressing emerging challenges in quantum information processing, such as quantum computing[4] and quantum cryptography[5], since the breakthrough in 2001 by Knill et al. demonstrating efficient quantum computation with linear optical elements, single-photon sources, and detectors[6]. Yet again, in light of the necessity for miniaturization and simplification, advancing a chip-based scalable and robust on-demand quantum-light source remains a significant hurdle.

This thesis confronts the requirement for on-chip, electrically-driven quantum-light sources and resolves some current limitations in the development of integrated photonic circuits. The material of interest is focused on semiconducting single-walled carbon nanotubes (SWCNTs), as they exhibit desirable electrical and optical properties for (quantum) photonic applications[7,8]. SWCNTs, in the form of roll-up graphene sheets in needle-like shape, offer a unique set of advantages, for instance, the prominent role of excitons in photophysics, the versatile structural-dependent light emission in the near-infrared wavelength range (between 850 nm and 2 µm depending on the chirality), and the compatibility in numerous processing methods. Along with the advancements in the synthesis and sorting techniques to achieve high-quality and chirality-enriched material[9], SWCNTs have opened up promising potential for their application in photonics and, indeed, exhibiting single-photon emission (photon antibunching) through both optical and electrical stimulation at cryogenic temperatures[10,11]. Despite these progresses, addressing the challenge of low emission quantum yield associated with the low-lying dark exciton states and undesired quenching sites remains a priority. Integrating SWCNT with optical microcavities presents a viable path and is often accompanied by additional improvements in emission directionality and enhancement, although, it often adds complexity to sample preparation[12–14]. A significant breakthrough occurred with the incorporation of a low degree of sp^3 quantum defects on the sidewall of SWCNTs forming potential traps, achieved mainly through mild oxidation or organic chemistry reaction (for example, the aryl sp^3 defect formation via diazonium-based functionalization used in this thesis)[15,16]. These approaches not only substantially improved the emission quantum yield (from <1 % up to 28 %) but also allowed for the tailoring of emission wavelength by the localization of excitons at potential traps of 100 – 300 meV. The intrinsic large binding energy of excitons that rules the emission characteristics of SWCNTs (a few hundred of meV) with moderate potential depths at sp^3 defect sites indeed extended single-photon emission to room temperature, as has been experimentally validated under optical excitation[17,18]. However, the development of an on-chip electrical-driven single-photon emitter based on SWCNTs by fully harnessing the advantages of covalently functionalized SWCNTs, regardless of the operation temperature, remains uncharted territory.

In this thesis, the electroluminescence characteristics of SWCNTs with sp^3 quantum defects and their potential development of an on-chip electrical-triggered single-photon emitter in the telecom band are explored. The primary approach involves the integration of functionalized SWCNTs into field-effect transistor configurations with CVD graphene as electrical contacts. To begin, the study of switchable defect-induced electroluminescence spectroscopy of functionalized SWCNTs at the single-tube level (Chapter 4)[19] is presented. The sp^3 defects on SWCNTs are formed with dichlorobenzene molecule treatments, and the functionalized SWCNTs are bridged between the graphene electrodes via electric-field-assisted dielectrophoresis (DEP) deposition. A comprehensive correlation between the defect-induced electroluminescence and the electrical transport measurements to assign the controllable excitonic and trionic defect-state emission is performed, and emission spectra with high spectral purity are achieved. Additionally, a hypothesis to explain the observed unconventional satellite electroluminescent emission lines from functionalized SWCNTs is proposed, and, lastly, the tunable electroluminescence via electrostatic gating and the photoluminescence via redox-chemical doping are compared. Subsequently, photon antibunching measurements of functionalized SWCNTs through a constant current bias at 77 K (Chapter 5)[20] are conducted. The role of a pre-patterned bowtie-structure graphene strip as a thermal emitter for experimental setup alignment is firstly proposed, and electrical-driven single-photon emission by coupling excitonic or trionic defect-induced electroluminescence in the telecom band into the Hanbury Brown and Twiss (HBT) setup is demonstrated. The photon antibunching measurements are correlated with the electrical excitation power and the defect-state emission wavelength, and additionally, the simultaneously recorded time traces of photon count rates and the electrical power dissipation are analyzed to understand the current limitation of the photon correlation measurement setup. Besides, a detour is taken to characterize the fiber-coupled superconducting single-photon detectors as one of the key elements of the HBT system. Finally, a versatile approach for the full electrical control of electroluminescent SWCNTs in hybrid photonic circuits with the utilization of nanocrystalline graphene (NCG) electrodes (Chapter 6)[21] is introduced. A hybrid platform addressing the challenges of site-selective placement and conventional metal electrodes hindering low-loss integration in integrated photonic circuit development is proposed, featuring the heterogeneous integration of pristine SWCNTs into Si_3N_4 cross-bar photonic crystal (PhC) cavity devices by DEP deposition between the NCG electrodes in the cavity region. The structure enables full dynamic control (switching on and off) of enhanced electroluminescent emission in the telecom band via electrostatic gating and offers the opportunity to directly probe the PhC cavity properties through the additional patterned NCG strip as an incandescent nanoemitter. Overall, this thesis explores the unique characteristics of functionalized SWCNTs in the development of on-chip electrical-driven single-photon emitters and provides a comprehensive insight into the potential and challenges associated with SWCNT-based on-chip quantum-light sources in the scope of integrated photonic circuits.

1.2 Outline of thesis

The structure of the thesis to explore the electroluminescence characteristics and the development of an electrical-driven quantum-light source on a chip based on carbon nanotube with sp^3 quantum defects at the single-tube level will be described in this section.

Chapter 2 establishes the theoretical background for studying on-demand quantum-light sources on a chip. Beginning with an overview of the carbon nanotube structural properties and the synthesis techniques, the chapter delves into the optical properties of pristine and functionalized carbon nanotubes and ends with reviewing carbon nanotubes as a non-classical light source.

Chapter 3 focuses on the experimental methods employed throughout the thesis. The chapter is divided into three parts, namely the device fabrication, the device characterization, and photon correlation measurement based on HBT configuration for exploring the electroluminescent single-photon emission of carbon nanotubes with sp^3 quantum defects.

Chapter 4 presents electroluminescence spectroscopy results of carbon nanotube with sp^3 quantum defects at the single-tube level. The chapter demonstrates the tunable defect-induced emission from carbon nanotube devices via electrostatic gating and correlates the emission characteristics with the electrical transport measurements. Additionally, the chapter reveals the unconventional phonon-assisted hot-exciton electroluminescence at cryogenic temperature and also compares electroluminescence with photoluminescence spectroscopy via chemical doping.

Chapter 5 demonstrates carbon nanotubes with quantum defects as electrical-driven quantum-light sources at low temperatures. The chapter starts with the characterization of superconducting single-photon detectors, a crucial element for our photon correlation measurement, and follows with the discussion of electroluminescent single-photon emission from carbon nanotubes via electrical excitation at 77 K and the foreseeable challenges of further development for room-temperature electrically-triggered single-photon emitter.

Chapter 6 proposes a versatile protocol for integrating controllable electrical-driven nanoscale light sources into photonic circuits. The hybrid 2D-3D photonic crystal cavity structure addresses the dynamic control and low-loss integration challenges of carbon nanotubes as electroluminescent nanoemitters by using nanocrystalline graphene electrodes within the photonic crystal cavity.

Chapter 7 highlights the main results from each chapter of the thesis and includes a discussion of challenges and prospects for advancing electrical-driven quantum-light sources based on carbon nanotubes with sp^3 quantum defects.

2 Theoretical Background and Literature

The theoretical backgrounds in this chapter are aimed at studying the electroluminescence of semiconducting single-walled carbon nanotubes (SWCNTs) as potential on-demand quantum light sources on a chip. To begin, we elaborate more on the material property side, including introducing carbon-based nanomaterials, such as graphene, and describe the basic structure and electronic properties. Based on that, we continue with SWCNTs including various synthesis techniques and functionalization methods. In the second part, we focus on the optical properties of SWCNTs but will start with the fundamental basis and describe the electronic band structure based on graphene. We discuss the optical property characterization methods and the fundamental theory behind, for instance, absorption, photoluminescence, and Raman spectroscopy. Before moving on to the electroluminescence of carbon nanotubes and the relevant literature review, we touch a bit on the electrical properties of SWCNT-based devices. Then we address the well-accepted electroluminescence mechanisms of pristine SWCNT and further explore the state-of-art studies of electroluminescence of SWCNTs with sp^3 quantum defects. In the third part, to delve into the realm of quantum photonics and the development of an on-demand electrical-driven single-photon source on a chip, we describe some theories behind the nature of different light sources and the common characterization approach, namely photon correlation measurements. After reviewing some pioneering works of pristine and functionalized SWCNTs as quantum emitters, we lastly discuss the integration of functionalized SWCNTs into nanophotonic environments to account for the last experimental chapter of this thesis.

2.1 Carbon-based nanomaterials

A simple carbon element that has six electrons in the ground-state orbital occupancy $1s^2 2s^2 2p^2$, could form various allotropes depending on the chemical bond formation resulting in different nanomaterials in various dimensions from 3D to 0D. For instance, diamonds are a commonly seen three-dimensional (3D) carbon allotrope forming a crystal structure of four covalent bonds with nearest neighbors via sp^3 hybridization. Diamond has exceptional hardness and good thermal conductivity and is usually considered an insulator with a bandgap of 5.5 eV, falling in the deep ultraviolet wavelength range. On the other hand, the most famous fullerene, Buckminsterfullerene C_{60} informally named ‘buckyball’, is a zero-dimensional (0D) molecule with sp^2-hybridized carbon atoms in a cage-like structure. It was first discovered in 1985 by Kroto et al.[22] and later awarded the 1996 Nobel Prize in Chemistry. Perhaps the most renowned carbon allotrope at the moment is the isolated two-dimensional (2D) carbon layer, graphene, which was first successfully exfoliated from graphite by Novoselov and Geim et al.[23] via the scotch tape technique in 2004 and awarded the Nobel Prize in Physics in 2010. Graphene consists of a single layer of carbon atoms arranged in a hexagonal honeycomb lattice with sp^2 hybridization and is well-known for its extraordinary electrical conductivity, mechanical strength, flexibility, and transparency. To understand the superior properties, one needs to look into the atomic and electronic structure. Each unit cell of graphene contains two atoms and each carbon atom bonds with three other neighboring atoms in a triangle structure (bond angle of 120°) under sp^2 hybridization. The hybridization of one s-orbital and two p-orbitals (p_x, p_y) from a carbon atom forms three equivalent rigid sigma (σ) bonds between carbon atoms, resulting in outstanding mechanical strength. The additional unhybridized p-orbital (p_z) on each carbon atom, perpendicular to the plane of the graphene sheet, overlap sideways with neighboring carbon atoms and form pi (π) bonds. The delocalized π electrons are not tightly bound to specific carbon atoms, leading to excellent electrical conductivity. The lattice vectors $\mathbf{a_1}$ and $\mathbf{a_2}$ of the graphene unit cell in x-y coordinates can be written as

$$\boldsymbol{a}_1 = \frac{a_{c-c}}{2}(\sqrt{3}, 1), \quad \boldsymbol{a}_2 = \frac{a_{c-c}}{2}(\sqrt{3}, -1)$$

, where $a_{c-c} \approx 1.42$ Å is the nearest bond distance between carbon atoms (A and B) as shown in **Figure 2.1a**. The basis vectors in the reciprocal space $\boldsymbol{b}_1$ and $\boldsymbol{b}_2$, in **Figure 2.1b**, in the x-y coordinate can be expressed as

$$\boldsymbol{b}_1 = \left(\frac{1}{\sqrt{3}}, 1\right)\frac{2\pi}{a_{c-c}}, \quad \boldsymbol{b}_2 = (\frac{1}{\sqrt{3}}, -1)\frac{2\pi}{a_{c-c}}$$

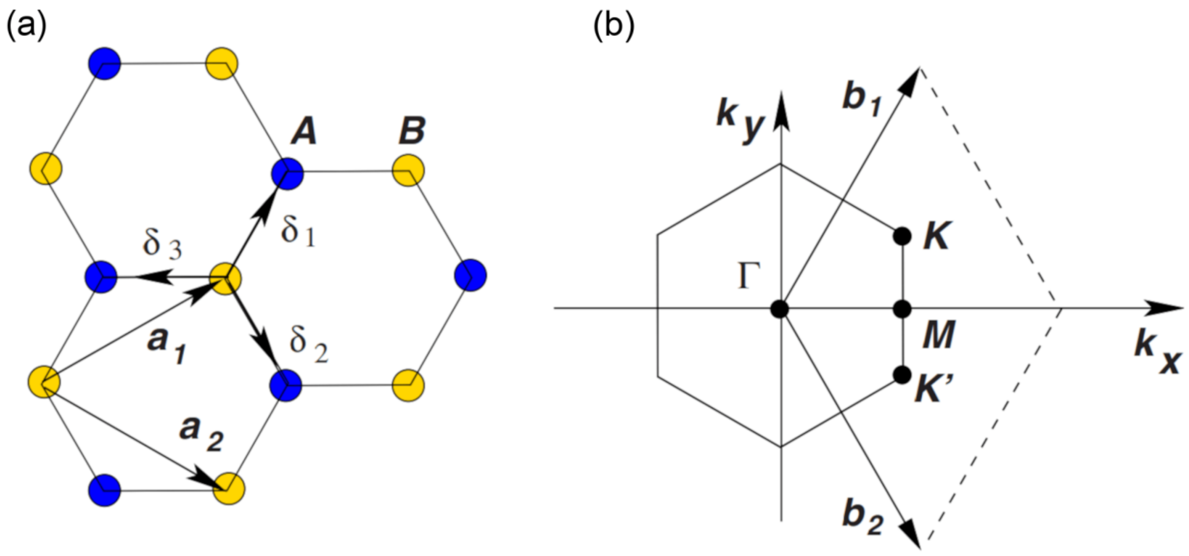

Figure 2.1: The honeycomb atomic structure and the Brillouin zone of graphene (a) The hexagonal lattice in real space with the lattice vectors a_1 and a_2 of the unit cell comprising two carbon atoms (A and B), and (b) in reciprocal space with lattice vectors b_1 and b_2. [Adapted and reproduced with permission from reference[24], American Physical Society.]

Considering only the two bonding π- and anti-bonding π*- orbitals by neglecting the bonding and anti-bonding σ-bands due to the large energy gap (>10 eV at the center of the Brillouin zone Γ point)[25], the π valence band and the π* conduction band meet at the $\boldsymbol{K}$ ($\boldsymbol{K'}$) points of the Brillouin zone corners. As a consequence, graphene is a unique semimetal or zero-bandgap semiconductor. The electronic band structure can be described using the energy dispersion relation derived from the first-order tight-binding approximation:

$$E(k_x, k_y) = \pm\gamma_0 \sqrt{1 + 4\cos(\frac{\sqrt{3}k_x a}{2})\cos(\frac{k_y a}{2}) + 4\cos^2(\frac{k_y a}{2})}\ ;\ a = \sqrt{3}a_{c-c}$$

, where γ_0 is the carbon-carbon interaction energy (tight-binding integral) between the nearest neighbors, with typical values between 2.9 – 3.1 eV[26]. The positive and negative signs refer to the unoccupied π* conduction band (+) and the fully occupied π valence band (-). Therefore, the electronic band structure of graphene can be visualized in **Figure 2.2** where the conduction and valence bands touch at the six $\boldsymbol{K}$ points, also named Dirac points, and the Fermi level E_F is the zero energy reference. Close to the $\boldsymbol{K}$ points, the electronic band dispersion shows a linear relation in contrast to conventional semiconductors which can be expressed as

$$E(\boldsymbol{\kappa}) = \pm\hbar v_F|\boldsymbol{\kappa}|$$

, where $\boldsymbol{\kappa} = \boldsymbol{k} - \boldsymbol{K}$ and $v_F \approx 10^6$ m/s is the electronic group velocity (Fermi velocity) implying that electrons can be considered as massless particles in graphene. Additionally, the density of state (DOS) for such a linear band dispersion in a two-dimensional system per unit of energy is linear.

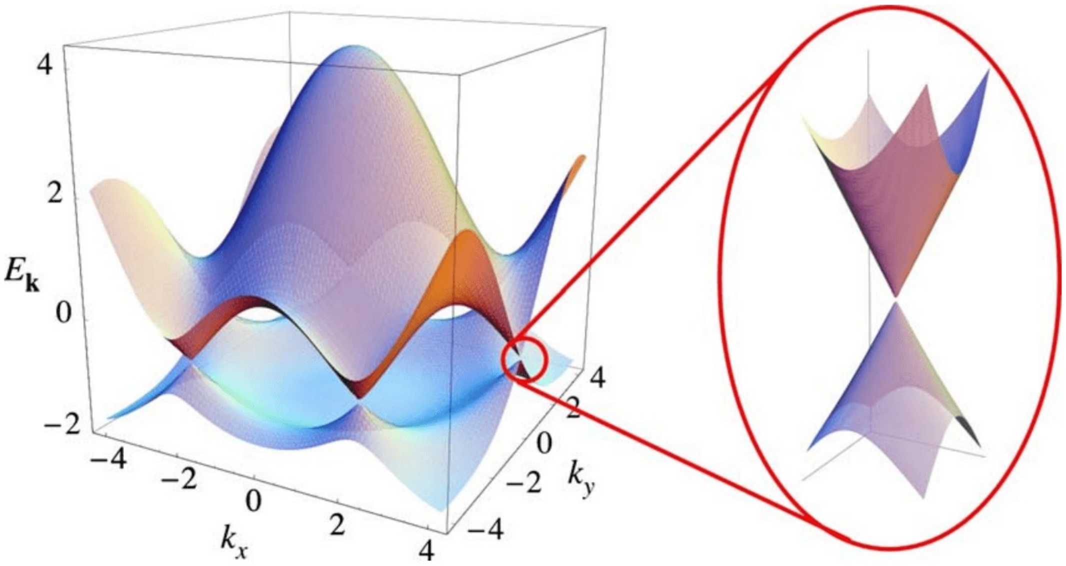

Figure 2.2: Electronic band structure of graphene The conduction (π*) band and the valence (π) band meet at the six *K* points (Dirac points) of the Brillouin zone at the Fermi level. The zoom-in energy dispersion relation near one Dirac point. [Adapted and reproduced with permission from reference[24], American Physical Society.]

2.1.1 Single-walled carbon nanotubes

As we briefly covered the carbon allotropes in different dimensions, this section continues with the remaining 1D allotrope, the carbon nanotube (CNT). CNTs can be visualized as roll-up graphitic carbon sheets into needle-like tubes and were first discovered and published in 1991 by a Japanese scientist, Sumio Iijima[27]. Back then, they were observed in the form of double-walled carbon nanotubes (DWCNT) or multi-walled carbon nanotubes (MWCNT), and only two years later, SWCNTs were reported by Iijima et al.[28] as well as Bethune et al.[29] from IBM. To the interest of our work, we focus on SWCNTs which can be understood as a roll-up single-layer graphene sheet constructed into a cylinder shape.

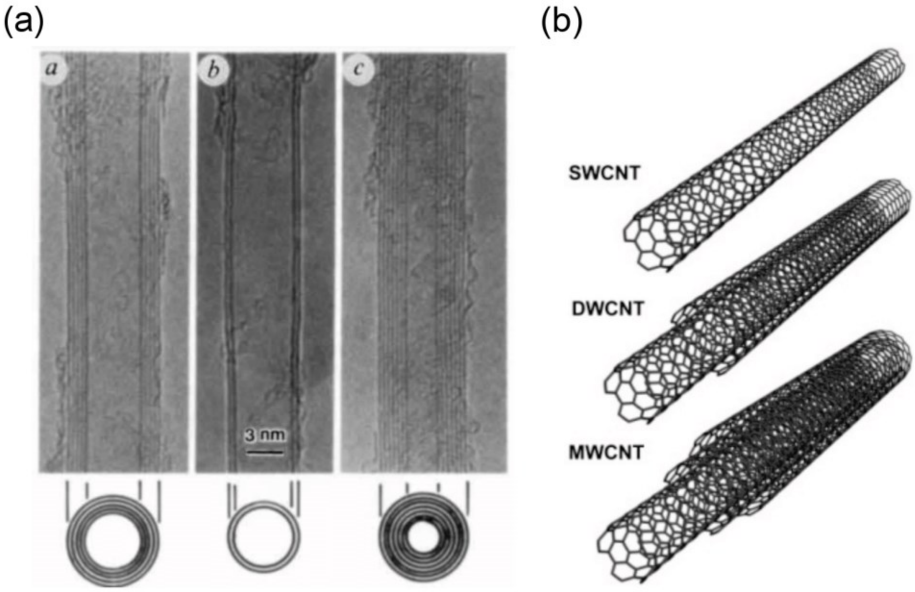

Figure 2.3: Transmission electron microscopy images and schematic models of carbon nanotubes (a) The first reported TEM images of multi- and double-walled carbon nanotubes in 1991 with the cross-section illustrations of each tube below. (b) Molecular structure illustrations of single-, double-, multi-walled carbon nanotubes. [Adapted and reproduced with permission from (a) reference[27], Springer Nature; (b) reference[30], American Chemical Society.]

By seamlessly rolling up the graphene sheet in different ways, for instance, depending on the rolling direction or angle, nanotubes with various diameters and unique electronic and optical properties are formed. Distinct from a planar graphene sheet, the structural and electronic properties of different CNTs are confined by the rolling circumference[31], as shown in **Figure 2.4a**, which can be expressed as the chiral (roll-up) vector $\boldsymbol{C}_h$

$$\boldsymbol{C}_h = n\boldsymbol{a}_1 + m\boldsymbol{a}_2$$

, where $\boldsymbol{a}_1$ and $\boldsymbol{a}_2$ represent the lattice vectors of a graphene unit cell with an angle of 60° and lengths of $|\boldsymbol{a}_1| = |\boldsymbol{a}_2| = \sqrt{3}a_{c-c} \approx 2.46$ Å in which $a_{c-c} \approx 1.42$ Å is the carbon bond distance. The (n, m) refer to the chiral indices of each unique CNTs and both n and m are integers (n ≥ m). According to the chiral indices (n, m), one can calculate the nanotube diameter d

$$d = \frac{|\boldsymbol{C}_h|}{\pi} = \frac{\sqrt{3}a_{c-c}}{\pi}\sqrt{n^2 + nm + m^2}$$

The angle between the chiral vector (roll-up direction) $\boldsymbol{C}_h$ and the lattice vector $\boldsymbol{a}_1$ is defined as the chiral angle θ and is described as[32]

$$\cos\theta = \frac{\boldsymbol{a}_1 \cdot \boldsymbol{C}_h}{|\boldsymbol{a}_1||\boldsymbol{C}_h|} = \frac{2n+m}{2\sqrt{n^2+nm+m^2}}$$

The value of the chiral angle θ lies between 0 and 30° due to the six-fold rotational symmetry in the hexagonal lattice. Depending on the chiral indices (n, m), SWCNTs can be classified into two groups, namely metallic SWCNTs (m-SWCNTs) and semiconducting SWCNTs (sc-SWCNTs). When the following conditions[33]

$$n - m = 3i$$

are fullfilled, where i is an integer, the SWCNTs show metallic behavior. As a consequence, one-third of SWCNTs belong to metallic SWCNTs, and the other two-thirds show semiconducting behavior. Additionally, SWCNTs are often categorized into zig-zag (n = m), armchair (n, 0), and chiral SWCNTs as shown in **Figure 2.4b**. The chiral angle θ for zig-zag SWCNTs is 0°, 30° for armchair SWCNTs, and values in between for the case of chiral SWCNTs[34]. A map of SWCNTs with different (n, m) chiral indices indicating various types is shown in **Figure 2.5**.

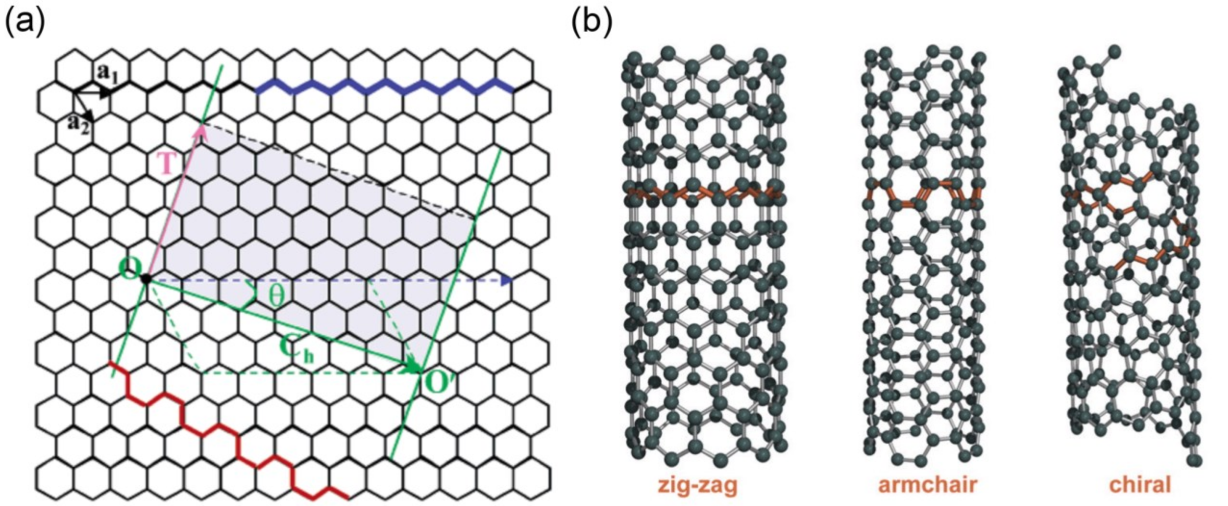

Figure 2.4: Graphene sheet roll-up and various types of SWCNTs (a) The chiral vector and angle of rolling up a graphene sheet. (b) Molecular models of zig-zag, armchair, and chiral SWCNTs. [Adapted and reproduced with permission from (a) reference[35], American Chemical Society; (b) reference[36], Elsevier.]

To determine the unit cell size of each SWCNT, the translational vector $\boldsymbol{T}$, which is perpendicular to the roll-up vector and parallel to the tube axis, needs to be considered. The translational vector $\boldsymbol{T}$ defines the minimum structure periodicity along the long (tube) axis and is expressed as[31]

$$\boldsymbol{T} = t_1\boldsymbol{a}_1 + t_2\boldsymbol{a}_2, \quad t_1 = (2m+n)/d_R, \quad t_2 = -(2n+m)/d_R$$

, where t_1 and t_2 are integers and d_R is the greatest common divisor of (2n+m, 2m+n). Therefore, the length (magnitude) of the translational vector $|\boldsymbol{T}|$ and the number of hexagons (two carbon atoms per hexagon) N can be described as

$$|\boldsymbol{T}| = \frac{\sqrt{3}|\boldsymbol{C}_h|}{d_R}, \qquad N = \frac{|\boldsymbol{C}_h \times \boldsymbol{T}|}{|\boldsymbol{a}_1 \times \boldsymbol{a}_2|} = \frac{2(n^2 + nm + m^2)}{d_R}$$

Generally speaking, the translational vector for a chiral SWCNT is rather large and results in a large unit cell size. For instance, a zig-zag (6, 6) metallic SWCNT has only 24 carbon atoms per unit cell whereas a chiral (7, 5) semiconducting SWCNT has 436 carbon atoms per unit cell despite the similar nanotube diameters of ~8.2 Å.

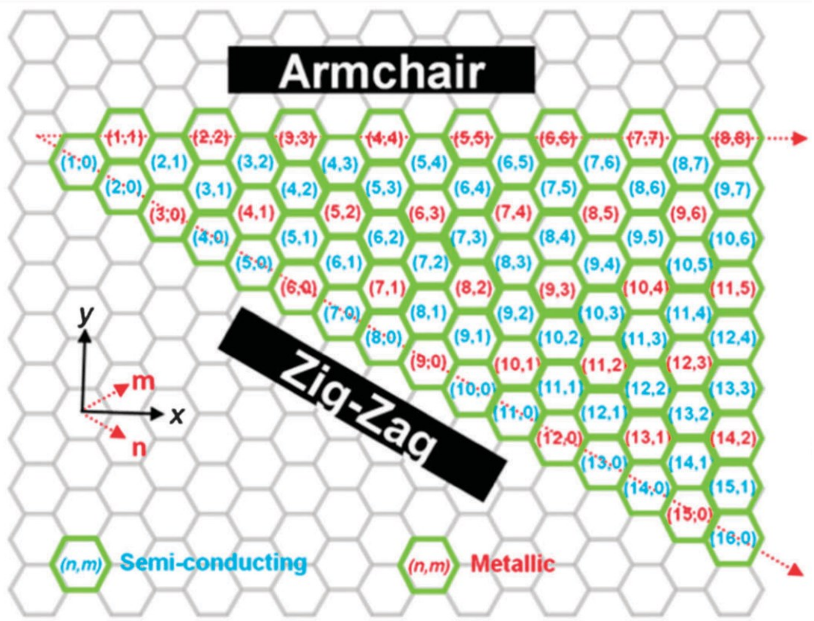

Figure 2.5: A map of metallic and semiconducting SWCNTs categorized based on chiral indices [Adapted and reproduced with permission from reference[37], Royal Society of Chemistry.]

2.1.2 Synthesis and functionalization of carbon nanotubes

Since the discovery of CNTs in 1991, in principle, three categories of well-established synthesis techniques have been developed, namely arc discharge[28,29], laser ablation[38,39], and chemical vapor deposition (CVD)[40–42]. Among these different techniques, there are some common basic elements which are the carbon sources, catalysts, and the required driving force. The variation of each element determines the synthesis outcome, for example, the purity, diameters, and tube types, as well as the growth/production rate of the CNTs.

Arc discharge

The arc discharge method is the first synthesis technique for CNTs, which basically is a modified version of the large quantity synthesis of buckyballs C_{60} developed by the group of Huffman[43]. In that case, a plasma is formed by applying bias through two graphite rods as the starting material, in an inert gas (helium) atmosphere, to vaporize part of the graphite soot on the anode and harvest on the cathode. The first observation of CNTs was conducted similarly with arc discharge evaporation in an argon-filled vessel[27]. It turned out to produce mainly multi-walled CNTs using pure graphite rods, and only with the graphite rods of the anode containing metal nanocatalysts such as iron (Fe)[28], cobalt (Co)[29], nickel (Ni), or relevant bimetal catalysts[44], facilitated SWCNTs synthesis. Different metal catalysts also result in different tube diameter sizes or distributions, and the production up-scale was only improved after the study of using a bimetal nickel-yttrium (Ni-Y) catalyst[45].

Laser ablation

The laser ablation method is the technique used in 1985 for the discovery of fullerenes C_{60}. A pulsed laser beam was focused on a rotating graphite disk to vaporize the starting material which was carried out by helium flow and characterized by time-of-flight mass spectroscopy[22]. It was later further developed and applied by the same research group to produce CNTs. Similar to the arc discharge method, the target graphite rod or disk was mixed with metal catalysts but laser-vaporized in a rotating fashion while heated at 1200 °C under argon flow[38,39]. Previous studies have shown that not only do various metal catalysts[46] change the CNT production and the diameter control, but the target temperature[47] and gas flow rate[48] also play a role. However, laser ablation as well as arc discharge methods usually produce not only CNTs but undesired contaminants such as amorphous carbon and metal catalysts, which require additional subsequent processes for purification[49,50].

Chemical vapor deposition

The chemical vapor deposition (CVD) method is nowadays a widely used “clean” technique to grow CNTs developed in a later phase. Compared to the previous two methods, this technique allows continuous-flow processes at a relatively lower temperature which favors industrial-scale production. Typically, the three crucial elements are the hydrocarbon source, the metal catalysts, and the growth temperature. In general, the hydrocarbon source decomposes at the catalyst sites where the hydrogen evaporates, and the carbon dissolves in and precipitates out from the metal catalyst resulting in the growth of CNTs. The growth process is usually associated with two distinct mechanisms, tip-growth[51] and base-growth[52] models, as depicted in **Figure 2.6** below, and studies have found that the catalyst particle size dictates the tube diameter[53]. The additional advantage is that each of the elements could be altered to achieve control over growth parameters or mechanisms. For instance, in the HiPCO® (refers to high-pressure carbon monoxide) method[40,54], CO is used as the carbon feedstock while $Fe(CO)_5$ is the catalyst precursor. The catalyst precursors decompose thermally (800 – 1200 °C) into gas-phase iron clusters and acts as nuclei for CNT growth by CO disproportionation under high pressure (30 – 50 atm). The process can be optimized for a high yield of SWCNTs with a broad diameter distribution. The work from Maruyama et al.[41] is a great example to show the versatility of the CVD technique by using liquid-phase hydrocarbon (alcohol) as the source material and porous zeolite-supported Fe/Co catalysts on substrates to enable lower temperature synthesis and vary tube diameter distribution. Resasco et al. modified the HiPCO® process by introducing cobalt and molybdenum (Mo) bimetallic catalysts in a fluidized bed reactor[42]. In the reactor, the gas-phase carbon source passes through granular bimetallic catalysts with enough velocity to suspend the catalyst particles (prevent them from falling as if in fluid) and allow high growth selectivity owing to the superior control over catalysts, such as the composition-dependent Co-Mo interaction[55]. The modified process is later known as the CoMoCAT® method which contains mostly small diameter tubes (~0.8 nm) with narrow distribution and enriched (6, 5) and (7, 5) semiconducting SWCNTs.

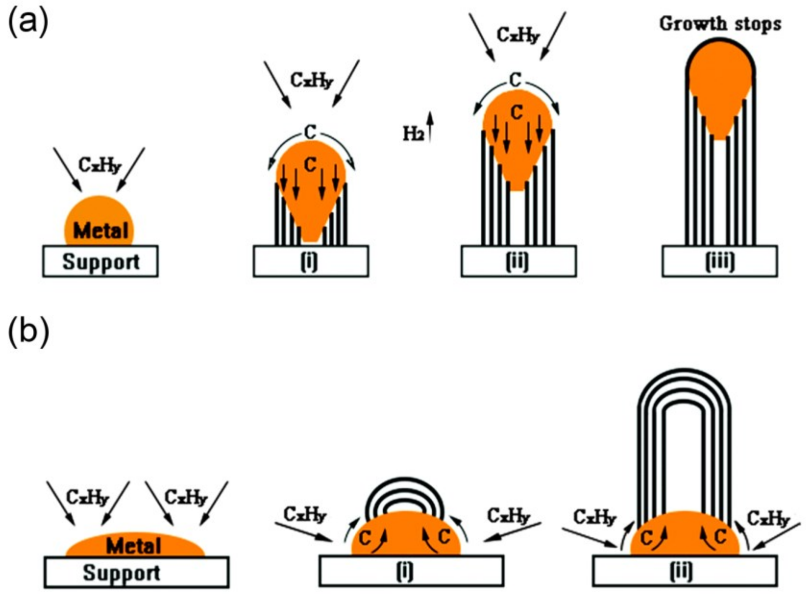

Figure 2.6: Illustrations of the mechanism of carbon nanotube growth process (a) Schematic of tip-growth model and (b) base-growth model. [Adapted and reproduced with permission from reference[53], Royal Society of Chemistry.]

From the application perspective, utilization of synthesized CNTs at the individual level is easier when dispersed in the liquid phase compared to the solid counterpart. Commonly, the raw synthesized CNTs are dispersed in an aqueous or organic solvent with various tactics for separation. Yet, despite the progress in the selective synthesis of nanotubes, the product still contains variations of electronic type, tube length, diameter, chirality, etc. Post-synthesis sorting techniques are hence often required for suspensions with high purity and monodisperse properties for device fabrication purposes. In terms of optoelectronics fabrication, the metallicity of nanotubes is one of the detrimental factors. Dielectrophoresis (DEP), shown in **Figure 2.7a**, is one of the early techniques proven to effectively separate semiconducting tubes from metallic tubes based on the competition of the positive and negative dielectrophoretic force for metallic and semiconducting SWCNTs under certain operating parameters[56]. Another more straightforward and scalable method for separating the electronic types is using density-gradient ultracentrifugation (DGU)[57] as shown in **Figure 2.7b**. In the early demonstration, tube types were separated in a co-surfactant (sodium dodecyl sulfate/sodium cholate, SDS/SC) aqueous dispersion depending on how the surfactants arranged and interacted around the SWCNTs. In the same work, this method has shown the potential of separating SWCNTs by diameter and later progressed to enable length[58], chirality, and enantiomer[59] sorting. Similarly, the separation of tube types and chirality sorting of semiconducting SWCNTs can be achieved by gel chromatography (gel filtration), displayed in **Figure 2.7c**, due to the different interaction strengths of surfactants-covered SWCNTs and the porous gel columns[60]. The surfactant-based separation techniques were further developed into a so-called aqueous two-phase extraction (ATPE) method first reported by Khiripin et al. to achieve effective chirality separation in two immiscible aqueous phases[61]. The two aqueous phases, as shown in **Figure 2.7d**, are formed by adding hydrophobic polyethylene glycol (PEG) and hydrophilic dextran (DX) which alter the hydrophobicity of SWCNTs for chirality differentiation[62]. Also for aqueous suspensions, using particular DNA strands for wrapping selective nanotubes, in **Figure 2.7f**, was first studied by Zheng et al.[63,64] and later demonstrated by Liu et al.[65] for sorting specific chiralities which opened the gate to advancing in biomedical application topics. Another effective sorting technique was introduced in 2007 by Chen et al.[66] as well as Nish et al.[67] via the usage of conjugated polymers, illustrated in **Figure 2.7e**. As specific polymer tends to possibly helically wrap around by forming π - π stacking with selective SWCNTs in certain solvents (usually organic solvents)[68], it results in excellent separation purity and extremely low residual metallic SWCNTs[69]. For instance, polyfluorene poly(9,9-di-n-octylfluorenyl-2,7-diyl) (PFO)[66,67] has been used for sorting enriched (7, 5) SWCNTs, poly(9,9-di-n-dodecylfluorenyl-2,7-diyl) (PODOF)[70] was used for sorting (9, 8) SWCNTs, and polyfluorene copolymers such as poly[(9,9-dioctylfluorenyl-2,7-diyl)-alt-co-(6,6´-{2,2´-bipyridine})] (PFO-BPy)[71] has been used as extracting agent for enriched (6, 5) SWCNTs. All three polymer-wrapped SWCNTs can be dispersed in toluene. When polymer-wrapped SWCNT dispersions are additionally followed by gel filtration, instead of chirality separation, it’s a powerful tool for sorting tube length which often is critical for SWCNT-based device fabrication[69].

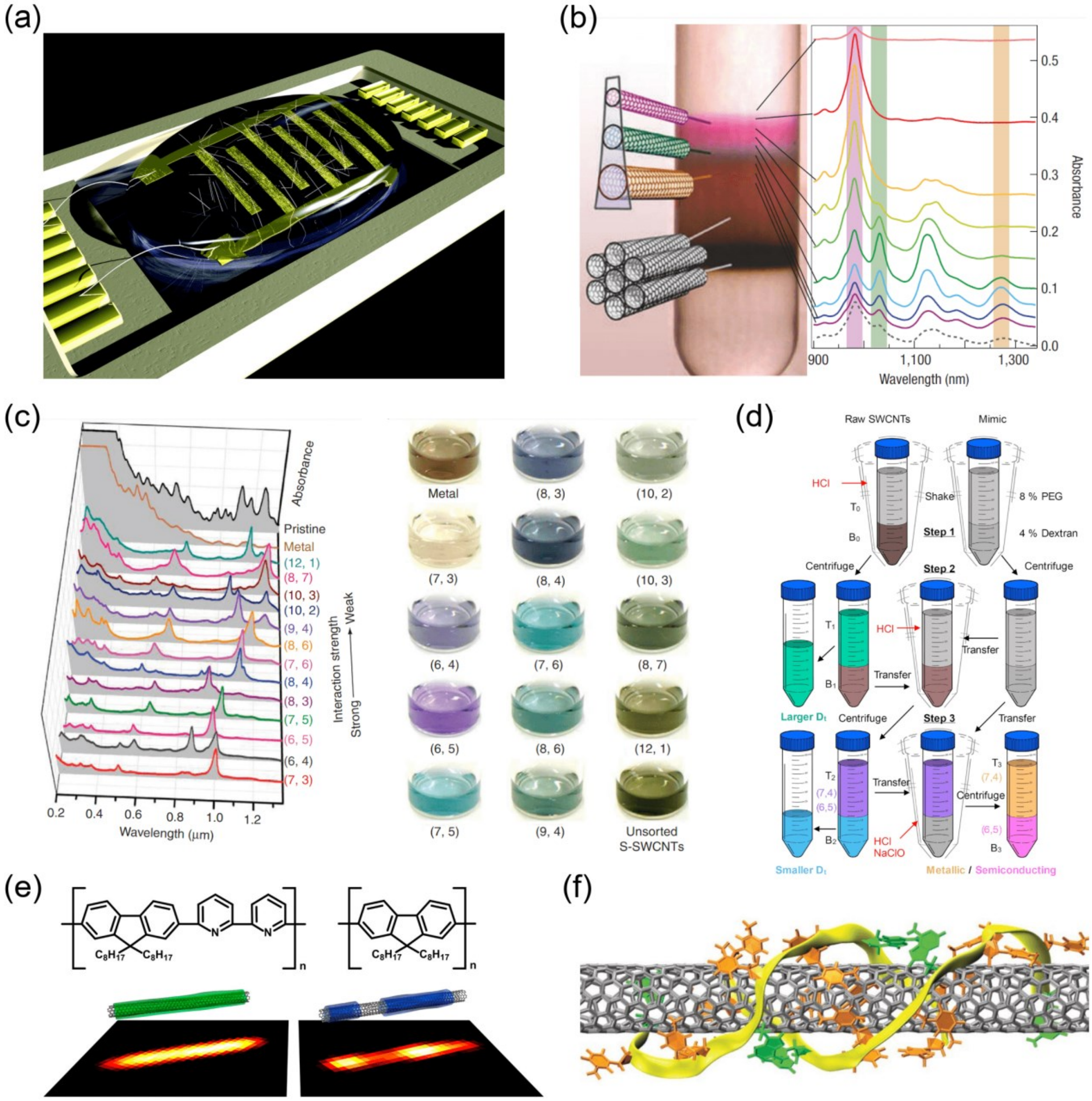

Figure 2.7: Carbon nanotube sorting techniques (a) Representative illustrations of dielectrophoresis (DEP), (b) density-gradient ultracentrifugation (DGU), (c) gel chromatography, (d) aqueous two-phase extraction (ATPE), (e) non-covalent polymer wrapping, and (f) DNA wrapping as sorting techniques. [(a) From "Krupke et al., Separation of Metallic from Semiconducting Single-Walled Carbon Nanotubes. Science 301, 344-347 (2003)."[56] Reprinted with permission from AAAS. Adapted and reproduced with permission from (b) reference[57], Springer Nature; (c) reference[60], Springer Nature; (d) reference[62], American Chemical Society; (e) reference[72], American Chemical Society; (f) reference[65], Springer Nature.]

The sorting techniques can be viewed as a means of extracting certain SWCNTs by non-covalent functionalization. The extracting agents, such as surfactants or conjugated polymers, interact weakly with the SWCNTs to minimize the perturbation of electronic structures and intrinsic properties[73]. On the contrary, covalent functionalization of SWCNTs is often avoided for sorting purposes but instead, for instance, used for sensing[74] or biological[75] applications. However, later studies have shown that a low degree of covalent functionalization[16,76], which locally alters the electronic structure and forms luminescent potential traps, gives rise to intriguing optical properties such as red-shifted emission with enhanced efficiency and room temperature single-photon emission[17,18], the details of which will be discussed later. Some important factors of this technique are, for example, to decide upon the usage of functional groups and to control the degree of functionalization. The pioneering work can be traced back to 2010 by Ghosh et al., as shown in **Figure 2.8a**, when bright red-shifted emission lines of SWCNTs were observed with mild oxidation[15]. Some following reports reveal an in-depth investigation of how various oxygen functional groups change the local electronic structure differently by reshaping the sp^2 lattice structure[77]. Different kinds of molecules as depicted in **Figure 2.8b**[78], usually alkyl and aryl groups, were later explored which serve a similar purpose. It provides on the one hand more diversity, for instance, different functional group/SWCNT interactions associated with the binding configuration or environment[79–82], but on the other hand additional controllability, for example, synthetic controls[83–86] or post-synthesis treatments[87]. The covalent functionalized SWCNTs open up new potential applications in the field of quantum photonics[18,88–91] or biosensing[92–94], etc., and also bring up interesting fundamental topics such as the quantification of defect (functional groups) density[95–97].

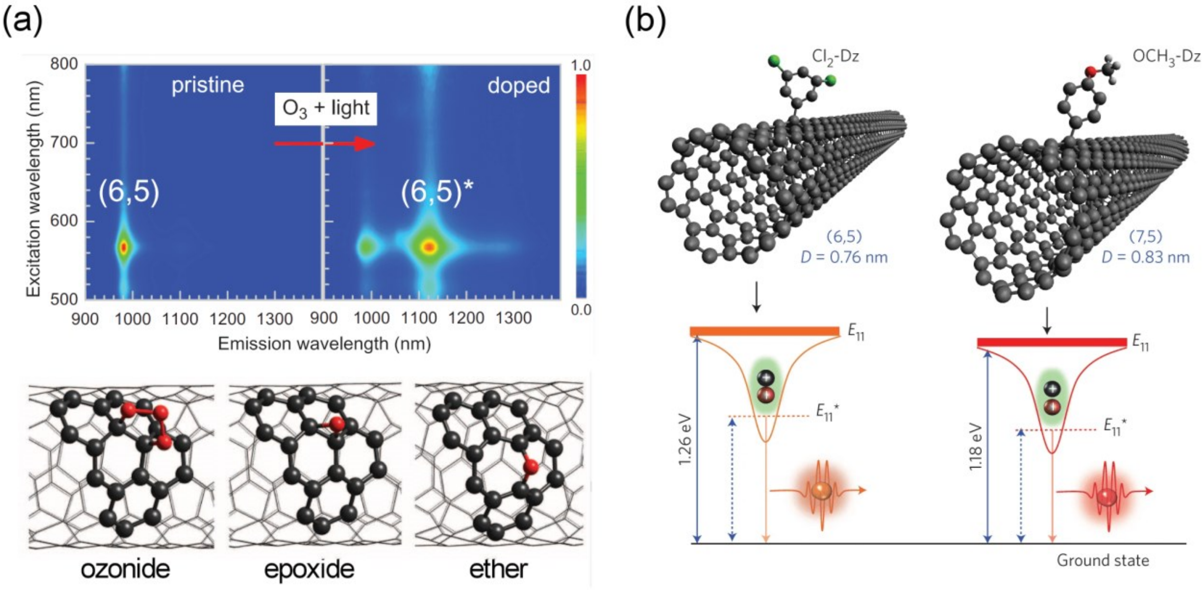

Figure 2.8: Luminescent defects of carbon nanotubes by covalent functionalization (a) The red-shifted functionalized emission line and the possible oxygen functional groups. (b) Covalent functionalization with aryl groups. [(a) From "Ghosh et al., Oxygen Doping Modifies Near-Infrared Band Gaps in Fluorescent Single-Walled Carbon Nanotubes. Science 330, 1656-1659 (2010)."[15] Reprinted with permission from AAAS. Adapted and reproduced with permission from (b) reference[18], Springer Nature.]

2.2 Optical properties of carbon nanotubes

To look into the optical properties of SWCNTs, one can start with the electronic structure and combine it with additional theory. In this section, we begin with the electronic structure of SWCNTs which can be understood as a modification of the graphene band structure. Then we discuss the common optical characterization approaches, namely absorption, fluorescence, and Raman spectroscopy, and the early works of pristine SWCNTs along with recent works of sp^3-functionalized SWCNTs. To close the section, we review the electrical-driven light emission of pristine and functionalized SWCNT field-effect transistors.

2.2.1 Electronic structure of carbon nanotubes

The electronic band structure of SWCNTs can be derived by the energy dispersion relation of graphene from the tight-binding approximation with additional zone folding approximation as the energy levels around the circumference of a 1D nanotube system are confined. The corresponding reciprocal lattice vectors of the chiral vector $\boldsymbol{C}_h$ and the translational vector $\boldsymbol{T}$ in real space can be described as $\boldsymbol{K}_1$ and $\boldsymbol{K}_2$, where $\boldsymbol{K}_2$ is continuous along the tube axis whereas $\boldsymbol{K}_1$ is quantized along the tube circumference[98]:

$$\boldsymbol{K}_1 = \frac{1}{N}(-t_2\boldsymbol{b}_1 + t_1\boldsymbol{b}_2), \quad \boldsymbol{K}_2 = \frac{1}{N}(m\boldsymbol{b}_1 - n\boldsymbol{b}_2)$$

with reciprocal lattice vectors $\boldsymbol{b}_1$ and $\boldsymbol{b}_2$, integers t_1, t_2, m, and n as the coordinates of the translational and chiral vectors, and N as the number of hexagons per unit cell. The quantization of $\boldsymbol{K}_1$ can be seen by considering the wave vector of a quasi-particle (such as an electron) that the allowed wavelength λ follows a phase shift of 2π due to constructive interference, which can be expressed as

$$|\boldsymbol{K}_1| = \frac{2\pi}{\lambda} = \frac{2\pi}{|\boldsymbol{C}_h|}\cdot\mu = \frac{2}{d}\cdot\mu$$

, where d is the diameter of the tube, and $\mu = -\frac{N}{2}, \ldots, -1, 0, 1, \ldots, \frac{N}{2}$, meaning there are N discrete one-dimensional electronic bands separated by $2/d$. Therefore, the $\boldsymbol{K}$ vectors can be visualized as N parallel cutting lines in the first two-dimensional Brillouin zone of graphene with the length of $|\boldsymbol{K}_2|$ and distanced by $|\boldsymbol{K}_1|$ given that

$$\boldsymbol{K} = k_z\frac{\boldsymbol{K}_2}{|\boldsymbol{K}_2|} + \mu\boldsymbol{K}_1, \quad |\boldsymbol{K}_2| = \frac{2\pi}{|\boldsymbol{T}|} = \frac{2d_R}{\sqrt{3}d}$$

with $-\pi/|\boldsymbol{T}| < k_z < \pi/|\boldsymbol{T}|$ as shown in **Figure 2.9**. The electronic band structure of SWCNTs can then be derived based on the energy dispersion relation of graphene in the first Brillouin zone of nanotubes (zone folding approximation) and written as[99]

$$E_{1D}^{\pm}(\boldsymbol{K}) = E_{2D}^{\pm}\left(k_z\frac{\boldsymbol{K}_2}{|\boldsymbol{K}_2|} + \mu\boldsymbol{K}_1\right)$$

Since each SWCNT has its specific (n, m) chiral index, as a result, each SWCNT owns a unique electronic band structure. If the cutting lines of a certain SWCNT pass through the $\boldsymbol{K}$ ($\boldsymbol{K}'$) points of the graphene Brillouin zone, the energy band shows zero-band gap behavior, similar to graphene, and the SWCNT can be classified into a m-SWCNT, or else it goes into the group of sc-SWCNTs with a finite band gap.

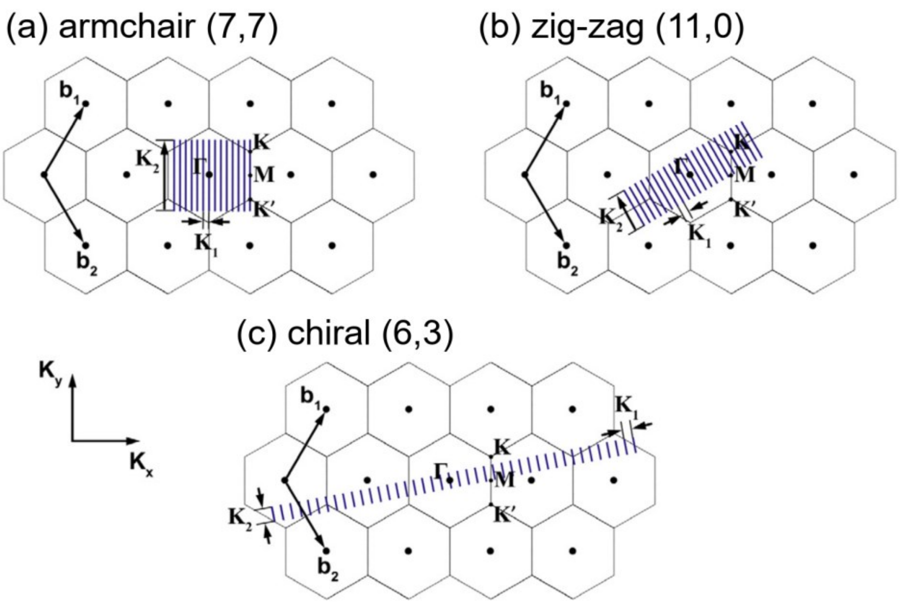

Figure 2.9: Quantized 1D wave vectors of SWCNTs (a) An armchair (7, 7), (b) a zig-zag (11, 0), and (c) a chiral (6, 3) SWCNTs in the first two-dimensional Brillouin zone of graphene. [Adapted and reproduced with permission from reference[100], Elsevier.]

The density of states (DOS) of SWCNTs can be derived from the energy dispersion relation, examples given in **Figure 2.10** for metallic and semiconducting SWCNTs. The multiple spikes in the DOS followed by an inverse square root dependence in energy ($1/\sqrt{E}$) are called van Hove singularities (vHs). They appear close to the 1D parabolic band edges and are arranged symmetrically in the conduction and valence bands relative to the Fermi level. For metallic SWCNTs, in which the allowed wave vectors go through the $\boldsymbol{K}$ points of the graphene Brillouin zone, they show zero band gap and lead to a constant finite density of states at the Fermi level. On the other hand, for semiconducting SWCNTs no cutting lines pass the $\boldsymbol{K}$ points and, as a result, the density of states is zero at the Fermi level. The accumulation of states at the vHs suggests the preference for interband optical transition between the spikes. Due to the selection rule concerning light polarized parallel to the tube axis, pronounced optical transitions only occur between the symmetrically appeared vHs in the conduction and valence bands[101,102]. The energy difference between the first pair of spikes (vHs) from the lowest conduction band and highest valence band for semiconducting and metallic SWCNTs can be expressed as[99]

$$E_{11}^{S} = \frac{2a_{c-c}\gamma_0}{d}, \qquad E_{11}^{M} = \frac{6a_{c-c}\gamma_0}{d}$$

, indicating the inverse proportionality of the optical transition to the tube diameter. It’s worth mentioning that the deduction of the electronic structure of SWCNTs with the zone folding model does not consider the curvature effect of the rolled-up CNTs, as it’s based on a planar graphene sheet. The curvature effect[32], especially for smaller diameter tubes, could influence the basic vectors $\boldsymbol{a}_1$ and $\boldsymbol{a}_2$ and alter the conditions of defining wave vectors. For instance, the deformation causes the cutting lines of non-armchair metallic SWCNTs to deviate from the $\boldsymbol{K}$ points at the graphene Brillouin zone corners[103] and open an intermediate gap proportional to $1/d^2$. For armchair SWCNTs, the curvature-induced deformation shifts the wave vectors only along the allowed lines. As a consequence, they preserve the truly metallic property with zero band gap which has been experimentally proven by scanning tunneling spectroscopy[104].

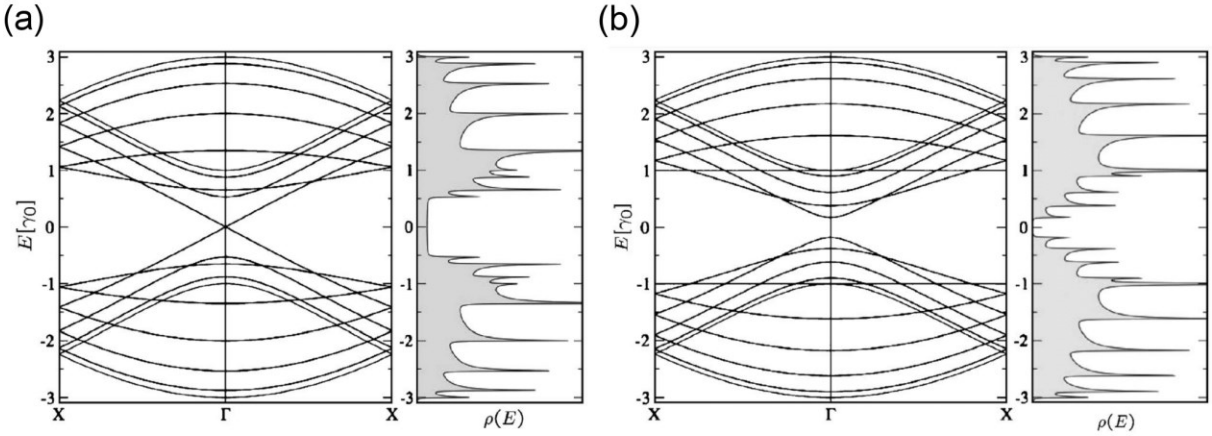

Figure 2.10: SWCNT band structures and density of states (a) From metallic (9, 0) zig-zag SWCNT and (b) from semiconducting (10, 0) zig-zag SWCNT. [Adapted and reproduced with permission from reference[32], American Physical Society.]

2.2.2 Absorption and photoluminescence

In this section, we focus on some optical characterization techniques often used in the field of SWCNTs, such as absorption and photoluminescence spectroscopy. We discuss the basic working principle including the role of excitons in the optical characteristics and application. Basic Raman spectroscopy will also be included as being a common technique for probing SWCNTs sp^3-functionalization. Lastly, we move on to the defect-state photoluminescence of functionalized SWCNTs. We introduce the defect-induced optical properties and the mechanism behind them. Additionally, we point out the challenges in synthesizing functionalized SWCNTs in a controlled manner and interesting works published throughout the development.

Absorption spectroscopy

As discussed in the previous section, the optical properties of SWCNTs can be interpreted in association with the energy difference between the van Hove singularities (vHs) symmetrically appearing in the conduction and valence bands. The interband transitions are regulated by the selection rule, therefore, the transitions predominantly occur only between the symmetrical i-th vHs pair with the same angular momentum in the valence band and conduction band[102]. Additionally, due to the 1D anisotropic geometry, the transition mainly involves the coupling of polarized light which is parallel to the tube axis. In principle, light-matter interaction of light polarized perpendicular to the tube axis is possible between states in the i-th and (i±1)-th band edges of the conduction and valence bands, the depolarization effect yet strongly suppresses the coupling[105].

Conventionally, the optical transition of semiconducting and metallic SWCNTs are denoted as E_{ii}^{S} (or S_{ii}) and E_{ii}^{M} (or M_{ii}), which refers to the i-th pair of vHs, given in **Figure 2.11a**.

Absorption spectroscopy in the visible to near-infrared range is a convenient tool to experimentally characterize the optical transition energy of SWCNTs (especially in suspension), and reveal the chiral indices (n, m). Theoretically, the dominant optical transition energy for specific (n, m) SWCNTs can be derived based on the electronic structure by the tight-binding method. As depicted in **Figure 2.11b** below, the transition energies vs the tube diameters are known as the Kataura plot[106,107], and show an inverse relation. For semiconducting SWCNTs in aqueous suspension, the computed Kataura plot has been modified with empirically based results for a more accurate interpretation[107]. Apart from identifying the chiral index from the absorption spectra, various studies have also shown analytical methodology to evaluate, for instance, the purity or concentration of the SWCNT suspension[108,109].

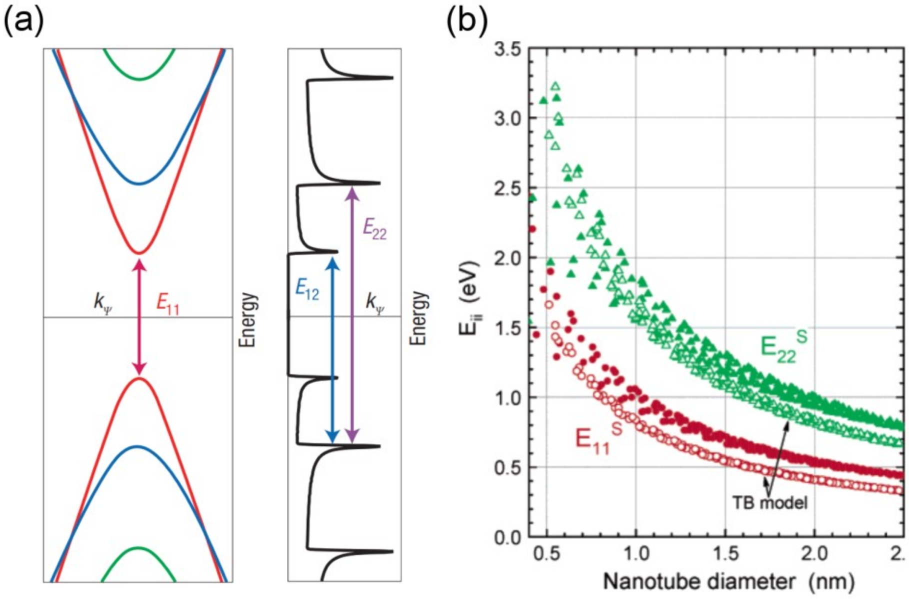

Figure 2.11: Optical transition schematic and Kataura plot (a) The schematic of optical transition and the transition energy between states. (b) The modified computed Kataura plot based on the empirical values. [Adapted and reproduced with permission from (a) reference[7], Springer Nature; (b) reference[107], American Chemical Society.]

Fluorescence spectroscopy

Fluorescence measurements, especially photoluminescence spectroscopy (PL), are nowadays common techniques used for characterizing semiconducting SWCNTs, in which each (n, m) SWCNT structure gives a specific characteristic emission. The photoluminescence measurement is performed by exciting SWCNTs with higher excitation energy, usually absorbing photons in the second van Hove optical transition E_{22}, in which the excited states relax to the lowest conduction band and subsequently to the highest valence band, the first van Hove optical transition E_{11}, and emit photons by radiative relaxation. As is shown in the illustration in **Figure 2.12**, the correlation between the first and second van Hove optical transitions provides a more straightforward approach for (n, m) chiral indices assignment. Metallic SWCNTs can't be distinguished via photoluminescence as the absorbed energy leads to a non-emissive relaxation. The pioneering studies of semiconducting SWCNTs photoluminescence in the near-infrared were reported first by the group of Weisman in 2002 in aqueous suspensions[110,111]. In that work, photoluminescence excitation (PLE) 2D contour maps of SWCNT suspensions were presented, by varying the optical excitation energy and recording the corresponding emission wavelength. Different semiconducting SWCNT species could be identified from their distinct absorption and emission optical transitions.

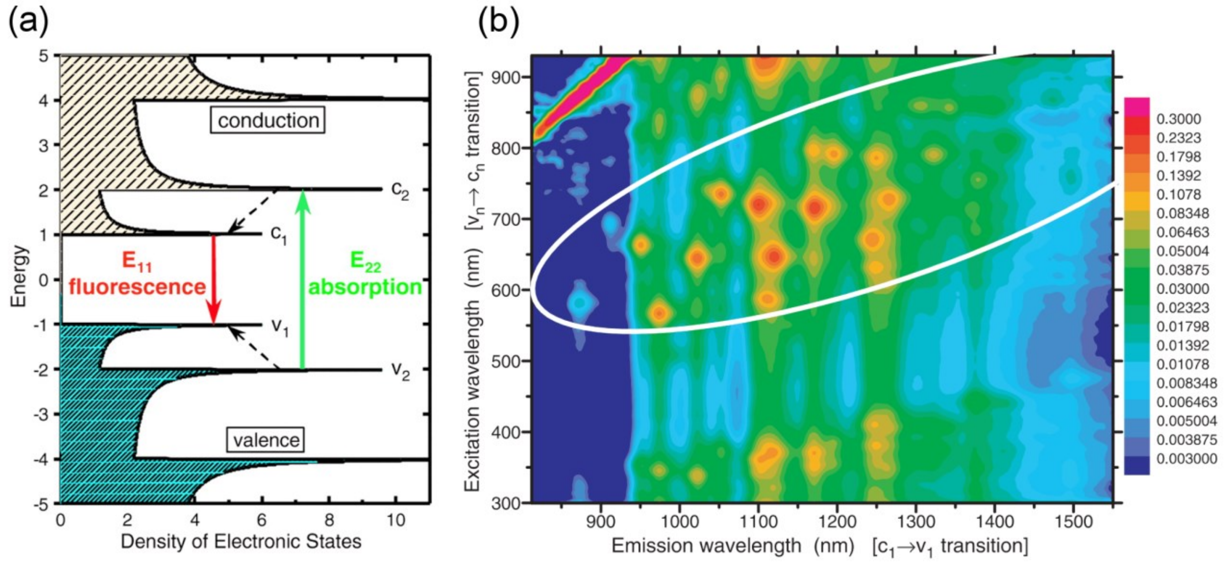

Figure 2.12: Schematic of photoluminescence process and photoluminescence excitation map (a) A schematic for optical transition for the PL process. (b) PLE map for SWCNTs dispersed in aqueous surfactant suspensions. [From "Bachilo et al., Structure-Assigned Optical Spectra of Single-Walled Carbon Nanotubes. Science 298, 2361-2366 (2002)."[111] Reprinted with permission from AAAS.]

These early works also initiated discussions regarding the nature of the excited states in SWCNTs when the well-known ratio problem was pointed out. The experimentally extracted ratio between the second and first optical transitions (E_{22}/E_{11}) is around 1.8[111] and deviates from the theoretically calculated ratio of 2 based on the tight-binding model[99], which essentially considers only single particle excitation. It turns out that the discrepancies can be well explained by accounting for the electron-electron and electron-hole interactions, namely the many-body effect in the excited states, as the opposite contributions from the repulsive electron-electron interaction and attractive electron-hole Coulomb interaction compensate for the deviation[112]. Owing to the reduced dimensional systems, the 1D confinement and the reduced dielectric screening, the electron-hole Coulomb interaction becomes large and forms bound states usually called excitons[113,114]. The exciton binding energy of semiconducting SWCNTs, with an inverse relationship to the tube diameter, is typically in the range of a few hundred millielectron volts, and therefore, has a significant role in the optical properties of SWCNTs even at room temperature[115]. However, not all the excitons are optically allowed to emit photons during recombination. According to the theoretical prediction, there are in total 16 possible excitonic states, yet only one with matched momentum and spin is expected to be optically active, “bright” exciton, and the remaining 15 are energetically low-lying (a few meV) optically forbidden “dark” excitons[116,117]. The excitonic effect on optical spectra has more than just the influence in terms of energy shift, but for instance, on the spectral line shapes as well. In absorption and fluorescence spectra, the experimentally observed line shapes often have a Lorenzian distribution[111,118] instead of the asymmetric van Hove transition feature associated with the DOS predicted theoretically[112]. The nature and properties of exciton such as the diffusion length, lifetime, or the environmental effect also affect the emission characteristics[119–122]. By altering the carrier doping density, it’s possible to promote the formation of charged excitons, referred to as trions, and lead to distinct optical spectral features[123,124].

Raman spectroscopy

Raman spectroscopy is another powerful analytical tool for optically characterizing CNTs. Instead of probing SWCNTs by involving exciton generation/recombination via optical transition for absorption and fluorescence spectroscopy, Raman spectroscopy mainly relies on the inelastic scattering of incident photons with various vibrational (phonon) modes of molecules. By spectrally resolving the scattered photon energy difference (Raman shift), Stokes shift when the photons lose energy and anti-Stokes shift when the photons gain extra energy, the Raman spectra fingerprints often feature structural properties. In the case of SWCNTs, the commonly observed Raman scattering features are, for instance, the radial breathing mode (RBM) at ~100 – 300 cm^{-1}, the G band at ~1580 cm^{-1}, and the D band at ~1350 cm^{-1}, as in **Figure 2.13a**[125]. The RBM mode refers to the out-of-plane coherent oscillation along the radial direction that is inversely related to the tube diameter and shows an environmental effect. The G band is attributed to the in-plane bond stretching mode which often splits into G^+ and G^- peaks due to the curvature effect. The D band, on the other hand, indicates the defect-induced peaks from the defects in the hexagonal sp^2 structure[126]. The Raman scattering signal is weak inherently but can be strongly enhanced if the excitation incident photon energy matches the optical transition energy of SWCNTs, which is called resonant Raman scattering. As a result, by recording the Raman signals with variable excitation energy, identifying the optical transition energy of specific SWCNTs is feasible. Moreover, resonant Raman spectroscopy is a technique applicable for both semiconducting and metallic SWCNTs, in contrast to fluorescence spectroscopy. Typically, the preferred assignment of SWCNT chirality would require two correlated characteristics, such as the absorption (E_{22}) and emission (E_{11}) energy extracted from a photoluminescence excitation (PLE) map. Similarly, resonant Raman spectroscopy can be applied to reliably determine the tube diameters, electronic types, and chiral indices of SWCNTs by the RBM frequency and the optical transition energy as referred to in the Kataura plot in **Figure 2.13b**[127].

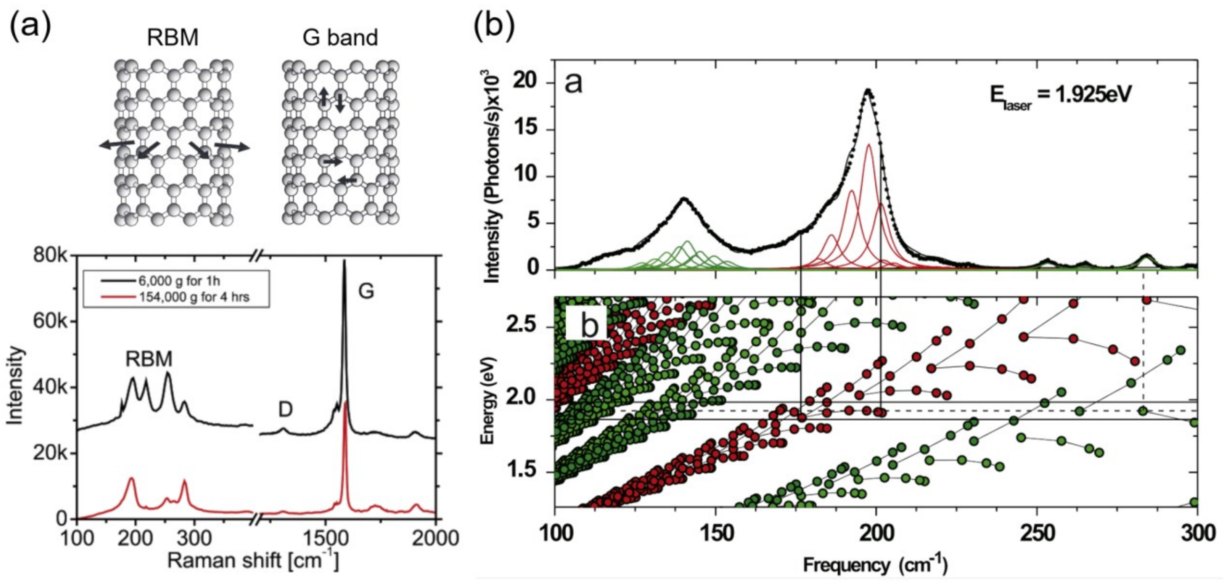

Figure 2.13: Raman spectroscopy of SWCNTs (a) Example Raman spectra of a HiPco SWCNTs suspension with the schematics of the atomic vibrations for RBM and G band. (b) Raman spectrum fitted by using Lorentzians obtained with a 644 nm laser line (1.925 eV), top. The Kataura plot, bottom, in which red circles stand for metallic SWCNTs, and the green circles stand for semiconducting SWCNTs. [Adapted and reproduced with permission from (a, top) reference[128], Royal Society; (a, bottom) reference[129], American Chemical Society; (b) reference[130], Elsevier.]

Defect-state photoluminescence

When the chemical functionalization of SWCNTs comes into the picture, as briefly discussed previously in Section 2.1.2, instead of considering the excitonic effect on optical spectra as excitons being mobile quasiparticles in the one-dimensional system, many of the luminescent characteristics can be explained by the localization of mobile excitons in quantum dot-like (0D) potential traps (sp^3 quantum defects)[16,79]. The absorption spectra usually won't change much due to the low degree of functionalization[78,131], that is to say, the characteristic distance between defects is large compared to the exciton size[132], which avoids the complete disruption of the electronic structure. The potential depths of sp^3 quantum defects due to the surface functionalization of alkyl or aryl groups generally are in the range of 100 – 300 meV[78], and attributed to the red-shifted functionalization-induced emission lines (E_{11}*) by providing additional radiative relaxation pathways. The potential traps also redistribute the exciton population by lowering diffusive quenching due to defects/tube ends[119,133], and/or non-radiative recombination due to optically forbidden low-lying dark excitonic states[117], which often results in enhanced emission efficiency and luminescence lifetime[82,131,134], as depicted in **Figure 2.14**. Perhaps the most intriguing characteristic observed after the introduction of luminescent sp^3 defects is the extension of single-photon emission nature to room temperature[17,18,83]. In 2017, He et al. demonstrated room-temperature single-photon defect-state emission from single SWCNTs with aryl sp^3 quantum defects[18], which was only possible in pristine SWCNT at cryogenic temperature owing to the existence of shallow exciton traps in an unstable electrostatic environment[10,11].

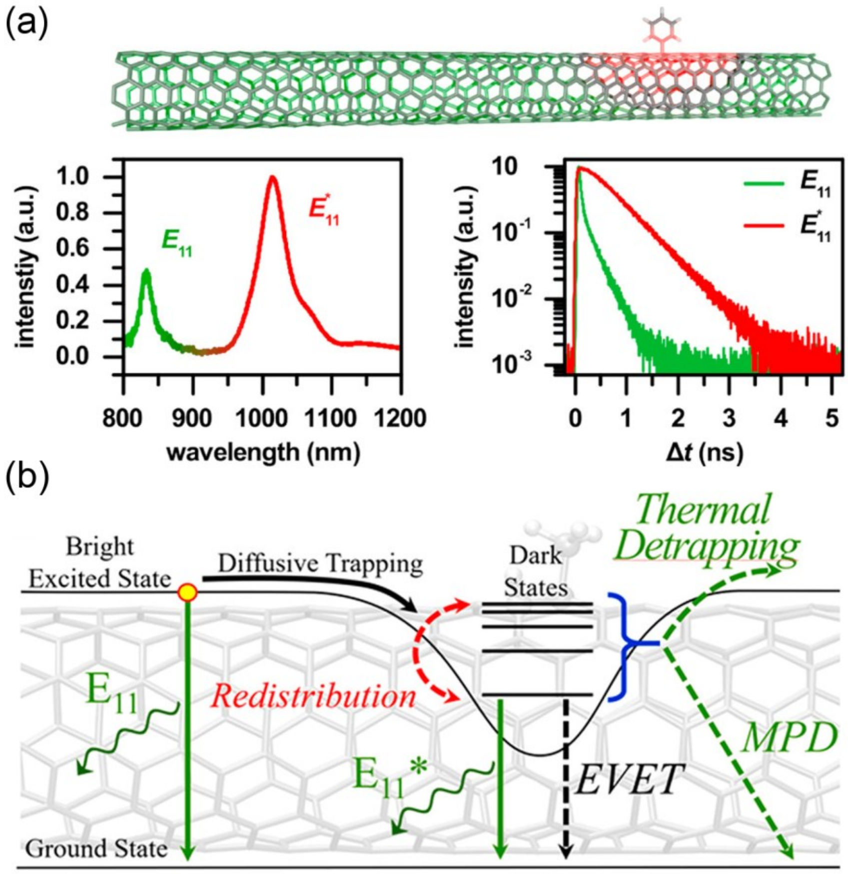

Figure 2.14: The defect-induced emission characteristics and relaxation processes (a) The red-shifted defect-induced emission line (E_{11}*) and enhanced luminescence lifetime. (b) Illustration of exciton relaxation pathways with defect state formation. [Adapted and reproduced with permission from (a) reference[131], American Chemical Society; (b) reference[82], American Chemical Society.]

The variation of alkyl or aryl groups for creating quantum defects alter the potential depths which affect the defect-induced emission properties, on top of that, studies have shown that the trap depths also have a dependence on the SWCNT chiral indices which generally have an inverse relation with the tube diameter[135]. Opposite to the intrinsic excitonic luminescence (E_{11}) of a specific chirality, in which the emission wavelength, in general, falls in a narrow window, the red-shifted defect-state luminescence, however, spreads over an extremely broad spectral range. According to the theoretical simulation, the spectral diversity can be ascribed to the topological variation between the chemical binding configurations of the monovalent functional group concerning the CNT axis, in shown in **Figure 2.15**[81,84]. In order to remain in a neutral closed-shell configuration when a functional group forms a sp^3 quantum defect on the sidewall, another neighboring sp^2 carbon atom must also be sp^3 hybridized, possibly by a pairing group from the solvent such as hydrogen or hydroxide, leading to six chemically distinct functional group configurations. These defect conformations contribute mainly to the red-shift of defect-state emission in the range of 100 – 300 meV and the spectral complexity. Experimentally, this results in two defect-state emission bands usually denoted as E_{11}* and E_{11}^{*-}, in which the E_{11}^{*-} refers to the lower lying energy defect states. The divergence between E_{11}* and E_{11}^{*-} can be reduced when forming defects on near zig-zag SWCNTs due to the structural symmetry, and the more uniform emission is a prerequisite for conducting single-photon emission measurement. Apart from the diverse binding configurations as the main contribution to red-shifted emissive localized excitons, the electron-withdrawing ability and arrangement of the functional groups, interrelated to dipole moments and local induced charges, are also factors in the potential depth, but in a smaller scale of a few tens of meV[136–139].

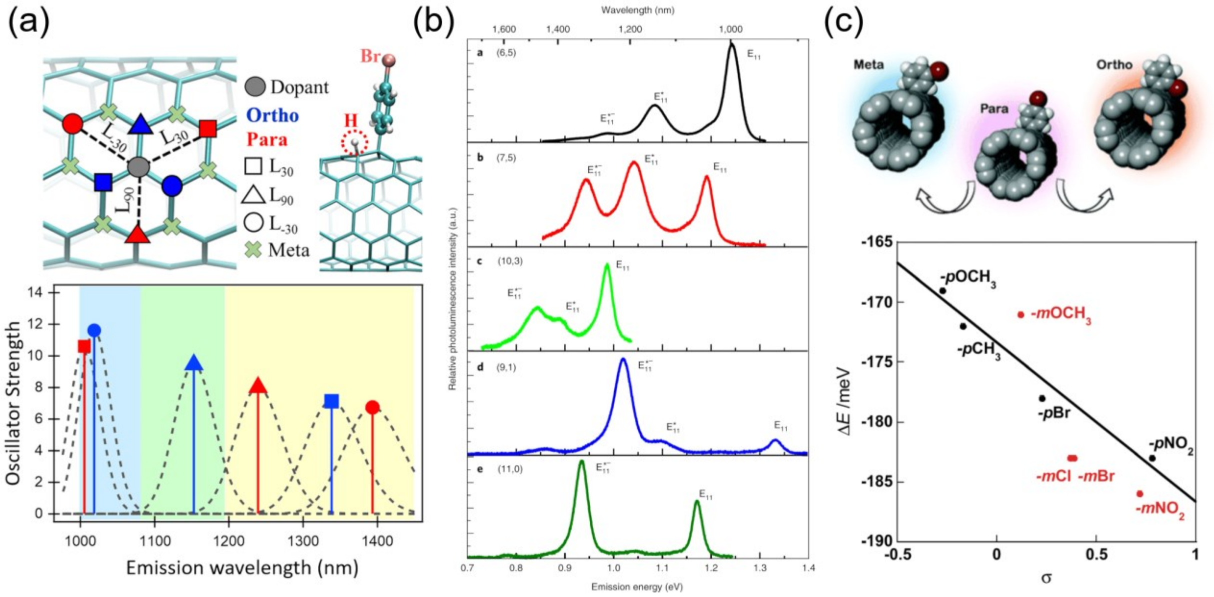

Figure 2.15: The diverse defect-induced red-shifted emission spectra (a) Six possible emissive binding configurations of the functional group and the pairing group (hydrogen), and the calculated oscillator strength *versus* the emission wavelength respectively. (b) Example defect-state photoluminescence spectra of different SWCNT chiralities. (c) The red-shifted defect-state emission can be modulated by the substituent positions of the functional group. Sigma (σ) stands for the Hammett constant, which is associated with the electron-withdrawing or electron-donating ability (σ>0 indicates an electron-withdrawing substituent) of the substituent group[140]. [Adapted and reproduced with permission from (a) reference[81], American Chemical Society; (b) reference[84], Springer Nature; (c) reference[136], Royal Society of Chemistry.]

There have been many reports regarding synthetic methods of SWCNT functionalization (doping) with various alkyl or aryl functional groups[16,141]. In this thesis, since we used only aryl-functionalized SWCNTs via a diazonium reaction, the following description will focus on this type of functional group. To introduce aryl sp^3 quantum defects on SWCNTs in the liquid-phase dispersion is arguably the most common technique, which is highly scalable and versatile, and can seamlessly be performed after SWCNTs purification and sorting. Both solution functionalization methods of aqueous dispersion with surfactants and organic solvent with polymer wrapping have been demonstrated in simple, reproducible, and large-scale manners[142,143]. Additionally, pristine SWCNTs (films) dispersed on solid substrates can also form quantum defects by similar liquid-phase dip-doping methods to achieve spatially defined functionalization areas via pre-patterning[144] or light-driven photochemical reactions[145,146]. To meet the specific needs of certain device structures, such as air-suspended SWCNTs, vapor-phase reaction provides extra diversity for quantum defect formation[147].

Throughout the development of synthetic techniques of SWCNT functionalization for luminescent quantum defects, trends in dealing with some fundamental challenges can be observed, namely the control over uniform defect-state emission as well as the quantification of quantum defect density. The other aspect of the diverse defect-state emission, mainly owing to different functional group binding configurations as discussed previously, is the hurdle of reaching uniform defect-state luminescence. As briefly mentioned, due to the chiral-dependent functionalization, defect-state luminescent uniformity could be improved by choosing near zig-zag SWCNTs[84]. Since then, a few more works of various synthetic approaches from different perspectives have been published. Settele et al. demonstrated the selective creation of sp^3 quantum defects via base-mediated nucleophilic functionalization in UV-light radiation or dark environments[83]. Wang et al. proposed controlling the binding configuration of the functional group and the paring group based on the steric hindrance effect under different reaction conditions[86]. On the other hand, Yu et al. studied the molecular design by altering the arrangement of π-conjugated substituents of the functional group to enhance interaction with nanotube sidewalls and facilitate the formation of specific defect binding configurations[139]. Instead of tackling the issue directly from the synthesis point of view, Qu et al. showed that post-laser irradiation at the E_{22} transition energy of the SWCNT hosts could reduce the defect-state emission wavelength distribution by converting the chemical bonding into a more thermodynamically favored configuration[87].

Another nontrivial question for functionalization is the determination of defect density. Since the sp^3 defect formation disturbs the sp^2 carbon lattice, it inevitably hampers the electrical properties which in principle can be used to detect the defect formation by monitoring the discrete steps in electrical resistance. This approach however has only been reported until now from metallic SWCNTs[148,149]. For semiconducting SWCNTs, non-destructive optical characterization becomes preferable, usually via fluorescence or Raman spectroscopy. Typically, the correlation of moderate reactant agent (diazonium salts) concentration and the intensity ratio of defect-induced fluorescence (E_{11}*) to intrinsic optical transition intensity (E_{11}) provides reasonable information about the defect density. Ma et al. monitored real-time E_{11} and E_{11}* fluorescence on single SWCNT and molecule levels, which allows for quantifying the defect number given a certain SWCNT length distribution[96]. The advantages of this method are also the less demanding measuring setup requirements. On the other side, Raman spectroscopy is a well-known technique probing defects in the sp^2 carbon lattice as the signature of the D band in Raman spectra[150]. The integrated intensity ratio of the D band to the G band was conventionally an indicator of defect formation under various reactant agent concentrations. Sebastian et al. reported the correlation of the D/G intensity ratio with the defect density, and by combining with the E_{11} photoluminescence quantum yield (PLQY) of functionalized SWCNT under different diazonium salt concentrations enables quantitative evaluation of the sp^3 defect density for SWCNT with small diameters[97,151]. Besides, the intermediate frequency mode (IMF) features, which position between the radial breathing mode (RBM) and the D mode in Raman spectra, were activated upon covalent functionalization, and Soltani et al. as well as Weight et al. have further investigated in similar directions[152,153]. The studies pointed out the increase of IMF along with the decrease of RBM in intensity with higher defect density and offered another methodology of quantitatively evaluating the functionalization based on the correlation between the integrated intensity ratio of IMF to RBM bands and chirality-specific defect density.

2.2.3 Electroluminescence

In this section, we focus on the electroluminescence of pristine and functionalized SWCNTs. We start with a brief discussion of the electrical properties, focusing on the roles of electrical contacts as electroluminescence characterization requires the integration of SWCNTs into device configurations. Then we introduce the common electrical-driven light emission mechanisms, the ambipolar carrier recombination and unipolar impact excitation, and discuss some published works of pristine SWCNTs. Finally, we review the recent studies related to the electroluminescence of sp^3-functionalized SWCNTs in terms of network or single-tube geometries.

Electrical properties

Field-effect transistors integrated with semiconducting SWCNTs (sc-SWCNTs) have shown superior electrical properties in early studies, for instance, the high on-state current with an on/off ratio in the range of 10^7. It is also well-known that the SWCNT/electrode contacts play a significant role in device performance[154,155]. In this section, we focus on the roles of electrical contact. Conventionally, metallic electrodes are used for the SWCNT device fabrication, and studies have pointed out the advantage of using palladium (as well as larger diameter nanotubes) to lower the Schottky barrier for higher on-state current, as shown in **Figure 2.16a**, which is related to the weaker metal/CNT hybridization[156]. In 2018, Engel et al. demonstrated the usage of graphene electrodes to enable large-scale nanomaterial placement via electric-field-assisted dielectrophoresis (DEP)[157], as the methods visualized in **Figure 2.16b**. In the work, large-scale integration of CNTs into device configuration was presented, and the additional geometrical and electrostatic advantages of graphene electrodes were explained. In other words, the reduction of electrode thickness localizes the electric field distribution at the substrate for ideal deposition, as well as reduces the bending of the deposited nanomaterials at the contact edge, examples of which are depicted in **Figure 2.16c**. Despite the limited understanding of the graphene/CNT hybrid system, Özdemir et al. modeled the device performance by associating it with the graphene/CNT spacing and contact length[158]. Additionally, the work elucidates the experimentally observed ambipolar transport behavior, which brings insight into developing efficient all-carbon field-effect transistors and may refer to the study of the electroluminescence characteristics.

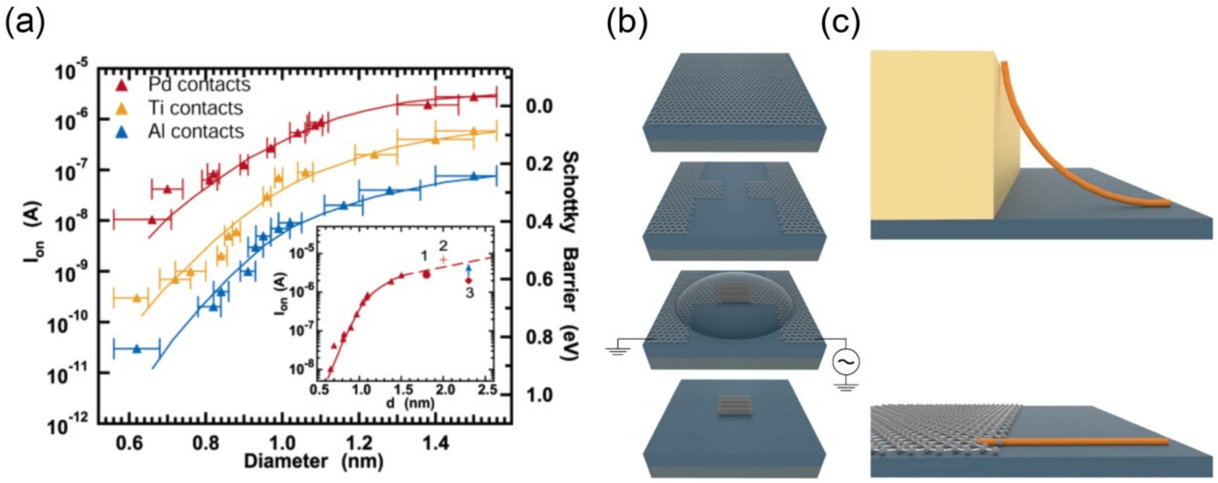

Figure 2.16: The roles of electrical contact in SWCNT field-effect transistors (a) The influence of metal contact and nanotube diameter on the on-state current and Schottky barrier. (b) Sketches of nanomaterial placement via DEP. (c) The geometrical advantage of using graphene contact instead of metal contact. [Adapted and reproduced with permission from (a) reference[155], American Chemical Society; (b, c) reference[157], Springer Nature.]

Electroluminescence mechanism

Electroluminescence spectroscopy can be performed by electrically exciting SWCNTs integrated into a device configuration, usually in a three-terminal (source, drain, and gate) field-effect transistor (FET) geometry. Light emission occurs while current is injected into the SWCNT channel to form excitons which further relax radiatively. Generally speaking, there are two common well-accepted mechanisms of exciton generation, namely carrier recombination and impact excitation. For the case of carrier recombination, the electrons and holes are injected simultaneously into the channel from opposite sides of the electrodes, the source and drain, in an ambipolar FET as shown in **Figure 2.17a**. The carriers form excitonic bound states and recombine radiatively for light emission. The earliest work regarding this emission mechanism was reported by Misewich et al. in 2003[159]. The emission intensity was maximum while the overall injected current was at minimum, in other words, the device was in the off-state. Further works from Freitag et al. also have demonstrated the mobile ambipolar domains, where the electrons and holes overlap, by changing the gate and source-drain voltages in a long nanotube device with symmetric contact electrodes, and an emission efficiency of 10^{-6} to 10^{-7} photons/electron−hole pair on SiO_2/Si substrate[160,161]. To improve emission efficiency, tactics such as asymmetric contact electrodes, split-gate configuration, or air-suspended geometry have been reported[162–165].

On the other hand, for impact excitation, a high electric field is necessary to accelerate “hot” carriers (single type) to generate excitons that radiatively decay in a unipolar SWCNT device and has been reported by Chen et al. in 2005[166]. With enough driving bias, the accelerated energetic carriers inelastically scatter and transfer excess energy across the bandgap to excite SWCNTs, which forms excitons in the end, as shown in **Figure 2.17b**. A minimum threshold field, related to the lowest transition energy and energy necessary for momentum conservation, is required to trigger light emission, and the emission intensity is exponentially proportional to the applied bias[166,167]. Additionally, the creation of abrupt change in the potential can be introduced by intentionally perturbing the local interface, for instance, partial suspension or various defects[166,168]. Despite the potential for bright emission and theoretically better emission efficiency than carrier recombination under ambipolar conditions, the high electric field often causes self-heating of SWCNTs and is responsible for the broad spectral features with linewidths on the order of 100 meV[165,169,170]. In terms of biasing metallic SWCNTs, thermal light emission due to Joule heating can take place under a high electric field and the emission features of thermally excited electrons and holes refer to the interband transition[171,172]. Similarly, thermal (incandescent) emissions of SWCNTs have also been reported in which the emission spectra fit to the blackbody radiation from Planck's law[173–176]. Since the electrically driven light emission of SWCNTs from thermal radiation and electron-hole recombination based on impact excitation both require a high electric field and result in a broad emission spectrum, electroluminescence of SWCNTs excited at high driving bias could sometimes be attributed to both components[177].

The exciton picture in the optical properties of SWCNTs can be applied both to electroluminescence (EL) and photoluminescence (PL). Therefore, many fundamental emission characteristics are similar despite the different means of exciton generation. Both EL and PL are polarized owing to the 1D structure along the nanotube axis[159,178]. The dominant emission mostly follows the lowest optical transition energy E_{11} with comparable linewidth[165]. Tuning the carrier doping level of SWCNTs to facilitate charged exciton (trion) formation has also been demonstrated[124,179], as given in **Figure 2.17c**. However, the difference between forming excitons by photoexcitation (PL) or electrical excitation (EL) still influences the emission properties. Generally, the emission linewidth of EL is broader than PL emission linewidth due to the current-induced self-heating effect through exciton-phonon interactions[180,181]. Besides, electrical pumping has a higher chance of forming free electron-hole pairs in comparison to photoexcited excitons which are often subject to the optical transition selection rules[167,182]. Consequently, the emission spectral features by various excitations can be different. Additionally, the reported emission quantum efficiency of photoluminescence (around 1 %[183,184]) is generally higher than that of electroluminescence (around 0.01 – 0.1 %[70,185]). However, the essential drawback of photoexcitation comes from the limited absorption cross section (absorption coefficient less than 1 %[186]), and the further requirement of an external excitation source hindering on-demand on-chip integration.

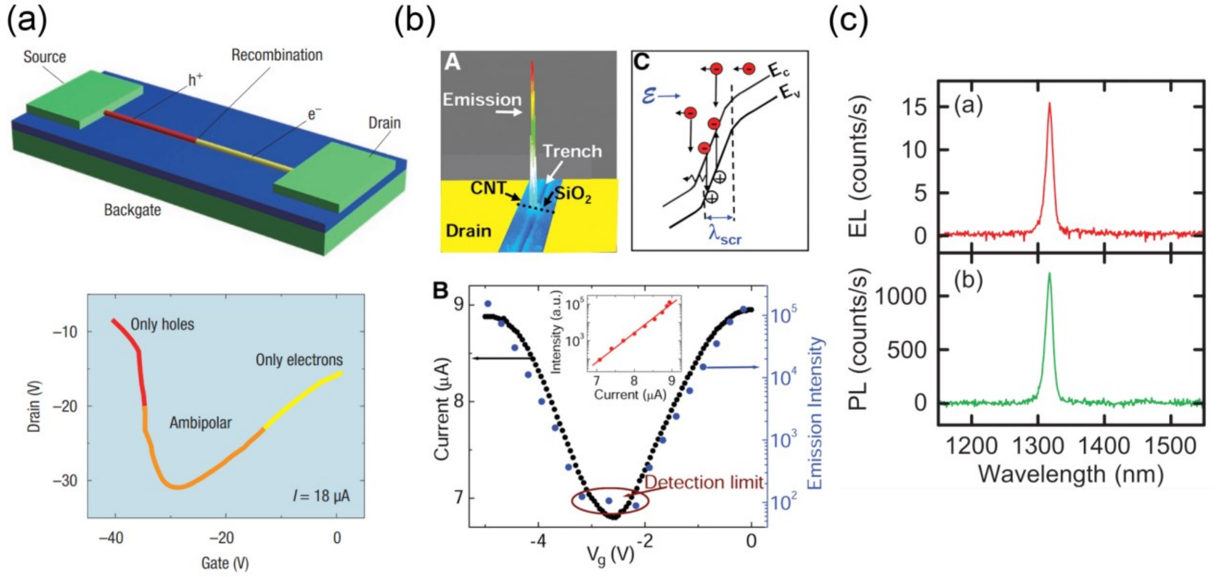

Figure 2.17: Electroluminescence mechanism and comparison between PL and EL of SWCNTs (a) Electroluminescence from carrier recombination in the ambipolar regime. (b) Light emission from impact excitation under high excitation bias in the unipolar regime. (c) Comparable emission characteristics in terms of emission wavelength and linewidth of EL and PL. [Adapted and reproduced with permission from (a) reference[7], Springer Nature; (c) reference[165], AIP Publishing. (b) From "Chen et al., Bright Infrared Emission from Electrically Induced Excitons in Carbon Nanotubes. Science 310, 1171-1174 (2005)."[166] Reprinted with permission from AAAS.]

Defect-state electroluminescence of functionalized SWCNTs

Since the pioneering work of presenting electroluminescence based on SWCNTs in 2003[159], SWCNTs have been explored as active materials for light-emitting devices due to their unique electrical and optical properties. The ambipolar characteristic as well as the high carrier mobility facilitate both electron and hole carrier injection. Moreover, the exciton photophysics and tunable chiral-dependent emission wavelengths in the near-infrared make SWCNTs promising as classical and non-classical on-chip emitters. However, similar to the fundamental challenges of low emission quantum yield for photoluminescence, the electroluminescence of SWCNTs also faces even lower emission efficiency owing to the enhanced screening and non-radiative decay due to excess free carriers[169,187] along with the additional substrate effect[188]. Therefore, replacing the pristine SWCNTs with the sp^3-functionalized SWCNTs by taking advantage of the superior optical properties based on the exciton localization, as discussed in Section 2.2.2, appears to be a reasonable tactic for developing SWCNT light-emitting devices. However, since the covalent functionalization of SWCNTs disturbs the sp^2 lattice structure, which correlates with the electrical properties, the influence of the sp^3 defects and the defect density on electrical properties would require further investigation. Indeed, Gordeev et al. reported that moderate covalent functionalization would not be detrimental to the charge transport of single-tube semiconducting SWCNTs[144]. In this study, the direct on-device functionalization reaction was activated by laser radiation with *in situ* control via Raman spectroscopy, as displayed in **Figure 2.18a**. Similarly, Zorn et al. exhibited that despite the decrease of electron and hole carrier mobilities with the introduction of sp^3 defects (drop ~70 % with the highest defect density, as shown in **Figure 2.18b**), dense semiconducting SWCNT network light-emitting devices remain fully functional[189]. Besides, the electrical-driven defect-state electroluminescence, which shows similar red-shifted emission as defect-state photoluminescence, varies with the degree of functionalization monitored by the Raman D/G peak area ratio. The defect-state electroluminescence occurred via ambipolar carrier recombination. On the other hand, in **Figure 2.18c**, defect-state electroluminescence via impact excitation by unipolar carrier injection has also been demonstrated by Xu et al. from thin film SWCNT network devices[190]. The emission intensity showed an exponential dependence on the applied source-drain current. Apart from the defect-state electroluminescence associated with localized excitons, electroluminescence from localized charged excitons (trions) was presented by spatially correlating the photoluminescence and electroluminescence from functionalized SWCNT devices. In terms of tunable defect-state emission wavelengths based on the binding configuration of functional groups, see **Figure 2.18d**, Zorn et al. tailored the electrical-driven emission from small-diameter nanotube devices into the telecommunication O-band (1260 – 1360 nm)[191]. It was mainly achieved by a controlled synthetic method to preferably introduce lower energy defect states ($E_{11}{}^{*-}$) with a BCB-passivated substrate surface (a cross-linked benzocyclobutene-based polymer), enabling near-intrinsic light emission. Most of the defect-state electroluminescence works were investigated in the form of dense or sparse SWCNT network devices. However, to address the possibility of developing single-photon emitters, a single-tube device is necessary and has been reported by our group and will be discussed in detail in this thesis[19], as depicted in the 3D illustration of **Figure 2.18e**.

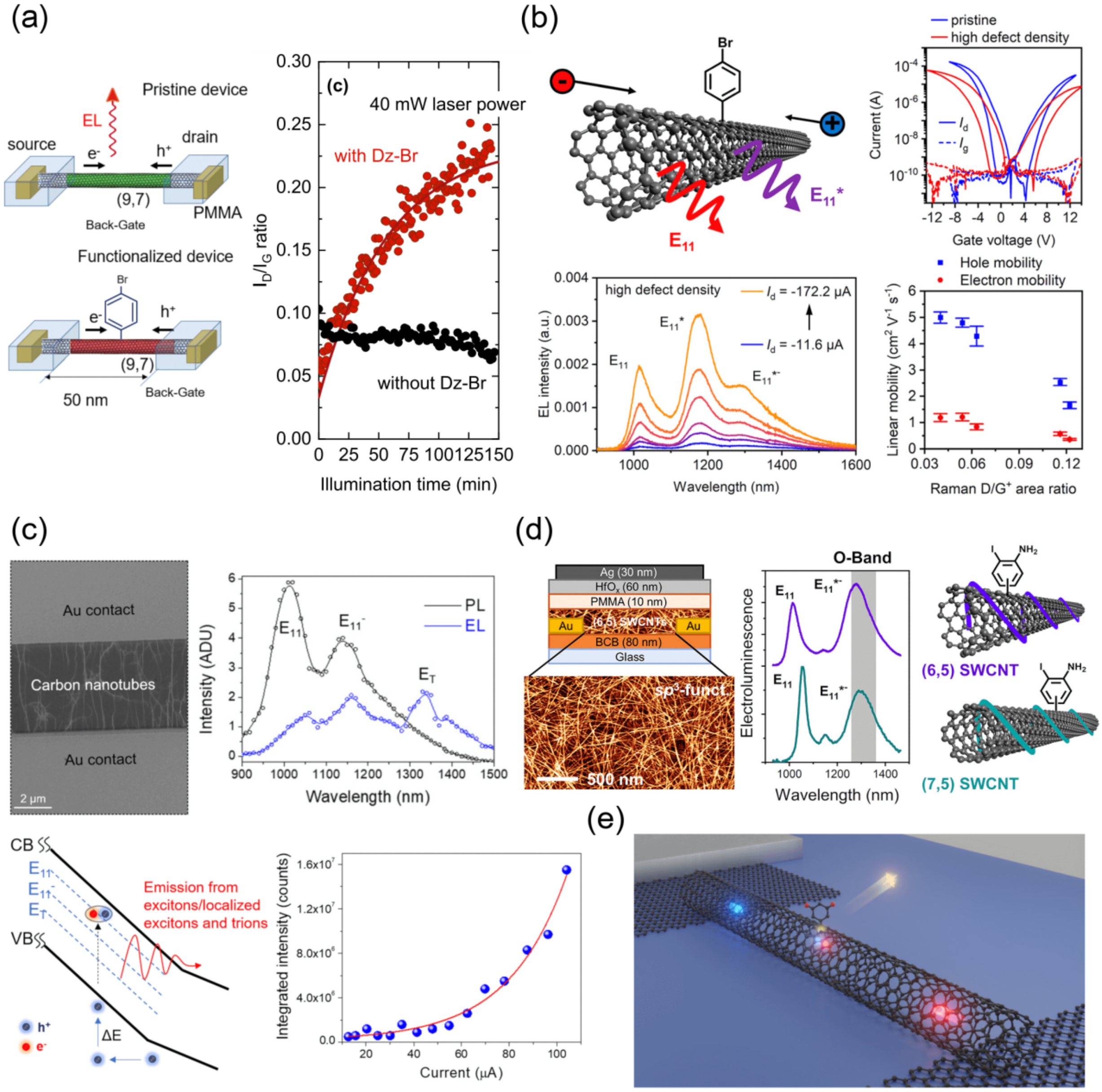

Figure 2.18: Defect-state electroluminescence from carrier recombination (a) The laser-assisted selective functionalization and *in situ* monitor with Raman spectroscopy. (b) The influence of charge carrier mobility of dense SWCNT network devices under sp^3 functionalization, and defect-state electroluminescence via carrier recombination. (c) Defect-state electroluminescence of sparse SWCNT network devices from impact excitation. (d) Modifying the red-shifted emission wavelength into the telecommunication O-band. (e) Defect-state electroluminescence from single-tube devices with sp^3 quantum defects. [Adapted and reproduced with permission from (a) reference[144], American Chemical Society; (b) reference[189], American Chemical Society; (c) reference[190], AIP Publishing; (d) reference[191], American Chemical Society; (e) reference[19], American Chemical Society.]

2.3 Carbon nanotubes as non-classical light sources

One of the important reasons for SWCNTs to continuously grab attention is the potential development of single-photon emitters, which is an essential building block in the quantum photonic field. The tunable near-infrared emission wavelength is an additional advantage regarding integration with optical fiber communication. In this section, we start with some reviews of single-photon emission of SWCNTs, first reported in 2008 by observing photon antibunching in photoluminescence at cryogenic temperatures. The intentional sp^3 functionalization of SWCNTs further extends this characteristic to room temperature. Then we introduce some works on coupling SWCNT emitters into optical microcavities to boost the light emission characteristics by strengthening the light-matter interaction as we will demonstrate our contribution regarding SWCNT emitters in photonics in Chapter 6. To begin, we describe the basics of photon statistics as the theoretical foundation for correlation measurements.

2.3.1 Photon statistics and correlation measurement

Before jumping into the topic of reviewing non-classical light emission from SWCNTs, especially the single-photon emission behavior in the near-infrared, we now discuss the classes of light sources based on the photon statistics and the experimentally related photon correlation measurement. Usually, regarding the temporal distribution of light, three types of light sources can be distinguished, namely coherent (random), bunched (chaotic), and antibunched (non-classical) light sources. Light emission from a laser operated well above the threshold is a typical example of coherent light with a random photon spacing as a function of time. The photon statistics for the coherent light with constant power follows a Poisson distribution and can be described as

$$P(n) = \frac{\bar{n}}{n!} e^{-\bar{n}}$$

, where n=0, 1, 2, … refers to the photon number, $P(n)$ is the probability of detecting n photons, and $\bar{n}$ is the mean value of the photon number. The actual (detected) photon number fluctuates around the average value $\bar{n}$ with a standard deviation of $\Delta n = \sqrt{\bar{n}}$ according to the Poissonian statistics. In terms of bunched light, such as thermal light, super-Poissonian statistics can be expected which shows larger standard deviation $\Delta n > \sqrt{\bar{n}}$. Larger fluctuations in the photon numbers can be anticipated in a given time interval than from the coherent light. On the other hand, antibunched light can refer to sub-Poissonian statistics with a smaller standard deviation $\Delta n < \sqrt{\bar{n}}$, meaning a more equal spacing distribution of detected photons as a clear evidence of the quantum nature of light.

To experimentally differentiate the classes of light sources, photon correlation measurements are usually performed and the second-order correlation function g^2(τ), which is associated with the correlation of intensity fluctuations, is extracted. The experiment can be performed in a Hanbury Brown and Twiss (HBT) configuration, schematic in **Figure 2.19a**, where the incident stream of photons is equally divided by a 50/50 beam splitter and detected by two independent detectors. The output signals from the two detectors are fed into a correlator which precisely records the arrival time of incoming photons. Since the intensity of incident light is proportional to the registered photon counts on the detectors, the second-order correlation function can be expressed as

$$\mathrm{g}^2(\tau) = \frac{\langle I(t)\cdot I(t+\tau)\rangle}{\langle I(t)\rangle\langle I(t+\tau)\rangle} = \frac{\langle n_1(t)\cdot n_2(t+\tau)\rangle}{\langle n_1(t)\rangle\langle n_2(t+\tau)\rangle}$$

with $n_i(t)$ being the photon count numbers registered on detector i at time t, and $\langle n_i(t)\rangle$ referring to the average value of photon counts. In other words, the $\mathrm{g}^2(\tau)$ value is proportional to the probability of detecting another photon on the second detector at time τ, assuming the first detector registers a photon at time $t = 0$. Now, if we take a coherent light source with a constant output power and perform the HBT experiment, it's reasonable to consider that $\langle I(t)\rangle = \langle I(t+\tau)\rangle$ given the constant average intensity. Additionally, the intensity fluctuations at times t and $t + \tau$ will be uncorrelated when τ is greater than the coherence time τ_c, namely

$$\mathrm{g}^2(\tau \gg \tau_c) = \frac{\langle I(t)\cdot I(t+\tau)\rangle}{\langle I(t)\rangle^2} = \frac{\langle I(t)\rangle^2}{\langle I(t)\rangle^2} = 1$$

and $I(t) = \langle I\rangle + \Delta I(t)$ with $\langle \Delta I(t)\rangle = 0$, where $\Delta I(t)$ is the deviation from the mean intensity $\langle I\rangle$. That being said, when characterizing the photon stream of a single-photon emitter in an HBT setup, in which the time interval between subsequent emitted photons is more regular, the first incoming photon triggers only one of the two detectors to start the time counting of the correlator. At the same time, the other detector will record no photon at $\tau = 0$. As every incoming photon has a 50 % probability of being directed to either detector due to the 50/50 beam splitter, the correlator will complete an event when eventually a subsequent photon hits the other detector and triggers the stop process. Prior photons that go to the same first detector will be ignored. As a result, we can expect the $\mathrm{g}^2(\tau)$ value at $\tau = 0$ in principle to be zero and it increases for larger τ values until it reaches the value of unity. Indeed, the antibunched light can be identified when $\mathrm{g}^2(0) < 1$. On the other hand, the bunched light is defined by $\mathrm{g}^2(0) > 1$, which can be straightforwardly understood as such the probability of detecting another photon for a small value of τ is expected to be higher since the photon stream consists of photons in bunches. Illustrations of photon streams from different classes of light sources and examples of second-order correlation function measurement results of different light sources are summarized in **Figure 2.19b,c**.

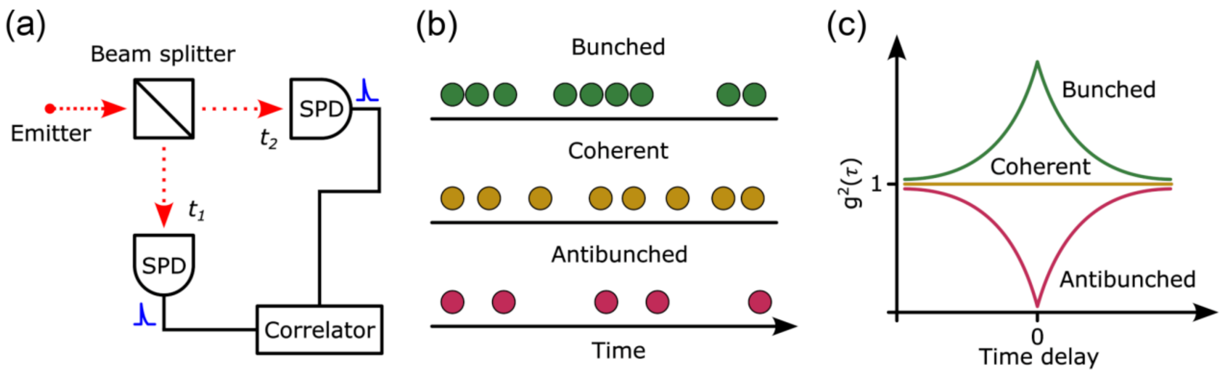

Figure 2.19: Photon correlation measurement and the class of light sources (a) A schematic of the Hanbury Brown and Twiss setup for photon correlation measurement. (b) Illustrations of photon streams from different classes of light sources. (c) Example of the second-order correlation function from different light sources.

2.3.2 Single-photon emission

The first experimental demonstration of photon antibunching in photoluminescence from pristine SWCNTs was reported by Högele et al. in 2008[10], as shown in **Figure 2.20a**. The single-photon emission was achieved owing to the localization of excitons in the shallow trap states formed in the 1D system in the disordered dielectric environment[192]. The antibunching behavior was observed only at cryogenic temperature and depended on the excitation pumping power as a consequence of the thermal de-trapping effect. At a similar temperature, Khasminskaya et al. demonstrated in 2016 electrically driven photon antibunching in the electroluminescence from SWCNTs integrated into nanophotonic waveguides[11]. As a side note, room-temperature single-photon emission was exhibited in 2017 by Ishii et al. from mobile excitons in pristine micrometer-long air-suspended SWCNTs due to efficient exciton-exciton annihilation in which the exciton diffusion and environmental confinement play critical roles[193–195]. To reduce the de-localization of excitons due to thermalization, creating deep exciton trap states to extend the single-photon emission nature to higher temperatures, in contrast to the unintentional and uncontrollable shallow traps at low temperatures, becomes an obvious strategic approach. Indeed, the room-temperature single-photon emission of SWCNTs with deep excitonic trap states was reported by Ma et al. in 2015. The SWCNTs were embedded into an electron-beam deposited SiO_2 matrix in which low concentrations of oxygen dopants were indirectly introduced to create deep trap states with various potential depths[17], displayed in **Figure 2.20b**. In 2017, shown in **Figure 2.20c**, He et al. demonstrated tunable room-temperature single-photon emission from aryl sp^3 functionalized SWCNTs with remarkable single-photon purity in the telecom wavelengths (C-band)[18]. Additionally, Nutz et al. observed both antibunching of defect-induced exciton and trion (charged exciton) photoluminescence from SWCNTs with quantum defects by covalent alkyl groups attachment and studied the photoexcited exciton population distribution at cryogenic temperature[90]. Meanwhile, Zheng et al. presented single-photon emission characteristics from SWCNTs covalently functionalized by single-stranded DNA at both cryogenic and room temperature, which provide a new engineering route for quantum defect formation[89]. Generally speaking, the high spectral purity of emitters is one of the prerequisites for successful photon antibunching observation. It often could be resolved by the minimization of substrate interaction, which indeed was demonstrated in early works from Hofmann et al. by air-suspending pristine nanotubes to boost the correlation measurement outcomes[196]. Walden-Newman et al. presented that embedding pristine nanotubes into nonpolar polystyrene as a cavity dielectric enhances not only the spectral purity but also light extraction[197]. On the other hand, the covalent sp^3 functionalization of SWCNTs most of the time results in diverse emission spectra, as was discussed in the previous section, which inspired many fundamental works on improving spectral purity. As has been studied in many additional cases of pristine SWCNTs, integrating nanotube emitters into optical microcavities effectively boosts certain emission properties, such as bringing out brighter and cleaner emission lines. Naturally, the integration of functionalized SWCNTs into similar photonic structures could overcome the challenge of achieving single-photon emission. In the next section, we will discuss some published works on coupling functionalized SWCNTs with photonic structures and their single-photon emission performance.

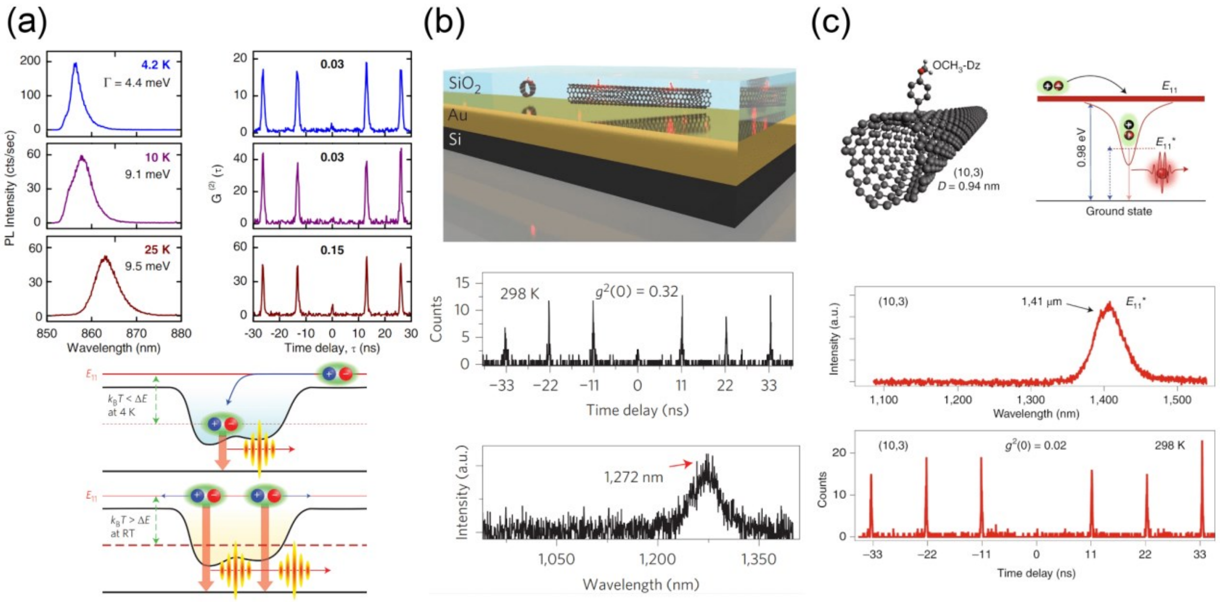

Figure 2.20: Single-photon emission of SWCNTs via pulsed optical excitation (a) Photon antibunching observed from pristine SWCNTs at cryogenic temperature due to the local shallow excitonic trap states. (b) Room temperature single-photon emission of SWCNTs with solitary oxygen dopant-induced deep trap states. (c) Room temperature single-photon emission of SWCNTs with sp^3 quantum defects via aryl diazonium reactions. [Adapted and reproduced with permission from (a) reference[10], American Physical Society; (b) reference[17], Springer Nature; (c) reference[18], Springer Nature.]

2.3.3 Functionalized carbon nanotubes in nanophotonics

Integration of nanoscale emitters into optical cavities or resonators, which provide a confined space for light to oscillate and generate resonant modes to strengthen the light-matter interaction, has been a common strategy to enhance the emission characteristics. For the case of pristine SWCNTs, both photonic and plasmonic nanocavity platforms have been utilized to tailor the emission properties, such as the emission efficiency and emission line width based on the Purcell effect[12,13,21,198,199]. The Purcell enhancement of the emitters refers to the enhancement of the spontaneous emission, increasing the radiative decay rate, and can be described by the ratio between the emission rate of the resonant cavity mode and the free-space emission as the Purcell factor F_P,

$$F_P = \frac{3}{4\pi^2}(\frac{\lambda}{n})^3 \frac{Q}{V}$$

Here, λ is the wavelength of the emitted light, n is the refractive index of the medium, Q is the quality factor of the cavity, and V is the optical mode volume. Since the introduction of intentional sp^3 quantum defects into SWCNTs, a few works have been reported that tackled various challenges including enhancing single-photon emission and the spectral diversity from different defect-states. Ishii et al., in **Figure 2.21a**, demonstrated room-temperature single-photon emission from functionalized SWCNTs on silicon microcavities with enhanced emission brightness and reduced emission lifetime at the cavity mode wavelengths[200]. The study also presented the preservation of antibunching behavior even under higher optical excitation power. In **Figure 2.21b**, Luo et al. have reported even higher cavity-enhanced quantum efficiency with defect-state emission lifetime down to 10 ps by integrating functionalized SWCNTs into plasmonic nanocavities[91]. Meanwhile, room-temperature single-photon emission in the telecom O-band with a purity of up to 99 % was also observed. Recently, Borel et al. presented the coupling of functionalities SWCNTs into a fiber microcavity, as displayed in **Figure 2.21c**, and reported a brightening effect of fiber-coupled single photon emission with an output count rate of up to 20 MHz in the Purcell regime[88]. Owing to the advantage of the reconfigurable fiber cavity, tunable single-photon emission was achieved in the telecom wavelengths.

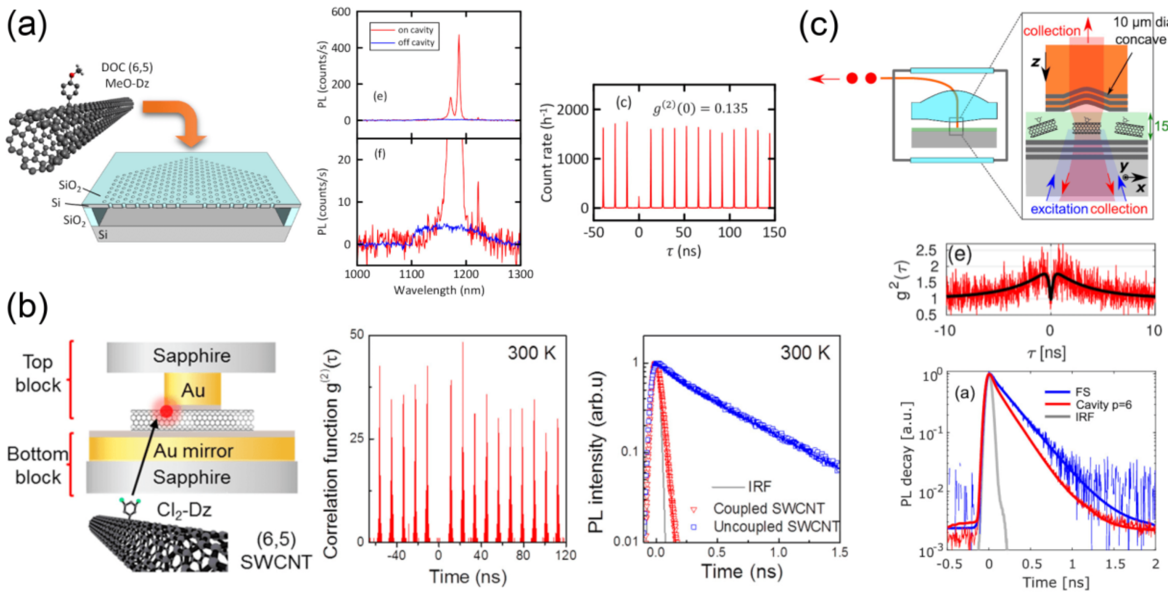

Figure 2.21: Integration of functionalized SWCNTs into microcavities (a) Light-matter interaction strengthening of functionalized SWCNT on a silicon photonics platform. (b) Coupling of functionalized SWCNTs in plasmonic nanocavities. (c) Brightening of functionalized SWCTNs in a tunable fiber microcavity. [Adapted and reproduced with permission from (a) reference[200], American Chemical Society; (b) reference[91], American Chemical Society; (c) reference[88], American Chemical Society.]

– this page left intentionally blank –

3 Experimental Methods

In this chapter, we will discuss the experimental methods generally used throughout the thesis. As a side note, some approaches may vary according to the need for different projects but will be pointed out when required. The chapter will be divided into three parts, namely the fabrication of single-walled carbon nanotube (SWCNT) devices, the characterization of SWCNT devices, and lastly the photon correlation measurement. In the first section, which can be roughly viewed as two parts, we first describe the preparation of SWCNT dispersion, including purification, length sorting, and further functionalization. We then continue discussing the fabrication of SWCNT devices, covering structure patterning via electron beam lithography and SWCNT deposition via electric field-assisted dielectrophoresis. In the second section, we introduce characterization techniques involving charge transport measurement for electrical properties, electroluminescence spectroscopy for electrical-driven light emission characteristics, and scanning electron microscopy for device imaging. In the third part, we focus on the setup of photon correlation measurement based on the Hanbury Brown and Twiss (HBT) configuration. Finally, we elaborate on the necessary setup alignment and approaches for data analysis.

3.1 Device fabrication

This section describes the SWCNT dispersion preparation and device fabrication. Since the device configuration for the results in Chapter 4 and Chapter 5 are rather identical, similar electron beam lithography procedures were implemented. However, for Chapter 6, different SWCNT chirality was used, and the different device configurations with cross-bar photonic crystal (PhC) cavities require more complex fabrication processes. Nevertheless, the dielectrophoresis for SWCNT deposition remains applicable throughout the work.

3.1.1 Dispersion preparation and functionalization

The pristine and aryl-functionalized (7, 5) SWCNT dispersions were kindly prepared with the courtesy of our long-term collaborator, Dr. Frank Hennrich from Karlsruhe Institute of Technology, and the aryl-functionalized (6, 5) SWCNT dispersion was provided by collaborators from Los Alamos National Laboratory. The raw SWCNT soot for pristine (9, 8) dispersion was provided by collaborators from the University of Sydney. The dispersion preparation is described generally as the following:

The preparation of pristine (7, 5) SWCNT dispersion has been described in detail in our previous work[69]. The PFO polymer-wrapped (7, 5) SWCNT dispersion was prepared by dissolving the raw material soot (CoMoCAT, Sigma-Aldrich) and the polymer poly(9,9-di-n-octylfluorenyl-2,7-diyl) (PFO, Sigma-Aldrich) in toluene. The suspension then went through a sonication treatment in a water-circulation cooling bath and centrifugation aiming for high purity. Size exclusion chromatography was followed for length sorting resulting in suspension fractions with various length distributions. UV−vis−NIR absorption spectra and photoluminescence excitation maps were recorded by using a home-built setup as described elsewhere[201]. The spectra were corrected for wavelength-dependent excitation intensity and the instrumental response of the spectrometer. The (6, 5) SWCNT dispersion was produced similarly except for the polymer poly[(9,9-dioctylfluorenyl-2,7-diyl)-alt-co-(6,6 ´ -{2,2 ´ -bipyridine})] (PFO-BPy) (American Dye Source) was used[72], and poly(9,9-di-n-dodecylfluorenyl-2,7-diyl) (PODOF) (Sigma-Aldrich) was used for sorting (9, 8) SWCNTs[70]. For the functionalization, 3,5-dichlorophenyldiazonium tetrafluoroborate was added to pristine suspension with a suitable nanotube length distribution and heated slightly less than the boiling point temperature of toluene in a dark environment[19]. Right after the functionalization process, PL spectra were measured to ensure the appearance of red-shifted defect-state emission.

3.1.2 Electron beam lithography

Electron beam lithography, e-beam lithography, is a widely used direct writing technique for nanofabrication by patterning structures down to the sub-10 nm scales. The system often is similar to a scanning electron microscope (SEM) except additionally equipped with a pattern generator. The focused electron beam changes the properties of the electron-sensitive films (usually referred to as resists) on substrates and alternates their solubility. The resist after sufficient electron beam exposure, either becomes more soluble (positive resist) or less (negative resist) which enables selective dissolving during development and often is followed by various processes such as etching and metal deposition. One of the first developed positive e-beam resists which still remains to this day, PMMA, Poly(methyl methacrylate)[202,203], is used in this work (PMMA 950 K, Microresist). We used the scanning electron microscope (LEO Gemini 1530, Zeiss) with a pattern generator (ELPHY Plus, Raith) and ran by the CAD Elphy-32 design software.

Two types of three-terminal SWCNT field-effect transistors with different source-drain electrode materials on heavily p-type (B-doped, < 0.005 Ω·cm) silicon substrates with a 300 nm thermal SiO_2 layer as the global back-gate electrode were fabricated in this thesis. Namely, devices with monolayer CVD graphene electrodes (Graphenea) and with conventional metallic electrodes. For the graphene-based electrode devices, three e-beam lithography steps with proximity correction were required for patterning electrodes. PMMA was used as a positive resist (PMMA 950 K A4.5 in Anisole, 6000 rpm). Samples were spin-casted with resist and prebaked on a hot plate for 3 minutes at 150 °C. After the e-beam patterning, cold development was followed in a solution of methyl isobutyl ketone (MIBK) and isopropanol (1:3) placed in an ice bath at 0 °C for 30 seconds. Samples were rinsed with isopropanol, dried in a stream of nitrogen, and annealed at 90 °C for 1 minute on a hot plate. Alignment markers were defined in the first e-beam lithography followed by depositing 50 nm tungsten via RF (300 W) sputtering technique (Bestec). In the second step, graphene strips were defined in which the remaining graphene apart from the PMMA-covered strips was etched via oxygen plasma (RIE Oxford Plasmalab 80 plus, 15 sccm O_2, 60 mTorr, 30 W for 75 s). The graphene strips have channel lengths of 100 – 200 nm and were perforated with holes to minimize the contact resistance[204]. The bowtie-structured graphene stripe used for setup alignment in Section 3.3.2 was also patterned in this step. In the last lithography step, metal leads were defined and subsequently deposited with 3 nm chromium (Cr, 100 W RF) and 42 nm palladium (Pd, 70 W DC) by sputtering. The lift-off process was carried out in acetone to complete the fabrication. An illustrated process flow of the last two e-beam lithography steps for SWCNT device fabrication is shown in **Figure 3.1**.

On the other hand, for devices with metallic source-drain electrodes, only one e-beam lithography step (similar to the last step for graphene-based electrodes) is required to define electrodes with a 200 nm gap size. The PMMA resist (PMMA 950 K A2.0, 5000 rpm) was spin-coated on 300 nm SiO_2/Si wafers (Active Business Company), e-beam patterned, cold developed, and followed with 3 nm Cr and 42 nm Pd metallization. The lift-off process is performed in acetone with mild sonication. In the outlook, SWCNT devices coated with polytetrafluoroethylene (PTFE, Teflon AF-2400, Sigma-Aldrich) were prepared by spin-casting 1 % purified PTFE solution (15 µL) at 3000 rpm for 60 s and followed by 100 °C and 150 °C post-annealing on the hotplate for 5 min each in ambient conditions. The detail of the PTFE solution is referred to the work of Kumar et al[205]. To probe the metallic contact pads under the 30 nm PTFE layer, direct electron beam patterning using an exposure dose of 2.6 mC/cm^2 at 10 keV beam energy was performed to remove the Teflon layer locally[206].

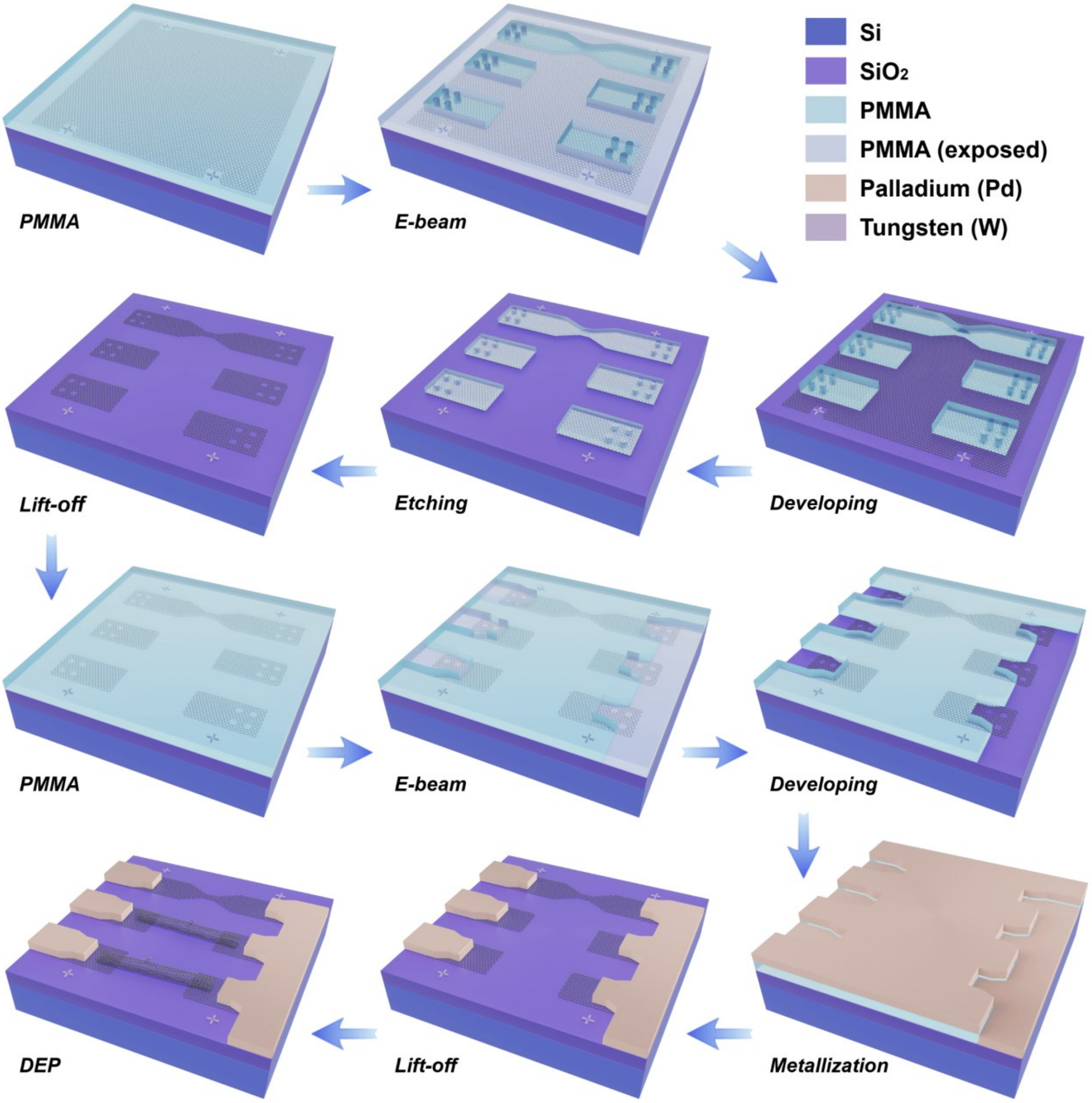

Figure 3.1: Schematic illustrations of SWCNT device fabrication process flow Fabrication steps of SWCNT devices with graphene-based electrodes starting from a CVD graphene film on SiO_2/Si substrate with alignment markers to the final integration of SWCNTs via dielectrophoresis (DEP). The process includes two e-beam lithography steps for defining graphene electrodes and metallic leads. PMMA was used as the resist and graphene electrodes was contact with palladium (Pd) metallization. The bowtie-sturctured graphene stripe for measurement setup alignment is also presented in the graphene etching process. The lithography step for patterning alignment markers, out of tungsten (W), is ignored for simplicity.

The electron beam lithography processes for preparing the device used in Chapter 6 were performed by our collaborator, Dr. Anna Ovvyan, at Universität Münster, and the nanocrystalline graphene was synthesized by Dr. Sandeep Kumar. The hybrid cross-bar PhC devices were prepared from commercial 335 nm stoichiometric Si_3N_4 on 3.320 µm thick SiO_2 layer on top of 525 µm Si substrate. The 5 nm thick nanocrystalline graphene (NCG) was synthesized on top of the Si_3N_4 surface by spin-coating photoresist (S1805 G2, Microposit) and graphitizing under high vacuum at high temperature. The photoresist solution was prepared by diluting to a 1:4 ratio with Propylene Glycol Monomethyl Ether Acetate (PGMEA, Sigma-Aldrich). The spin-coated photoresist on the substrate was followed by 110 °C annealing and further graphitization in a high-temperature (1000 °C for 10 h) vacuum furnace ($< 10^{-6}$ mbar) equipped with a quartz glass tube. The thickness of the synthesized thin film is determined by atomic force microscopy in tapping mode.

Fabrication of hybrid cross-bar PhC devices involves several steps of e-beam lithography followed by reactive ion etching (RIE). In the first e-beam lithography step alignment markers were defined with positive photoresist PMMA. A 100 nm Gold (Au) with an underneath 7 nm chromium (Cr) adhesion layer were deposited on the chip followed by a lift-off process in acetone. The challenge of patterning the desired Si_3N_4 structure without damaging the covered NCG layer was overcome by the development and optimization recipe based on e-beam lithography patterning of negative tone photoresist ma-N 2403 with underneath sacrificial layer of PMMA. After e-beam lithography exposure, the remaining not-exposed negative resist was removed in the developer MF-319. The structures were fully dry-etched into the silicon nitride layer using a CHF_3/O_2 plasma, and both resists were removed in acetone. In the next step, NCG electrodes were defined in a similar spin-coated sandwich of resist layers. After a similar e-beam exposure and development process, the noncovered NCG layer was removed in O_2 plasma and again lifted off in acetone. In the last e-beam lithography step, contact pads were transferred into the PMMA layer with deposition of 7 nm Cr adhesion layer and 120 nm Au, followed by lift-off in acetone. Finally, in the last fabrication step, 3D coupling structures were realized on each terminal of the cross-bar nanophotonic waveguides by optimized additive manufacturing using direct laser writing (DLW) with a Nanoscribe tool.

3.1.3 Dielectrophoresis deposition

Dielectrophoresis (DEP) is a technique used for manipulating dielectric nanoparticles based on the interaction of the induced dipole moment under an external inhomogeneous electric field. The dielectrophoretic force is proportional to the relative polarizability of the particle and the solvent medium along with the strength and frequency of the applied electric field. In terms of SWCNTs, the length, diameter, and tube type as well as the conductivity of the solvent medium are factors that change the interacting force described in an early work of Krupke et al.[207] by considering the SWCNT a needle-shaped particle. As an application example, the technique has been demonstrated to separate metallic (m-SWCNT) and semiconducting (sc-SWCNT) carbon nanotubes in an aqueous suspension. Under high frequency of the alternating electric field, the dielectric constant of metallic SWCNT (ε_t^m) is greater than solvent medium (ε_m) which is greater than semiconducting SWCNT (ε_t^{sc}). The opposite dielectrophoretic force for metallic (positive DEP, attractive) and semiconducting (negative DEP, repulsive) leads to opposite movement according to the external electric field gradient[56]. Apart from separating and sorting SWCNT, in this work, we use the DEP technique to achieve site-selective deposition to assemble SWCNTs into pre-patterned structures.

In this thesis, single-chirality SWCNTs were integrated into the three-terminal device using electric field-assisted dielectrophoresis[208]. Individual SWCNT deposition was achieved by diluting the toluene-based SWCNT suspension with a factor of 10 – 100 to obtain an optical density of E_{11} optical transition around 0.01 – 0.001. A 15 µL droplet of suspension was drop cast onto the device array, and a DC bias between 0.1 – 2 V was applied on the common drain electrode with the back-gate grounded by using a Keithley 2000 multimeter or an Agilent 33250 function generator for 3 min. A reference signal was monitored via an Agilent DSO1022A oscilloscope to secure proper electrical contact. The samples were rinsed with toluene several times to get rid of excess polymer residue and dried gently with a nitrogen stream. The devices were annealed at 70 °C for 10 – 15 minutes to remove residual solvent and improve contact resistance. To confirm the successful deposition of SWCNT(s) between source-drain electrode pairs, transfer characteristics of the device were conducted at ambient conditions with a probe station using an Agilent 4155C semiconductor parameter analyzer.

3.2 Device characterization

Typical characterizations of light-emitting SWCNT devices involve preliminary electrical measurements to identify working devices and the basic electrical properties, and electroluminescence spectroscopy for the main research interests. The scanning electron microscope is often used for studying the CNT length distribution of the dispersion and visualizing the device structure/numbers of nanotubes between electrodes. The scanning electron microscopy was conducted only after acquiring all necessary results to avoid undesired charging or defect formation after electron beam exposure.

3.2.1 Electrical transport measurement

Electrical properties of the SWCNT devices were characterized by probing the devices either via a probe station with triaxial probes which have a current detection limit of 30 fA or electrically wired to a home-built sample holder[70] using a universal wedge bonder (Kulicke & Soffa Model 4123) equipped with aluminum alloy (Al-Si 1 %) bonding wires. Minimum bonding power was utilized to avoid underneath oxide SiO_2 damage. The measurements were performed using Agilent 4155B/4155C semiconductor parameter analyzer operated by the EasyEXPERT software interface. For biasing, we used separate source-measurement units (SMU) for each terminal: source, drain, and gate. The bias applied to the source and gate electrode was referenced to the drain potential.

In ambient conditions, the transconductance measurements were carried out with source-drain bias no higher than 3 V and gate voltage sweep of ±4 V with 80 mV sweeping intervals to prevent device degradation or dielectric breakdown in the SiO_2 layer[209]. Here, the main purpose was usually to determine the success of

SWCNT deposition via DEP, therefore the number of power line cycles (NPLC) was set to 1 for a faster measurement rate. Higher source-drain bias, if necessary, and the constant source-drain current mode was only operated in vacuum and/or low temperature. In this case, transconductance measurements were conducted with 5 power line cycles (PLC) for better signal accuracy and 3 s hold time (no extra delay between the sampling points) for device stabilization before the measurement began. These basic electrical characteristics provide valuable information to evaluate the device's stability and the initial parameters for electroluminescence measurements.

3.2.2 Electroluminescence spectroscopy

The SWCNT devices were mounted on a home-built holder and loaded into a 4 – 500 K continuous-flow, sample-in-vacuum, optical cryostat (MicrostatHiResII, Oxford Instruments). On-chip devices were electrically wire-bonded to the palladium pads on the sample holder. The samples were vacuum annealed (below 10^{-6} mbar) in situ at 70 – 120 °C via the integrated heater (ITC 503) and electroluminescence measurements were followed without breaking the vacuum. SWCNT devices were driven by using an Agilent 4155B semiconductor parameter analyzer where source-drain electrodes were operated in constant-current mode whereas the gate electrode was running in constant-voltage mode. The cryogenic temperature (4 K or 77 K) was reached by introducing liquid helium or liquid nitrogen. As shown in the **Figure 3.2**, the optical cryostat was placed under a customized optical microscope (Zeiss Axiotech Vario) where the light from the emitter was collected with a Zeiss objective LD Plan-Neofluar (40×/NA0.6) in Chapter 4 and an Olympus objective LCPLN20XIR (20×/NA 0.45) in Chapter 5. The SWCNT device was positioned via focusing the reflected global light from the sample by a silver-coated off-axis parabolic mirror (MPD149-P01, f/4, Thorlabs) into an imaging spectrograph (Acton SP-2360, f/3.9, Princeton Instruments) and on a 1024×256 pixels charge-coupled device (CCD) array with thermoelectric cooling (PIXIS, Princeton Instruments) in the mirror mode. The electroluminescent light was focused in a similar light path into the imaging spectrograph and dispersed via a diffraction grating (85 g/mm, 1.35 µm) onto a liquid-nitrogen-cooled 1024×1 pixels linear InGaAs photodiode array (PyLon-IR, Princeton Instruments), sensitive from 950 to 1610 nm. The spectra were recorded via the Lightfield software with the built-in function for background subtraction due to the dark signals (thermal background or leakage current). Wavelength (peak position) calibration of the 1D InGaAs detector was performed by using the built-in function with a mercury-argon calibration light source (WITec). To compensate for the wavelength-dependent intensity scaling factor of the setup, all spectra were calibrated by the relative spectral sensitivity curve. The acquisition and calibration of the setup spectral sensitivity and some more details of the setup were described in our previous report[70]. The precise and stable positioning of the emitter was achieved via a motorized XY positioning stage (8MTF, Standa) along with a high-precision objective piezo scanner (P-721 PIFOC, Physik Instrumente) for tuning the focusing distance.

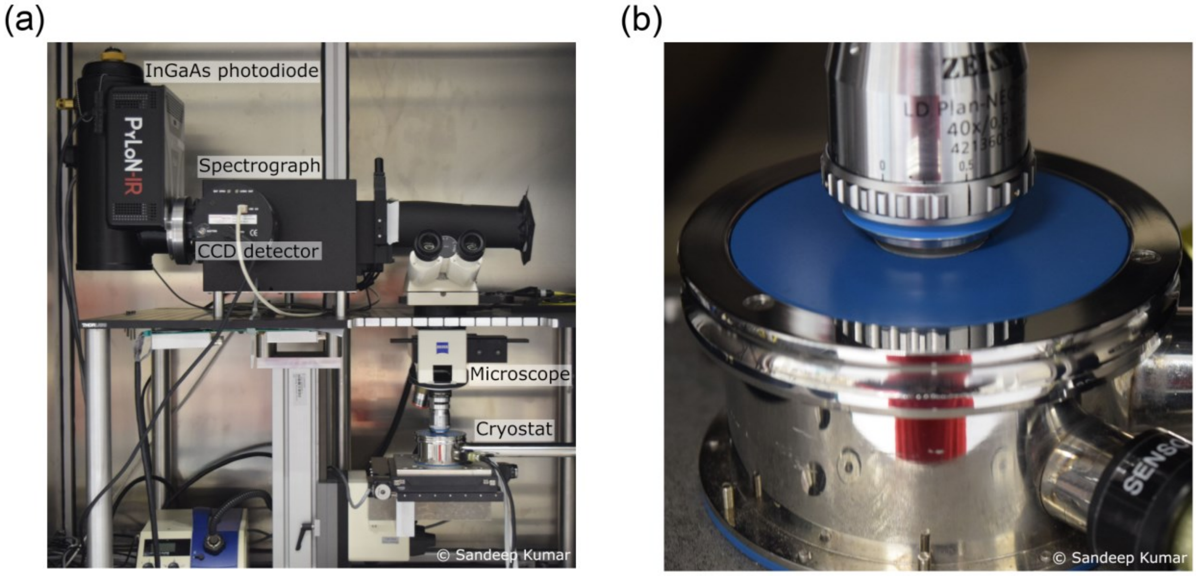

Figure 3.2: Electroluminescence (EL) spectroscopy measurement setup (a) The EL measurement setup mainly comprises the continuous-flow optical cryostat on the motorized stage, the concentrically customized optical microscope, and the imaging spectrograph equipped with two CCD and InGaAs photodiode arrays. (b) A zoom-in photograph of the optical cryostat when the microscope objective was in focus. Photographs of the EL setup were kindly taken by Dr. Sandeep Kumar.

3.2.3 Scanning electron microscopy

Scanning electron microscopy (SEM) is a common imaging technique by scanning the sample surface with a focus electron beam in a raster scan pattern. The interaction between electrons and the sample generates various information concerning the surface topography and element composition depending also on different implementations of detectors. The fabricated SWCNT field-effect transistors and the individually dispersed SWCNTs on the polished p-type silicon substrate (B-doped, > 1 Ω·cm, CrysTec GmbH) for length analysis were imaged with a field emission scanning electron microscope (Zeiss Ultra Plus). Primarily type I secondary electrons (SE1), originating from the impingement of the primary electron beam in the specimen, were collected using an immersion lens (in-lens) secondary electron detector at a 1 kV electron high tension (EHT) voltage with a 20 µm aperture and a working distance between 2 – 3 mm. The combination of low accelerating voltage and the collection of SE1 signals via an in-lens detector reveals high-resolution and surface-sensitive information, which is ideal for imaging nanoscale topographical features. To investigate the length distribution of the SWCNT dispersion, the sample was prepared by first cleaning the Si wafer with acetone/isopropanol followed by 1 minute of oxygen plasma cleaning (30 % power, Atto Plasma Cleaner, Diener electronic GmbH), and spin-coating the dispersion at 1500 rpm for 1 minute with 3 minutes post-annealing at 150 °C. The microscope system was operated using the SmartSEM user interface, and the length distribution analysis was carried out with ImageJ software.

3.3 Photon correlation measurement

The photon statistics of a light source in terms of the arrival time could be divided into three categories according to the second-order correlation function: antibunched, bunched, and random light emission. Experimentally, the statistic distribution can be recorded based on the HBT effect which correlates the photon events (intensity) of the two photodetectors from a single photon stream split equally by a beam splitter. For instance, the coherent light from a laser often exhibits a random photon spacing (uncorrelated), and classical thermal emission is a typically correlated (bunched) light, whereas light from a single-photon source shows anti-correlation. In this thesis, we performed intensity correlation measurements to characterize the defect-state electroluminescence of functionalized SWCNTs.

3.3.1 Measurement setup description

To perform second-order correlation function measurements, $g^2(\tau)$ measurements, based on the HBT configuration, the SWCNT device was driven in a similar way to electroluminescence spectroscopy measurement in the optical cryostat at 77 K. The different part is that the collected emission light was coupled into a single-mode 50/50 fused fiber coupler (TW1300R5F1 or TW1550R5F1, Thorlabs) via a protected silver reflective collimator (RC08FC-P01, Thorlabs) mounted behind the objective (LCPLN20XIR, Olympus) and a spectral filter (Hard-Coated Bandpass/Longpass Filters, Thorlabs) with an optical density greater than 5 in the rejection region inserted when necessary. The light was further guided to two separate fiber-coupled superconducting single-photon detectors (TCOPRS-CCR-TW35, SCONTEL) which are connected each to the input channels of the time-correlated single photon counting system (PicoHarp 300, PicoQuant). The two low-jitter (≤35 ps) superconducting single-photon detectors (SSPDs) were maintained at a base temperature of 2 K, well below the superconducting critical temperature, and operated at a constant DC bias around 90 % of the critical current, such that a good compromise between high detection efficiency and low dark count rate (less than 100 cps) was achieved. The electrical signals generated from the SSPDs are amplified by low-noise high-frequency amplifiers (ZFL-1000LN+, Mini-Circuits) in negative polarity before reaching the input ports of the correlator. A schematic illustration of the experimental setup is shown **Figure 3.3** including the motorized stage (8MTF, Standa) and the reflective collimator behind the objective for positioning and light collection, spectral filters, a 50/50 fused fiber coupler, and two single-photon detectors with the correlator in compliance with the HBT experiment. The maximum measured count rate was on the order of 10 MHz limited by the dead time of the correlator (~90 ns for PicoHarp 300). The SWCNT device was triggered to emit light with a count rate higher than 10^3 cps to accumulate sufficient event pairs. Coincidence histograms were analyzed and generated by the QuCoa software from PicoQuant in time-tagged (T2) mode or by the PicoHarp software in histogram mode with 8 or 12 ps bin sizes.

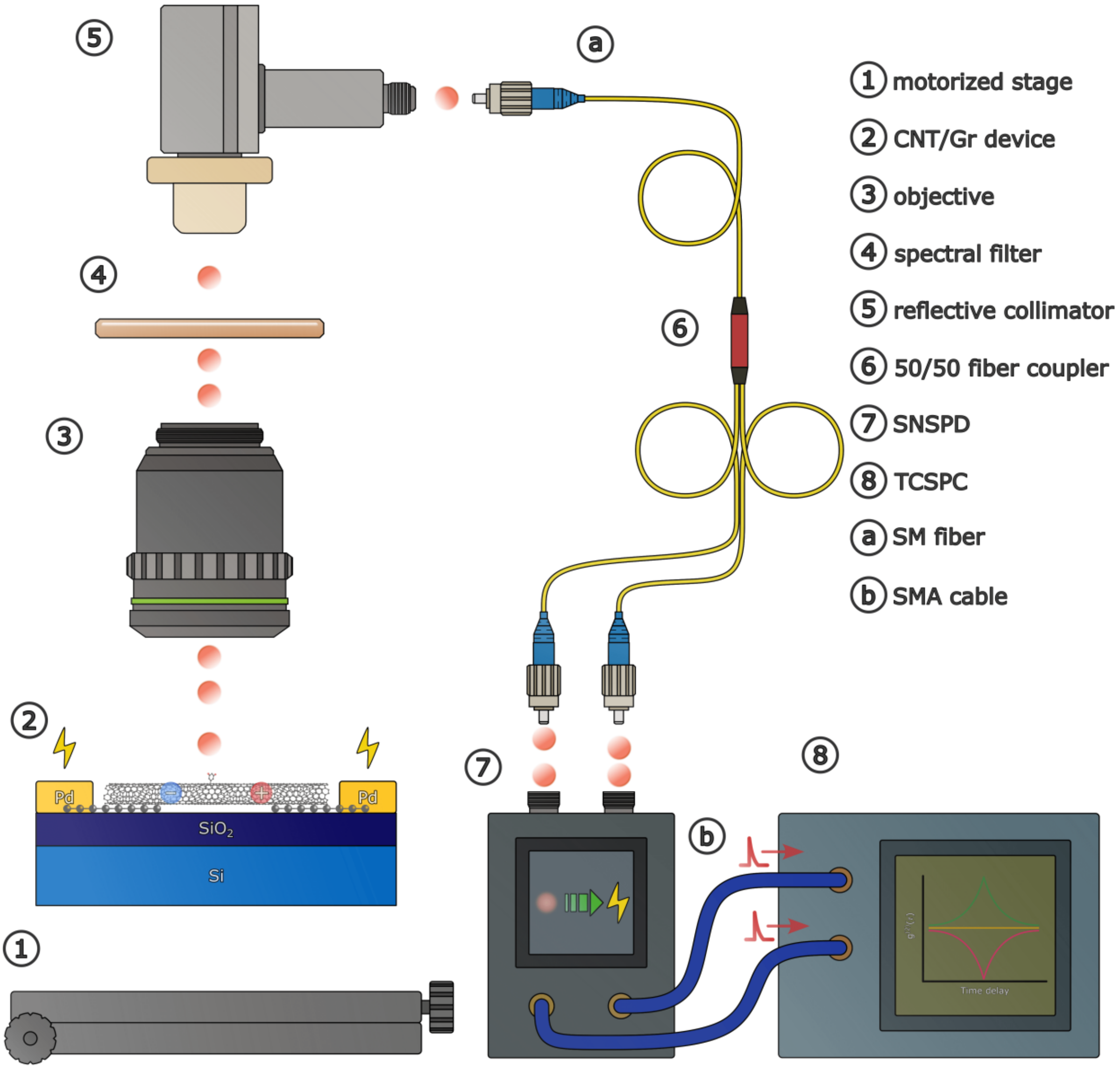

Figure 3.3: A schematic illustration of the HBT experimental setup The intensity correlation measurement of electrically driven defect-state light emission from functionalized SWCNTs is based on the Hanbury Brown and Twiss configuration. The emitted photons were coupled into a single-mode 50/50 fused fiber coupler via a reflective collimator, and used to trigger two independent superconducting single-photon detectors. Photon statistics were recorded by using the time-correlated single photon counting (TCSPC) technique in the histogram or time-tagged (T2) mode. Each of the crucial components in the setup is noted in the figure.

3.3.2 Setup alignment and data analysis

Setup alignment is necessary to switch from electroluminescence measurement to intensity correlation measurement, where the emitted light needs to be guided into a fiber-based 50/50 beam splitter for a HBT experiment as shown in **Figure 3.3**. The reason lies in the fact that the photon detectors/counters are different in both experiments, namely, the xy lateral focus position to couple light into the single-mode fiber via a reflective collimator for intensity correlation measurement is different from dispersing light onto the InGaAs photodiode for electroluminescence measurement. The focus position precision for the collimator coupling was also more demanding than the other. To accommodate the issue, during the device fabrication process, we patterned one extra graphene field-effect transistor in a bowtie structure that can act as a bright and stable incandescent light emitter[210] for light-coupling alignment, see **Figure 3.4**. For example, the coordinate of the focus position of the X-Y motorized stage configuration for EL measurement was set to be (0, 0), and we found the coordinate to be (64, -24) to couple light into the single-mode fused fiber via the reflective collimator. Since we know the relative positions between the graphene strip and other SWCNT devices while designing the structure, once we finish the alignment, we could simply shift from the graphene strip to any specific SWCNT device by controlling the motorized positioning stage in sub-µm precision. As a side note, the position difference for the two measurements will inevitably change if using a different objective.

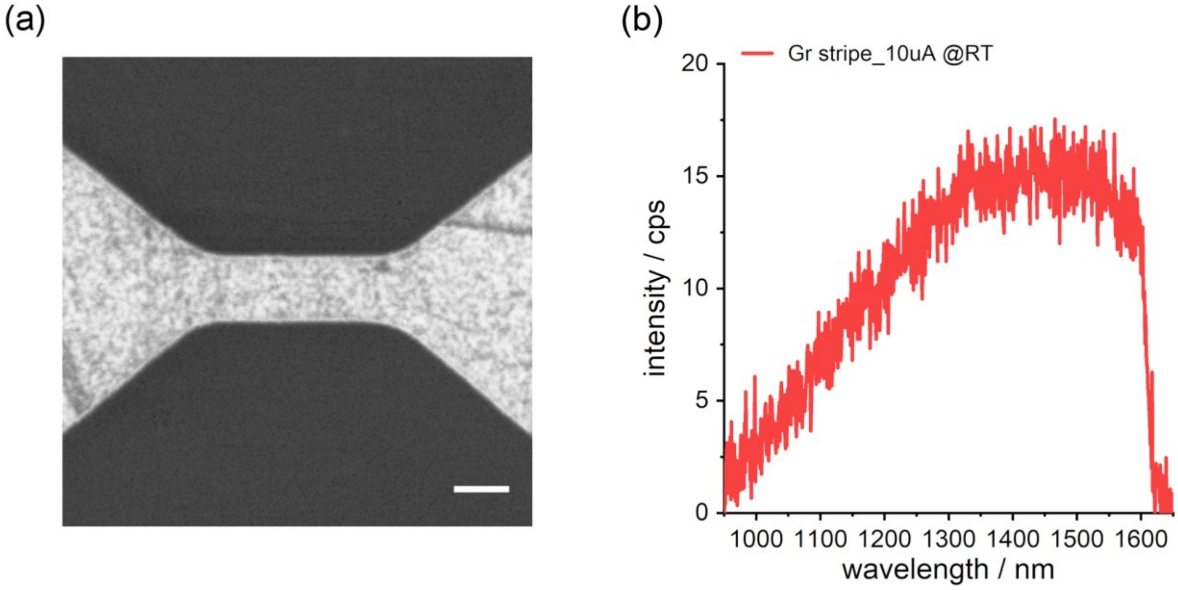

Figure 3.4: Incandescent light emission of graphene stripe for setup alignment (a) A scanning electron microscopy image of the graphene field-effect transistor patterned in a bowtie structure used as an incandescent emitter for alignment of the single-mode optical fiber. The scale bar is equal to 300 nm. (b) The incandescent emission spectrum from the graphene stripe device biased under a constant source-drain current of 10 µA at room temperature. The emission intensity drops significantly around 1600 nm due to the response wavelength range of the InGaAs photodiode.

For the intensity correlation measurements of functionalized (7, 5) SWCNTs which will be discussed in Chapter 5, we mostly used the time-tagged (T2) mode of the time-correlated single photon counting (TCSPC) software to compile coincidence histograms out of the continuous stream of electric pulses generated by the two superconducting single-photon detectors. The T2 mode means that every single registered event contains a time stamp information of the arrival time concerning the start of the measurement in 4 ps time resolution. Both the input channels of the correlator work independently and are identical in terms of functionality. The generated coincidence histograms (selected bin size should be a multiple of 4 ps) are based on the start-stop method and the correlated start-stop events are formed out of the continuous stream of electrical pulses generated by the two superconducting single-photon detectors. The signal-to-noise ratio is enhanced when using bidirectional start-stop events to compose the histograms. However, for this method, the system time delay, due for instance to fiber/cable and electronics delay, has to be taken into account and is critical to compensate for the time offset to not misinterpret results, as demonstrated below in **Figure 3.5**.

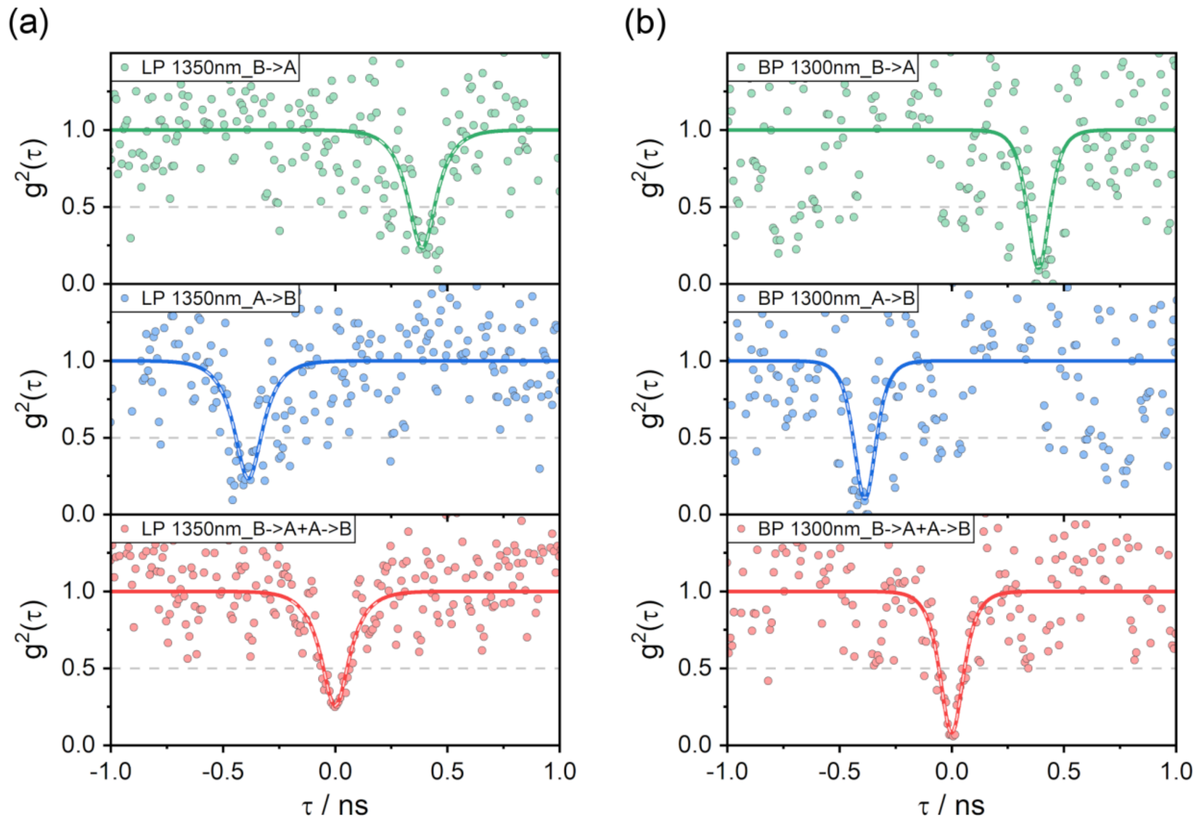

Figure 3.5: Data processing of $g^2(\tau)$ measurement for time offset adjustment Processing of the TCSPC software data (QuCoa, PicoQuant) for eliminating the time differences of the recorded start-stop event pairs from the two channels. The processing is demonstrated in (a) and (b) for the data shown in Figure 5.14 and Figure 5.15a,b, respectively. Each of the first two plots in (a) and (b) are histograms composed of one direction of start-stop events. The histograms comprised of the sum of the time offset-corrected bidirectional start-stop pairs were at last normalized, the bottom two plots.

To fit the photon correlation measurement results, we normalized the collected coincidence histograms to the median value in the given time delay in the figures. The data were fitted according to the correlation function, describing a sum of two exponential decays, $g^2(\tau) = 1 - c_1 e^{-\gamma_1|\tau-\tau_0|} - c_2 e^{-\gamma_2|\tau-\tau_0|}$ convoluted with the Gaussian distribution of time errors $g(\tau) = 1/\sqrt{2\pi\sigma^2}\, e^{-\tau^2/2\sigma^2}$, where σ=30 ps is the standard deviation of the jitter. From the convoluted function, a nonlinear least-squares fit based on the Levenberg-Marquardt algorithm was performed in which the fit results included the error estimation in terms of standard deviations as in previous work[11]. Here we only fitted the antibunching dip region since the data quality was not optimum with the initial guess for the fit parameters of c_1=0, c_2=0.8, γ_2=5 GHz, and τ_0=0. In the nonlinear procedure, the iterations repeated until the fitting parameters stabilized up to the ninth significant digit.

4 Electroluminescence from Carbon Nanotubes with Quantum Defects

This chapter includes content from a research article[19] that has been published by our group. Reprinted with permission from *ACS Nano* **2022**, *16*, 8, 11742–11754. Copyright © 2022 American Chemical Society.

Individual single-walled carbon nanotubes (SWCNTs) with covalent sidewall sp^3 quantum defects have emerged as a class of photon sources whose photoluminescence spectra can be tailored by the carbon nanotube (CNT) chirality and the attached functional group/molecule. Here we present electroluminescence spectroscopy data from single-tube devices based on (7, 5) SWCNTs, functionalized with dichlorobenzene molecules, and wired to graphene electrodes. We observe electrically generated, defect-induced emissions that are controllable by electrostatic gating and strongly red-shifted distinct from emissions of pristine nanotubes. The defect-induced emissions are assigned to excitonic and trionic carrier recombination by correlating electroluminescence excitation maps with electrical transport and photoluminescence data. At cryogenic conditions, additional gate-dependent emission lines appear which are assigned to phonon-assisted hot-exciton electroluminescence from quasi-levels. Similar results were obtained with functionalized (6, 5) nanotubes. Lastly, we also compare functionalized (7, 5) electroluminescence data with photoluminescence of pristine and functionalized (7, 5) nanotubes redox-doped using gold(III) chloride solution. This work shows that electroluminescence excitation is selective toward neutral defect-state configurations with the lowest transition energy, which in combination with gate-voltage control over neutral *versus* charged defect-state emission leads to high spectral purity.

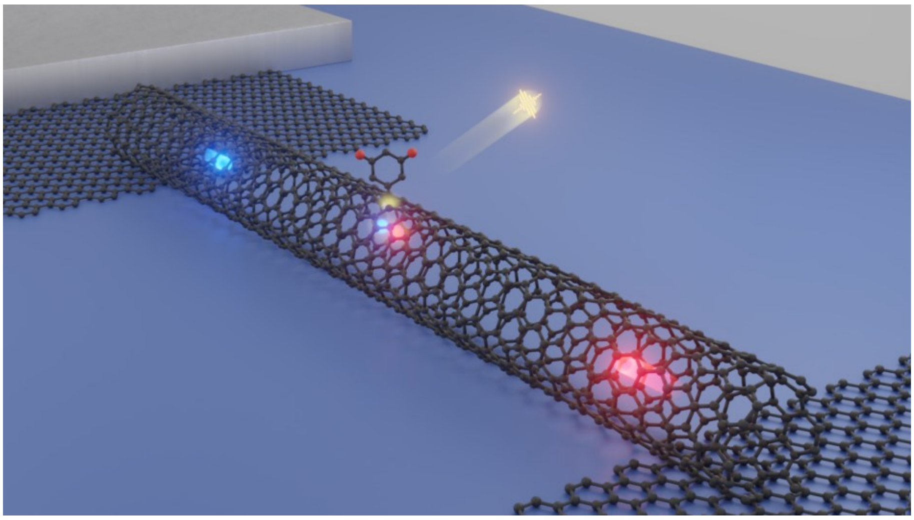

Figure 4.1: 3D model illustration of light emission from an electrically-biased graphene-contacted single-walled carbon nanotube with a quantum defect.

4.1 Introduction

Photonic quantum technology has been widely explored in recent years aiming to improve the current limitations in quantum information processing, such as quantum computing[6] and quantum cryptography[5]. Single-photon sources are indispensable components of these technologies, and tremendous effort has been devoted to the integration of low-dimensional nanoscale solid-state sources[211,212] such as color centers in diamond[213], quantum dots[214], and single molecules[215]. However, realizing electrical excitation, room temperature operation, and stable emission in technologically relevant telecom bands (1.3 – 1.6 µm) of optical fiber-based quantum communications remains a formidable challenge for these emitters. Semiconducting SWCNTs, on the other hand, possess many desirable properties for photonic applications[7], especially structure-dependent, excitonic emission wavelengths, that can be tuned from 850 nm to 2 µm, and which can be triggered optically and electrically. Photon anti-bunching in photoluminescence[10], as well as electroluminescence[11], have been demonstrated. However, small luminescence quantum yields, mainly owing to the low-lying optically forbidden 'dark' exciton states[117] and undesired quenching sites[119], as well as the cryogenic temperatures required to achieve single-photon emission behavior still frustrate the development of CNTs as quantum-light sources.

Recent progress has shown how the introduction of quantum dot-like (0 D) defects to the sidewalls of CNTs through low-level oxygen[15], alkyl[78,216], or covalent aryl sp^3 functionalization[16,217] not only significantly enhance the photoluminescence emission efficiency (from <1 % up to 28 %)[16,76] but also redshift the photoluminescence emission wavelength deeper into the near-infrared regime. The sp^3 defects, which trap mobile excitons in potentials of 100 – 300 meV depth, extend the single-photon emission characteristics of CNTs to room temperature[17,18] and may thereby facilitate their use in sensing and imaging applications[218]. From an applied research perspective, an on-chip source with electrical controllability is an important component of applications. Although extensive studies have focused on understanding the emission characteristics of functionalized SWCNTs, mostly through optical means, only a little has been reported regarding electrically driven luminescence. Xu et al. showed electroluminescence from a functionalized SWCNT film network via an impact excitation mechanism[190]. Zorn et al. demonstrated the interplay between charge transport and electroluminescence from functionalized SWCNT networks[189]. However, an electroluminescence study of functionalized SWCNT at the single tube level, which is crucial for quantum photonics, has so far not been reported. Also, despite the observation of electroluminescence from localized trions in previous works[190], a comprehensive understanding of the formation condition of trions and the interrelation between electrical transport and emission behavior is still missing.

In this work, we fabricated dichlorobenzene-functionalized (7, 5) SWCNT field-effect transistors with graphene electrodes and demonstrated defect-induced excitonic and trionic electroluminescence through carrier recombination at the single tube level. The spectral weight of defect-induced emission was tuned by electrostatic gating and further correlated with electrical transport measurements. At cryogenic temperature and under certain gating conditions, unexpected emission lines were observed which we could attribute to phonon-mediated hot-exciton electroluminescence. Finally, electroluminescence and photoluminescence from SWCNTs with and without functionalization were compared to help better understand the intrinsic and defect-related emission behavior.

4.2 Electroluminescence of functionalized (7, 5) carbon nanotubes

In this section, we starte with the introduction of the preparation of the light-emitting material of interest, functionalized (7, 5) SWCNTs, and the kind of device structure for SWCNTs integration. Then, we followe with studying the low-temperature (77 K) electroluminescent defect-state emission and assigning the origin of different emission peaks to the localized excitons or trions in the trap states of sp^3 quantum defects. We substantiate the hypothesis by correlating the interplay between the defect-state emission and the gating/doping conditions derived from the simultaneous recorded electrical measurements. Later on, we compare electroluminescence measurements of functionalized (6, 5) SWCNT devices which exclude our observation to be chirality specific. Meanwhile, we notice unconventional satellite emission lines between the intrinsic and defect-state emission peaks at a very low temperature (4 K). Finally, at the end of the section, we propose a hot-exciton electroluminescent model to explain the low-temperature emission lines observation.

4.2.1 Functionalized carbon nanotube and device fabrication

Chirality-enriched CNT suspensions were prepared from CoMoCAT SWCNTs by polyfluorene (PFO) polymer-wrapping and dispersing in toluene, length sorted and purified by gel filtration chromatography[69]. The functionalization reaction was carried out by adding 3,5-dichlorophenyldiazonium tetrafluoroborate to the suspension and heating close to the boiling point of toluene for an hour in a dark environment. Photoluminescence measurements were performed directly following the functionalization process to confirm the successful formation of sp^3 covalent defects by monitoring the defect-induced emission lines. For details, we refer to Experimental Methods in Section 3.1.1. Absorption spectra of the polymer-wrapped pristine and functionalized (7, 5) SWCNT suspensions with the prominent E_{11} and E_{22} optical excitonic transitions are shown in **Figure 4.2a**. From the integrated intensities of the E_{11} optical transition peak, we have determined a >99 % chiral purity with minor (6, 5) and (7, 6) impurities.

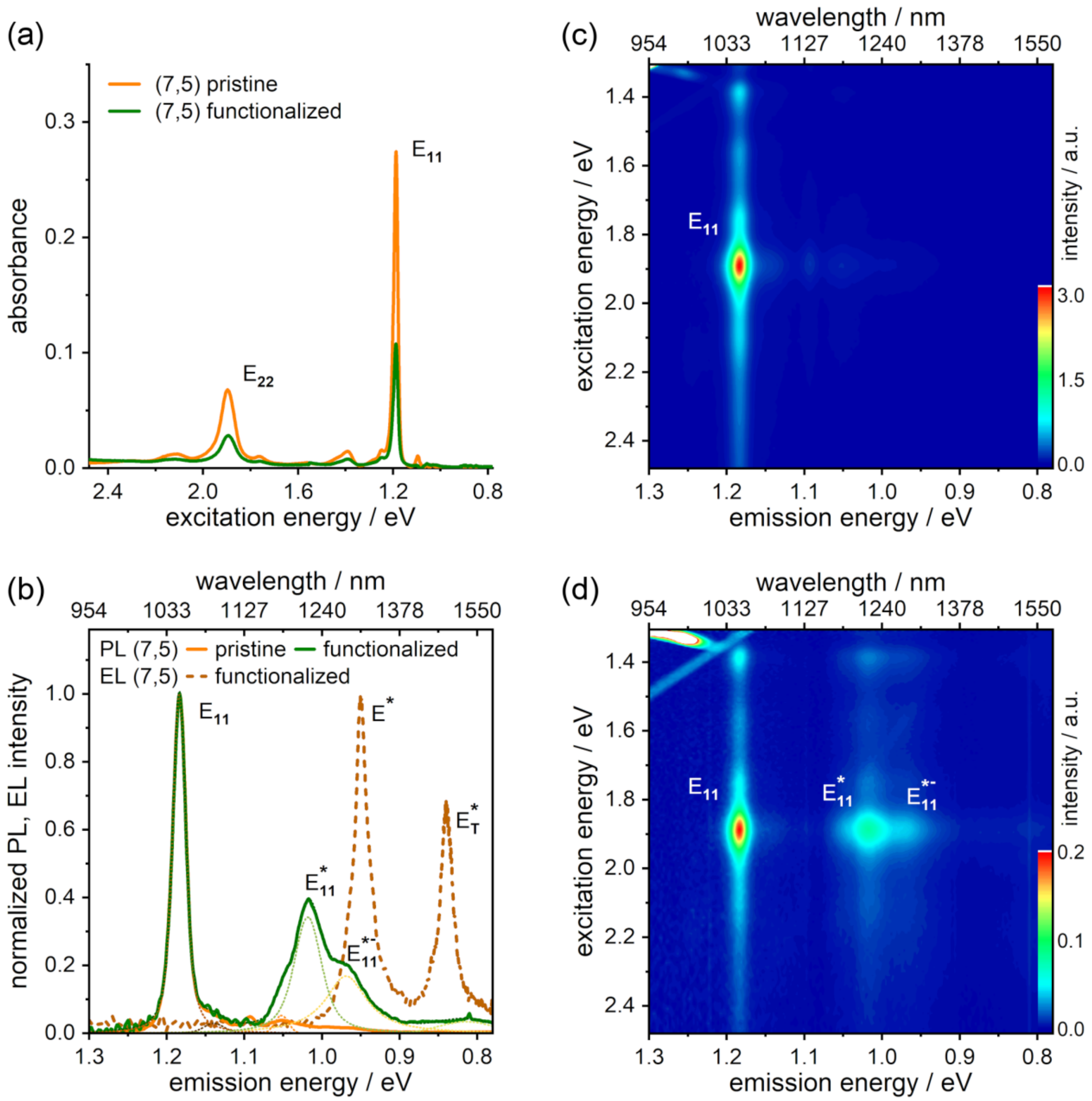

Figure 4.2: Optical properties of pristine and functionalized SWCNT suspensions (a) Absorption spectra of pristine and 3,5-dichlorobenzene-functionalized polymer-wrapped (7, 5) SWCNTs dispersed in toluene. The corresponding photoluminescence spectra excited at E_{22} (1.89 eV) are shown in (b). Photoluminescence excitation (PLE) map of the suspension with pristine and functionalized (7, 5) are shown in (c) and (d), respectively. E_{11} emission and the red-shifted defect-state emission (E_{11}* and E_{11}*$^-$) are labeled. The electroluminescence (EL) spectrum of a single-tube device, measured at 40 nA source-drain current and 4 V gate-voltage at 77 K, is overlaid in (b). The defect-state EL emission (E*) is at the similar emission energy as E11*$^-$ emission in the PL measurement. E^*_T is the trionic defect-state EL emission, as discussed in the text. The PL spectra were fitted with Voigt functions. All data except the electroluminescence spectrum was recorded at RT.

After functionalization, the E_{11} and E_{22} peak absorbance has dropped to around 60 % partially due to dilution. **Figure 4.2c,d** show the corresponding photoluminescence excitation (PLE) maps of the pristine and functionalized (7, 5) nanotube suspensions. The E_{11} excitonic emission of the (7, 5) tubes occurs at 1.18 eV (1050 nm) under E_{22} excitation at 1.89 eV (657 nm). Impurity species become visible only for logarithmic intensity scaling (**Figure 4.3**). The additional functionalization-induced emission bands (denoted here as E_{11}* and E_{11}*⁻) are visible in **Figure 4.2b,d**, similar to previous reports on aryl sp^3-functionalized nanotubes, where E_{11}* and E_{11}*⁻ are associated with the formation of sp^3 quantum defects and exciton localization at deep traps[18]. Compared to the narrow intrinsic E_{11} emission from mobile excitons, the functionalization-induced emission emerges over a rather broad energy range, which has been attributed to spectral diversity in chiral nanotubes caused by multiple covalent binding configurations for an aryl group to the nanotube lattice[81,84].

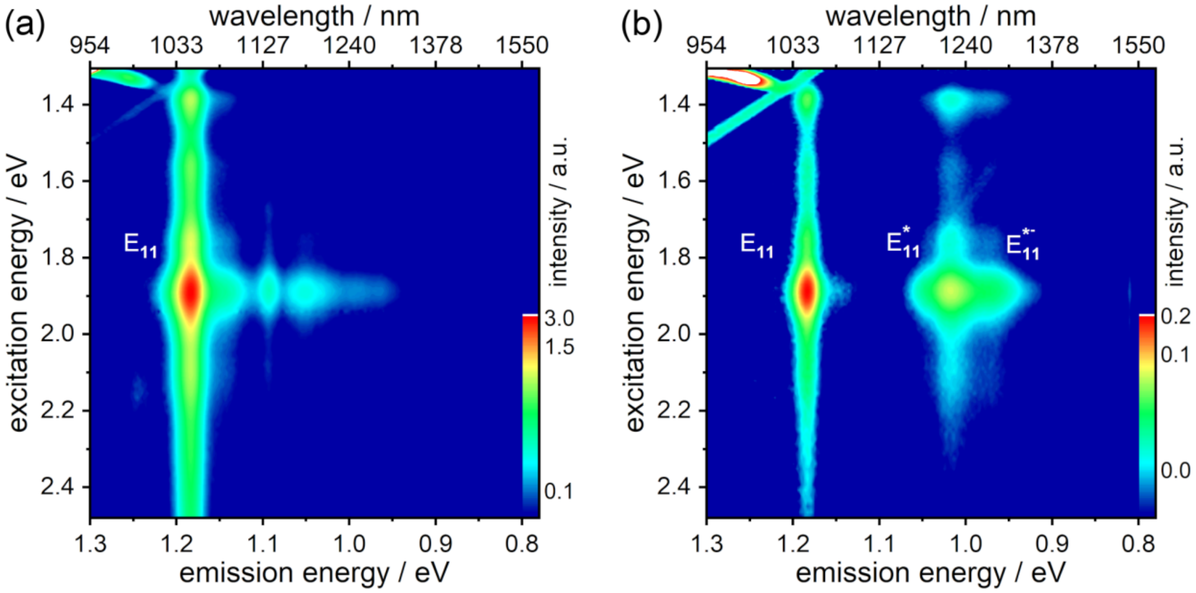

Figure 4.3: Photoluminescence excitation maps in logarithmic intensity scaling Photoluminescence excitation maps of (a) pristine and (b) functionalized (7, 5) suspensions. Intensity plotted on log-scale. Pristine suspension shows (7, 5) as the majority with visible minor impurities of (6, 5) (1.24 eV @ 2.15 eV excitation) and (7, 6) (1.09 eV @ 1.89 eV excitation) chiralities. The RBM (1.14 eV) and K-momentum dark exciton (1.05 eV) phonon sidebands of (7, 5)[72] are also observed in (a). E_{11} emission and the red-shifted defect-state emission (E_{11}* and E_{11}*⁻) are indicated.

From a diluted suspension, individual functionalized (7, 5) nanotubes - on average 500 nm long (**Figure 4.4a**) - were deposited onto source-drain graphene electrodes with a 100 nm gap via DC dielectrophoresis[208]. The deposition conditions were adjusted to obtain single-tube devices (**Figure 4.4c-e**). The devices were electrically wire bonded, in a field-effect transistor configuration using the p-Si as a global back-gate, and mounted into the optical cryostat of our near-infrared optical microscopy and spectroscopy setup. The cryostat was evacuated to 10^{-7} mbar and the samples were vacuum annealed and subsequently cooled down to 77 K or 4 K to suppress gate voltage hysteresis. The devices were biased in constant current mode to obtain stable light emission and bias-independent electrostatic doping of the nanotube channel via the gate voltage[70]. The light emitted from the SWCNT devices was dispersed via an imaging spectrograph grating onto a linear InGaAs photodiode array with a wavelength range from 950 to 1610 nm. All spectra were calibrated by the relative spectral sensitivity of the setup[70].

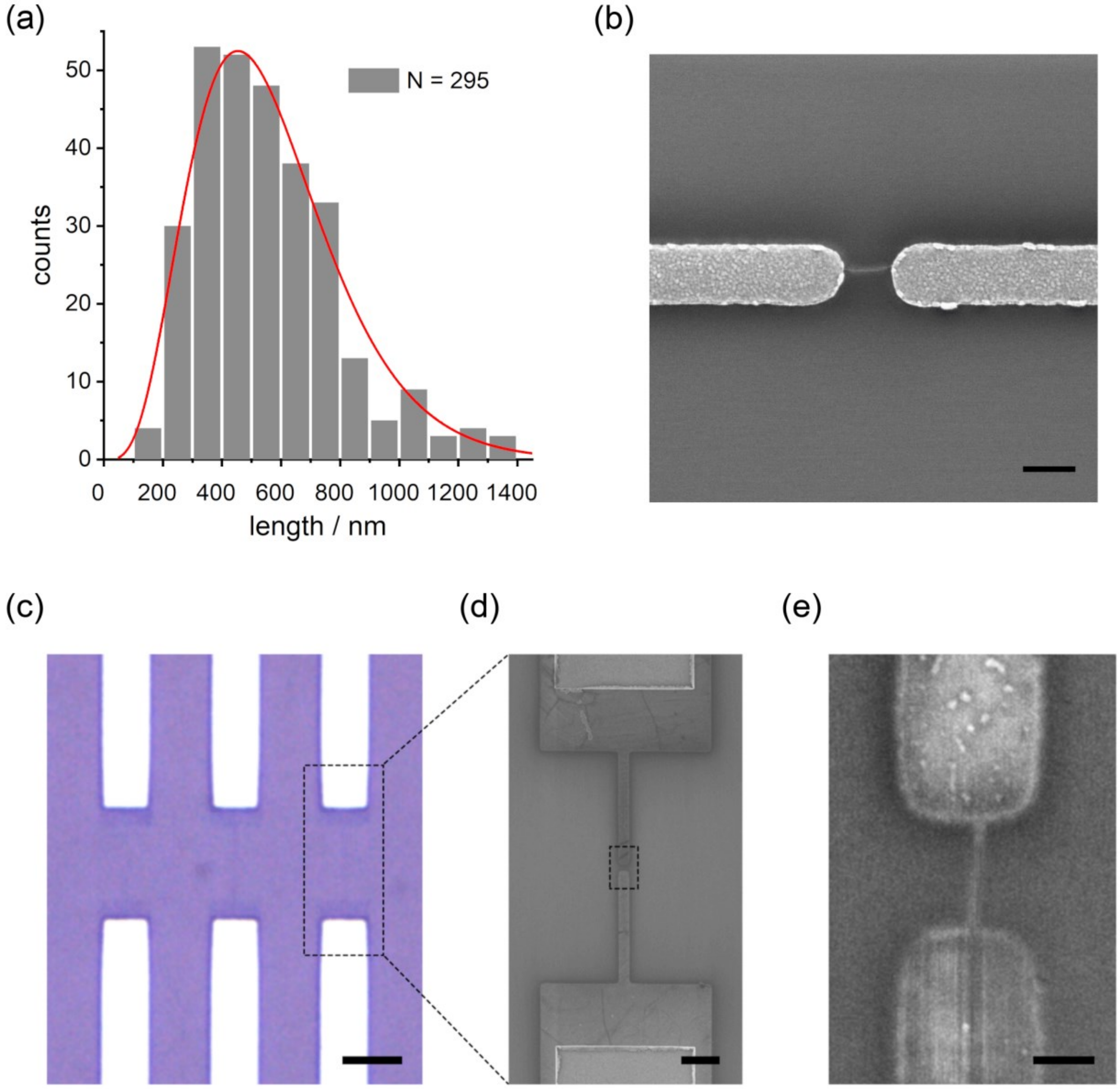

Figure 4.4: Length distribution of SWCNT suspension and images with single-tube devices (a) The average nanotube length is around 500 nm. The data was extracted from SEM image data analysis of 295 individually resolved tubes. The sample was prepared by using the same SWCNT suspension as the devices used for electroluminescence measurement. The Gamma distribution was fitted to the histogram. (b) A representative scanning electron microscopy image of a single-tube device with palladium (Pd) source-drain electrodes. Scale bar equals 200 nm. (c-e) Optical and scanning electron microscopy images of a single-tube device with graphene electrodes, taken after electroluminescence characterization. Scale bar equals (b) 5 µm, (c) 1 µm, and (d) 100 nm.

4.2.2 Electroluminescence from functionalized (7, 5)

Figure 4.5a,b show electroluminescence excitation maps of electroluminescence (EL) spectral intensity *versus* gate voltage from a representative functionalized (7, 5) device, measured at 10 and 40 nA source-drain current and 77 K. Spectra were recorded in 42 subsequent steps of gate-voltage sweeping with an integration time of 10 s for each spectrum at a given constant current bias. The corresponding source-drain voltage was simultaneously recorded to monitor the doping level of the nanotube channel. The EL maps show that the electroluminescence spectral weight is entirely red-shifted from the intrinsic E_{11} emission at 1.18 eV (1050 nm) to new emission lines at 0.95 eV (1305 nm) and 0.84 eV (1476 nm) marked as E* and E^*_T, and that these lines can be switched ON and OFF with the back-gate voltage. We emphasize that the red-shifts of 230 meV and 340 meV are so large that we can rule out a contribution of the (7, 5) intrinsic trionic emission, which we have measured previously with pristine (7, 5) and which appears red-shifted by 160 meV at 1.02 eV (1215 nm)[70]. An example spectrum with the trionic emission of a pristine single-tube (7, 5) device is also presented later in **Figure 4.18c**.

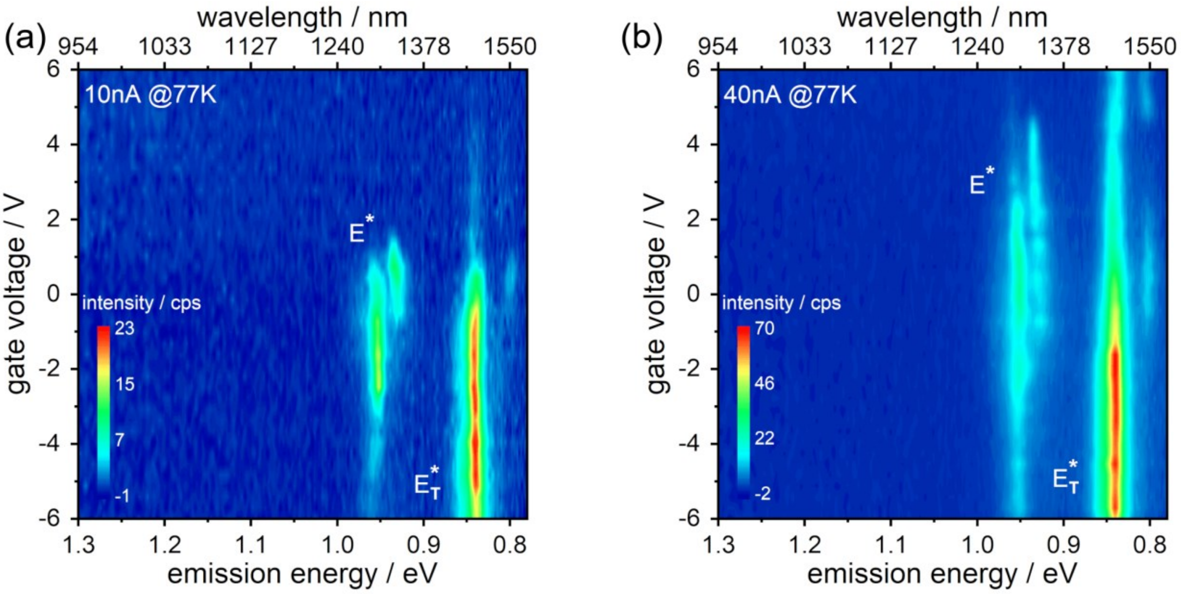

Figure 4.5: Electroluminescence excitation maps Electroluminescence (EL) spectral intensity *versus* gate voltage of a functionalized (7, 5) device measured at (a) 10 nA and (b) 40 nA source-drain current and 77 K. Excitonic and trionic defect-state emissions are indicated as E* and E^*_T, respectively.

When comparing the positions of the E* and E^*_T with the photoluminescence spectrum of functionalized (7, 5) nanotubes (**Figure 4.2b**), we find that the electroluminescent emission occurs in the broad region of functionalization-induced photoluminescent emissions that have been assigned previously to the E_{11}^{*-} (or E_{11}^{**}) defect-state emissions of aryl-functionalized nanotubes[81,83,84,219], and to the corresponding defect-state trion[220]. Therefore, the two new emission lines must be defect-induced. To understand the nature of the two distinctive defect lines it is instructive to realize that the emission at ~0.95 eV (E*) is predominant in the gate-voltage range of 2 to -3 V, whereas the emission at ~0.84 eV (E^*_T) is predominant from 0 to 6 V, for all current biasing conditions. This gate-induced switching of emission lines is similar to the previously studied gate-induced switching between excitonic and trionic emission from pristine SWCNTs[70]. In analogy, we assign the two defect-induced lines to an excitonic defect-state emission (E*) and the corresponding trionic defect-state emission (E^*_T). This assignment will become further substantiated when correlating the electroluminescence spectra with electrical transport data.

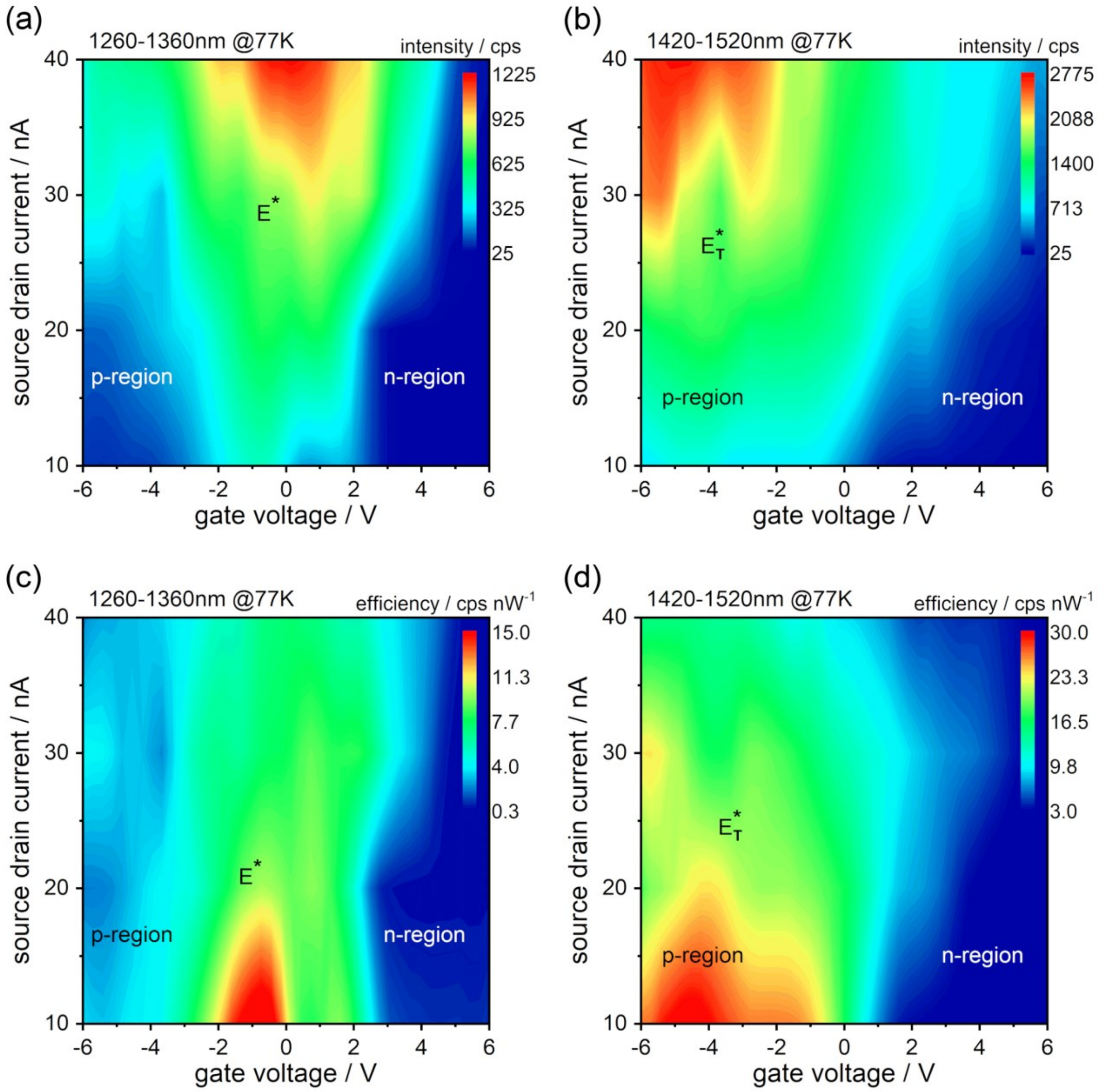

Figure 4.6: Integrated defect-state emission intensity maps (a) Integrated excitonic and (b) trionic defect-state emission intensity *versus* source-drain current and gate-voltage (excitonic range: 1260 – 1360 nm; trionic range: 1420 – 1520 nm). The efficiency of (c) excitonic defect-state emission and (d) trionic defect-state emission is given in count rate / electrical power. Regions of electron (n) and hole (p) conduction are labeled. The excitonic defect-state emission appears near the charge neutrality region, whereas the trionic defect-state emission is dominant in the p-region. Data recorded at 77 K.

To determine under which biasing and gating conditions defect-mediated excitons and trions would form and radiatively recombine we have integrated the intensities associated with the excitonic defect-state emission (1260 – 1360 nm) and the trionic defect-state emission (1420 – 1520 nm) over the wavelength and plotted against source-drain current and gate voltage in **Figure 4.6a,b**. The integrated electroluminescence excitation maps reveal distinctive regions in which trapped excitons and trions are formed and emit light. From the corresponding source-drain voltage map (**Figure 4.7a**), we identify the gate voltage regions where the nanotube channel is p doped, n doped, and charge neutral[70]. These regions are indicated in **Figure 4.6** and are used to correlate light emission with charge transport. **Figure 4.6a** shows that the excitonic defect-state emission is dominant in the gate-voltage range of ±2 V, where charge neutrality is met (between p-region and n-region). Such an intensity maximum at charge neutrality is a unique signature of exciton formation via carrier recombination and excludes unipolar impact excitation[159,160,166].

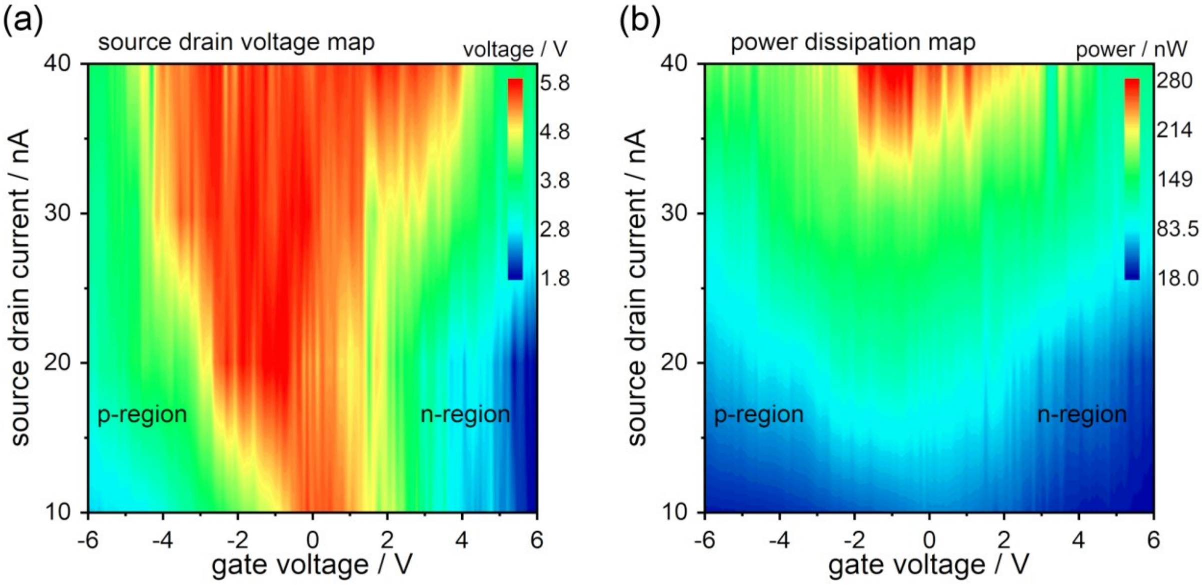

Figure 4.7: Contour maps of source-drain voltage and electrical power dissipation Contour maps of (a) Source-drain voltage and (b) electrical power dissipation *versus* source-drain current and gate-voltage of a functionalized (7, 5) device at 77 K.The p-doped, n-doped, and charge-neutral regions (between p- and n-doped) are indicated.

Likewise, trionic defect-state emission occurs in a limited gate voltage range, where electrons and holes are injected but the channel is significantly doped[70]. In **Figure 4.6b** the positive trion appears in the p region at gate voltages below -2 V. The appearance of the negative trion is shown later. To identify conditions with enhanced efficiency of defect-state emission we have normalized the electroluminescence excitation maps with the corresponding electrical power dissipation map (**Figure 4.7b**) and created in **Figure 4.6c,d** maps of emission efficiency for the defect-state emissions. The excitonic and trionic emission efficiencies are maximized at low current bias, where the gate-voltage range for the formation of excitons and trions is narrow.

4.2.3 Influence of gating and doping

So far we have described the general behavior of defect-induced emission on the biasing conditions. Upon closer inspection, one finds that the spectral evolution as a function of gate voltage is more complex, as is shown for two sets of data in **Figure 4.8a,b**.

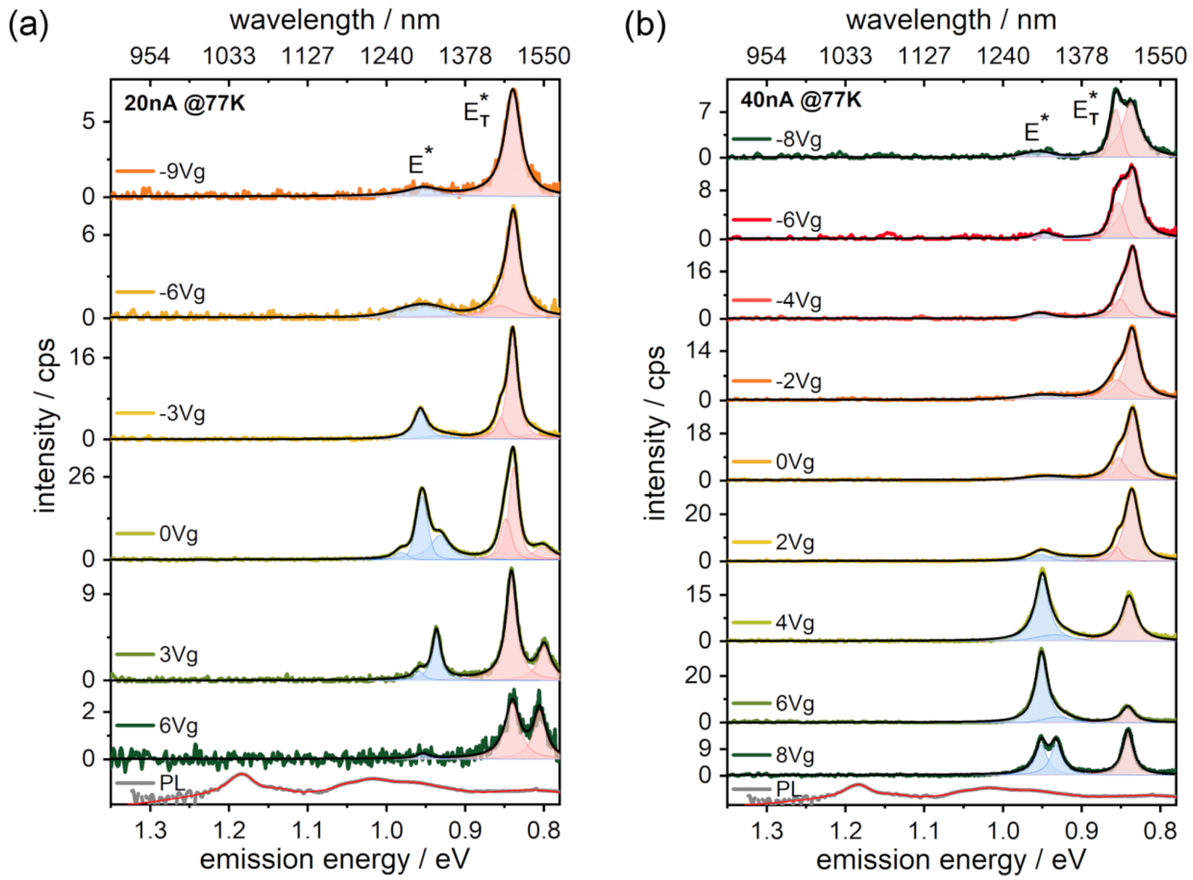

Figure 4.8: Gate-voltage dependence of EL spectra Gate-voltage dependence of EL spectra of functionalized (7, 5) devices with different unintentional doping. In (a) channel is undoped at zero gate voltage, and in (b) channel is hole-doped. Excitonic and trionic defect-state peaks labeled as E* and E*$_T$. The spectra were fitted with Voigt functions. The PL spectrum of the suspension is shown for comparison and plotted on logscale. Data recorded at 77 K.

We observe that the E* and E*$_T$ emission lines consist of more than one peak and are often split into pairs of peaks that could be fitted with Voigt profiles (details in **Figure 4.9**). In addition to the overall gate dependence discussed above, we observe that the relative intensity of the components varies with the gate voltage, whereas the peak positions within one set of data remain constant. The energy scale of the peak splitting is about 18 meV and much smaller than the around 110 meV energy difference between E* and E*$_T$. The nature of the peak splitting could be caused by two different defect sites on the same tube with the same binding configuration but existing in different local chemical/dielectric environments[81].

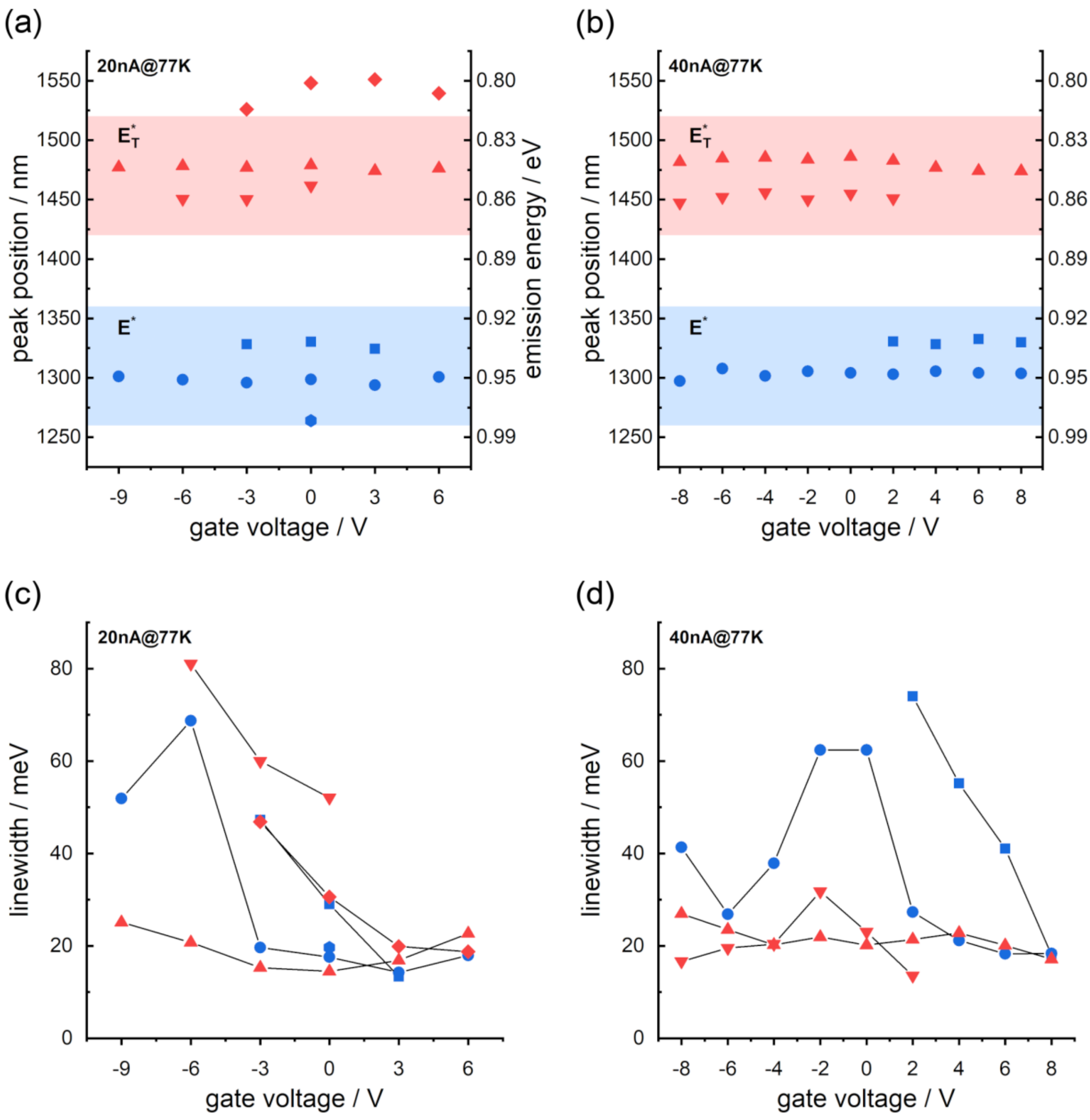

Figure 4.9: Peak positions and linewidths from functionalized (7, 5) EL spectra Peak positions (a,b) and linewidths (c,d) *versus* gate-voltage from the fitting of the electroluminescence spectra of the data sets shown in Figure 4.8 (20 nA and 40 nA data set measured at 77 K) to Voigt profiles.

The energy difference between the defect-exciton E* and the defect-trion E*$_T$ is similar to recent chemical doping studies with defective nanotubes[220]. Apart from general reproducibility, the data in **Figure 4.8a** and **Figure 4.8b** are not identical. For example, an additional peak appears below the energy of the E*$_T$ for positive gate voltages, and an additional set of data (**Figure 4.10**) shows E*$_T$ absent while the splitting of E* is observed. Some of the differences are due to unintentional doping of the nanotube channel, for instance by charge trapping in the substrate.

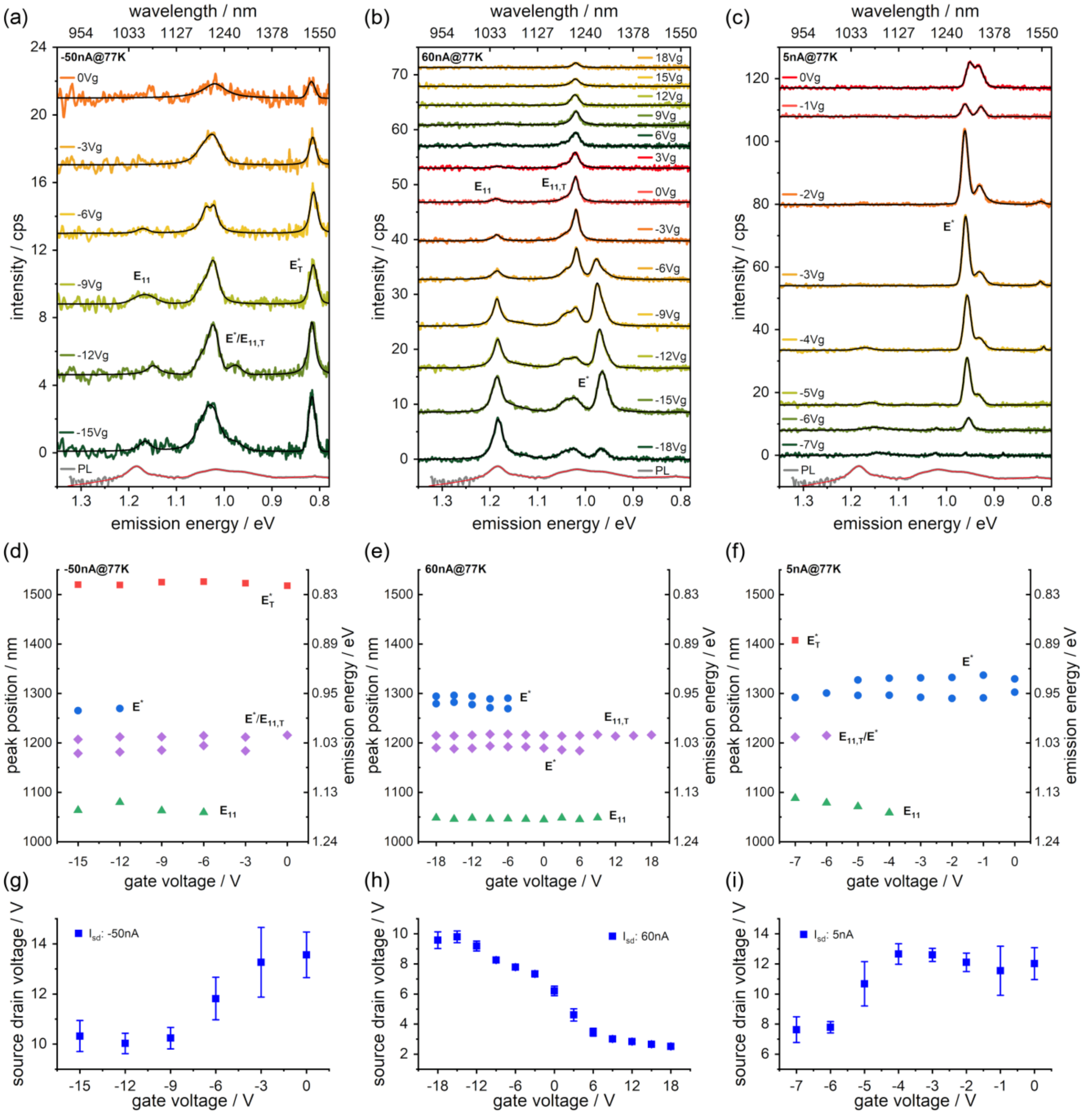

Figure 4.10: Additional EL data of functionalized (7, 5) SWCNTs Three additional data sets of functionalized (7, 5) electroluminescence spectra from different devices (a-c) and the respective transport data (g-i) measured at 77 K. Electroluminescence spectra were fitted with Voigt functions, and the positions of the resolved peaks are shown in (d-f). Defect-induced excitonic emission E* and trionic emission E^*_T are labeled. E* is plotted in blue and violet if the peak position is similar in energy to the photoluminescence defect peaks PL-E_{11}^* and PL-E_{11}^{*-}, respectively. In (b) the trion $E_{11,T}$ becomes visible at 1.02 eV which is at similar energy as the PL-E_{11}^*.

Doping can be detected from the transport data in **Figure 4.11a,b**, where the source-drain voltage is plotted *versus* the gate voltage at constant current. The nanotube channel is charge neutral when the source-drain voltage is at maximum, which is reached in **Figure 4.11a,c** at zero gate voltage. In contrast, in **Figure 4.11b,d** the maximum source-drain voltage and charge-neutrality are reached at +6 V. At zero gate voltage the nanotube channel is p doped. The excitonic defect-state emission reflects this difference in residual doping since E* becomes predominant at the respective gate voltages where the nanotube channel is charge neutral. The trionic defect state emission is sensitive to doping in the same manner. E^*_T intensifies when the channel hosts excess charges that are required for the trion formation. This mutual dependence between E* and E^*_T and the gate voltage at charge neutrality is better captured in **Figure 4.11c,d**, where the relative spectral weight of the integrated excitonic and trionic defect-state emission intensity is plotted *versus* the gate voltage. The same behavior is observed in more sets of data (**Figure 4.10**).

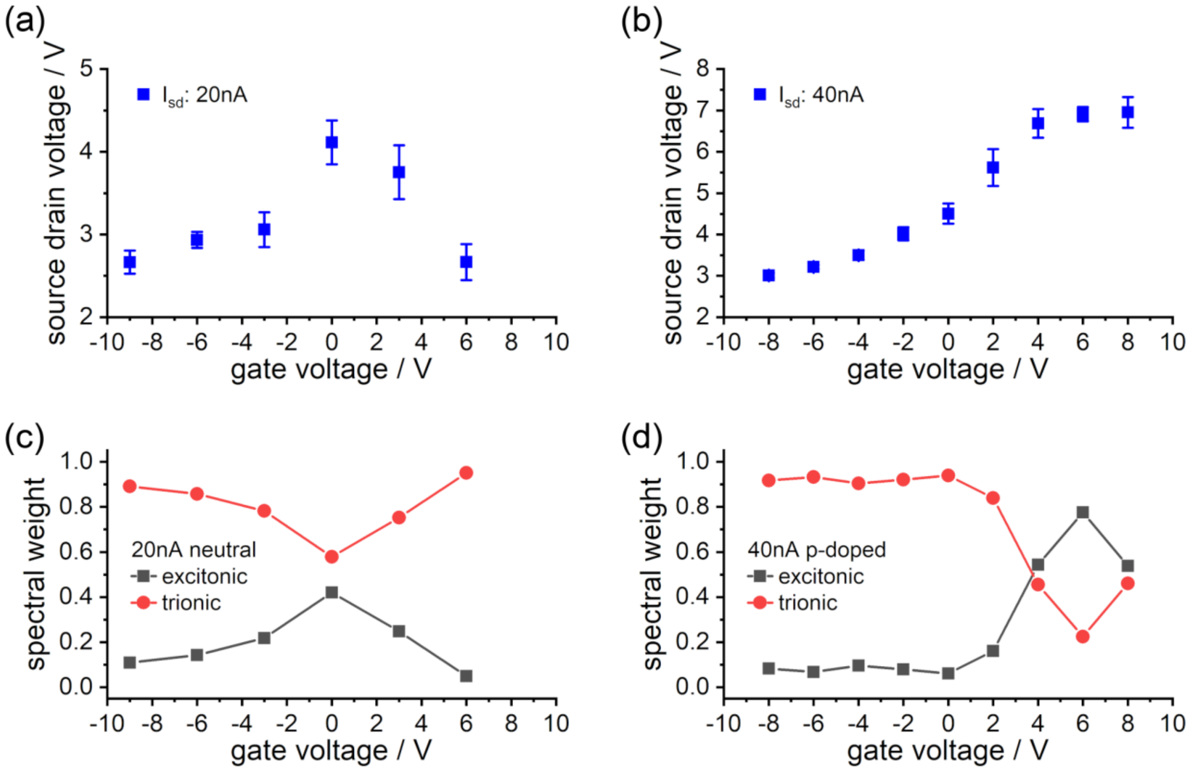

Figure 4.11: Correlation between gate-voltage dependent emission and transport data (a,b) Simultaneously recorded gate-dependent transport data. Maximum source-drain voltage corresponds to charge-neutrality/off-state and is reached in (a) at zero gate voltage and in (b) at 6 V gate. (c,d) Relative spectral weight of excitonic and trionic defect-state emission from the integrated intensity of E* and E^*_T lines in Figure 4.8. Data recorded at 77 K.

4.2.4 Comparative electroluminescence data from functionalized (6, 5)

The observations that we made are not unique to the (7, 5) nanotube chirality, the type of polymer, or electrode material. Similar measurements were performed on 3,5-dichlorobenzene-functionalized, PFO-BPy wrapped (6, 5) nanotubes wired to Pd source-drain electrodes. Device fabrication details see Section 3.1, and an representative scanning electron microscopy image of a single-tube device is shown in **Figure 4.4b**. We observe excitonic and trionic defect-state emissions from functionalized (6, 5) that are similar to the functionalized (7, 5) SWCNTs, with chirality-related shifts of peak positions. In **Figure 4.12a** we see that the E* and E^*_T peaks, highlighted in blue and red, respectively, respond to the gate-voltage in the same way. Also, a splitting of the E* and E*$_T$ lines is visible. As before, we added the photoluminescence data from the corresponding dispersion in logarithmic scaling. For the functionalized (6, 5) SWCNTs we also see that the electroluminescent excitonic defect-emission lines fall into the broad region of functionalization induced photoluminescence (more data in **Figure 4.12**).

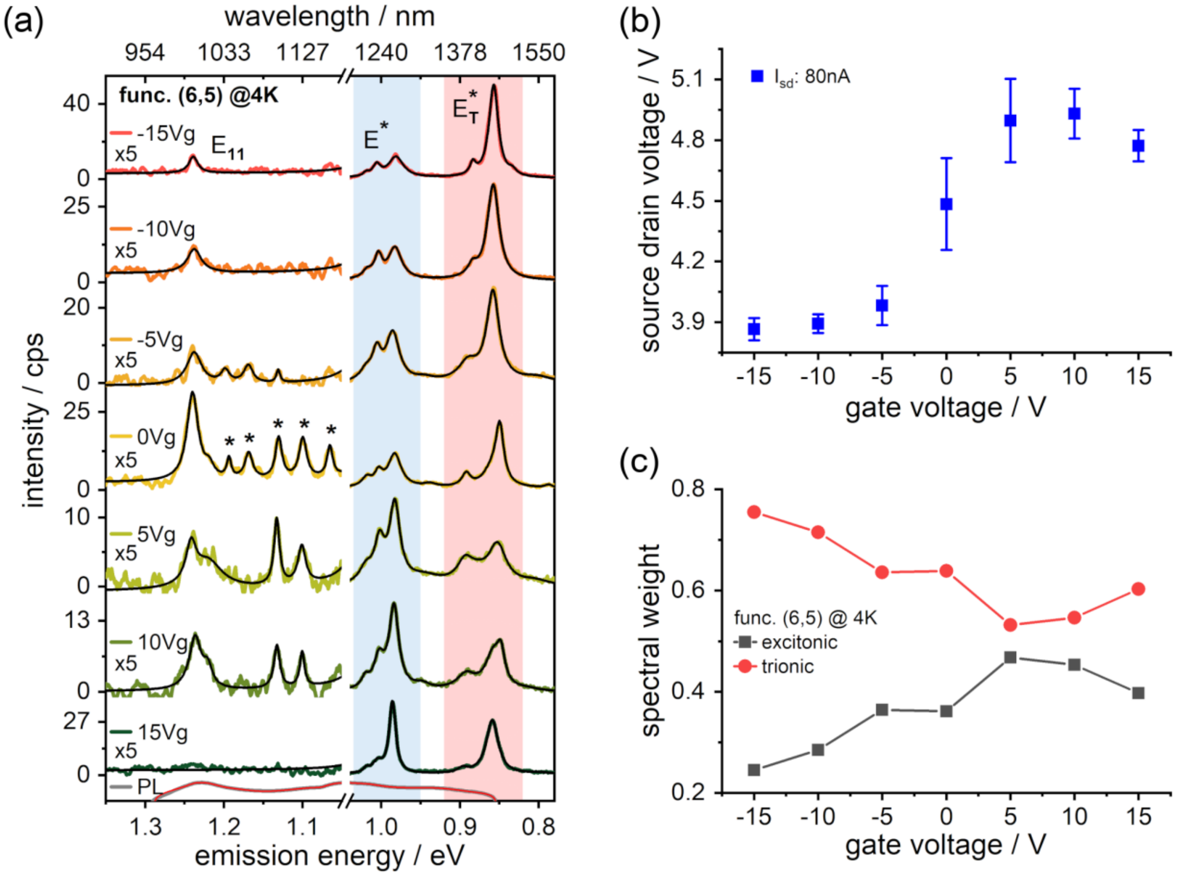

Figure 4.12: Electroluminescence data of functionalized (6, 5) SWCNTs at 4 K (a) EL spectra of functionalized (6, 5) measured at 4 K over a wide gate voltage range. Intrinsic E_{11} emission and additional starred peaks become visible at charge neutrality. Excitonic and trionic defect-state peaks are labeled as E* and E*$_T$. The spectra were fitted with Lorenzian functions. Intensity scaled by factor 5 above 1.05 eV for clarity and PL spectrum of suspension added in logscale. (b) The transport data where the maximum source-drain voltage corresponds to charge-neutrality/off-state. Data recorded at 4 K. (c) Relative spectral weight of excitonic and trionic defect-state emission from integrated E* and E*$_T$ lines.

The data shown in **Figure 4.12a** was recorded at 4 K and interestingly, the intrinsic E_{11} emission is visible in addition to the defect-state emission. The E_{11} emission becomes weaker with increasing temperature (**Figure 4.13a**) and disappears above 60 K (**Figure 4.13b**). We have introduced in **Figure 4.12a** and **Figure 4.13a** an x-axis break (0.01 eV), and rescaled the y-axis in the energy range >1.05 eV to allow a clearer distinction of peaks of different peaks. We believe that the localization of excitons at very low temperatures by shallow traps plays a role[192,221]. Shallow traps, e.g. induced by interaction with the polymer or substrate surface, do not lead to a significant change of the emission wavelength but can give rise to single-photon emission[10,11].

Such a trapping of mobile E_{11} excitons by shallow traps makes the probability of reaching a deep defect induced trap less likely and the shift of spectral weight from E_{11} to the defect state emission is reduced. Vice versa, with rising temperature the de-trapping from shallow traps increases[10], and the probability for mobile excitons to get trapped by the defect deep trap becomes large, provided the nanotube length is comparable or shorter than the exciton diffusion length[222], as is the case in this work. We observe the localization of E_{11} excitons also with functionalized (7, 5) nanotubes and show in **Figure 4.14b** a measurement at 4 K, where the intrinsic E_{11} emission is visible together with the defect-state emissions. We have one set of functionalized (7, 5) data where we observe the E_{11} emission also at 77 K (**Figure 4.10**), which we attribute either to the presence of a deeper shallow trap or to a second tube without a defect.

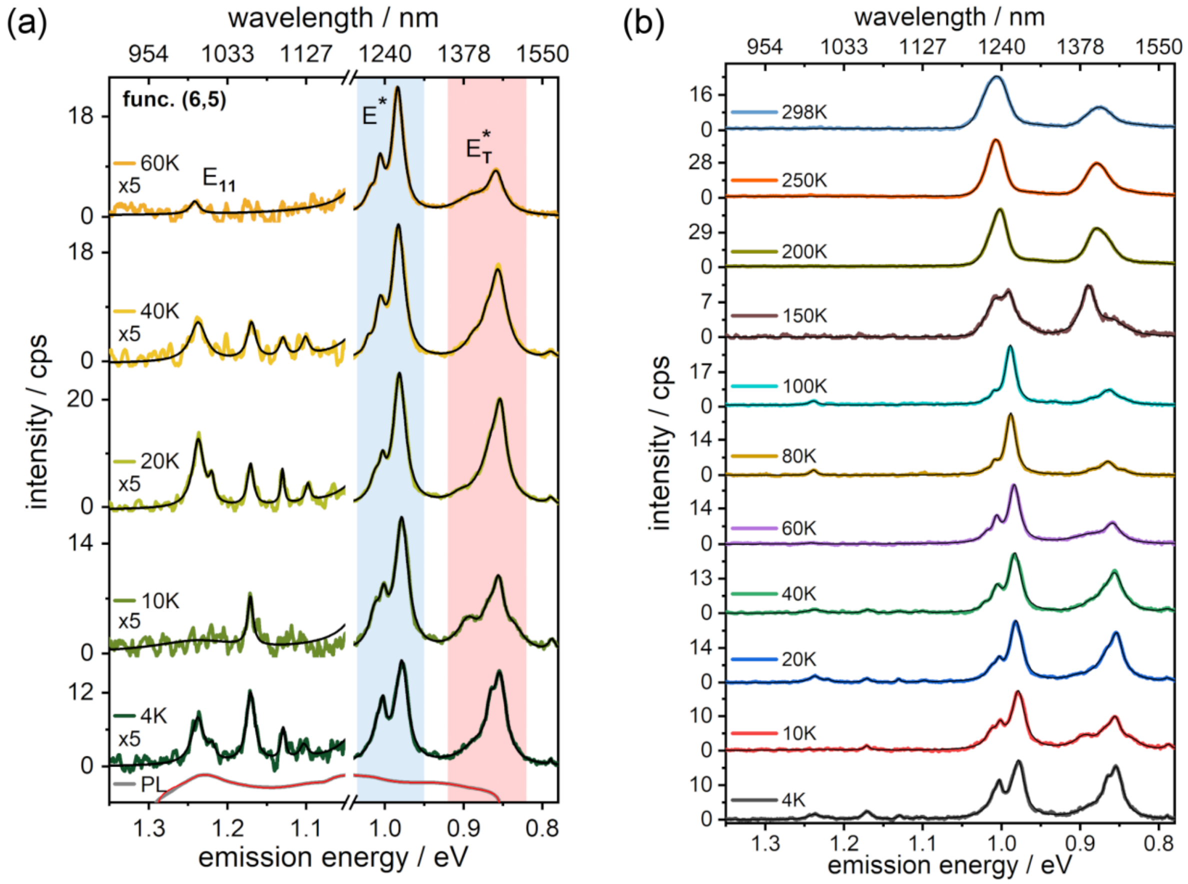

Figure 4.13: Temperature-dependent EL spectra of functionalized (6, 5) SWCNTs (a) Temperature dependence of EL spectra from functionalized (6, 5) nanotubes. Excitonic and trionic defect-state peaks are labeled as E* and E^*_T. The spectra were fitted with Lorenzian functions. Intensity scaled by factor 5 above 1.05 eV for clarity and PL spectrum of suspension added in logscale. (b) Complete temperature-dependence of the electroluminescence of functionalized (6, 5) device.

4.2.5 Emission lines at very low-temperature

We now discuss the appearance of a series of new peaks between the E_{11} and the defect emission lines, seen in **Figure 4.14**. The peaks (marked with stars) become only visible at very low temperatures when the intensity of the E_{11} emission is comparable to the defect emission. This is shown in **Figure 4.14a** for functionalized (6, 5)

SWCNTs, and a similar case is presented in **Figure 4.14b** for functionalized (7, 5) SWCNTs. **Figure 4.13** shows that the starred peaks are temperature-dependent, and disappear simultaneously with the E_{11} emission between 40 and 60 K. In addition, we see in **Figure 4.12a** that complete suppression of the starred peaks can be induced by applying large gate voltages. Also, in this case, the correlation with the E_{11} intensity is visible and we conclude that the starred peaks are associated with the formation of weakly localized E_{11} excitons in proximity to a defect. We note that functionalization is essential since we do not observe the starred peaks on pristine nanotubes[70].

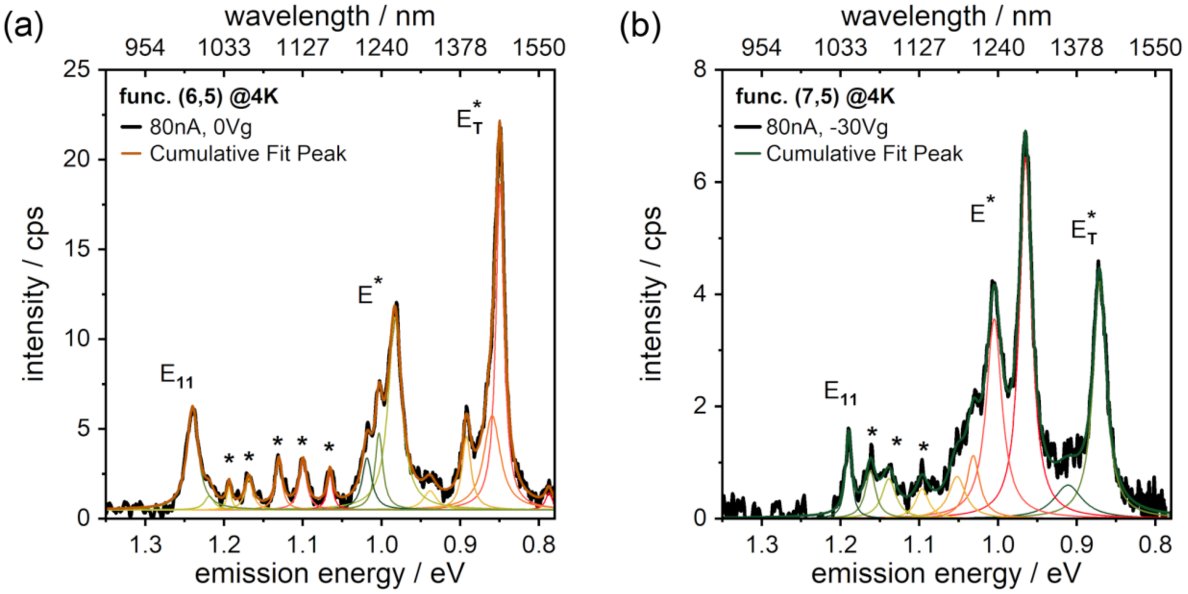

Figure 4.14: Additional emission lines at very low-temperature (a) Enlarged view on functionalized (6, 5) spectrum at zero gate-voltage from Figure 4.12a. Multi-peak fitting with Lorentzian. (b) EL spectrum of functionalized (7, 5) device recorded at 4 K. Excitonic and trionic defect-state peaks are labeled as E* and E^*_T.

Of the 15 devices that we examined, all devices showed defect-state emission, and for 5 devices we were able to find a gate voltage range at 4 K where the additional peaks appear. For the data in **Figure 4.14**, we have fitted the new peaks to Lorentzian functions and analyzed the spacing in energy between neighboring peaks (see **Figure 4.15**). We find that the energy spacing is approximately equidistant and the average spacing in energy is 34.9±8.0 meV and 31.2±9.9 meV for functionalized (6, 5) and (7, 5) nanotubes, respectively, which is close to the radial breathing mode (RBM) energies of the (6, 5) and (7, 5) nanotubes, 38 meV and 35 meV, respectively[71,223–226]. Therefore, and because of the correlation of the peaks with the E_{11} intensity, we assume that the series of peaks is related to a coupling between the E_{11} exciton and RBM phonons.

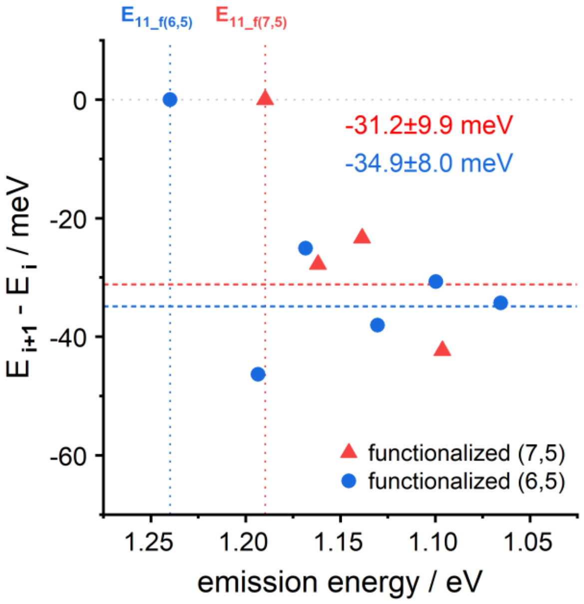

Figure 4.15: Energy spacing of starred peaks The energy difference between the neighboring starred peaks shown in Figure 4.14. The peak positions were extracted via the Lorentzian function fitting.

4.2.6 Hot-exciton electroluminescence

In CNTs, distinct phonon sidebands have been described by Lefebvre et al[227]., who assigned peaks appearing below 20 K to replicas of low-energy squashing modes of the nanotube. The energy spacing was 2 – 3 meV. Low energy wings, often observed in CNT photoluminescence are typically several meV wide and have been assigned to coupling to low energy phonons of nanotubes[228], while spectral gaps in the low-energy wing were attributed to phonon confinement[229,230]. Recently, Nutz et al. assigned multiple peaks in the low-energy photoluminescence wing of PFO decorated nanotubes to phonon replicas of the vibrational modes of the PFO monomer[231]. These modes have a characteristic energy scale of ~2 meV. In our experiment, the energy spacing is much larger. We have performed density functional theory (DFT) calculations of the 3,5-dichlorobenzene molecule covalently bound to a graphene flake and performed a normal mode frequency analysis[232]. In the relevant energy range we found normal mode frequencies around 48 meV, which lead to a deformation of the local graphene lattice that is absent in simulations without the molecule (**Figure 4.16**). Given that our DFT calculations are only an approximation to the problem we cannot rule out that vibrational modes of the functional group might also play a role, but the energy spacing of the peaks fits much better to the RBM energies.

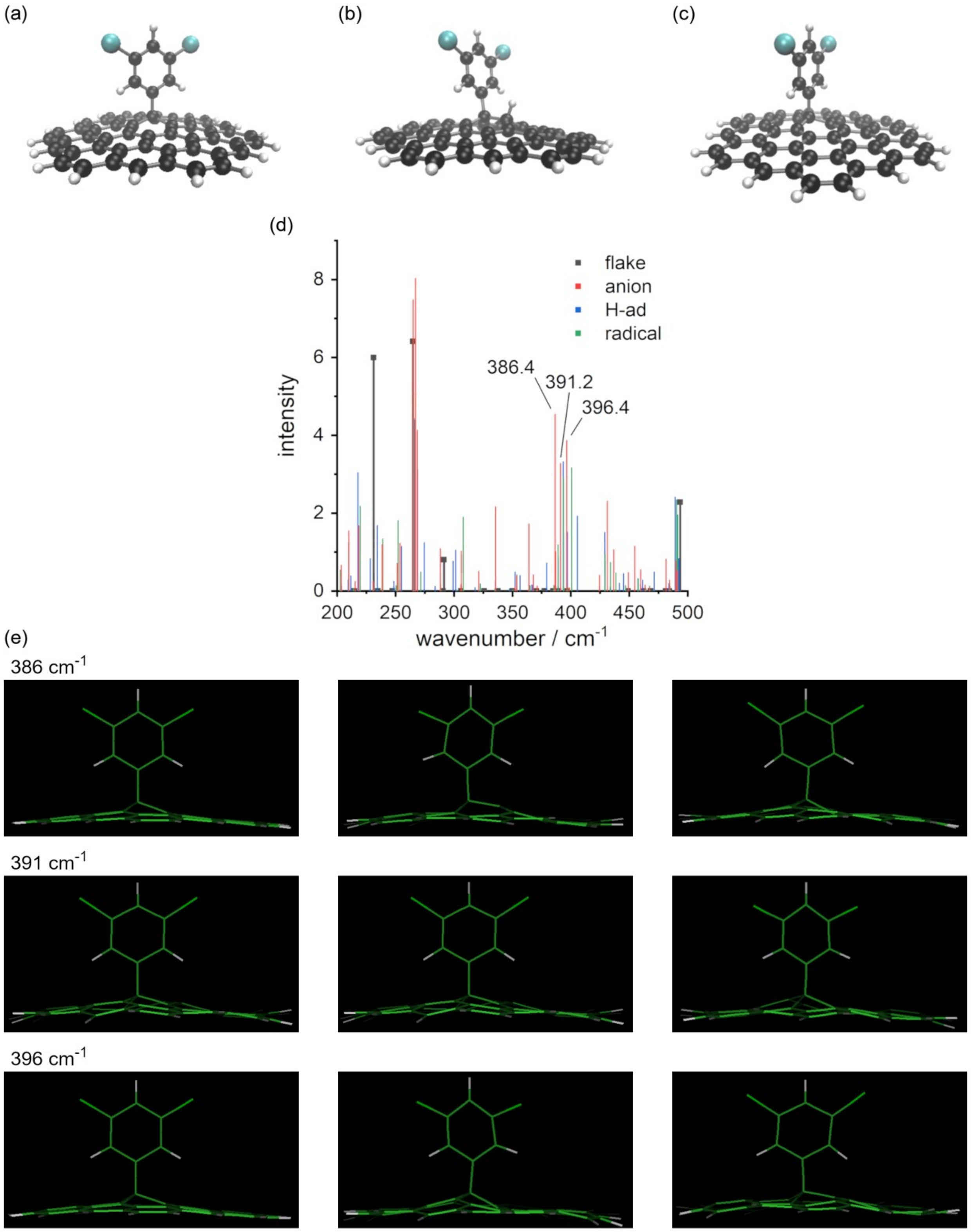

Figure 4.16: Simulation of normal mode frequencies of 3,5-dichlorophenyl-graphene(19) Normal mode frequencies specific for 3,5-dichlorophenyl bonded to a graphene(19) flake. The optimized structures for simulation with a 3,5-dichlorophenyl (a) anion, (b) in presence of adjacent hydrogen, and (c) radical. (d) The vibrational spectra for the three simulations with the 3,5-dichlorophenyl and for the bare flake. (e) The snapshots correspond to the most intense vibrations that are absent for a graphene flake without molecule, and show the motion of the molecule and the local deformation of the graphene lattice.

The question arises why the starred peaks only appear when the E_{11} exciton becomes weakly localized by a shallow trap in the vicinity of a defect-induced deep trap. The explanation that we consider is presented in **Figure 4.17a**. It depicts the conversion of a weakly trapped E_{11} exciton into a deeply trapped E* exciton via the emission of multiple optical phonons.

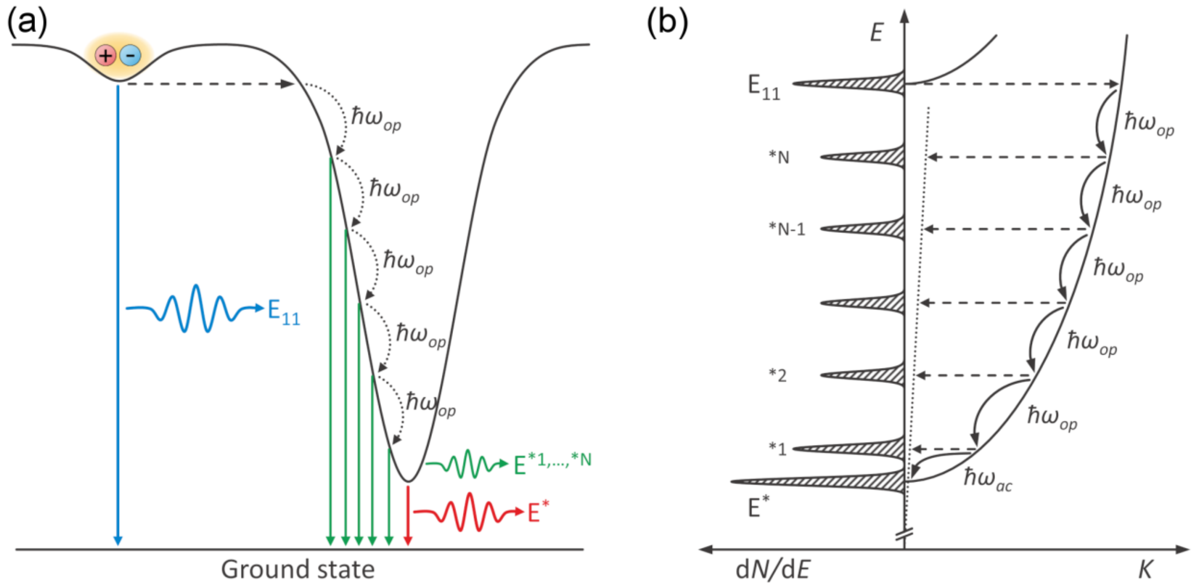

Figure 4.17: Hot-exciton electroluminescence via phonon-mediated relaxation (a) Schematic depiction of hot-exciton injection from a shallow trap into a deep trap and the subsequent energy relaxation by optical phonon emission. The transition energies for the shallow trap (E_{11}), the deep trap (E*), and from the hot-exciton quasi-levels ($E^{*1},..,^{*N}$) are indicated. (b) Simplified model of exciton kinetic energy relaxation. The parabolic curves describe the energy E *versus* momentum K dispersions of the E* defect exciton and of the E_{11} exciton, which is converted into a hot exciton at the defect (right-headed dashed arrow). The full arrows show the optical ($\hbar\omega_{op}$) and acoustic ($\hbar\omega_{ac}$) phonon relaxation processes. The left-headed dashed arrows indicate the momentum scattering that is required for radiative recombination via the photon dispersion (dotted line). The left part in (b) shows the exciton distribution on energy with the hot-exciton quasi-levels *1,*2,..,*N.

This process can be seen in analogy to the phonon-mediated relaxation of hot excitons in optically excited II-VI semiconductors[233–236]. The mechanism that leads to multiple emission lines, located energetically below the hot-exciton quasi-level, has been described in great detail by Permogorov[237]. It requires that the exciton lifetime is short compared to the thermalization processes and that the optical-phonon relaxation rate is larger than the rates of acoustic-phonon relaxation, non-radiative decay, and radiative decay. The generation of hot excitons by excitation with monochromatic light of energy *hv* can then lead to the formation of exciton quasi-levels of energy $E_n = hv - n\hbar\omega_{\mathrm{op}}$ (n is an integer). In our case, shown in **Figure 4.17b**, hot excitons are formed from the electrically-generated E_{11} excitons in the vicinity of the defect by phonon/defect scattering. In this picture, hot-exciton quasi-levels will then form at energies $E_n = E_{11} - n\hbar\omega_{\mathrm{op}}$, and $\hbar\omega_{\mathrm{op}}$ would correspond to the RBM energy. The population of these levels can be calculated with balance equations. Under stationary conditions, the populations P_{N} and $P_{\mathrm{N\text{-}1}}$, of the levels N and N-1, can be derived from[237]

$$\mathrm{d}P_{\mathrm{N}}/\mathrm{d}t = A - P_{\mathrm{N}} \cdot (W_{\mathrm{nrad}} + W_{\mathrm{op}}) = 0,$$

$$\mathrm{d}P_{\text{N-1}}/\mathrm{d}t = P_{\mathrm{N}} \cdot W_{\mathrm{op}} - P_{\text{N-1}} \cdot (W_{\mathrm{nrad}} + W_{\mathrm{op}}) = 0,$$

with A, the hot-exciton generation rate, W_{nrad}, the non-radiative decay rate, and W_{op}, the rate for relaxation with optical phonon emission. The populations of P_{N} and $P_{\text{N-1}}$ are then given by

$$P_{\mathrm{N}} = A/\left(W_{\mathrm{nrad}} + W_{\mathrm{op}}\right),$$

$$P_{\text{N-1}} = P_{\mathrm{N}} \cdot W_{\mathrm{op}}/(W_{\mathrm{nrad}} + W_{\mathrm{op}}).$$

With the assumption that $W_{\mathrm{op}} \gg W_{\mathrm{nrad}}$ it follows that $P_{\mathrm{N}} \approx P_{\text{N-1}}$ Similar results can be obtained for the other hot exciton quasi-levels and the population of these levels would approximately be the same. For the radiative recombination from the quasi-levels, a scattering process is required that accounts also for the momentum mismatch (as indicated in **Figure 4.17b**). This could be satisfied by the optical phonon scattering itself, provided the phonon dispersion bandwidth is small. We note that the RBM bandwidth is found to scale inversely with the unit cell size[238], and for the chiral (6, 5) and (7, 5) nanotubes with large unit cells, the RBM bandwidth is expected to be small. In the case of the (6, 5) nanotube, the RBM frequency, calculated within a tight-binding model, shows only a slight variation of about 1 % throughout the Brillouin zone of the nanotube[239], and therefore the RBM bandwidth is small enough to consider the RBM frequency as a constant. To identify the piece of the RBM branch, relevant to the relaxation processes, we use the E_{11} exciton mass, derived within a tight-binding model, and find that the exciton states in the energy range from E* to E_{11} (**Figure 4.17b**) have wavevectors in the first Brillouin zone. The selection rules for exciton-phonon scattering then limit the wavevectors of the scattering phonons of the RBM branch to the latter zone too, where the RBM frequency is approximately constant. This result is in excellent agreement with the measured almost equidistant starred peaks for this nanotube. Similar arguments can be provided for the (7, 5) nanotube as well.

The above scenario nicely explains our observation that the starred peaks are approximately equidistant, have similar intensities, and are seen only for nanotubes with defects. The quenching of the emission intensity with increasing temperature is expected for the hot-exciton luminescence model because of the decreasing hot exciton lifetime due to an increasing nonradiative decay probability at elevated temperatures. We exclude that the starred peaks are due to electron-phonon-coupling induced side-band phonon-replicas because even a very large Huang-Rhys parameter could not explain the intensity distribution[240]. We, therefore, conclude, that the new peaks can be assigned to hot-exciton quasi-levels and can be considered as a signature of hot-exciton (electro)luminescence. We note that multi-phonon Raman scattering, which can be triggered by optical excitation[237,241], can be excluded in our experiment due to the electrical excitation. Besides, the approximately equal population of the quasi-levels and the temperature dependence would not fit a Raman process[237].

4.3 Photoluminescence from chemically doped nanotubes

In this last section, we discuss the assignment of the electroluminescence (EL) defect peaks E* to the photoluminescence (PL) defect peak E^{*-}. Since we observe in the EL experiment a massive influence of the electrostatic gating on the appearance and intensity of the defect peaks, we performed redox doping of pristine and functionalized (7, 5) dispersions with $AuCl_3$. **Figure 4.18a** shows the PL result for the pristine (7, 5) nanotube dispersion. As expected, the E_{11} exciton becomes weaker with hole-doping, and the corresponding trion $E_{11,T}$ increases in intensity and eventually becomes dominant. The doping dependence agrees very well with the EL data from pristine (7, 5) devices (individual nanotubes at 77 K), shown in **Figure 4.18c**. The E_{11} and $E_{11,T}$ transitions are sharper for the low-temperature EL data, but the peak positions are identical and the evolution of the peak intensities with doping shows the equivalence of electrostatic gating and chemical doping. Also, a blue-shift of E_{11} due to exciton confinement at large doping levels is observed in PL and EL and reproduces previous PL data of redox-doped (6, 5)[242,243]. No blue-shift is observed for the $E_{11,T}$ trion.

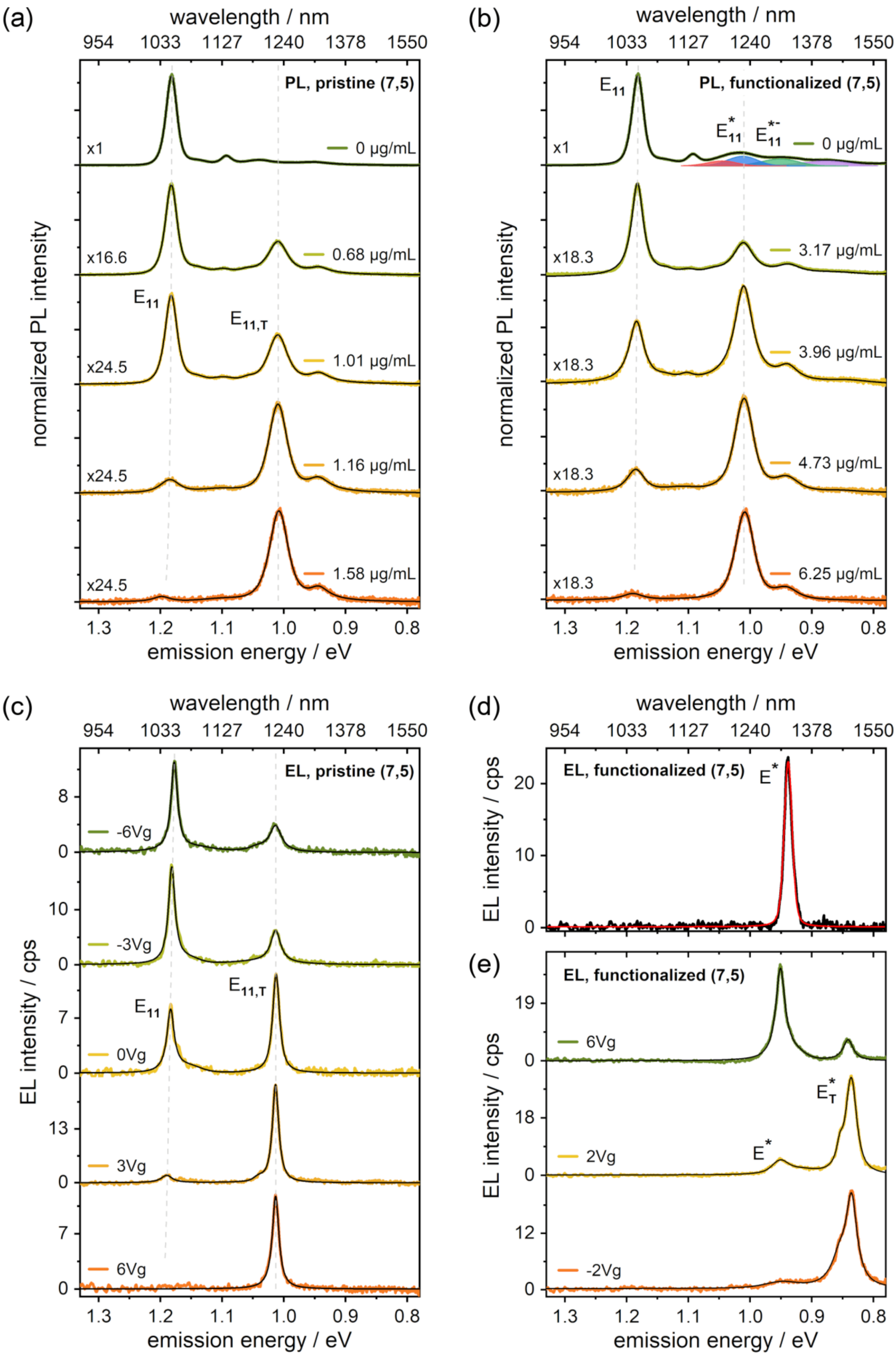
(a)
wavelength / nm
954
1033
1127
1240
1378
1550
PL, pristine (7,5)
x1
0 µg/mL
x16.6
0.68 µg/mL
E_{11}
$E_{11,T}$
x24.5
1.01 µg/mL
x24.5
1.16 µg/mL
x24.5
1.58 µg/mL
normalized PL intensity
1.3
1.2
1.1
1.0
0.9
0.8
emission energy / eV
(b)
wavelength / nm
PL, functionalized (7,5)
E_{11}
E^*_{11}
E^{*-}_{11}
x1
0 µg/mL
x18.3
3.17 µg/mL
x18.3
3.96 µg/mL
x18.3
4.73 µg/mL
x18.3
6.25 µg/mL
normalized PL intensity
emission energy / eV
(c)
wavelength / nm
EL, pristine (7,5)
8
0
-6Vg
10
0
-3Vg
E_{11}
$E_{11,T}$
7
0
0Vg
13
0
3Vg
7
0
6Vg
EL intensity / cps
emission energy / eV
(d)
wavelength / nm
EL, functionalized (7,5)
E^*
20
10
0
EL intensity / cps
(e)
EL, functionalized (7,5)
19
0
6Vg
E^*_T
18
0
2Vg
E^*
12
0
-2Vg
EL intensity / cps
emission energy / eV

Figure 4.18: Electroluminescence of electrostatic gating and photoluminescence of redox doping Comparison of photoluminescence (PL) spectra of redox-doped (a) pristine (7, 5) and (b) functionalized (7, 5) suspensions with electroluminescence (EL) spectra of gate-voltage controlled (c) pristine (7, 5) and (e) functionalized (7, 5) single-tube devices. The $AuCl_3$ concentration in (a) and (b) increases from top to bottom. Intensity scaling factors are given. Excitonic E_{11} and trionic $E_{11,T}$ emissions are labeled. (b) The defect-state emissions E_{11}^* and E_{11}^{*-} are observed for the functionalized (7, 5) at zero doping. Data recorded at RT and under excitation at 1.91 eV/650 nm. (c) EL spectra of pristine (7, 5) single-tube devices measured at 77 K. The peak positions of the gate-voltage controlled excitonic E_{11} and trionic $E_{11,T}$ emissions are marked by dashed lines in the PL spectra. (d) EL defect-state emission E* with high spectral purity under optimum source-drain current (3 nA) and gate-voltage (6 Vg) conditions at 77 K. (e) EL spectra of functionalized (7, 5) single-tube device recorded at 40 nA source-drain current and 77 K. All spectra were fitted with Voigt functions.

Figure 4.18b shows the analogous PL doping study for the functionalized (7, 5) nanotube dispersion. The difference to **Figure 4.2b** is due to reabsorption effects in optically dense dispersions[244,245], as discussed in **Figure 4.19**. Overall, the spectra are very similar to the pristine nanotube data, in particular regarding the doping dependence of E_{11} and $E_{11,T}$. The major difference to **Figure 4.18a** is visible at zero doping, where additional defect-state PL peaks E_{11}^* (blue curve) and E_{11}^{*-} (green curve) appear. Interestingly, the position of E_{11}^* matches well to $E_{11,T}$ at a higher doping level, which makes it difficult to determine whether E_{11}^* in this data is a signature of a deep exciton trap, or due to trion formation because of functionalization with a charged species. The literature often discusses neutral aryl defects[81,84], however evidence for the existence of radical aryl defects giving rise to E_{11}^* has also been given[246,247]. It has also been shown that the defect formation is influenced by the condition under which functionalization takes place[83]. A further discussion about the binding configuration and charging state would go beyond the scope of this work.

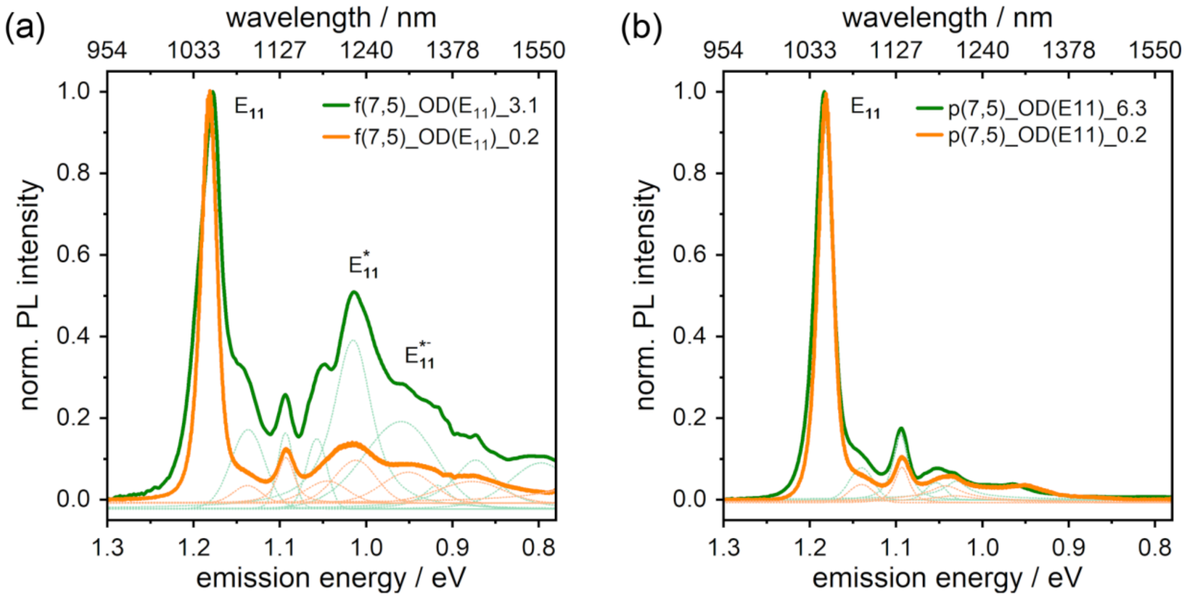

Figure 4.19: PL spectra of (7, 5) SWCNT suspensions with different optical densities Effect of optical density (OD) on the PL spectra of functionalized (a) and pristine (b) SWCNT suspensions. All spectra are normalized to the E_{11} emission peak and the given ODs were measured at E_{11}. The green curves show the spectra of the as-prepared dispersions which have a large optical density (OD>>1). For the titration experiments, these dispersions were diluted to OD=0.2 and the spectra after dilution are shown in orange. These orange spectra are identical to the chemically undoped spectra shown in Figure 4.18a,b. The difference in peak appearance between the orange and green curves is due to the photon reabsorption effect[244,245]. The spectra shown in Figure 4.2b have similar OD to the green spectra shown here.

If we compare the PL doping study of functionalized (7, 5) with the corresponding EL data in **Figure 4.18e** and previous figures we notice that the electroluminescent defect-exciton emission E* occurs in nearly all of our EL data at a wavelength that is close to the E_{11}^{*-} PL emission, which is distinctively of the PL emissions E_{11}^{*} and $E_{11,T}$ (see **Figure 4.2b**). It seems that by electrical excitation the lowest energy state is populated although it is known from PL that defects of different binding configurations can exist on the same tube. This is an important observation in view of chemical attempts to yield tubes in which defect-state emission originates from only a single type of bonding configuration[83,84,87,248,249]. Beyond such efforts at chemical control, EL may give additional control as it not only seems to naturally access the lowest energy defect configuration but also provides gate control over accessing emission from neutral versus charged defect states. As a result, defect-state electroluminescence spectra with high spectral purity can be obtained under optimized operating conditions (see **Figure 4.18d**).

4.4 Summary

We have shown that electroluminescence excitation of single-tube devices with covalent defects triggers emission from neutral defect-state configurations with the lowest transition energy. The intrinsic excitonic and trionic emissions are thereby completely suppressed. With gate-voltage, the emission can be switched from neutral to charged defect-state-emission (defect trion). As a result, a high spectral purity was reached, which is important for the development of on-chip quantum sources based on functionalized carbon nanotubes. At cryogenic temperatures and under specific bias conditions, the intrinsic excitonic emission becomes visible, and new, nearly-equidistant, emission lines appear between the intrinsic and defect emissions. Based on the energetic spacing of the lines, simulations of vibrational modes of the functional group, and correlation with transport measurements, we have assigned these new lines to RBM-phonon mediated hot-exciton electroluminescence. We provide a model for the electrical hot-exciton generation and emission from quasi-levels, analogous to hot-exciton generation in II-VI semiconductors. Finally, we have compared the electroluminescence data with photoluminescence spectra from chemically doped pristine and functionalized nanotubes. For the pristine nanotubes, we find an excellent agreement between EL and PL, and the assignment of the excitonic (E_{11}) and trionic ($E_{11,T}$) emissions are consistent. Regarding the functionalized nanotubes, the neutral defect emission (E*) observed in EL does fit to the E_{11}^{*-} band in the PL spectrum, however, this band also appears in the chemical-doping study of the pristine nanotubes. Moreover, the charged defect emission, seen in EL under electrostatic gating (E^{*}_{T}), has no equivalent peak in the PL of doped functionalized nanotubes. Fortunately, the electroluminescence spectra from gate-controlled single-tube devices under vacuum and at low-temperature in correlation with the charge transport characteristics is conclusive in itself.

5 Photon Correlation Measurements for Carbon Nanotubes with Quantum Defects

This chapter includes content from a research article[20] that has been published by our group. Reprinted with permission from *ACS Nano* **2024**, *18*, 13, 9525–9534. Copyright © 2024 American Chemical Society.

Single-photon sources are one of the essential building blocks for the development of photonic quantum technology. Regarding potential practical application, an on-demand electrically driven quantum-light emitter on a chip is notably crucial for integrating photonic integrated circuits. Here, we propose functionalized single-walled carbon nanotube (SWCNT) field-effect transistors as a promising solid-state quantum-light source by demonstrating photon antibunching behavior via electrical excitation. The sp^3 quantum defects are formed on the surface of (7, 5) SWCNTs by 3,5-dichlorophenyl functionalization, and individual SWCNTs are wired to graphene electrode pairs. Filtered electroluminescent defect-state emission at 77 K is coupled into a Hanbury Brown and Twiss (HBT) experiment setup, and single-photon emission is observed by performing second-order correlation function measurements. We discuss the dependence of the intensity correlation measurement on electrical power and emission wavelength highlighting the challenges of performing such measurements while simultaneously analyzing acquired data. Our results indicate a route toward room-temperature electrically-triggered single-photon emission. Apart from single-photon sources, single-photon detectors are another key component for quantum photonic integrated circuits, for instance, in 2001, Knill et al. demonstrated the possibility of establishing linear optical quantum computing by using beam splitters, phase shifters, single-photon sources, and single-photon detectors[6]. Besides, single-photon detectors are one of the essential elements in the HBT experiment which has been widely used in this chapter. Therefore, proper understanding and characterization of the single-photon detectors would be necessary. In the following chapter, we start with a general introduction to single-photon detectors (SPDs) and focus on the performance metric of one of the promising types, superconducting single-photon detectors (SSPDs), which will be used throughout this work. Following this, we characterize the SSPDs individually and the overall correlation measurement setup to figure out important experimental parameters and performance limitations. Finally, we continue the discussion on the low-temperature correlation measurement of SWCNT field-effect transistors with sp^3 quantum defects as the core of this chapter.

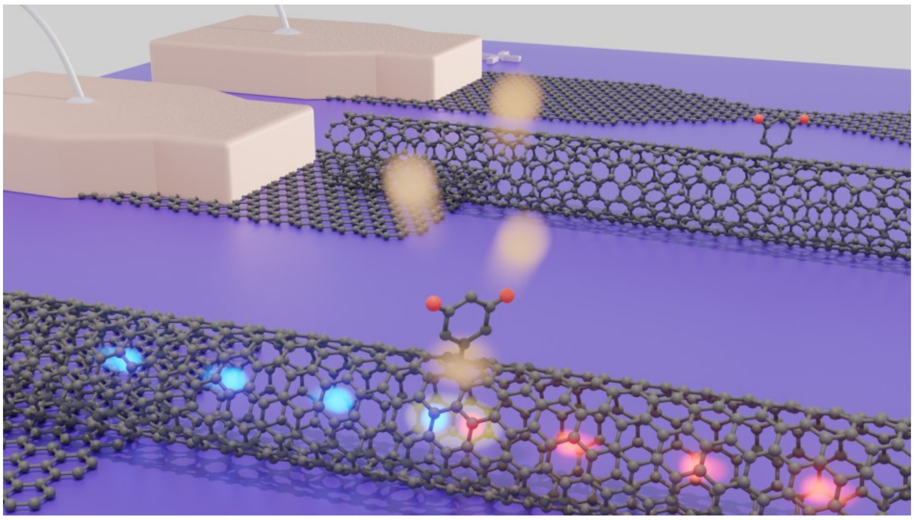

Figure 5.1: 3D model illustration of single-photon emission from an electrically-biased quantum defect in graphene-contacted single-walled carbon nanotube device arrays.

5.1 Introduction

With the increased demand for data transmission and information processing, technology based on optics has played an increasingly important role. For instance, since the demonstration of optical fibers as a technologically feasible platform for telecommunication, optical networks have replaced a large proportion of electrical communication media[1]. The emergence of photonics integrated circuits has also led to the realization of multifunctional devices by combining individual photonic components on a chip[2]. However, the challenges of developing suitable on-demand light sources that are at the same time compatible with on-chip integration hinder the progress. Meanwhile, in the context of quantum technologies, photons have been demonstrated as a system for quantum information processing protocols[4,6] owing to their high-speed transmission and low-noise nature[3]. Despite the rapid advancement of electrically driven quantum-light sources in various material systems including quantum dots[250,251], atomic defects in diamond[252,253], and 2D materials[254,255], the deployment of solid-state quantum emitters on chips with compatibility for hybrid systems and potential scalability remains elusive as of yet.

SWCNTs are among the most promising systems for realizing on-chip quantum emitters[7,8]. Their versatile light emission in the near-infrared, including the telecom band depending on the chiral index[111] and excitation modes[161,166], facilitates the integration with optical fiber communication. Besides, compatibility with various photonics platforms[91,199,256,257] has been studied, and demonstrations of overcoming scalability challenges have also been reported[258–260]. Indeed, SWCNTs as quantum-light sources have been demonstrated via both optical[196] and electrical[11] excitation. However, their lack of exciton localization sites unless at very low temperatures[11], which is the essence of nonclassical light emission, makes practical implementation unrealistic. This demand can be addressed by forming sp^3 quantum defects (0D) at the sidewall of SWCNTs through mild oxidation[15,77] or covalent alkyl-, and aryl-functionalization[78,217,261]. These sp^3 defects can serve as exciton traps with potential depths of 100 – 300 meV, which provide alternative pathways for exciton radiative recombination[82,131] resulting in superior emission yields (from <1 % up to 28 %)[16], and extending the single-photon emission range of SWCNTs up to room temperature[17,18]. However, the advantages of correspondingly functionalized SWCNTs in the development of on-chip quantum photonics as aforementioned have not yet been fully explored. A few works have studied electrically-triggered light emission of SWCNTs with sp^3 quantum defects[19,189,190], which would be the first step towards on-chip quantum emitters. To the best of our knowledge, functionalized SWCNTs as non-classical emitters have so far only been demonstrated in the context of optical excitation.

Complementary to single-photon sources, single-photon detectors are of equal importance in the recent expanding interest in optical quantum information applications[262] and quantum photonics integrated circuits[263]. Conventionally, single-photon detectors have been used in a wide range of fields, such as time-correlated single-photon counting (TCSPC) measurements and nondestructive diagnosis of very-large-scale-integrated (VLSI) circuits[264]. In the scope of this work, we aimed to study single-photon emission based on HBT configuration[265] in which the characteristics of the detectors profoundly affect the measurement precision and limitation. The HBT experiment is commonly used to investigate the statistical properties of photons and typically consists of the photon source of interest, a beam splitter, a pair of detectors, and a coincidence measurement unit. The type of single-photon detector we chose here was a superconducting nanowire single-photon detector (SNSPD or SSPD) due to the presence of theoretically picosecond range jitter (time uncertainty). This allows resolving the photon statistics of fast luminescence decay, for example, the picoseconds range effective luminescence lifetime of excitons in SWCNTs[266–268]. For characterization, in terms of individual SSPDs, we began with studying the temperature-dependent electrical properties and the corresponding inherent dark count rates and moving on to various photo-response measurements, for instance, the detection efficiency and photon number resolution capability. Then, we identified the overall correlation measurement setup characteristics including the system jitter (time uncertainty) by using a pulsed laser source and determined the system time offset via sub-threshold laser photon bunching measurement.

In this work, we demonstrate electrically driven single-photon emission at 77 K from defect-state electroluminescent emission of (7, 5) SWCNT field-effect transistors functionalized by introducing aryl sp^3 quantum defects with aryl diazonium salts. The second-order correlation function measurement was carried out based on the HBT experiment with the functionalized SWCNT emitters cooled down by liquid nitrogen in an optical cryostat. As was mostly necessary for optically excited single-photon emission of functionalized SWCNTs, spectral filtering was still required in this work[18]. We also compare the recorded coincidence histograms as a function of the applied electrical power or emission wavelength including data from our previous study regarding electrically triggered non-classical emission of pristine SWCNTs below 4 K[11]. For comparison purposes, we provide an example of coincidence histogram recorded via non-filtered electroluminescent defect-state emission. Finally, we evaluated the simultaneous recorded supplementary data, such as the temporal trace of collected photon count rate, and discussed the measurement performance restrictions.

5.2 Characterization of Fiber-coupled superconducting nanowire single-photon detectors

Most of the single-photon detectors (SPDs) involve some degree of conversion of photons into electrical signals associated with the photoactive material properties. For example, the first device that was designed for single-photon detection in the 1930s[269], the photomultiplier tube (PMT), comprised of mainly a photocathode (photosensitive element), several dynodes (electron multiplier), and an anode based on the photoelectric effect. Depending on the photoactive materials, single-photon detectors, in general, could be classified into two groups: semiconducting SPDs and superconducting SPDs[211]. The most commercially available semiconductor-based single-photon photodetectors, also known as single-photon avalanche diodes (SPADs), have been developed since the 1960s[270]. The SPADs usually are operated in a reverse bias at a level above the breakdown voltage, the so-called Geiger mode, that enables avalanche effect (signal amplification) via a series of impact ionizations from the photo-generated carrier. Various passive or active quenching circuits are necessary to terminate the avalanche process and restore the operating level. According to different spectral ranges, silicon-based SPADs work well in the visible to the near-infrared regime (up to ~1100 nm), and germanium or III-V groups such as InGaAs are preferable in and beyond near-infrared ranges including telecom bands (1.3 – 1.6 µm). However, generally speaking, the performance of SPADs is superior in the visible wavelength range.

On the other hand, single-photon detectors using superconductivity as the basis of the detection mechanism could be categorized into the second group. The most common type of superconducting SPD is likely the superconducting nanowire single-photon detector (SNSPD)[271]. Well below the transition temperature, the narrow superconducting wires (orders of 100 nm in width) are driven under a constant bias at the level close to the critical current. Therefore, the absorbed incident photon would locally break the superconductivity and revert a small region to a normal state which further expels the current to pass by, redistributes the current density in the adjacent area, and exceeds the critical current. As a consequence, the superconducting nanowire switches locally and temporarily into a normal resistive state and leads to a voltage spike generation[272]. Normally, the nanowire restores the original superconductivity after thermalization until the subsequent incoming photons. The process was also named hotspot formation. To some extent, this detection mechanism would typically not allow discriminating the number of incident photons, unless the presence of certain conditions. To resolve incident photon number, there are different types of superconducting SPDs, for example, superconducting tunnel junction (STJ) detectors[273,274] which consist of two superconducting layers separated by an ultrathin (~1 nm to maximize the tunnel probability) insulating barrier. If the absorbed photon provides enough energy to break Cooper pairs, forming free "quasiparticles," the flow of the quasiparticles tunneling through the insulating barrier would be measurable electrical current and proportional to the incident photon number. A superconducting transition edge sensor (TES) could serve a similar function[275], by operating as a sensitive bolometer that detects the rise of temperature owing to the absorbed photon. The sensor is biased at an operating temperature close to the transition between superconducting and normal state, hence, even a minor temperature variation due to photon absorption could induce a steep increase in resistance. An electro-thermal feedback control is indispensable to maintain the detector within the superconducting transition temperature region, and the photon number information is encoded in the reduction of current flowing through the device.

The fiber-coupled superconducting nanowire single-photon detector (SNSPD) used in this work from SCONTEL contains an electrically and optically accessible ultrathin superconducting layer, a niobium nitride (NbN) film with a thickness of several nanometers, and patterned into submicrometer width (orders of 100 nm) nanostripe with millimeters length arranged in a square meander geometry, which improves the detection efficiency[276]. The output end of the optical fiber is aligned to match the meander structure of the nanowire, aiming for low-loss fiber-to-detector coupling[277]. The SNSPDs offer moderate detection efficiency from visible to near-infrared wavelength range (influenced also by the spectral response of mounted optical fibers), short dead time, low dark count rates, and short timing jitter. The detectors are triggered at a temperature well below the critical temperature (T_c) of the niobium nitride thin film (around 11 K)[276,278] and a direct current (DC) bias is applied to the detectors. The applied bias is set close to the critical current (I_c) yet meanwhile maintains reasonable detection efficiency and dark count rates.

5.2.1 Performance metrics

There are a few important metrics to evaluate the performance of detectors, for example, the detection efficiency, dark count rates, timing jitter, spectral range, and so forth[279,280]. For the need of this work, the following description is mainly focused on the case of the fiber-coupled superconducting nanowire single-photon detector based on niobium nitride, which were purchased from SCONTEL (model: TCOPRS-CCR-TW35).

Detection efficiency

Detection efficiency, or to be precise, the system detection efficiency, is doubtlessly the most important parameter from the experimental point of view. It states the probability of recording an event, in the form of electrical signals, by the arrival of incident photons at the detector. A few factors could affect the overall efficiency: coupling efficiency, absorption efficiency, and internal efficiency. The coupling efficiency is attributed to the overall coupling loss of each of the experimental components. The absorption efficiency describes the yield of which an incoming photon is absorbed by the superconducting NbN film material. The internal efficiency is related to the probability that the absorbed photon could trigger a recordable output electrical signal. The detection efficiency, η_{system}, is usually calculated in the following equation[279]:

$$\eta_{system} = (R_{light} - R_{dark})/R_{incident}$$

, where R_{light} is the count rate of electrical signals generated by the detector during illumination, R_{dark} is the dark count rate when no light was introduced into the system, and $R_{incident}$ is the incident photon count rate which was coupled into the detector. The system detection efficiency of the SNSPDs is greater than 35 % at the given wavelength range between 900 and 1600 nm when operating below 2.5 K.

Dark count rate

Dark count rate (DCR) is, in general, defined as the undesired electrical signal generated except due to the incident photon under study, and usually could be broken down into three main contributions as shown in the following[279,281]:

$$DCR = R_{background} + R_{electronic} + R_{intrinsic}$$

The background noise, $R_{background}$, mostly is related to the scattered or stray light coupled into the detection system, e.g. blackbody radiation in the nearby environment of the detector[282,283]. The electrical noise from the biasing and counting electronics, $R_{electronic}$, may trigger the readout device to record electrical responses unrelated to the detectors. The intrinsic dark count rate, $R_{intrinsic}$, could be associated with, for instance, the imperfection or geometry-dependence of superconducting nanowires[284], or due to thermal fluctuation in the superconducting nanowire, such as current-assisted unbinding of vortex-antivortex pairs[285]. On the other hand, the power dissipation for detectors under biasing conditions at a level close to the critical current of the superconducting nanowire may cause switching between the superconducting state and normal (resistive) state, resulting in false electrical signals. The aforementioned process naturally leads to an increase in dark count rate with increasing current bias[286] or temperature[287].

Timing jitter

Timing jitter, or timing uncertainty, is used to describe the timing accuracy of the detector, which is defined by the fluctuation in the time domain of converting an absorbed photon event to an electrical output signal[279]. To characterize the time resolution of the detector, the timing jitter can be quantitatively acquired by using a pulsed laser source to trigger electrical readout signal from detectors and record many photodetection time delay events for the histogram. The full width at half maximum (FWHM) of the histogram would be the value of the timing jitter. One needs to note that the measured timing jitter, would be the convolution of the intrinsic to the detector[288–290], and of the jitter in the electronics for trigger and registration. The jitter of our SNSPD according to the manufacturer is around 35 ps.

Dead time

By definition, dead time (t_d), also known as recovery time, is the duration of time for the detector to restore to its full efficiency from the previous incident photon event before being able to convert the subsequent photon event into an electrical signal. During that period, the detector would temporarily not produce any electrical response. Therefore, the maximum count rate of the detector theoretically is limited by the inverse of the detector's recovery time, $1/t_d$. In practice, however, the maximum count rate is often limited by the photon event counting instrument. For instance, in our case, the SNSPDs used in this work have a dead time of less than 15 ns but the dead time of our photon event counting instrument (PicoHarp 300) is around 90 ns.

Spectral range

The spectral range is the specific bandwidth in which the detector can effectively absorb photons and produce electrical signals. For superconducting nanowire single-photon detectors, reports have shown the detector could efficiently operate from UV to mid-infrared regime[291,292], where the detection efficiency could vary from wavelength to wavelength. From the material properties standpoint, there is no lower limit for the shorter wavelength, but the upper limit for the longer wavelength is usually restricted by the superconducting energy gap and the nanowire geometry[293]. However, as an integrated SNSPD system, other optical components, such as optical fiber, would also be a factor in determining the spectral range. Take the SSPDs we used for example, the spectral response is around 1.3 – 1.6 µm mostly restricted by the single-mode optical fiber (SMF-28e).

Photon number resolution

In principle, the superconducting nanowire single-photon detector belongs to the group without photon number resolution (PNR) capability since it could be seen as a two-level threshold system in which distinguishing incident photon numbers is not an option. However, under specific bias and illumination conditions, it has been demonstrated that the detectors would respond if only a certain number of incident photons are absorbed simultaneously[271,294–296]. The count rate of the output electrical signal (probability) as a function of the incident photon count rate would show different dependencies under various current bias conditions as shown in the following[271]:

$$P(n) \sim \frac{m^n}{n!}$$

, where $P(n)$ stands for the probability of absorbing n photons simultaneously, and m is the mean value of photon flux per pulse. In this simplified formula, the value m should be much less than 1, indicating the incident illumination is highly attenuated.

5.2.2 Experimental setup

As most of the basic details regarding the experimental setup have been described in the Experimental Methods in Section 3.3.1, the purpose of this section is to refer the following characterizations to specific measurement setup configurations and briefly discuss the reasons behind the setup modification. The correlation measurement setup mainly is comprised of three parts: two superconducting single-photon detectors (SSPDs), which will be distinguished and abbreviated as “DET 0” and “DET 1” later, the SSPD biasing electronic (Control Unit), and the time-correlated single photon counting system (PicoHarp 300). The two SSPDs that require cryogenic operation temperature (below 2.5 K) were mounted in either a dilution refrigerator (Bluefors) at millikelvin range or a closed cycled cryo-refrigeration cryostat (Sumitomo RDK-101DL) with around 2 K base temperature and wired in the following configurations:

(1) SSPDs were installed and operated in the dilution refrigerator. Triggering bias was applied by connecting to the combined port of a low-temperature bias-tee of which the DC port went to the DC output and the RF port went to the RF input of the Control Unit, as shown in **Figure 5.2c**.

(2) SSPDs were installed in the dilution refrigerator and directly connected to the bias-tee (ZFBT-4R2GW-FT+, Mini-Circuits) mounted in the Control Unit as shown in **Figure 5.3b**.

(3) SSPDs were installed in the closed cycled cryostat and were connected to the bias-tee mounted in the Control Unit.

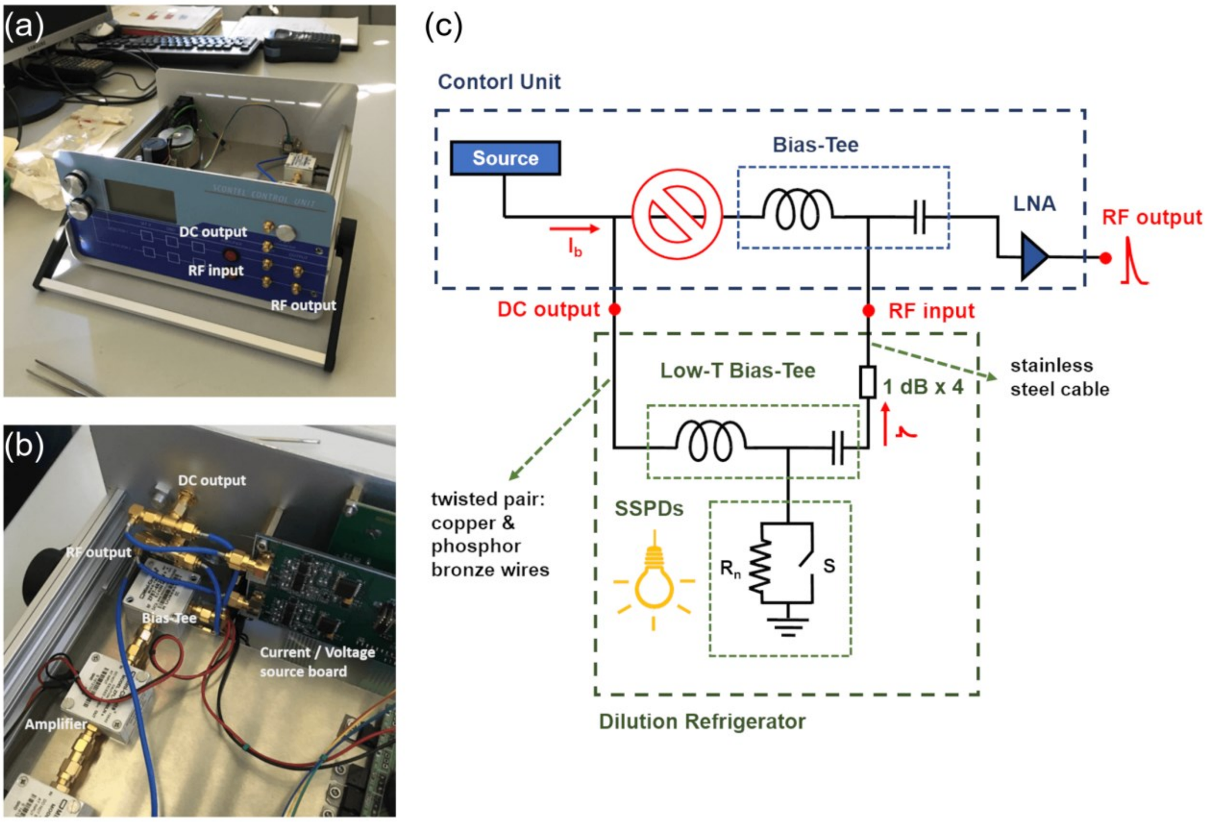

Figure 5.2: Control Unit photos and an overview schematic of connecting configuration (1) (a, b) Photos of the Control Unit where the DC output and the RF input are connected to the low-temperature bias-tee in the dilution refrigerator. The RF output is connected to time-correlated single photon counting system. (c) Schematic illustration of the electrical connections for the measurement setup as described in (1).

However, one needs to note that in the dilution refrigerator, leakage current would appear in the RF lines, which are made out of stainless steel, due to the inserted 1 dB attenuators (BW-S1W2+, Mini-Circuits) between cooling stages. Four 1 dB attenuators are installed at 50 K, 4 K, still plate (800 mK), and intermediate plate (50 mK) which are crucial elements to properly thermalize the inner conductor of the coaxial cable. Therefore, in configuration (1), to avoid the bypass of a significant fraction of DC bias current through the RF lines, it is necessary to break the connection between the biasing source board and the bias-tee in the Control Unit. Unfortunately, although in principle, configuration (1) should be functional, during setup characterization we noticed undesired crosstalk between the two SSPDs, as shown in **Figure 5.3a**. The issue may be traced back to the mechanically unstable installation of the twisted pair of phosphor bronze wires for DC bias, which may cause unintentional signal coupling from ground noise or between wires. This issue could be avoided by implementing configuration (2) to use the RF lines in the dilution refrigerator to both trigger SSPDs and receive photogenerated electrical pulse trains.

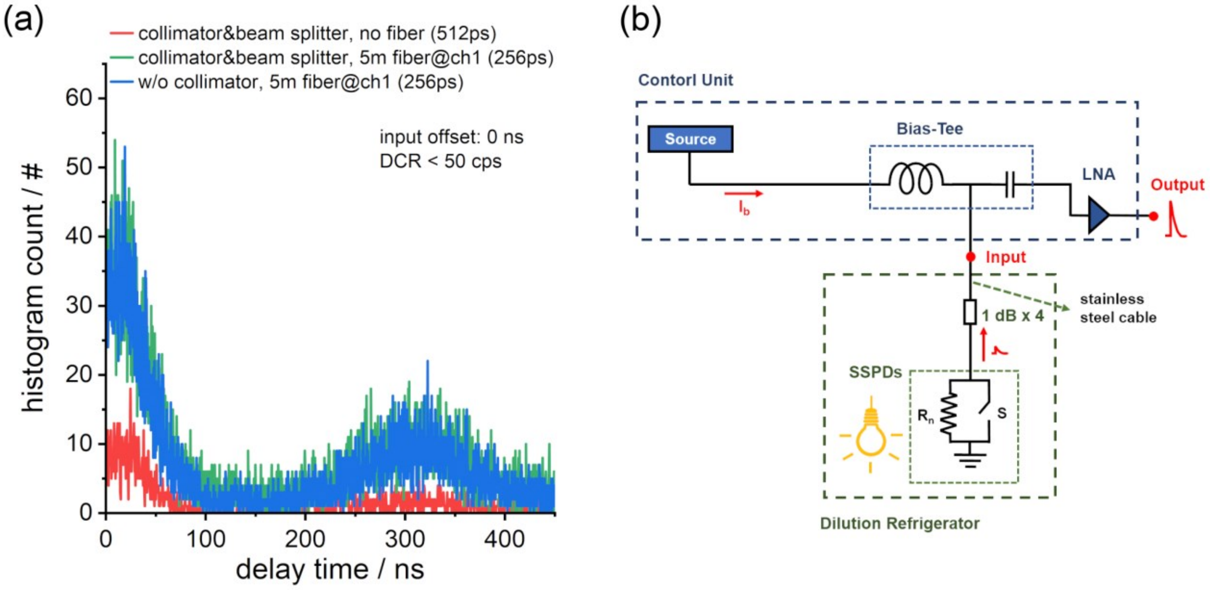

Figure 5.3: Crosstalk and schematics of configuration (2) (a) Undesired correlation between the two SSPDs was observed while recording the coincidence histogram of the dark counts. Different setup components were attached to the SSPDs for each test measurement to rule out the potential origin of crosstalk. (b) Schematic illustration of the electrical connections for the measurement setup as described in (2).

Nevertheless, the 1 dB attenuators in between RF lines for thermalization still provide an alternate path to the ground, and the DC leakage current persists. Additionally, the dilution fridge was placed around 40 m away from our spectroscopy system meaning it required long-distance light coupling via single-mode fibers and communication between electronics. To minimize the probability that unintentional ground is introduced, and to reduce communication challenges, for the intensity correlation measurement of functionalized SWCNTs, configuration (3) was chosen in which all components of the setup are nearby. The crosstalk between the two SSPDs didn’t affect much on their individual characterization. Therefore, the IV measurement and the pulse shape measurements remain valid in configurations (1) & (2), yet for dark count rate and photoresponse characterization, measurements were only carried out in configurations (2) & (3). Lastly, the two SSPDs mounted in the closed cycle cryostat, configuration (3), are not the same SSPD set used in the other configurations. Hence, variation in device performance could be expected.

5.2.3 Current-voltage characteristics measurement

We start the characterization with the current-voltage characteristics, or I-V curve, measurements of the SSPDs under different temperatures ranging from 7 mK to around 20 K. The temperature-dependent I-V curve measurements contain information regarding the critical current of the superconducting thin film and also reveal the critical temperature[276]. The measurements were carried out mostly in configuration (1) as to minimize the DC leakage current from the RF lines. We use the Control Unit as the source unit for biasing. For the voltage biasing I-V curves, the sweeping step size was usually set to 0.05 mV, and the step size of the current biasing I-V curves was 0.1 µA.

I-V curves measurement below 20 mK

Firstly, we demonstrate the current-voltage characteristics measured at 7 mK in configuration (1), namely we biased the SSPDs via twisted DC wires. I-V curves from both the SSPDs were recorded but have only shown results from one detector as an example. **Figure 5.4a** shows the current biasing I-V curve in which the critical current is around 27.2 uA for DET 0 at 7 mK. The slight difference in terms of current value in forward or backward sweep comes from the source unit offset, which depends on the environment. For instance, changes in cable connection may vary the offset slightly. And without surprise, some degree of offsets in current or voltage were observed in all the current-voltage characteristics. The critical currents were calculated after the offset compensation. The large jumps in recorded voltage above critical current were because the source unit ran into compliance. The voltage biasing I-V curves of DET 0 at 7 mK are shown in **Figure 5.4b**. The resistance of the superconducting state of the detector, derived from the I-V curve slope, was around 20 Ω, which was attributed to the normal conducting electrode contacts and leads. A similar critical current was recorded, and hysteresis between the forward and reverse voltage sweep was observed[297]. The hysteresis could be understood by the power dissipation and localized hotspot formation of nanowires in the normal state regime at low temperatures. The self-heating effect sustains local temperatures higher than the critical temperature even when the bias decreases and could arise from multiple factors such as device geometry or thermal environment[298]. Under voltage bias conditions and before the complete conversion to normal state, we observed a current plateau, the so-called hotspot plateau, which is commonly seen in long-channel superconducting devices. The hotspot plateau refers to the growing region of normal states under a DC bias by balancing the Joule heating from driven current and heat out-diffusion. The non-simultaneous transition of the whole structure might also explain the discontinuous jumps in the area. Additionally, the plateau length is affected by the device channel length, as a result, we did not observe a normal ohmic behavior of normal state in the given voltage bias window.

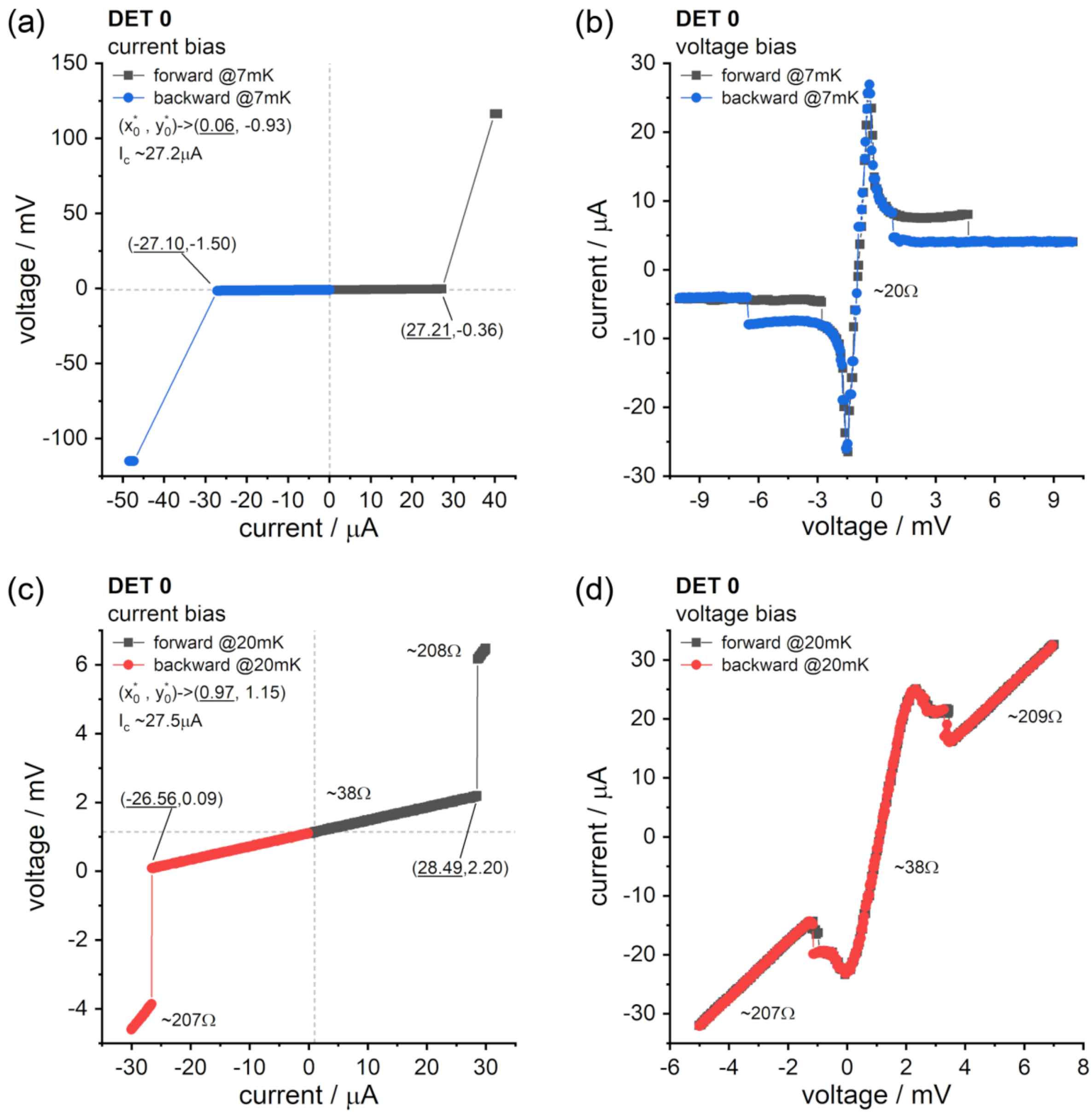

Figure 5.4: Current-voltage characteristics curves of configuration (1) and (2) at mK temperatures (a) The current biasing I-V curves for DET 0 at 7 mK in configuration (1), in which the critical current is around 27.2 μA. The current sweeps started from 0 to either positive or negative polarity. Source unit offsets were indicated. (b) The voltage biasing I-V curves for DET 0 in configuration (1) at 7 mK. Hysteresis between forward and backward sweep and the discontinuous jumps in the hotspot plateau (in normal state) are observed. (c) The current biasing I-V curves and (d) the voltage biasing I-V curves for DET 0 in configuration (2) at 20 mK. Source unit offsets were indicated. The low resistance of the detector in the normal state is mainly due to the resistance between the inner conductor and the outer grounding shield of four cascaded 1 dB passive attenuators in series.

For comparison, we show the current and voltage biasing I-V curves in configuration (2) measured at 20 mK in **Figure 5.4c,d**. As mentioned before, the source unit offset was different after changing the cable connection, yet the critical current calculated is still similar. The slightly higher value may be related to the small leakage current in the RF lines owing to the insertion of 1 dB attenuators for thermalization. The 1 dB passive attenuator has a π configuration circuit consisting of one series resistor (in theory, 5.8 Ω for 50 Ω characteristic impedance) and two shunt resistors (in theory, 870 Ω) to ground. Hence, the resistance between the inner conductor and the outer grounding shield of four cascaded 1 dB attenuators in series would be around 116 Ω theoretically and around 150 Ω measured with a multimeter. This value could well explain the resistance extracted from the I-V characteristics of the detector in the normal state combined with the influence of the conductive electrodes and leads.

Temperature-dependent measurements between 7 mK and 20 K

The temperature-dependent current-voltage characteristics measurements were performed only in configuration (1) to avoid DC leakage current and to allow us to measure roughly the resistance of the detector in the normal state. **Figure 5.5a** shows the current biasing I-V curves of DET 0 ranging from 7 mK to 4.2 K. The critical currents of the detector barely changed while raising the temperature from 7 mK to around 1 K[299]. But at 4.2 K, the critical currents decrease to 18 µA, approximately 35 % of its value at the millikelvin range. Sufficient waiting time for proper thermalization at each recording temperature was not feasible, as the measurement sets were carried out while collecting the circulating ^{3}He/^{4}He mixture back to the storage tank. Thus, the recorded temperatures refer to the nominal temperatures before each I-V sweep. **Figure 5.5b** displays the voltage biasing I-V curves of DET 0 at 7 mK and 4.2 K.

We further recorded the I-V curves from 4.2 K to the temperature above the critical temperature of NbN thin film, which is expected around 11 K[276] in **Figure 5.5c**. Similar to the measurements performed in **Figure 5.5b**, temperatures above 4.2 K were achieved by switching off the pulse tube cryocooler and letting the temperature increase continuously. Simultaneous I-V characteristics measurements were then conducted. Likewise, the nominal temperatures were marked before the start of each record and proper thermalization at each temperature was unfortunately not possible. The critical currents decreased with increasing temperature and the superconducting state almost vanished at around 8 K. Finally, we recorded the I-V curves at temperatures well above the critical temperature, as shown in **Figure 5.5d**, and estimated the resistance of the detector by linearly fitting the plots. At around 15 K, the normal state resistance of DET 0 is around 1.4 MΩ

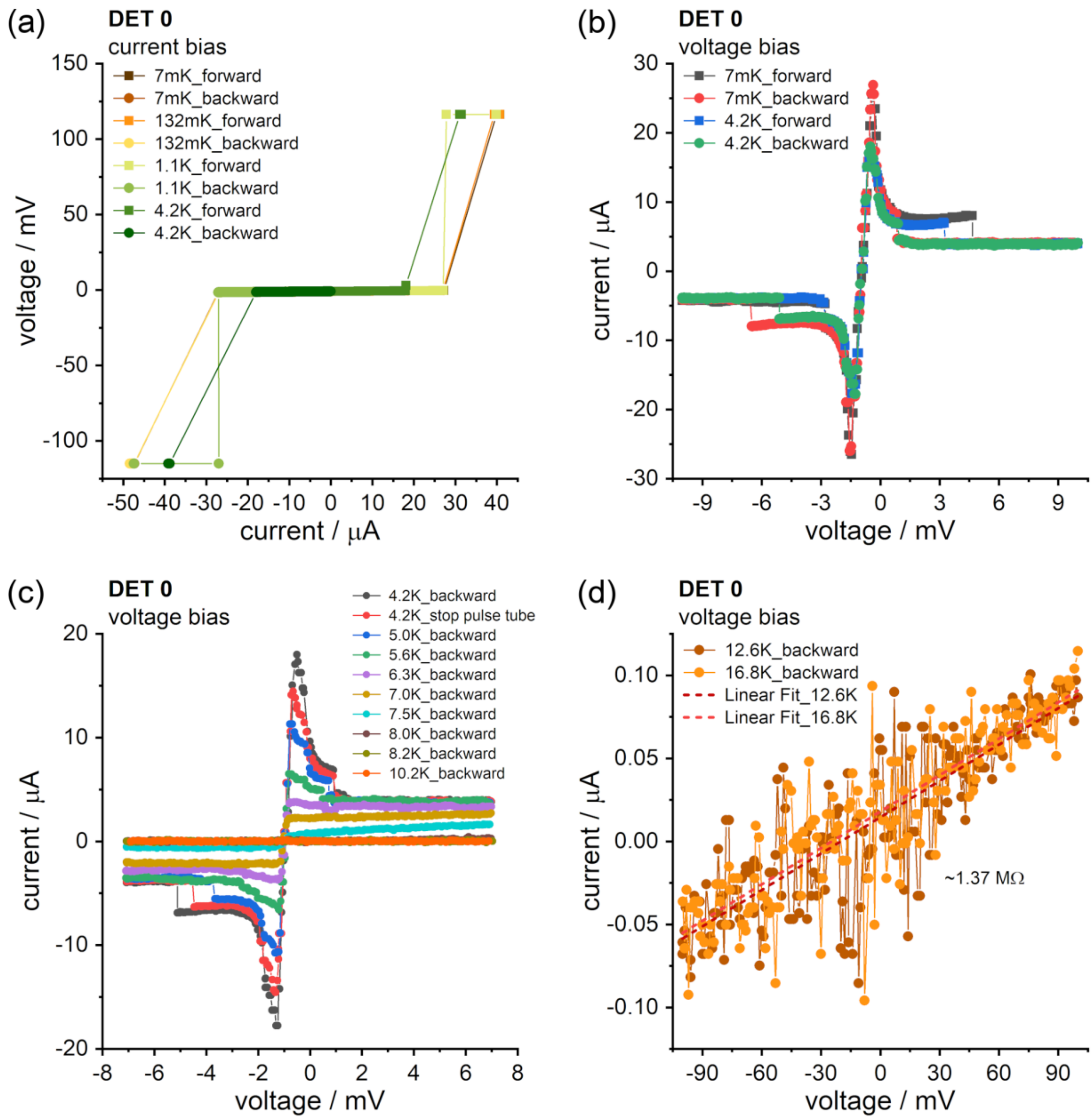

Figure 5.5: Temperature-dependent current-voltage characteristics curves of configuration (1) (a) Temperature-dependent current biasing I-V characteristics curves ranging from 7 mK and 4.2 K of DET 0. A clear drop of critical current can be observed above 1 K. (b) Voltage biasing I-V characteristics curves at 7 mK and 4.2 K for DET 0. (c) Temperature-dependent voltage biasing I-V curves recorded from 4.2 K to ~10 K for DET 0 after switching off the pulse tube cryocooler. The critical currents decrease with increasing temperature, and the superconducting state vanishes at around 8 K. (d) The voltage biasing I-V characteristic curve of the detector in the normal state (above critical temperature) for DET 0. The normal state resistance below 20 K is in the megaohm range.

5.2.4 Dark count rates and electrical pulses

We will discuss first the dark counts and photoresponse of the SSPDs in this section. In **Figure 5.3a** we pointed out the crosstalk issue of the SSPD set in configuration (1). Therefore, the following detector characterization was conducted only in configuration (2) unless otherwise mentioned. The SSPDs mounted in the dilution refrigerator were connected from the feedthrough on top of the fridge to the electroluminescence spectroscopy setup via ~40 m long single-mode optical fibers (SMF-28-J9, Thorlabs) with FC/PC connectors. The photo-induced electrical pulse trains were registered via the photon event counting system (PicoHarp 300) in negative polarity after signal amplification. We performed a series of tests to be sure the additional fibers or optical components added along were in a light-tight environment and did not contribute much to background noise, for instance, due to black body radiation[287].

Figure 5.6a,b show the count rates *versus* DC bias with and without illumination of DET 0 and DET 1, for investigating the light detection ability of SSPDs. The open symbols denote the count rates measured in our system while blocking all incoming light from the environment, namely the dark count rate. The dark count rate increased along with the DC bias until the bias applied went beyond the critical current and the transition from the superconducting state to the normal state occurred. On the other hand, the solid symbols represent the count rate *versus* current bias when some stray light was coupled into the detectors. Count rates detected at the current bias level, in which dark count rates were negligible, gave clear evidence regarding photo-induced electrical pulses owing to the hotspot formation mechanism[271].

We also measured the electrical pulses generated from both the SSPDs which were amplified via two 20 dB low noise amplifiers (ZFL-1000LN+, Mini-Circuits) by an oscilloscope (PicoScope 3206D, Pico Technology Ltd.) in the persistence mode. The persistence mode superimposes multiple input waveforms on the same view which is useful for viewing complex or changing signals. Negative DC bias at the level of 90 % critical current was applied to the SSPDs and electrical pulses of dark counts and counts under illumination were recorded, as shown in **Figure 5.6c,d**. Apart from the pulse amplitude, the pulse shapes are similar in different conditions. Also, in both cases, the electrical pulses appeared with slightly lower amplitude while coupling stray light into the system, which has been reported in an early work of Kitaygorsky et al. [300] The outcome of electrical pulse measurements provides valuable information regarding the setting for the constant fraction discriminators (CFDs) of the input channels of the photon event counter. In this case, the CFDs operate as simple level triggers to suppress background noise but remain having as little influence on the real count rate as possible. Typically, the CFD levels are set at around half of the input electrical pulse height.

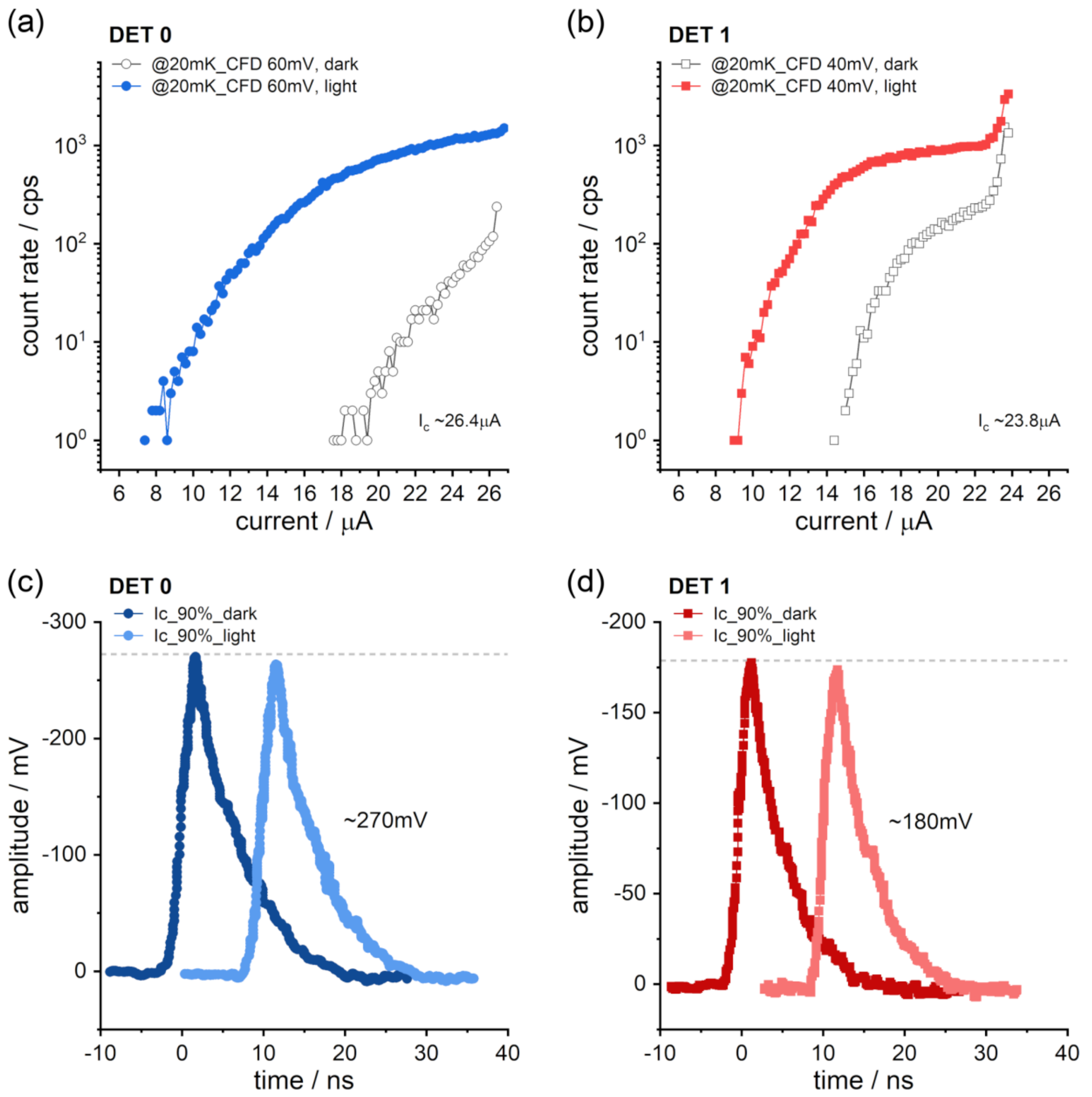

Figure 5.6: Count rates and generated electrical pulses in dark or under illumination (a) The count rate *versus* DC bias of DET 0 and (b) DET 1. The open symbols stand for the dark count rate, and the solid symbols refer to the count rate while stray light is coupled to the detectors. (c) The electrical pulses generated from DET 0 and (d) DET 1 after signal amplification with or without incoming radiation. The dash lines serve as a reference for amplitude comparison.

Additionally, we studied the influence of temperature on the dark count rate and the corresponding light detection ability. We carried out the measurements while performing temperature-dependent I-V characteristics measurements, as shown in **Figure 5.5a**, and therefore configuration (1) was implemented. Similar to the behavior of critical current in a function of temperature, in **Figure 5.7** neither did the dark count rates vary much at temperatures below 1 K, nor did the photoresponse ability vanish. However, at 4.2 K, noticeable dark count rates appeared earlier at a much lower DC bias region. Besides, take **Figure 5.7a** as a representative example, the photon detection ability at 4.2 K was almost completely suppressed.

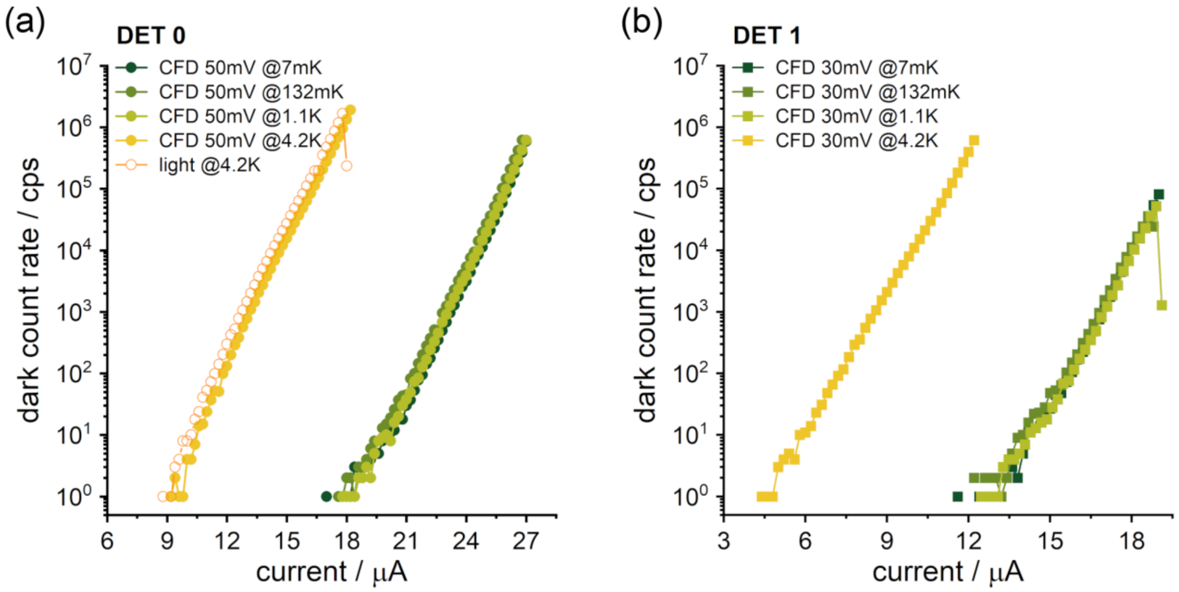

Figure 5.7: Temperature-dependent dark count rate measurements (a) Temperature dependence of dark count rate *versus* current bias for DET 0 and (b) DET 1. Clear changes in dark count rates at 4.2 K can be noticed. The recorded dark count rates were limited by the maximum count rate of the photon event counter (PicoHarp 300) whose dead time is around 90 ns.

5.2.5 Detection efficiency

To determine the detection efficiency, tunable light emission was coupled into the SSPDs with defined wavelength and power, so that the correlation between the input photon flux and generated electrical pulses can be calculated. **Figure 5.8a,b** show the photoresponse for DET 0 and DET 1 under various power of incident light including the dark count rate as the baseline at 20 mK. The solid symbols refer to photo-induced count rates and the open symbols represent the dark count rate. These measurements were done by directly coupling laser light into SSPDs with a 1550 nm laser diode (LPS-1550-FC, Thorlabs) which power was dimed down via a variable optical attenuator (VOAMatrIQ-1002-2-FC, Coherent Solutions) with additional single-mode fixed fiber optic attenuators (FA25T, Thorlabs), if necessary. The variable optical attenuator was running in a power control mode in which the power was regulated and read out by a built-in power meter. Besides, to extract the illumination power precisely, we used a femtowatt photoreceiver (FWPR-20-IN-FS, FEMTO) to determine the actual attenuation of cascaded fixed attenuators. **Figure 5.8c,d** display the calculated detection efficiency for different input power (ranging from 10^{-17} to 10^{-14} W) according to the formula of detection efficiency introduced in Section 5.2.1. The detection efficiency of 10^{-18} W illumination was excluded as the count rates were too close to the dark count rates and therefore appeared large deviation. The outcomes of 1550 nm excitation seem to be independent of the input photon fluxes and the efficiency was above 40 % when SSPDs were triggered around 90 % of the critical currents, in good agreement with what the manufacturer guarantees.

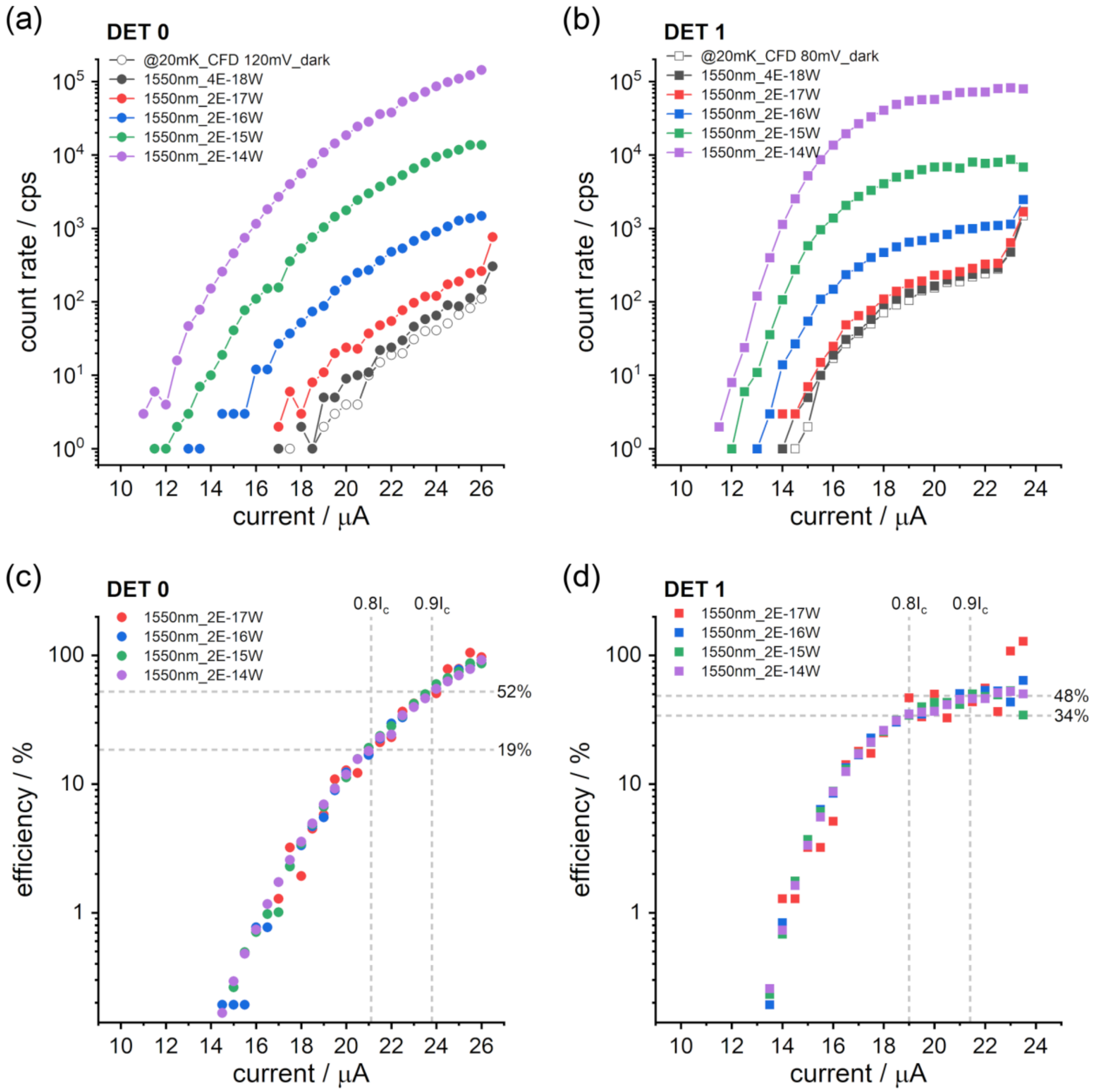

Figure 5.8: Photoresponse and detection efficiency (a) The photo-induced count rates of 1550 nm laser illumination under various power *versus* applied DC bias for DET 0 and (b) DET 1. Dark count rates in open symbols are included as baselines. (c) The calculated system detection efficiency of DET 0 and (d) DET 1 under different input power. The dashed lines serve as a guide to the eye of SSPD triggering DC bias and the corresponding efficiency.

5.2.6 Photon number resolution

It has been reported by Gol'tsman et al.[271,295] that the probability of photon detection as a function of the average incident photon number depends on the DC bias conditions. SSPDs respond to single photons when applied bias is close to the critical current, for instance, 90 % of the critical current. The detection probability changes linearly with the average incident photon number on a double logarithmic scale. At reduced DC bias, the energy of a single photon would not be sufficient to trigger a hotspot formation and as a result, the energy of two (or more) photons is required. In this regime, the detection probability depends quadratically on the incident photon flux, a characteristic of a two-photon event. In **Figure 5.9** we observe a linear dependence from the recorded count rates as a function of incident photon flux for DC bias between 70 % to 95 % of the critical current. This indicates that the SSPDs are capable of working in the single-photon detection regime over a certain applied bias range.

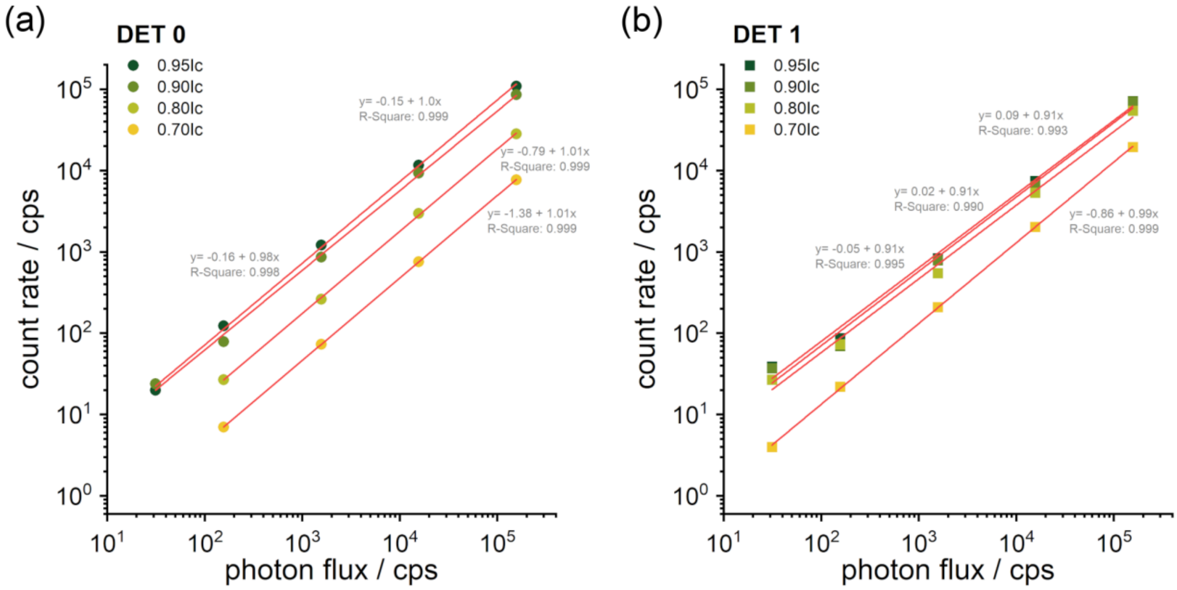

Figure 5.9: Photon number resolution of SSPDs (a) The count rates *versus* input photon flux of DET 0 and (b) DET 1 for DC bias ranging from 70 % to 95 % of the critical current. All curves show a linear dependence (the fitting parameters are included) of the count rate on the input photon flux in a log-log scale, indicating single-photon detection.

5.3 Photon correlation measurement setup characterization

One of the most critical requirements of the SSPDs for our project is the system jitter, as many of the other properties might be compensated in one way or another. For instance, extending data acquisition time if the detection efficiency wasn't good enough. Here, we first characterized the system jitter in configuration (3), as explained previously, to minimize the probability of unintentional ground. Also, we continued using this setup configuration for all other measurements discussed later in this chapter. Finally, we determine the system time delay offset by recording the photon bunching from a laser diode.

5.3.1 System jitter determination with pulsed laser

The overall system jitter is determined by performing the HBT experiment[265] using a pulsed laser with 5 ps pulse width at 1064 nm wavelength. The seed laser (SuperK EXTREME, NKT Photonics) was running in constant current mode with an output power of 0.1 % and RF power of 1 %. 25 dB fixed optical attenuators were added to avoid count rate overflow and the laser light was split by a 50/50 single-mode fiber coupler (TW1064R5F1A, Thorlabs) before reaching SSPDs. The SSPDs were triggered with ~90 % of the critical current and the corresponding dark count rates were below 100 Hz. The generated electrical pulse trains were registered by the time-correlated single photon counting unit in histogram mode with 4 ps time resolution.

Figure 5.10a shows the results of the correlation measurement based on the HBT configuration. The time difference between each two peaks in the coincidence histogram, around 12.5 ns, reveals the 80 MHz repetition rate of the pulsed laser. Ideally, the center of the first peak should appear at zero delay time. Yet internal time offset owing to the delay of cable or electronics shifts the peak ~0.4 ns away. The system jitter can be determined by extracting the full width at half maximum (FWHM) of the peak, as shown in **Figure 5.10b**. The measured jitter value is, however, ~90 ps which is clearly higher than 35 ps according to the manufacturer. One needs to note that the overall system jitter is a convolution of the jitter from each component, including the complete pulsed light source. Therefore, the measured jitter value could be viewed as the upper boundary of the time resolution of our experimental setup. In this case, the SSPDs should still be useful for defect-state emission of SWCNTs, given that the lifetime of localized excitons is in the range of hundred picoseconds.

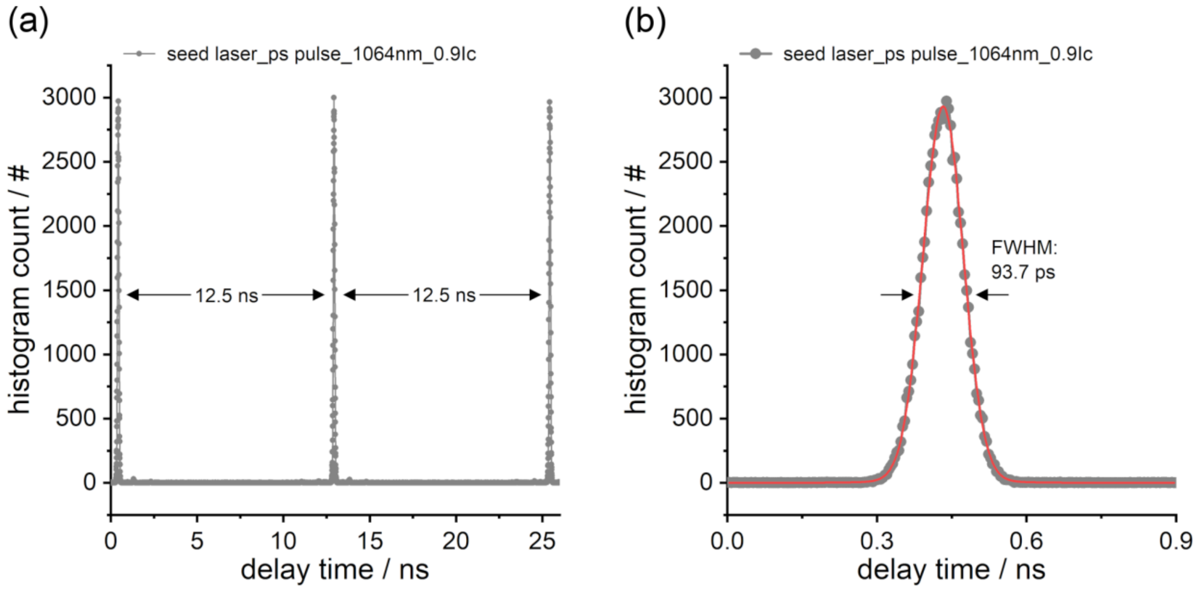

Figure 5.10: Determine system jitter by using a picosecond 1064 nm seed laser (a) Coincidence histogram of performing Hanbury Brown and Twiss experiment with a picosecond pulsed laser driven with 80 MHz repetition rate. Both SSPDs were biased at 90 % of the critical current at 2 K. The coincidence histogram was piled up with 4 ps time resolution in histogram mode. (b) An enlarged histogram plot fitted with a Voigt function to determine the jitter, namely the full width at half maximum (FWHM) of the peak.

5.3.2 Photon bunching from sub-threshold laser diode

The coincidence histogram of the time delay between photon events measured based on the HBT experiment provides information concerning the photon statistics. For instance, the photon bunching effect out of thermal emission or the photon antibunching effect from single-photon emission might be observed where the bunching peak or the antibunching dip appears at zero-time delay. However, in reality, each setup component, such as fibers/cables or SSPDs themselves, may contribute to different degrees of timing delay. Therefore, it's important to determine the system time offset in order not to misjudge the outcome or even acquire invalid results, especially when exploring an unknown emitter. In principle, measuring photon bunching out of thermal light could be a favorable approach in terms of electrically driven light emission, as thermal light exhibits temporal photon bunching characteristics[301]. Practically, it's quite challenging to observe photon bunching from thermal emission experimentally due to the inherent short temporal coherence unless heavy spectral filtering[200,302]. Instead, inspired by the work of Tan et al.[303], we operated a laser diode in the subthreshold regime and observed a photon bunching in the intensity correlation measurement which determines our system time offset simultaneously.

As the results of photon bunching shown in **Figure 5.11**, we either directly coupled emission light from the 1550 nm laser diode into a 50/50 fused fiber coupler (TW1550R5F1, Thorlabs) or via the reflective collimator (RC08FC-P01, Thorlabs) for photon bunching measurements. An in-line fiber polarizer[304] (ILP1550SM-FC, Thorlabs) was placed after the laser intensity was greatly attenuated to avoid count rate overflow at the output port (FC/PC connector). The remaining data acquisition was similar to the system jitter measurement (at 90 % critical current for SSPDs) except the coincidence histogram was compiled with 8 ps bin sizes in histogram mode, only the second plot was with 4 ps. In **Figure 5.11**, we normalized the collected histogram counts to the median value of the uncorrelated counts in the given time window as shown in the figures. The threshold current is around 11 mA, and the first two plots were recorded while driving the laser diode at the subthreshold regime. Besides, the photon bunching effect was also observed while driving the laser diode at certain biases above the threshold current. The unexpected results had been observed previously[305] and were suggested as a consequence of longitudinal mode competition[306] or bimodal behavior[307]. In general, the bunching peak recorded, had a lower amplitude than reported[303]. Aside from the difference in emission wavelength, our laser diode ran without distributed feedback for side mode suppression, and no additional spectral filter or temperature stabilizer[308] was implemented. Also, the single-mode fibers were non-polarization-maintaining fibers in which random birefringence, for example, due to fiber bending[309] may occur. Therefore, mode partitioning[310] may disturb the photon bunching outcome.

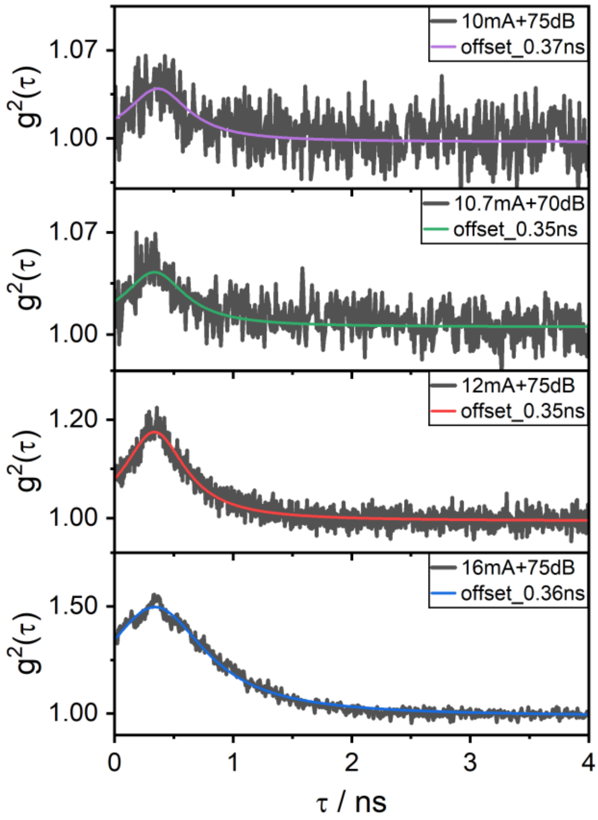

Figure 5.11: Photon bunching effect from sub-threshold laser diode Coincidence histograms of photon bunching measurement under different driven currents below or above the threshold current for system time offset determination. The time offsets are included in the figure. Photon bunching peaks were fitted with Lorentz functions and the peak positions appear at similar time delay in all cases.

5.4 Photon correlation measurements for carbon nanotubes with quantum defects at 77 K

In the following chapter, we will continue the correlation measurement of functionalized (7, 5) SWCNT field-effect transistors using the HBT configuration. The correlation measurement setup for functionalized SWCNTs has been described in Section 3.3.1 and therefore, we will focus on discussing the outcome of single-photon emission at cryogenic temperature, and the supplementary results.

5.4.1 Device fabrication

To study single-photon emission, we used functionalized (7, 5) SWCNTs and integrated them into field-effect transistors with CVD graphene electrodes in this work. The pristine semiconducting (7, 5) SWCNT suspension was prepared from CoMoCAT by polyfluorene (PFO) polymer-wrapping in toluene[69]. Gel filtration chromatography was followed for purification and length sorting. The pristine (7, 5) SWCNT suspension has an average length of around 550 nm, as in the length distribution shown in **Figure 5.12a**, and has a high (7, 5) chirality enrichment which can be seen in the photoluminescence excitation map (PLE) in **Figure 5.12c**. The E_{11} optical transition (1050 nm) of (7, 5) SWCNTs appeared in the PLE map while exciting the suspension at the E_{22} optical transition (657 nm). Weak emission sidebands associated with RBM and K-momentum dark exciton phonon sidebands[72,311–313] can also be noticed but no visible emission from sidewall defects nor other carbon nanotube chiralities[15,76,77]. The pristine suspension was further functionalized by adding reactive dichlorobenzene dopants to create 3,5-dichlorophenyl-functionalized sp^3 quantum defects as we reported in the recent work[19]. PLE measurement, **Figure 5.12d**, was performed on the as-prepared functionalized suspension to confirm the sp^3 defect formation in which the red-shifted defect-induced emission bands, denoted here as E_{11}^{*} and E_{11}^{*-}, can be observed[16]. The defect-state emission band originates from the localization of excitons at deep traps (in order of hundreds meV) and spreads over a rather wide wavelength range mainly due to the diverse binding configurations of the aryl group to the carbon nanotube lattice[81,83,84,87,137].

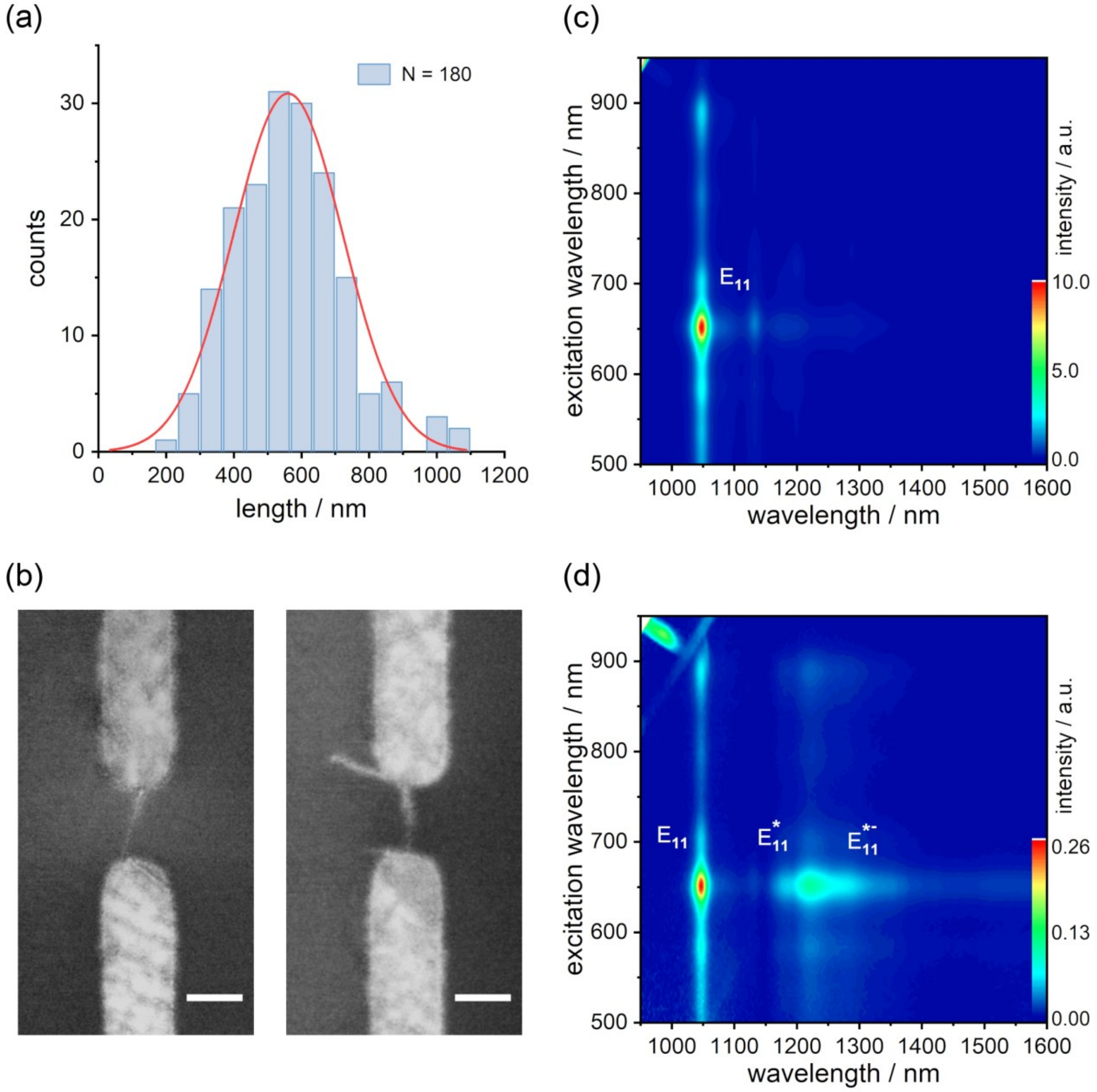

Figure 5.12: Images of single-tube device and properties of carbon nanotube suspensions (a) The mean length value of the nanotube for the devices of electroluminescence/intensity correlation measurement is around 560 nm. The statistic was extracted by analyzing 180 individually dispersed nanotubes from the SEM images. Normal distribution was fitted to the histogram. (b) Representative scanning electron microscopy images of SWCNT devices where a single nanotube was wired to monolayer CVD graphene electrode pair. The scale bar equals 150 nm. (c) The photoluminescence excitation map of the suspension from polymer-wrapped (7, 5) SWCNTs dispersed in toluene before introducing sp^3 sidewall defects with 3, 5-dichlorobenzene functionalization, and (d) after the functionalization process. E_{11} optical transition and the red-shifted defect-state emission (E_{11}^* and E_{11}^{*-}) are labeled.

The functionalized (7, 5) SWCNTs were integrated into three-terminal field-effect transistors via DC-dielectrophoresis[208] in which monolayer CVD graphene acted as the source-drain electrode pairs with 150-200 nm gap size and the heavily p-doped Si as the back-gate, similar to the method introduced in the previous chapter. Dielectrophoretic deposition conditions were adjusted to obtain devices with single or few tubes, and a representative SEM image of a SWCNT/graphene device was shown in **Figure 5.12b**. Devices were electrically wire bonded and mounted into the optical cryostat of our near-infrared optical microscopy and spectroscopy setup. The cryostat was fixed on a motorized XY scanning stage to allow precise positioning of the emitter. This is especially crucial when coupling emitted light into the single-mode optical fiber to perform second-order correlation function measurements, as mentioned already in Section 3.3.1. The device was vacuum annealed after the cryostat had been evacuated below 10^{-6} mbar and subsequently cooled down to 77 K without breaking the vacuum. Transconductance characteristics, examples displayed in **Figure 5.13**, and electroluminescence measurements were carried out before moving on to second-order correlation function measurements. The constant source-drain current mode was implemented to reliably drive devices for electroluminescence, and the emitted light was analyzed by a linear InGaAs photodiode array with a spectral response range between 950 to 1610 nm. All spectra were calibrated by the relative spectral sensitivity of the setup[70].

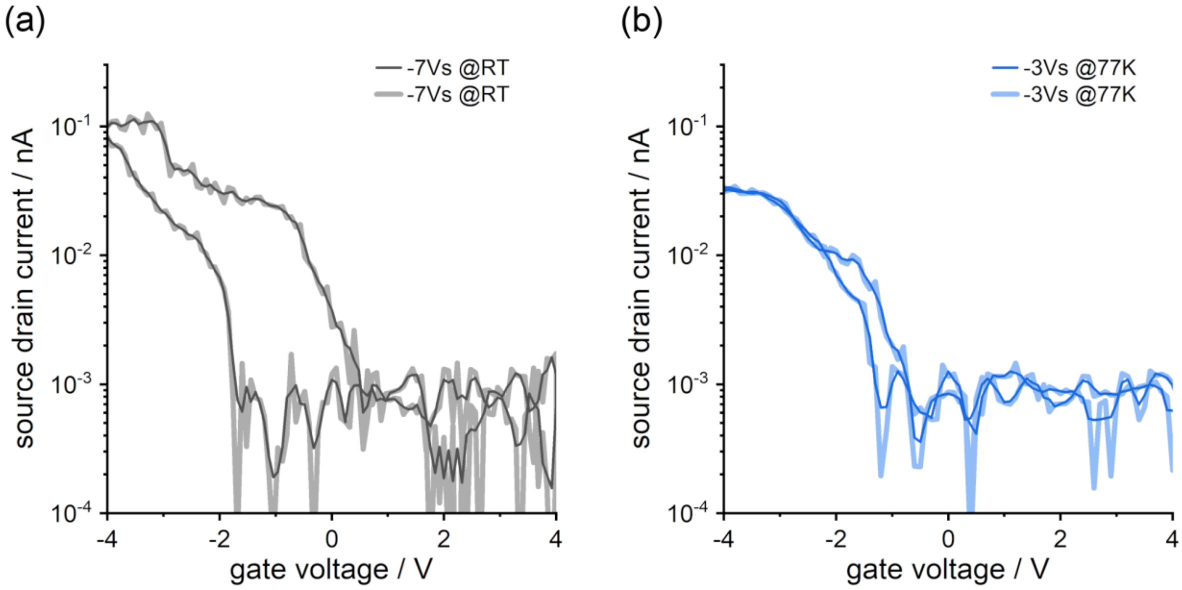

Figure 5.13: Transconductance characteristics of functionalized (7, 5) SWCNT devices (a) Transconductance measurement at room temperature and (b) at 77 K, liquid nitrogen, temperature with ±4 V gate voltage sweep and -7 V and -3 V source-drain bias respectively. The 3-point median smoothed data are presented in darker color lines.

5.4.2 Electroluminescence spectroscopy and intensity correlation measurement

The coincidence histograms in which antibunching behaviors were observed at 77 K and the electroluminescence spectra measured before starting the intensity correlation measurements are discussed in the following section. Clear antibunching behavior, around 75 % single-photon purity in **Figure 5.14b**, was observed from the functionalized (7, 5) SWCNT device by filtering the trionic defect-state emission (E^*_T)[19,220] via a 1350 nm long-pass filter (FELH1350, Thorlabs), as shown in **Figure 5.14a**. The single-photon purity refers to the probability of emitting a single photon instead of multiple photons, which can be quantified by the value of the second-order correlation function at zero-time delay, $g^2(0)$. The functionalized (7, 5) SWCNT device was triggered under a 2 nA constant source-drain current over a time period of around 38 ks, and the SSPDs were driven at around 90 % of the critical current with dark count rates of less than 100 cps. The histogram was accumulated with 8 ps time resolution from data acquired in time-tagged mode.

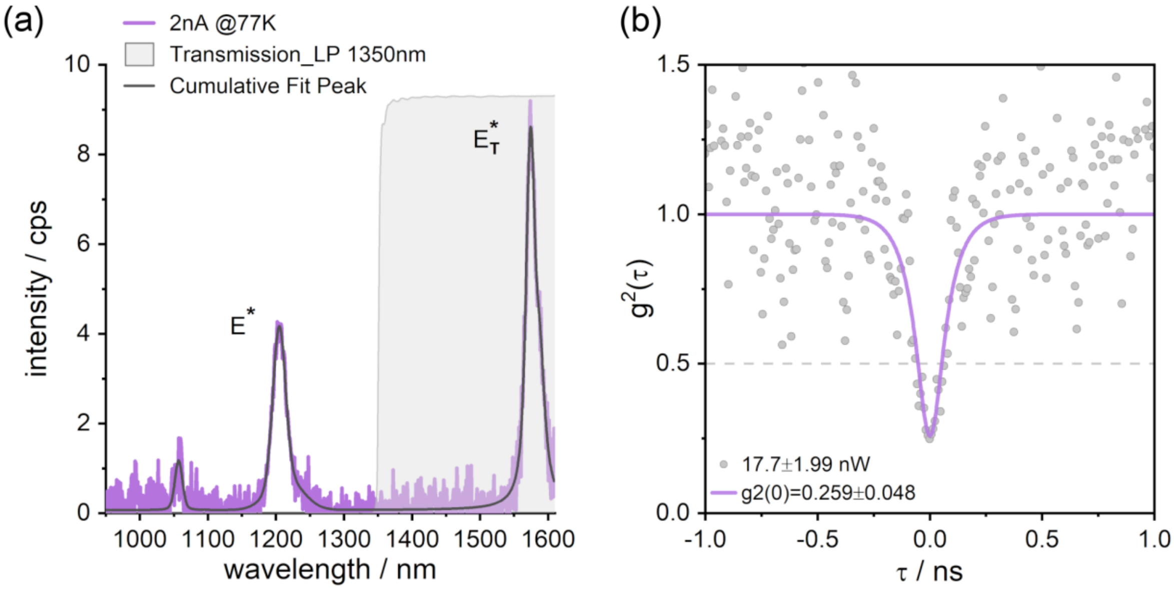

Figure 5.14: Electroluminescence spectroscopy and coincidence histogram (a) The electroluminescence spectrum of functionalized (7, 5) devices measured at 77 K under 2 nA constant source-drain current excitation. Excitonic and trionic defect-state emission, E* and E^*_T, are marked. The spectrum was fitted with Voigt functions and overlapped with the transmission spectrum (grey area) of the 1350 nm long-pass (LP) filter, indicating the filtered light emission for the intensity correlation measurement at 77 K. (b) The coincidence histogram measured at 77 K by collecting spectrally filtered electroluminescence. The histogram was accumulated with 8 ps time resolution using TCSPC software for data acquisition and analysis. The fitting curve is presented showing clear antibunching behavior with the second-order correlation function at zero-time delay $g^2(0)$ equals 0.26. The dashed grey lines served as a guide for the eye for $g^2(0) = 0.5$.

The best single-photon purity recorded in this work, around 92 % in **Figure 5.15b**, was observed from the functionalized (7, 5) SWCNT device by transmitting the excitonic defect-state emission with the lowest transition energy ($E_{11}{}^{*-}$) via a 1300 nm band-pass filter (FBH1300-12, Thorlabs), as shown in **Figure 5.15a**. The filter has a bandwidth of 12 nm. The histogram was accumulated with 8 ps time resolution from data acquired in time-tagged mode. On the other hand, the time-tagged data with the lowest single-photon purity is plotted with 12 ps bin sizes in **Figure 5.15d** with a value of around 60 %. For this measurement, a 1200 nm band-pass filter (FBH1200-10) was used in **Figure 5.15c** for spectral filtering with a bandwidth of 10 nm. Apart from the uncertainty that more than one emission center could be active, perhaps more than one nanotube, the similarity in terms of emission position of the excitonic defect-state emission ($E_{11}*$) and the trionic emission ($E_{11,T}$) could also be a reason to explain the poor purity. In our recent work, we already pointed out the difficulty of distinguishing between the defect-state emission and the intrinsic trionic emission[19].

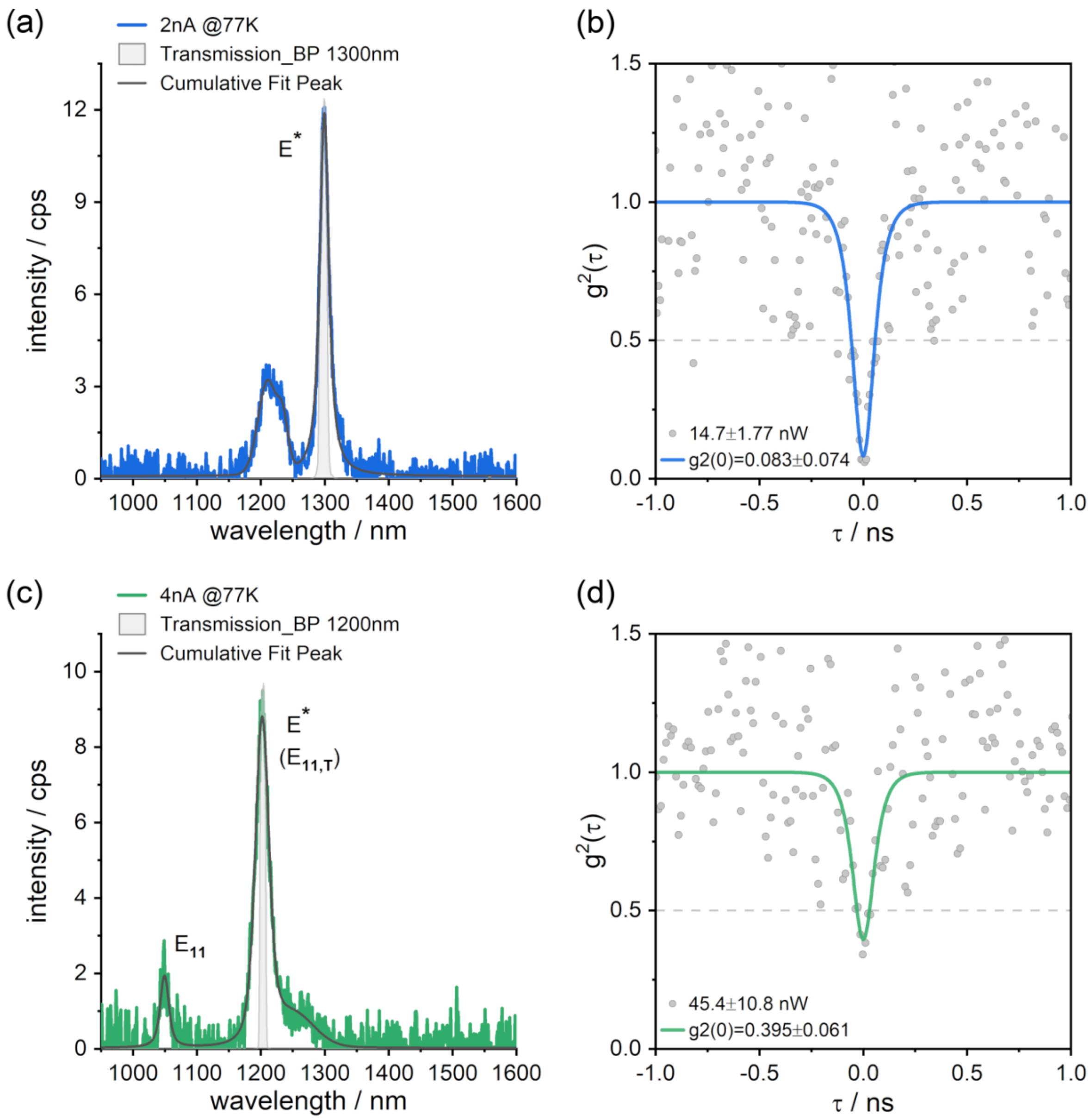

Figure 5.15: Intensity correlation measurement with band-pass (BP) filters (a), (c) Electroluminescence spectra of two other different functionalized (7, 5) devices measured at 77 K under constant source-drain current excitation, as indicated in the figures. The intrinsic excitonic (E_{11}) and trionic ($E_{11,T}$) emission, as well as the excitonic defect-state emission (E*) are marked. EL spectra were fitted with Voigt functions and overlapped with the transmission spectra (grey area) of respective spectral filters, indicating the filtered light emission for the intensity correlation measurement at 77 K. (b), (d) The respective coincidence histograms measured at 77 K by collecting spectrally filtered electroluminescence. The histograms were compiled with 8 ps time resolution for (b) and 12 ps for (d) using TCSPC software for data acquisition and analysis. Fitting curves are overlaid with the second-order correlation function at zero-time delay $g^2(0)$ equals 0.08 and 0.40. The dashed grey lines served as a guide for the eye for $g^2(0) = 0.5$.

The coincidence histograms of the electrically driven defect-state emission from functionalized (7, 5) SWCNT devices were composed out of the bidirectional start-stop events each with the time resolution aforementioned. As details explained in Section 3.3.2 and the analysis process demonstrated in **Figure 3.5**, the signal-to-noise ratio of the histograms is improved by correlating the received electrical pulse trains from the two superconducting single-photon detectors in both directions. To determine the constant time offset of our system which required to be compensated in analysis, we replaced the functionalized SWCNT sample with a 1550 nm laser diode (LPS-1550-FC, Thorlabs) and generated photon bunching signals by operating the laser diode in the subthreshold, detailed described in Section 5.3.2. By overlapping photon bunching peaks with the antibunching dips of defect-state light emission from functionalized SWCNTs, shown in **Figure 5.14a** and **Figure 5.15a** respectively, both accumulated by the start-stop events in the same direction, we confirmed the time offset of both experiments remains similar in **Figure 5.16**. All histogram curves were fitted by the sum of two exponential functions $g^2(\tau) = 1 - c_1 e^{-\gamma_1|\tau-\tau_0|} - c_2 e^{-\gamma_2|\tau-\tau_0|}$, where $c_1 < 0$ and $c_2 > 0$ indicate the amplitudes of bunching and antibunching, γ_1 and γ_2 represent the decay rates, and τ_0 corresponds to the center of the zero-time delay of the antibunching dip, adapted from our previous work[11]. The values of the source-drain current bias for electrical excitation, the average dissipated electrical power, the spectral filter, and the second-order correlation function at zero-time delay with the standard deviation extracted from fits and were provided in the figures.

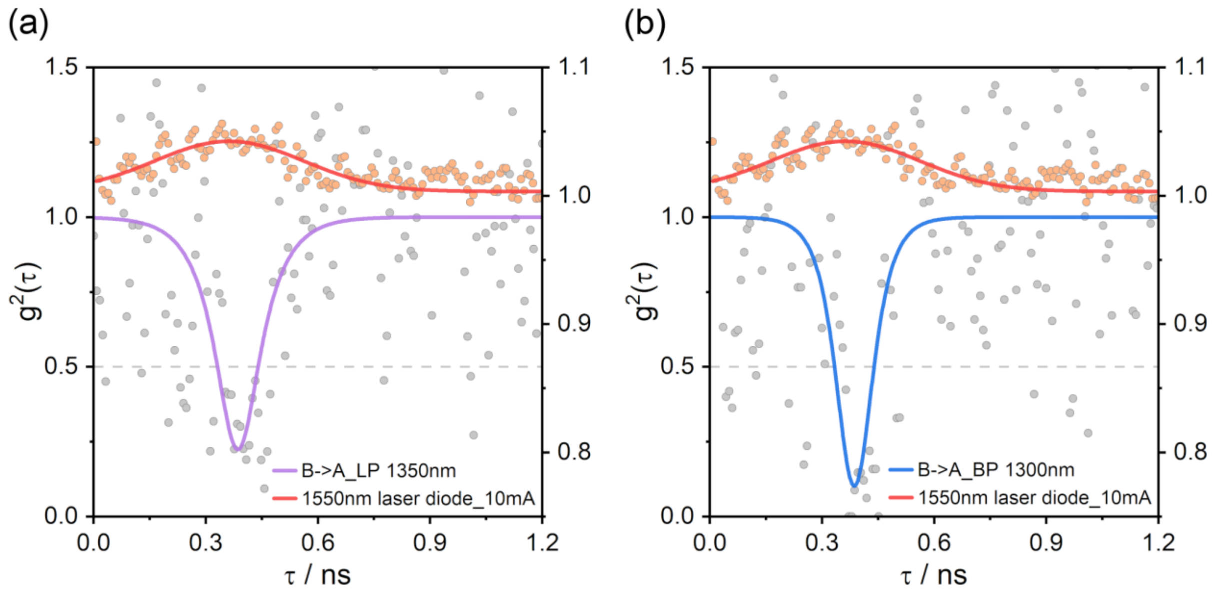

Figure 5.16: Comparison of time offsets recorded with a nanotube emitter and a laser diode The coincidence histograms measured from the functionalized SWCNT devices as shown (a) in Figure 5.14a and (b) in Figure 5.15a are compared with a photon bunching peak from a laser diode to confirm the constant system time delay between the two channels of the TCSPC. Both photon antibunching curves of functionalized SWCNT devices were composed of only one direction of start-stop event pairs, and as expected, the positions of the antibunching dip and the photon bunching peak appear at a similar time delay. The photon bunching was recorded in the histogram mode with an 8 ps bin size by operating a 1550 nm laser diode (LPS-1550-FC, Thorlabs) at the subthreshold regime (10 mA operating current) with sufficient attenuation (Fixed Fiber Optic Attenuators, Thorlabs) as inspired by the work of Tan et al.[303] and described in the previous section.

The extracted $g^2(0)$ values of the antibunching dip at zero-time delay from the intensity correlation measurement are shown in **Figure 5.17a** as a function of applied electrical power. Data adapted from the waveguide-integrated non-classical light emitter of pristine (9, 7) SWCNTs below 4 K[11] was included for comparison. At first glance, there seems to be a linear relation between the dissipated electrical power and the $g^2(0)$ value disregarding the presence of sp^3 quantum defects. However, one needs to note that the data were acquired under different temperatures, marked with red for 77 K and blue for 1.6 K separately. It has been pointed out in the literature that the probability of nonclassical emission due to exciton localization in an unstable electrostatic environment greatly depends on the temperature[10]. An in-depth study of the electrical power dependence of the antibunching from the functionalized SWCNTs was not the main focus of this work, nevertheless, a general picture was that the lower the electrical power, the better the $g^2(0)$ value, leading to a higher probability of single-photon emission. Part of the explanation may relate to one of the general challenges for electrically driven quantum emitters - namely how to concentrate the radiative recombination of electron-hole pairs at the defects instead of surroundings[212]. Also electrical power-dependent spectral purity of defect-state emission plays a role, which could be affected also by the defect density or characteristic displacement between defects. Unfortunately, to the best of our knowledge, a comprehensive study of spectral evolution as a function of triggering power or defect number/density at single- (few-) nanotube levels is still missing. **Figure 5.17b** presents the full-width at half-maximum (FWHM) of the antibunching curves as a function of electrical power, which correlates with the emission lifetime of SWCNTs[131]. Comparison of functionalized and pristine SWCNTs wouldn't be conclusive as the measurement conditions were quite different. However, a trend between FWHM and the emission wavelength could be observed, see **Figure 5.17b** inset, which is roughly in agreement with the sp^3 defect trap depths[82,131].

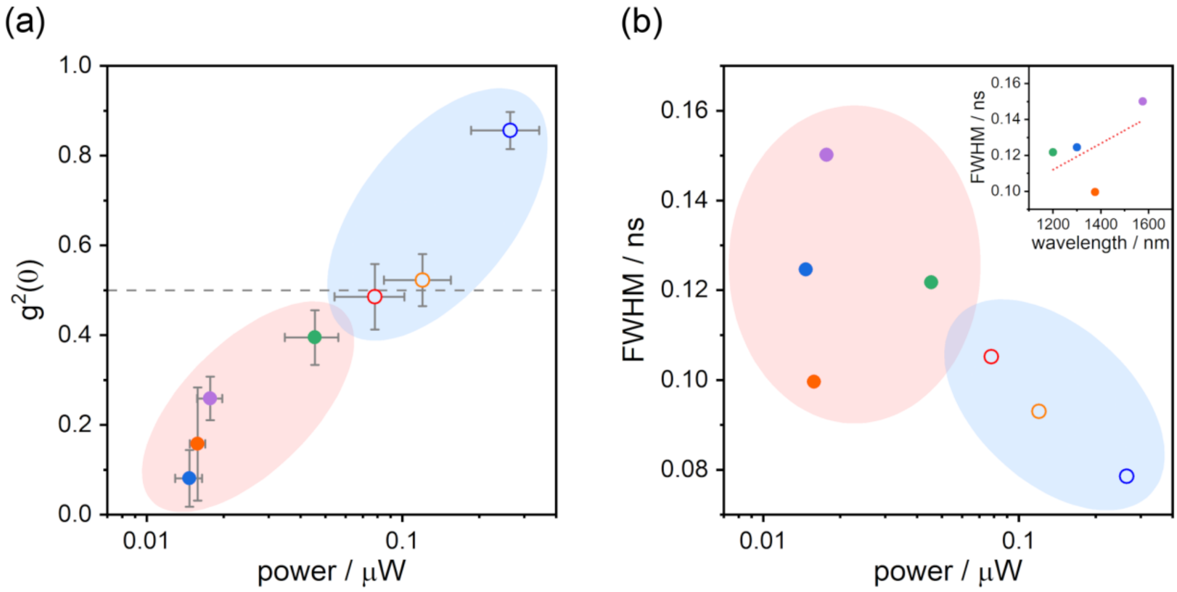

Figure 5.17: Electrical power dissipation *versus* the $g^2(0)$ value and FWHM (a) The extracted $g^2(0)$ values *versus* the dissipated electrical power. The solid circles correspond to the intensity correlation measurement of functionalized (7, 5) SWCNTs at 77 K (red area), and the open circles are data at 1.6 K for pristine (9, 7) SWCNTs (blue area) adapted from reference[11]. The y error bars stand for the standard deviation derived from the photon antibunching fit. The x error bars indicate the standard deviation of the recorded dissipated electrical power. (b) The full-width at half-maximum (FWHM) acquired from the fit results *versus* electrical power dissipation. The inset represents the wavelength dependence of the extracted FWHM values. The color of solid circles refers to the results shown in this section and outlook.

5.4.3 Second-order correlation function measurement without spectral filter

As mentioned previously, spectral filtering is still important owing to the emission stability over long data acquisition time and the potential existence of multiple emission spots (e.g., more than one quantum defect). An example coincidence histogram of intensity correlation measurement at 77 K without inserting a spectral filter is shown in **Figure 5.18b**. Despite being able to acquire electroluminescence spectra with narrow linewidth and high spectral purity at moderately low excitation current, displayed in **Figure 5.18a**, the possibility of having two (or more) identical quantum defects and additional emission related to mobile excitons cannot be completely ruled out and leads to a reduced single-photon purity. The most pronounced peak was around 1210 nm under a constant current excitation with linewidth around 15 meV. The coincidence histogram was generated in the histogram mode with 8 ps time resolution. Constant source-drain bias from -8 to -13 nA was applied during the measurement period to accommodate acceptable photon count rates. The outcome could relate to the non-ideal light emission intensity plus light collecting efficiency and will be further clarified in the following section.

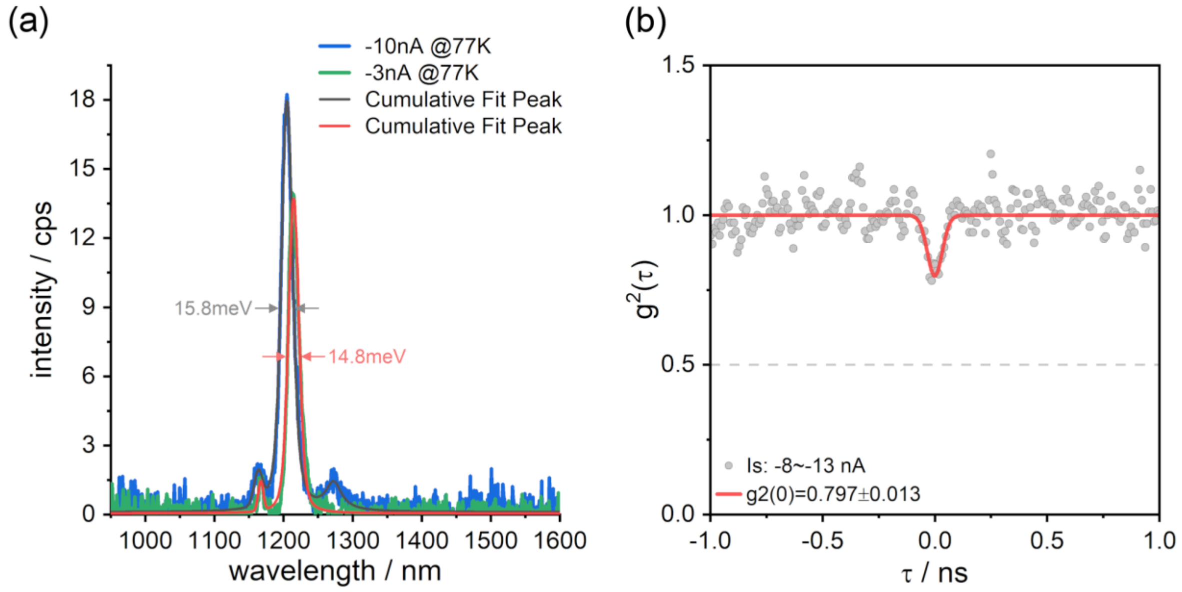

Figure 5.18: Intensity correlation measurement of functionalized (7, 5) without spectral filter (a) Electroluminescence spectra at 77 K from a functionalized (7, 5) SWCNT device measured at -3 and -10 nA constant source-drain bias respectively. The spectra were fitted with Voigt functions and the most pronounced peak was around 1210 nm which is attributed to the excitonic defect-state emission (E^*). However, it could be that intrinsic trionic emission ($E_{11,T}$) may also contribute since their emission peak positions are rather similar. (b) The coincidence histogram acquired from intensity correlation measurement $g^2(\tau)$ without any spectral filter at 77 K by running the TCSPC in the histogram mode with 8 ps time resolution. Constant source-drain bias from -8 to -13 nA was applied during the recording period of around 80 ks. The fitting curve was overlaid showing a low degree of photon antibunching ($g^2(0) \approx 0.8$) with the dashed grey lines serving as a guide for the eye at $g^2(0) = 0.5$.

5.4.4 Photon count rate and applied electrical power

Simultaneous to the time tagging of the incoming photons we continuously measured the voltage that was applied by the source-measurement unit to maintain the constant current bias. **Figure 5.19c** shows such a trace of the power which varies substantially over time. One notes that despite the variation, the mean value didn’t change dramatically during the measurement, suggesting the low hysteresis, which may be ascribed to the low-temperature and vacuum environment[70,314]. The data is the trace that corresponds to the coincidence histogram shown in **Figure 5.14**, but it is representative of what we have observed. For the other coincidence histograms in **Figure 5.15**, simultaneously recorded supplementary results are provided in the Appendix **Figure 0.1** and **Figure 0.2**. The recorded photon count rate, the sum of both input channels of the correlator, is plotted in **Figure 5.19a** and binned to a histogram in **Figure 5.19b**.

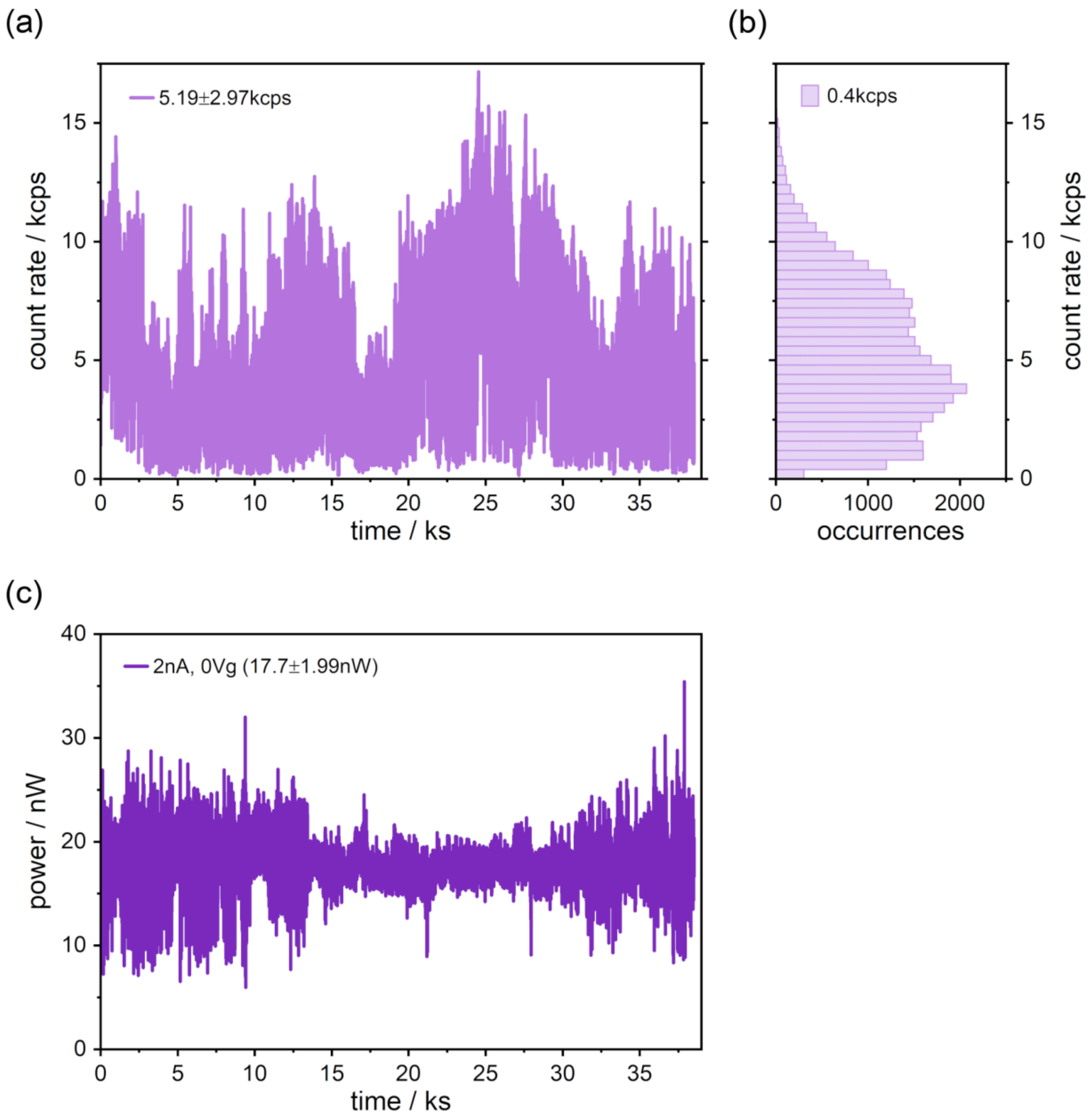

Figure 5.19: Photon count rate and electrical excitation time trace (a) The collected overall photon count rate over the time period (~38 ks) of intensity correlation measurement under 2 nA source-drain bias as in results shown in Figure 5.14. The average count rate is 5.19±2.97 kcps. (b) The accumulated histogram of the acquired photon count rates plotted with a bin size of 400 cps. (c) The time trace of the applied electrical power for the intensity correlation measurement. A constant source-drain bias of 2 nA was applied to the functionalized (7, 5) SWCNT device at 77 K.

The electrical power was maintained at a rather stable level despite an electrical noise of around 0.5V (standard deviation of the recorded source-drain bias), as demonstrated in **Figure 5.20a**. The overlaid normal distribution curve of its histogram in **Figure 5.20b** indicates the noise likely corresponds to Gaussian noise. The sudden changes of voltage in the time trace of the recorded bias may seem to refer to burst noise, however, this type of noise often has a time scale ranging from milliseconds to seconds. On the other hand, the photon count rate varied in a few factors over the period. On the other hand, the large fluctuation of the count rate is attributed not only to the emitter properties itself, for instance, owing to luminescence bleaching (decay) and blinking (intermittency)[315–317], but also to the setup stability. Due to the long measuring period, the sample mounted under the microscope would slowly drift away from the optimum focus point, mostly in the lateral position in the micrometer range, which caused a gradual decrease in the collected count rate over time and required moderate realignment in between data acquisition. Surprisingly, no correlation between the time trace of the dissipated electrical power and the count rate was found at the given time resolution (in seconds). Information on the mean values and the standard deviation are included in the figures. Thoughts on improvements in terms of correlation data collection and progress to avoid the need for spectral filters or cryogenic temperature will be disclosed in Outlook.

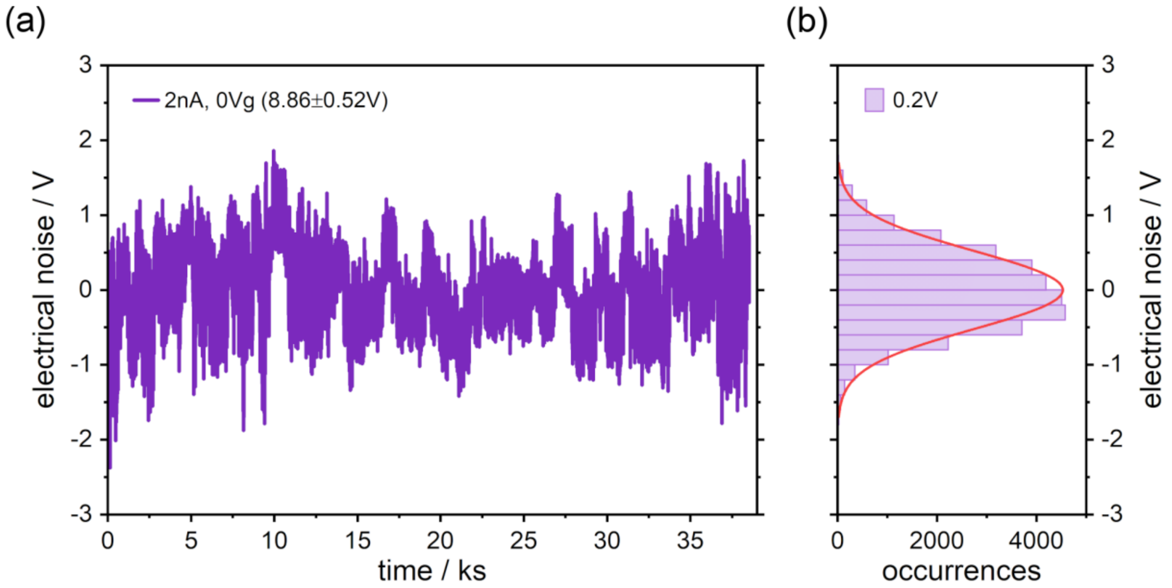

Figure 5.20: Electrical noise of the recorded source-drain voltage (a) The electrical noise (standard deviation of the measured source-drain voltage) time trace of a functionalized (7, 5) SWCNT device in Figure 5.14. The mean value of the source-drain voltage was subtracted. Values of the applied constant source-drain current and the recorded source-drain voltage bias were noted. (b) Histograms of the electrical noise time trace compiled in bin sizes of 0.2 V. Fitting curves with a normal distribution were overlaid.

5.5 Summary

In summary, we began the chapter with a general introduction to different types of single-photon detectors and their crucial performance metrics. We continued with the description of the experiment setup and further discussed the results of fiber-coupled superconducting nanowire single-photon detector (SNSPD) characterization including measurements of temperature-dependent current-voltage characteristics, dark count rates, pulse shapes, detection efficiency, and photon number resolution capabilities. With the understanding of individual detector performance and limitation, we characterized the complete measurement setup based on the HBT configuration to determine the upper limits of system timing jitter and internal system time delay via subthreshold laser photon bunching measurement. Then, we turned the focus back to our initial motivation of developing an on-demand single-photon emitter on a chip. With that, we demonstrated for the first time single-photon emission from aryl-functionalized (7, 5) SWCNTs with sp^3 quantum defects triggered via electrical excitation at 77 K. We observed antibunching behavior by coupling excitonic or trionic defect-state electroluminescence into the fiber-coupled HBT experiment setup. We further discussed the correlation between the zero-time delay second-order correlation function and the applied electrical power, including results regarding non-classical emission of pristine SWCNTs below 4 K from previous work[11]. Subsequently, we showed the relation between the full width at half maximum of the antibunching dips and the electrical power or emission wavelength. We included defect-state electroluminescence intensity correlation measurement without spectral filtering for comparison. Lastly, we analyzed the simultaneously recorded electrical and count rate data to point out the restrictions of the current measurement setup and device design, and suggestions on progressing towards room-temperature single-photon electroluminescent emission are described in the outlook, Section 7.2.

6 Cavity-Enhanced Electroluminescence of Carbon Nanotubes in the Telecom Band

This chapter includes content from a research article[21] that has been published by our group with the group of Prof. Dr. Wolfram Pernice from Universität Münster and Universität Heidelberg. Reprinted with permission from *Nature Communications* **2023**, *14*, 3933. Copyright © 2023 Springer Nature.

Emerging photonic information processing systems require chip-level integration of controllable nanoscale light sources at telecommunication wavelengths. Currently, substantial challenges remain in the dynamic control of the sources, the low-loss integration into a photonic environment, and the site-selective placement at desired positions on a chip. Here, we overcome these challenges using heterogeneous integration of electroluminescent (EL), semiconducting single-walled carbon nanotubes (sc-SWCNTs) into hybrid two-dimensional – three-dimensional (2D - 3D) photonic circuits. We demonstrate enhanced spectral line shaping of the EL emission from (9, 8) SWCNTs. By back-gating the SWCNT-emitters we achieve fully electrical dynamic control of the EL emission with high on-off ratio and strong enhancement in the telecommunication band. Using nanocrystalline graphene as a low-loss material to electrically contact SWCNT emitters directly within a photonic crystal cavity enables highly efficient EL coupling without compromising the optical quality of the cavity. Our versatile approach paves the way for controllable integrated photonic circuits.

6.1 Introduction

Electrically-driven light sources with a nanoscale footprint are desirable for integrated photonic circuits to avoid the requirement of external illumination with an excitation pump light and the accompanying high-fidelity optical filtration on the chip, thus reducing design complexity substantially. Meanwhile, semiconducting SWCNTs have emerged as promising nanoscale light sources that can be electrically stimulated into stable excitonic emission[159]. SWCNTs also show quantum light emission behavior at cryogenic[10,11,196] and at room temperature[17] as a result of localization of excitons at trap states. However, a common limitation for realizing scalable on-chip circuits is the site-selective placement of a nanoscale light source at the desired location on a photonic device, which is particularly important when coupling emitters into photonic cavities. Dielectrophoresis provides such a reliable deposition method for SWCNTs[208] and allows deterministic placement between electrodes. Additionally, the integration of electrically driven SWCNTs with nanophotonic waveguides requires suitable biasing paths for electrical stimulation. Conventionally used metallic electrodes induce optical absorption loss at the waveguide, leading to a substantial decrease in the coupling efficiency of emitted light into the propagating mode. Furthermore, metallic electrodes suppress and degrade resonance modes of nearby photonic cavities[12], which are associated with Purcell enhancement and spectral filtering of emitted light. Besides, metallic electrodes close to the SWCNTs could lead to the broadening of the light emission[70]. We overcome these challenges by using waveguide-compatible, transparent (a few nanometers thick), and low-loss nanocrystalline graphene (NCG) electrodes instead of metallic electrodes[318–320]. We embed NCG electrodes directly atop the photonic crystal (PhC) cavity with negligible optical insertion loss and degradation of the Q-factor of the resonance mode. We employ (9, 8) SWCNTs and enable controlled injection of electrons and holes into the SWCNT channel to generate narrowband electroluminescence (EL), which emits in the telecommunication E-band with an excitonic peak position around 1440 nm[19,70,318]. In order to increase the quantum yield of SWCNT[67,321], we engineer a suitable photonic environment with enhanced Local Density of States (LDOS) to raise the spontaneous emission rate of the incorporated (9, 8) SWCNTs according to Purcell theory[322]. We demonstrate the enhancement of the EL emission of SWCNTs by efficient coupling into a hybrid 2D nanocrystalline graphene – 3D photonic structure device. Importantly, our hybrid approach enables fully dynamic control over the intensity of modified narrow-linewidth EL spectra by electrical operation of the back-gate voltage, which in fact indicates the carrier recombination electroluminescent mechanism of the emitted light from SWCNTs. The applied low driving bias-current (tens of nA) to the SWCNT further proves the electroluminescent nature of the emitted light, in contrast to previous work by Pyatkov et al.[12] where three orders of magnitude higher biasing current were utilized to generate incandescent emission of SWCNTs. We achieve an on-off ratio close to 100 %. In the switched-on regime, we find a high enhancement factor up to $F_{int} = 188$ and coupling efficiency $\beta_{int} = 99.5$ % of the EL into the fundamental resonance mode, which is efficiently read out by 3D couplers terminating the nanophotonic waveguides. This way, we achieve high coupling efficiency of telecom electroluminescence in a tailor-made 1D PhC cavity mode in contrast to collecting photoluminescence from SWCNTs in a cavity[323] and exciton-plasmon coupling[13]. In addition, we show that the NCG strip in the cavity region can function as a thermal emitter, thus providing telecom-band polarized emission with a peak enhancement factor F = 80 and F = 112 at 77 K and 300 K, respectively. Such hybrid devices allow experimentally study of the Local Density of States (LDOS) in the cavity region, hence determining the optimal spatial point of efficient emitter coupling into resonance modes. The NCG strip incandescent emitter can be universally utilized for on-chip optical LDOS probing at room and cryogenic temperatures. The electrically controllable hybrid NCG-Si_3N_4 photonic circuits with deterministic placement of SWCNTs in the cavity region provide a versatile and scalable platform that meets the requirements of integrated photonic circuits for classical and quantum applications.

6.2 Hybrid cross-bar photonic crystal cavity device

We design cross-bar photonic crystal (PhC) cavities with embedded nanocrystalline graphene (NCG) electrodes, as illustrated in **Figure 6.1a**, in order to electrically control the cavity-enhanced emission rate of integrated light sources. The cross-bar design allows to position of NCG electrodes directly atop Si_3N_4 waveguides, while the enhanced EL optical signal is outcoupled through another perpendicular waveguides using 3D couplers[324]. The employed total-internal reflection couplers, a representative helium ion microscope (HIM) image in **Figure 6.1b**, provide a convenient and broadband out-of-plane readout of the optical signal with good efficiency.

The devices were realized on Si_3N_4/SiO_2 on Si substrates using a multi-step electron beam lithography protocol. Following the planar fabrication of the nanophotonic circuits, subsequently, the 3D couplers were printed on the chip. In the final fabrication step, polymer-wrapped (9, 8) SWCNTs were integrated with nanophotonic devices through selective deposition in between NCG electrodes via electric field-assisted dielectrophoresis[19,70,157]. This fabrication procedure allows the realization of scalable and reproducible hybrid devices on a chip, as discussed in Section 3.1. The cross-bar PhC cavity enhances the spontaneously emitted EL of SWCNTs in the cavity region and further enables its direct coupling to nanophotonic waveguides, as shown in **Figure 6.1a,d,e**. The light-matter interaction strengthens the radiative emission rate of SWCNTs by Purcell enhancement[322], while at the same time, the PhC cavity provides narrow-line spectral filtering of the emitted light. To minimize the influence of the crossed bar on the optical quality factor (Q factor) of the cavity, the arm is linearly tapered down from a width of 600 nm to 200 nm in the cavity region along 1 µm (**Figure 6.1d**). We employ 3D Finite Difference Time Domain (FDTD) numerical optimization of the PhC cavity to maximize the coupling efficiency of emitted light into resonance modes (β-factor). The β-factor correlates with the enhancement factor, the ratio of the on-resonance intensity to the free-space intensity at the corresponding resonance wavelength, and also the optical transmission through the device. The electric field distribution of subsequent odd resonance modes is shown in **Figure 6.2b**. Maximum enhancement is obtained by placing the emitter within the antinode of the electric field according to the Purcell theory[322]. Notably, our hybrid PhC design naturally allows obtaining high enhancement because the polarization of the EL of SWCNTs is aligned with the TE-like resonance mode of the cavity. The increase in the spontaneous emission rate leads to an increase in the coupling efficiency (β-factor) coupling into the corresponding mode, which is the ratio of enhanced emitted light outcoupled from both ends of the waveguides to the total amount of light emitted by the source.

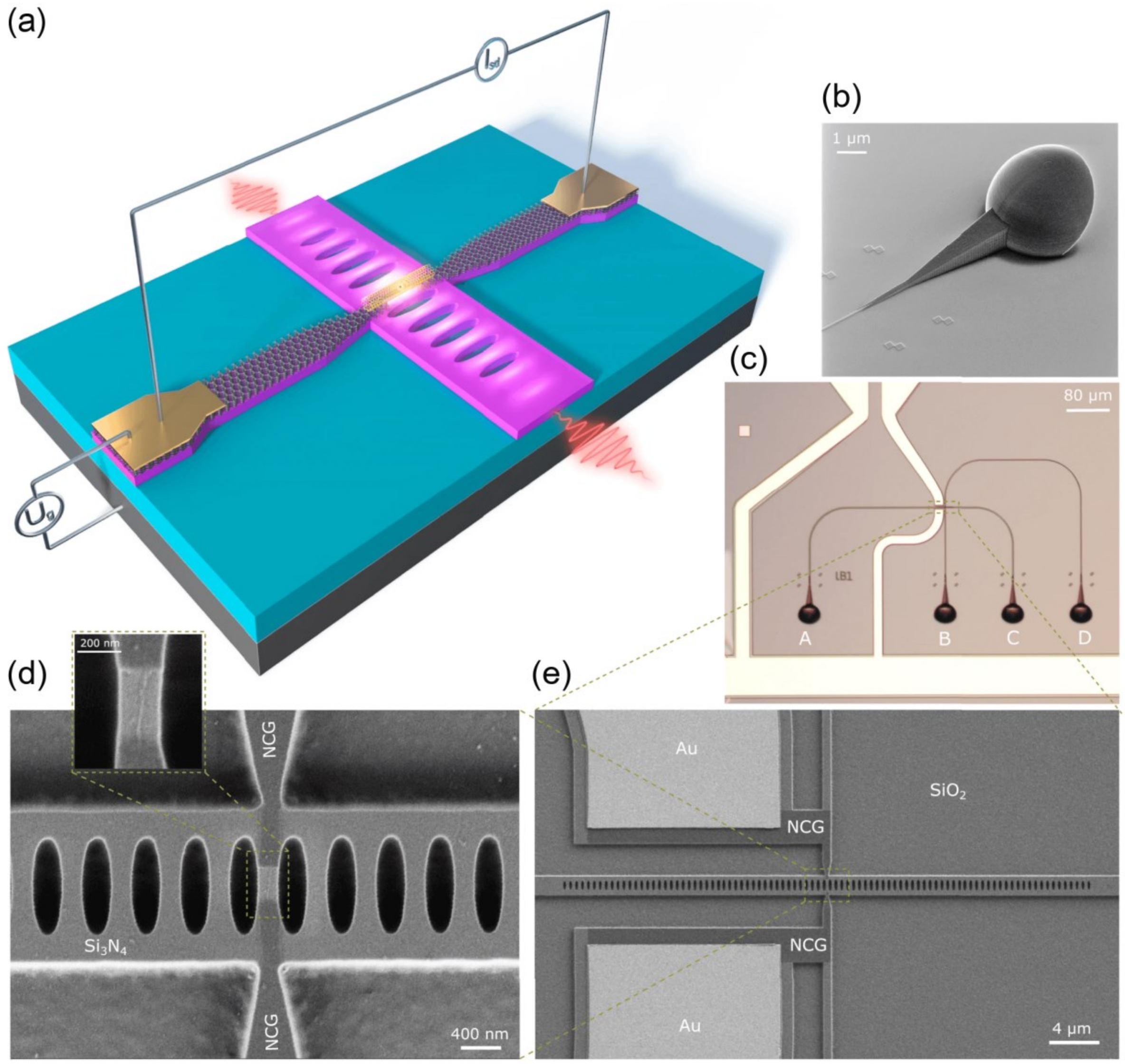

Figure 6.1: Electrically controlled cross-bar PhC cavity with integrated SWCNT emitter (a) Schematic of the hybrid device. The SWCNT is positioned between NCG electrodes on top of the cavity crossing. The electroluminescent emission is coupled out from both ends of the PhC cavity. (b) A helium ion microscopy image of a broadband 3D coupler connected to the ends of the nanophotonic waveguides. (c) Optical micrograph of the fabricated device with 3D output couplers and cavity region marked by the zoom-box. Output ports are marked from A to D. (d-e) Scanning electron microscopy (SEM) images of the hybrid device in the cavity region. The inset shows a close-up image of an individual SWCNT between NCG electrodes in the cavity. [Adapted and reproduced with permission from reference[21], Springer Nature.]

The optimal position of the source within the cavity region is determined via 3D FDTD simulations of the LDOS enhancement performed by Dr. Anna Ovvyan. The electroluminescent SWCNT emitter is modeled as a classical dipole source with an electric field aligned along the transverse electric (TE) mode of the cavity. The results for different positions of the emitter on top of the cavity region along transverse and longitudinal directions are summarized in on-resonance LDOS spatial maps in **Figure 6.2a** and **Figure 6.5a**, respectively. The LDOS-spatial maps qualitatively indicate an optimal central position of the SWCNT emitter in the cavity region to obtain the highest enhancement, where the coupling efficiency into odd modes is maximized. Light emitted from the source, placed on the center of the cavity, is coupled to odd resonance modes and enhanced. Moving the emitter away from the cavity center leads to a decrease in the enhancement of odd modes. This is in agreement with the corresponding electric field distribution of the resonance modes in **Figure 6.2b**. Owing to the structure design, a single SWCNT was site-selectively deposited near the optimal position of the cavity as shown in **Figure 6.1d** (inset).

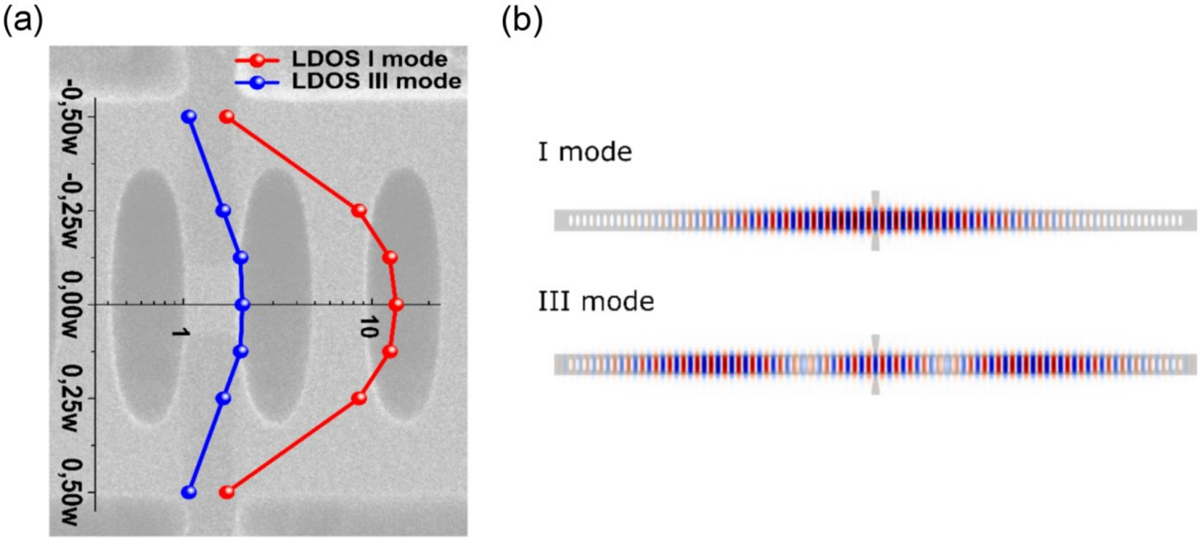

Figure 6.2: Simulated on-resonance LDOS enhancement spatial map and electric field distribution (a) Simulated on-resonance LDOS enhancement spatial map of the dipole source sitting atop the cavity region of a cross-bar PhC cavity with NCG electrodes. The PhC consists of N = 25 holes in each Bragg mirror. The emitter position is atop the cavity center and varied along the transverse direction. The position of the source along the y-direction is normalized to the width of the cavity (w). (b) Simulated electric field distribution of the I-order and III-order resonance modes. [Adapted and reproduced with permission from reference[21], Springer Nature.]

6.2.1 NCG-based incandescent nanoemitter in the telecom band

Besides functioning as contact electrodes, we patterned a 5 nm thick NCG strip with a narrow junction within the cavity center of PhC to form an incandescent emitter[318], as shown in **Figure 6.3a,c** complementing the electroluminescent SWCNT emitters. Such a thermal strip-nanoemitter incorporated in a predetermined position within a photonic device allows probing the LDOS factor experimentally and provides optimal coupling of emitted light into cavity modes at both cryogenic and room temperature. Importantly, the NCG strip-nanoemitter does not degrade the quality factor of the cavity (as shown in Appendix **Figure 0.3**) in contrast with the work of Shiue et al.[325], where a micro black-body radiator for optical communication applications was demonstrated. As a side note, the NCG strip can be removed by oxygen plasma while protecting the rest of the circuit, for example, with photoresist.

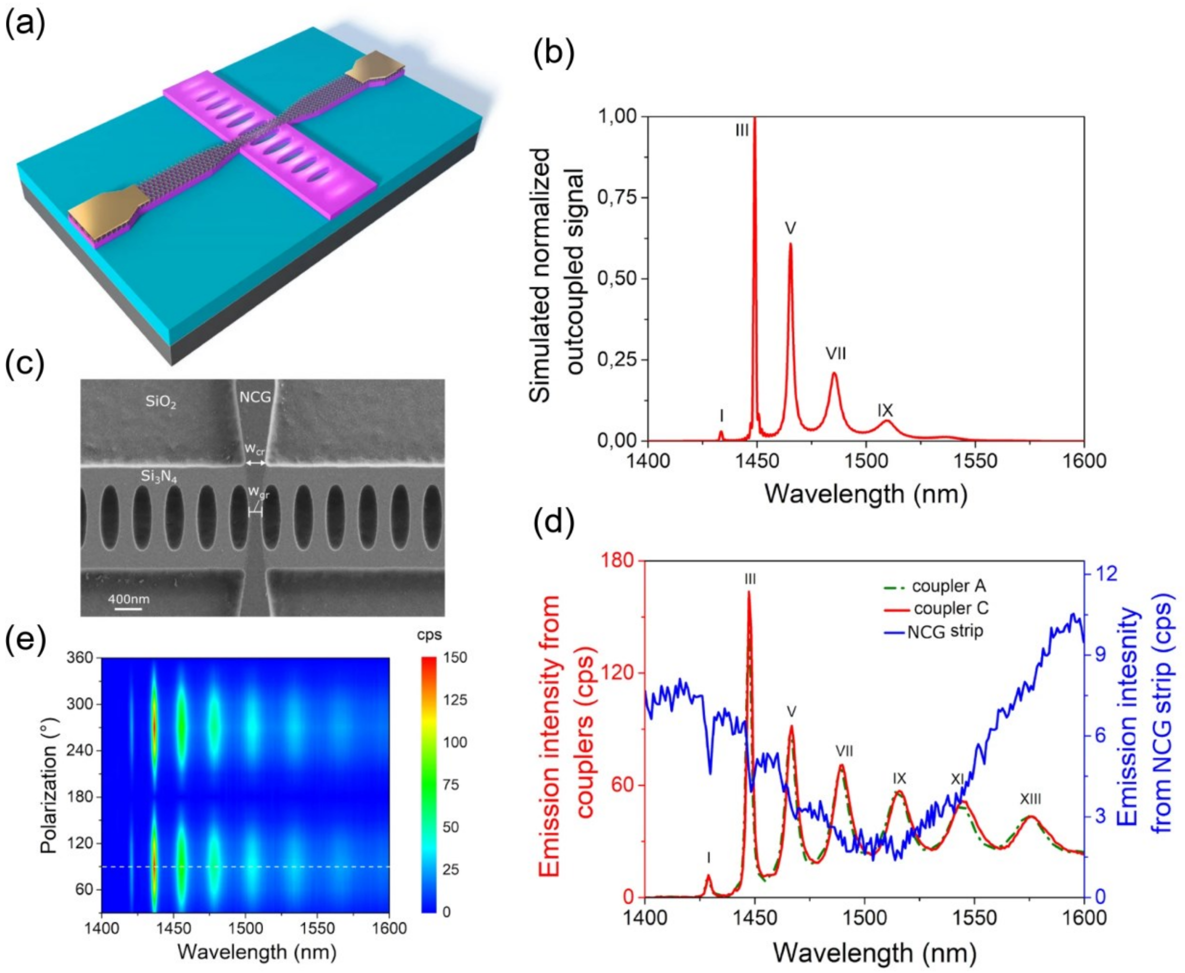

Figure 6.3: Nanocrystalline graphene-based nanoemitter (a) Schematic of the NCG strip integrated atop cross-bar PhC cavity. (b) 3D FDTD simulated spectrum (normalized) of light outcoupled from one end of the cross-bar photonic crystal (PhC) cavity. The symmetric design of the PhC cavity leads to equal incandescent emission on both sides. The resonance modes are labeled in Roman numbers (I–IX). (c) SEM image of the cavity region with NCG strip atop cavity. The waist of the strip is 250 nm in width. (d) Recorded spectra of electrically-biased enhanced thermal emission outcoupled from couplers A (green) and C (red) with 120 uA source-drain current (source-drain voltage 35.5 V) at 77 K. The spectrum from the NCG strip (blue) was acquired with the polarizer parallel to the TE mode of the waveguide. (e) Polarization map of measured incandescent emission spectra detected at coupler C, projected onto different polarization angles with a polarization filter. The dashed white line marks the polarization axis of the spectra acquired at couplers A and C. The cross-bar PhC cavity contains N = 45 segments in each Bragg mirror with a lattice period of a = 458 nm. [Adapted and reproduced with permission from reference[21], Springer Nature.]

The spectral properties of the resonance mode were determined by measuring the outcoupled enhanced light emission from electrically stimulated NCG strip at 77 K at the 3D couplers A and C with an InGaAs photodiodes array as shown in **Figure 6.3d**. We emphasize that in the case of the demonstrated biased NCG strip nanoemitter, the supplied electric energy is transformed into Joule heat and is dissipated in the NCG junction leading to incandescent emission. The estimated electron temperature of the NCG-based emitter on the Si_3N_4 waveguide at an applied electrical power of 2.87 mW (source-drain current 70 uA) reaches around 1000 K, as shown and discussed in Appendix (**Figure 0.4**). The central position of the NCG strip in the cavity region (**Figure**

6.3c) provides optimal coupling of emitted incandescent light into odd resonance modes, as predetermined by simulated LDOS spatial maps and electric field distributions (**Figure 6.5a** and **Figure 6.2b**). The measured spectra with narrow linewidth peaks in red and green depicted in **Figure 6.3d** are in good agreement with the simulated spectrum shown in **Figure 6.3b**. A free-space confocal emission spectrum of light detected from the NCG strip is shown in blue. The dips at the resonance wavelengths confirm the effective coupling of incandescent light into the resonance modes of the PhC cavity. The envelope of the spectrum is modulated by substrate-induced interference[326]. A polarization map of emission spectra at 77 K as depicted in **Figure 6.3e** proves that the incandescent light obtained from 3D couplers is strongly polarized, where the emission shows a maximum intenity at a polarization angle of 90° and vanishes almost completely at 180°. High polarization contrast is an indicator of successful coupling of NCG strip thermal emission into the PhC cavity, which can be further characterized by suitable figures of merit, such as the enhancement factor and the coupling efficiency.

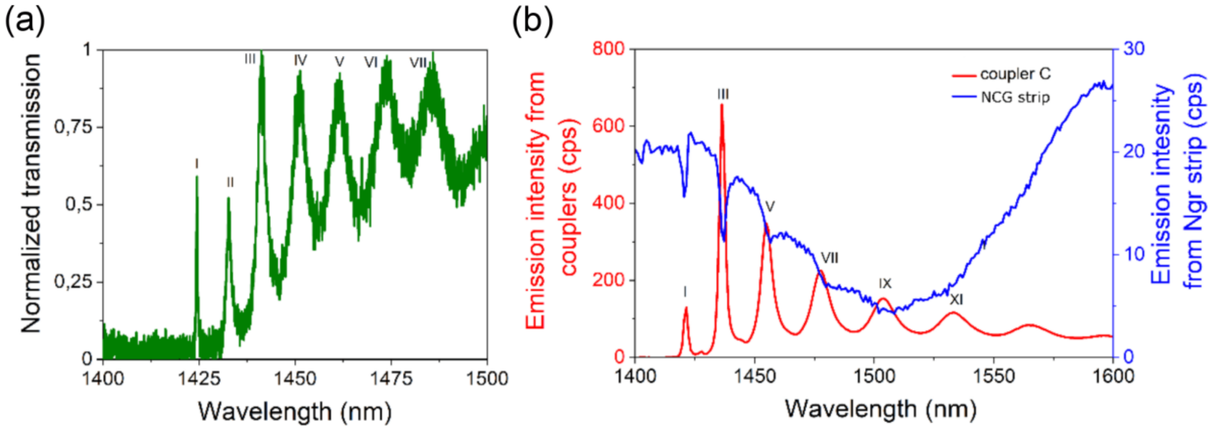

Figure 6.4: NCG-based incandescent nanoemitter at room temperature (a) Experimentally recorded transmission spectrum of a cross-bar PhC device with an integrated NCG strip. A broadband light source (supercontinuum laser) was coupled into the waveguide using the 3D coupler port A and the transmitted signal was read out at port C. The order of the resonance modes is labeled. (b) Spectra of enhanced incandescent emission extracted from coupler C (red) and the NCG strip (blue). The device is electrically excited with 120 uA source-drain current and the emitted output is projected onto a polarization parallel to the TE mode, acquired at 300 K. [Adapted and reproduced with permission from reference[21], Springer Nature.]

The cross-bar PhC cavity enables strong modification of NCG incandescent emission at cryogenic and at room temperature (**Figure 6.4**). Therefore, further measurements were performed in both regimes, at 77 K and 300 K, respectively. The cross-bar PhC cavity provides on-resonance enhancement of NCG incandescent emission evanescently coupled into odd modes, obtaining maximum values of $F_{III} = 80.6$ at cryogenic and $F_{III} = 112.7$ and room temperature. These factors are experimentally determined as the ratio of the sum of on-resonance integrated emission intensity outcoupled from couplers A and C to the free-space integrated intensity recorded confocally from the NCG strip junction at the corresponding resonance wavelength. Furthermore, we determine the on-resonance coupling efficiency (β-factor) as the ratio of enhanced emitted light at resonance wavelength detected from couplers A and C to the sum of the integrated intensity of light detected confocally at thermal source and at the couplers, resulting in a peak value β_{III} = 98.7 % at 77 K and β_{III} = 99.1 % at 300 K.

6.2.2 Electrically controlled electroluminescence from a SWCNT

To electrically drive the SWCNT emitter, we embed (9, 8) SWCNTs (excitonic emission wavelength around 1440 nm) at the single-tube level in between optimized NCG electrodes coupled to a cross-bar PhC cavity. The cavity region of the experimentally investigated device is shown in **Figure 6.1d**. The NCG electrodes serve as source and drain electrodes and the Si substrate underneath works as the back-gate electrode. The applied back-gate voltage produces a vertical electric field between the SWCNT and the Si substrate to capacitively control the carrier concentration of the SWCNT channel. In this three-terminal device configuration, photons can be emitted from the electrically driven SWCNT by a constant current biasing mode, and the device carrier concentration can be additionally tailored by the back-gate electrode. Electrons are injected at one SWCNT/NCG contact and holes at the other contact in a way that the carriers form excitons in the nanotube channel and radiatively recombine. Such an excitonic EL emission is maximized when the influx of electrons and holes into the channel are comparable, and the SWCNT channel is charge-neutral. For our device, this is the case when the source-drain voltage is maximal during a gate-voltage sweep under constant current bias (device in off-state, see **Figure 6.6b**). This scenario corresponds to the EL switched-on regime. The SWCNT is not charge-neutral anymore when the source-drain voltage is minimal (device in on-state). In this case, the excitonic EL emission is suppressed, corresponding to the EL switched-off regime. As a result, we demonstrate that the dynamically controlled emission intensity of the fundamental resonance mode provided that the EL emission could be switched by a gate voltage. The collected light in the waveguides is again outcoupled by 3D couplers and detected by an InGaAs photodiode linear array.

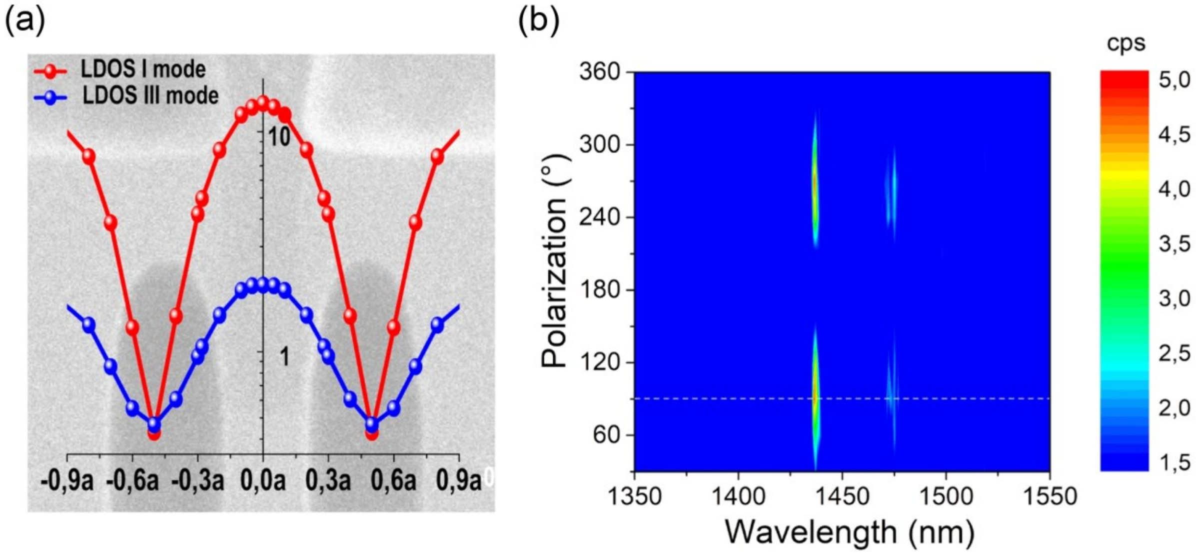

Figure 6.5: Simulated on-resonance LDOS enhancement spatial map and polarization map (a) Simulated LDOS enhancement spatial map of emitted EL from a SWCNT placed between NCG electrodes in a cross-bar PhC cavity. The PhC contains N = 25 holes in each Bragg mirror with a lattice period of a = 462 nm. The emitter is positioned in the cavity center and varied along the longitudinal direction. The position of the source along the x-direction is plotted normalized to the period a. (b) Spectra of EL emission detected at a 3D coupler C, projected onto different polarization angles. The white dashed line marks the polarization axis of all experimentally acquired spectra. [Adapted and reproduced with permission from reference[21], Springer Nature.]

The central orientation of NCG electrodes and deposited SWCNT ensures efficient coupling of the emitted light preferentially into the odd resonance modes due to a locally enhanced density of states (**Figure 6.5a** and **Figure 6.2b**). The polarization-dependent measurement of the cavity emission is shown in the acquired map as a function of the polarization angle of the inserted polarizer illustrated in **Figure 6.5b**. The collected emission at coupler port C exhibits a maximum at a polarization angle of 90° and vanishes completely at 180°, which demonstrates that the TE-like EL signal is strongly polarized and successfully coupled into the PhC cavity. The horizontal line in white corresponds to the polarization axis of the acquired spectra from the couplers shown in **Figure 6.6d**. Biasing the SWCNT atop the cross-bar cavity region with simultaneously applied back-gate voltage (Ug = 20 V) leads to an enhanced excitonic emission coupled into the fundamental resonance mode, where this regime corresponds to the EL switched-on state. The measured spectrum outcoupled from coupler C is shown by the red curve in **Figure 6.6d**, while the simulated spectrum of light coupled out from one of the ends of the investigated PhC is shown in **Figure 6.6a**. Importantly, the utilized biasing current for the SWCNT is three-four orders of magnitude lower in comparison with the NCG strip thermal emitter described in the previous section, as well as in comparison with the reported incandescence of SWCNT[12]. The presence of the EL signal at the coupler of the PhC cavity, red curve in **Figure 6.6d**, and the simultaneous absence of the free-space EL signal at the position of the investigated SWCNT, green curve in **Figure 6.6d**, in the EL switched-on state (Ug = 20 V) of the demonstrated device confirm successful coupling of EL into the fundamental resonance mode of the PhC cavity.

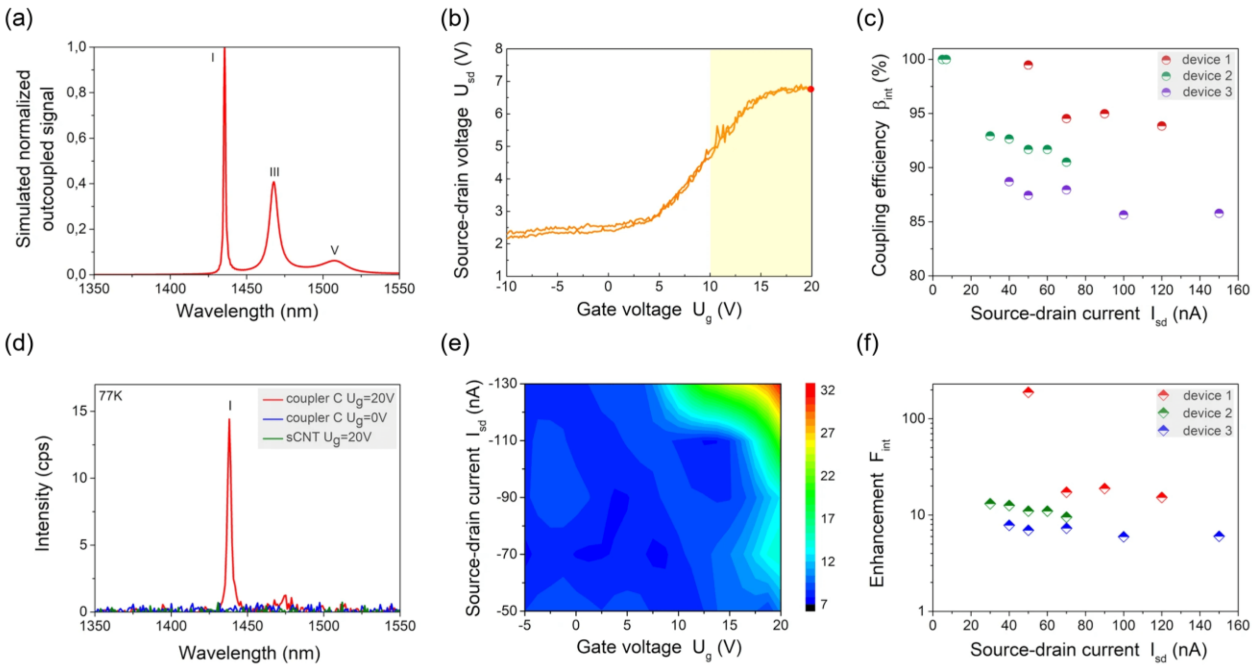

Figure 6.6: Dynamic control of electroluminescence (EL) from cavity-integrated SWCNT (a) Simulated spectrum of light coupled out from one end of the cross-bar PhC cavity. (b) Gate-dependent charge transport measurement acquired at constant biasing current equals -90 nA. Forward and backward traces are shown. The yellow area corresponds to the regime where the excitonic EL emission is in the switched-on state. The red point corresponds to the electric acquisition point of the spectrum shown in (d). (c) Measured dependence of full-bandwidth coupling efficiency β_{int} on source-drain current for several PhC devices. (d) The EL spectra of SWCNT coupled to the fundamental resonance mode at 1438.1 nm, acquired from coupler C of a PhC cross-bar device gated with gate-voltage Ug = 20 V (EL switched-on state), with Ug = 0 V(EL switched-off state), and the free-space EL recorded at the position of the SWCNT coupled to the cavity at Ug = 20 V of the same investigated device is shown by the green curve. Source-drain current is -90 nA. (e) EL excitation map of enhanced EL intensity integrated over the fundamental resonance mode (1430 – 1450 nm) outcoupled from coupler C of the explored device as a function of source-drain current and back-gate voltage. (f) Measured dependence of full-bandwidth enhancement factor F_{int} on source-drain current applied to the SWCNT for three cross-bar PhC devices, acquired at 77 K. Device 1 consists of N = 25 segments in each Bragg mirror with a lattice period of a = 462 nm; device 2: N = 35, a = 460 nm; device 3: N = 35, a = 455 nm. [Adapted and reproduced with permission from reference[21], Springer Nature.]

Turning off the gate voltage (Ug = 0 V) results in strong suppression of the excitonic emission, the EL switched-off state (blue curve) in **Figure 6.6d**. In order to demonstrate full control of the excitonic emission we acquire an electroluminescent excitation map shown in **Figure 6.6e** where the integrated EL intensity of the SWCNT coupled into fundamental resonance mode and detected at coupler C is plotted as a function of source-drain current and back-gate voltage. **Figure 6.6b** shows the source-drain voltage from the charge transport measurement as a function of the back-gate voltage that is required to maintain the fixed source-drain current. At a large positive back-gate voltage, the required source-drain voltage is large, and this corresponds to the regime when the device is charge-neutral, namely electrons and hole carrier density are similar. As described above this is the optimum condition for excitonic EL emission and yields the EL switched-on state. The transport data shows negligible hysteresis between the forward and backward sweeps due to the cryogenic environment (77 K)[70]. In addition, we demonstrate the EL switched-on state also at room temperature as depicted in **Figure 6.7**, resulting in enhanced narrow linewidth EL coupled into fundamental resonance peaks in the spectrum. Notably, the reported free-space SWCNT (9, 8) EL linewidth at room temperature was 50 nm (30 meV) and was reduced to 20 nm (12 meV) at 77 K[70]. The EL linewidth is considerably wider than the linewidth of the PhC cavity (1.7 nm), which illustrates the successful coupling of EL into the mode and suppression of emission outside the cavity resonances.

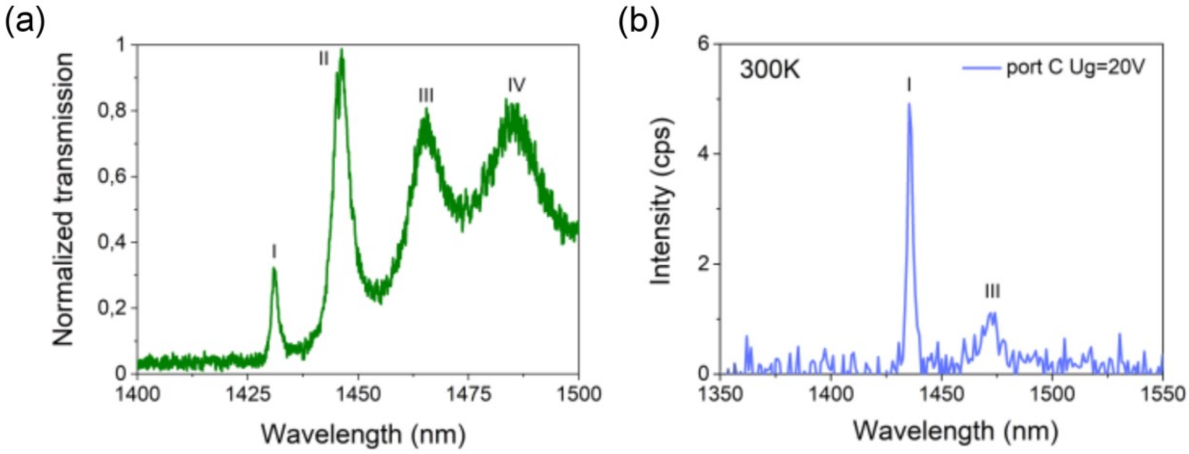

Figure 6.7: EL spectra of SWCNT coupled to a cross-bar PhC cavity at room temperature (a) Measured transmission spectrum of the hybrid device B1 with NCG electrodes before SWCNT integration. (b) Spectra of enhanced EL outcoupled from 3D coupler port C of device 1 in the switched-on regime at Ug = 20 V, acquired at 300 K. [Adapted and reproduced with permission from reference[21], Springer Nature.]

As a proof of principle of our versatile approach of full electrical control of an electroluminescent SWCNT, we demonstrate in **Figure 6.8** the experimental measurement of another hybrid device where the enhanced electroluminescence (which is coupled to a low-loss NCG photonic environment) is dynamically operated via back-gate voltage regulation. The electrically biased SWCNT with simultaneously applied back-gate voltage (Ug = -25 V) emits enhanced excitonic EL emission into the odd resonance modes of the cavity and the measured spectrum of light outcoupled from one of the ends (coupler C) of the investigated hybrid device is shown in **Figure 6.8a** (red curve). The data is obtained when the SWCNT is charge neutral, which corresponds to the EL switched-on state. Changing the gate voltage from -25 V to +30 V leads to a decrease in the intensity of the excitonic EL emission (light and dark green curves in **Figure 6.8a**). Switching the gate voltage to Ug = +30 V leads to complete suppression of the excitonic EL emission, corresponding to the EL switched-off state (blue curve in **Figure 6.8a**). Thus, we obtain dynamic control of the SWCNT enhanced EL emission with close to 100 % on-off ratio (depth) via active electrical operation of the back-gate voltage.

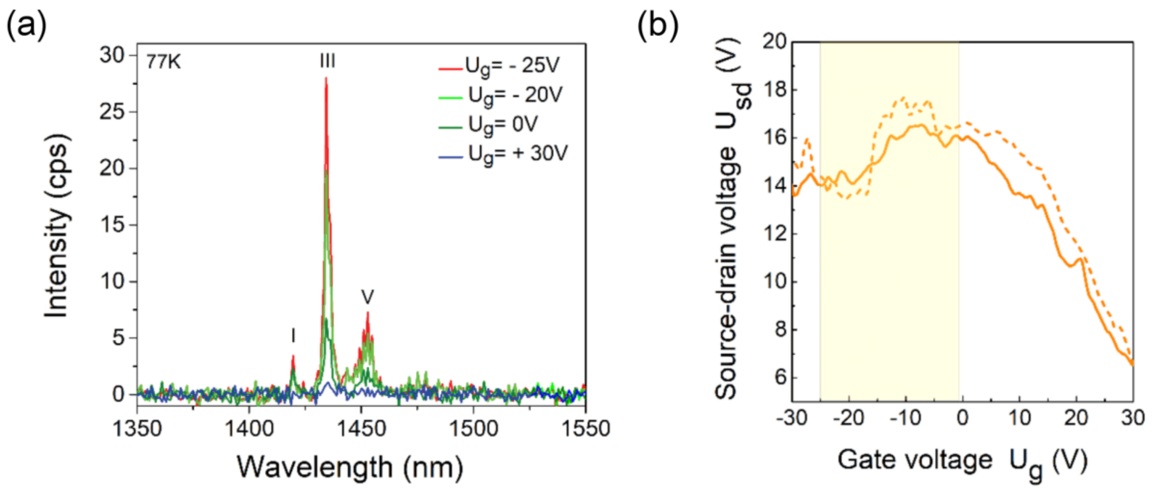

Figure 6.8: Dynamic control of EL from another cavity-integrated SWCNT device (a) The spectra of EL coupled to odd resonance modes at 1419.5 nm, 1434.4 nm, 1452.9 nm, acquired from coupler C of PhC cross-bar device gated with corresponding back-gate voltage. At Ug = -25 V – the EL is in the switched-on state (red curve) and at Ug = +30 V – the EL is in the switched-off state (blue curve). The biasing current is constant Isd = 30 nA. The cross-bar PhC cavity consists of N = 45 segments in each Bragg mirror with a lattice period of a = 457 nm. The resonance modes are labelled. (b) Gate-dependent charge transport measurement acquired at constant biasing current Isd = 30 nA. Forward and backward sweep traces are shown. The transport data shows negligible hysteresis between the forward and backward sweeps due to the cryogenic environment (77 K). The yellow area corresponds to the regime, in which the excitonic EL emission is in the switched-on state. [Adapted and reproduced with permission from reference[21], Springer Nature.]

The full-bandwidth enhancement factor F_{int} and coupling efficiency β_{int} of the emitted EL signal are experimentally determined in the same fashion as with the incandescent NCG strip, integrated over the full wavelength of the signal. These figures of merits are derived for several cross-bar PhC devices with integrated SWCNT as shown in **Figure 6.6c,f**, respectively. The electrically-biased SWCNT emits linearly polarized electroluminescence which is aligned with the tube axis and therefore also aligned with the TE mode of the cavity. We find β_{int} as high as 99.5 % and F_{int} up to 188. It should be noted that all experimentally investigated devices showed coupling of EL from SWCNT into the hybrid NCG-Si_3N_4 PhC cavities devices on-chip (**Figure 6.9**). The experimental results testify to the stability and reproducibility of developed hybrid PhC devices with incorporated SWCNT on a chip.

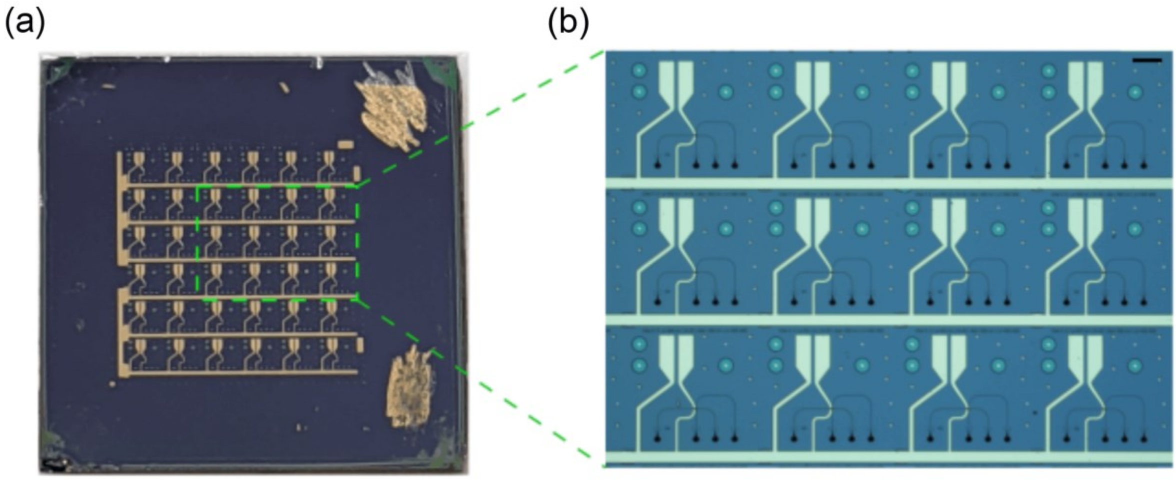

Figure 6.9: Fabricated hybrid devices on-chip (a) Photograph of the chip (1 cm^2) for fully dynamic electrical control of enhanced electroluminescent emission from SWCNTs. The chip area is 5.4 mm^2. (b) Optical micrograph of NCG-Si_3N_4 PhC cavity devices equipped with 3D couplers. Scale-bar: 200 µm. [Adapted and reproduced with permission from reference[21], Springer Nature.]

6.3 Summary

The implementation of electrically driven emitters removes the need for an external excitation light source and on-chip optical filtering which is challenging when a high extinction ratio is required and increases the device footprint. The heterogeneous integration of SWCNTs with cross-bar Si_3N_4 PhC cavity devices provides a viable route toward electrically controlled nanoemitters with enhanced and narrow emission linewidth in the telecommunication band. In particular, the use of NCG electrodes enables seamless integration with loss-sensitive photonic components, such as nanoscale cavities, and allows for the realization of reconfigurable photonic circuits. Our optimized fabrication protocol of combining the site-specific deposition approach and NCG electrodes provides not only the freedom to accurately position SWCNTs in a required region atop a photonic device, such as a PhC cavity, with negligible optical loss and degradation of the optical quality factor but also demonstrates reproducibility for photonic applications in the telecom band. Meanwhile, the implementation of NCG strip incandescent emitter offers the opportunity to experimentally probe the Local Density of States (LDOS). Therefore, the developed and demonstrated hybrid device addresses key challenges in advanced photonic circuits which require both optical and electrical control on the nanoscale. Besides applications in telecommunication, SWCNTs also provide promising characteristics for quantum photonic circuits. Cavity enhancement combined with low-loss electrical drive and additional electrical control via back-gate configuration, SWCNTs may allow for realizing tailored single-photon sources in a chip-scale framework. With recent advances in boosting emission efficiency and emission characteristics by sp^3 quantum defect engineering, our approach to site-selectively integrate SWCNTs in telecommunication photonic cavities provides promising avenues for hybrid quantum photonic circuits.

– this page left intentionally blank –

7 Conclusion and Outlook

7.1 Conclusion

In summary, the focuses of the thesis surround the study of the electroluminescence characteristics and the development of an on-chip electrical-driven quantum-light source in the telecom band based on the coupling of SWCNTs with sp^3 quantum defects into a three-terminal device configuration. Firstly, we demonstrated tunable defect-induced electroluminescence spectroscopy results of SWCNTs with sp^3 quantum defects at the single-tube level to lay the foundation of the thesis. Then, we conducted low-temperature photon antibunching measurements of functionalized SWCNTs by coupling filtered defect-state electroluminescence into HBT experimental setup as proof of principle of electrical-driven quantum-light sources in the telecom band based on SWCNTs. The last part of this work presented our versatile approach to full electrical control of electroluminescent SWCNTs in hybrid photonic circuits. By using NCG electrodes, we overcome the challenges of selectively low-loss integration of solid-state nanoemitter into photonic crystal cavities and advance in the development of photonic information processing systems.

In Chapter 4, we performed defect-induced electroluminescence spectroscopy measurements of SWCNTs functionalized with dichlorobenzene molecules to form deep exciton traps and wired to graphene electrodes. We demonstrated the controllable excitonic and trionic defect-state electroluminescence via electrostatic gating at 77 K and validated the emission peak assignments by the correlation of electrical transport and photoluminescence data. Later, we also achieved defect-induced emission with high spectral purity, which is crucial for on-chip quantum sources. At cryogenic conditions (4 K), we revealed unconventional gate-dependent satellite emission lines between intrinsic and defect-induced optical transitions attributed to phonon-mediated hot-exciton electroluminescence. Lastly, a comparison with photoluminescence spectra of chemically doped SWCNTs using gold(III) chloride solution exhibits not only the potential complexity of identifying emission due to charged excitons or localized excitons in defects but also the likelihood of naturally accessing the lowest energy defect configuration in electroluminescence.

In Chapter 5, we first focused on the characterization of fiber-coupled SNSPDs, one of the key elements of the HBT setup. The comprehensive analysis encompasses performance metrics such as temperature-dependent current-voltage characteristics, dark count rates, detection efficiency, etc. Using picosecond pulsed laser and operating laser diode in the sub-threshold regime, respectively, to determine the system time jitter and internal time delay, provides valuable insights into the limitations of the photon correlation measurements. Finally, the first demonstration of excitonic and trionic defect-state single-photon emission from aryl-functionalized (7, 5) SWCNTs through electrical excitation at 77 K represents a significant step towards practical quantum emitters. The analysis of simultaneously recorded electrical power and photon count rate suggests further refinements of the current restrictions and paves the way for achieving electrical-driven room-temperature single-photon emission on a chip.

In Chapter 6, we proposed a versatile hybrid platform to address challenges associated with external light source excitation and on-chip optical filtering for integrated photonic circuit development. The heterogeneous integration of pristine (9, 8) SWCNTs with Si_3N_4 photonic crystal cavity devices, facilitated by NCG electrodes, offers a promising route for electrically controlled solid-state nanoemitters with enhanced emission characteristics. We achieved full electrical dynamic control of the enhanced electroluminescent emission in the telecom band by back-gate voltage regulation. The use of NCG electrodes allows precise positioning of SWCNTs with negligible optical loss. The potential for experimental probing of the Local Density of States (LDOS) through NCG strip incandescent emitters within the cavity center further outlines the versatility of the hybrid device. This fabrication protocol of combining site-selective deposition and low-loss NCG electrodes offers scalability and reproducibility for photonic applications in the telecom band.

7.2 Outlook

At the end of Chapter 4, we presented narrow defect-state electroluminescence with high spectral purity from single-tube SWCNTs with sp^3 quantum defects by altering the electrical excitation parameters, mostly via electrostatic gating, which can potentially show single-photon emission behavior. However, there is still plenty of room for device operation optimization, for instance studying the electrical excitation power dependence on the spectral purity of defect-state emission. A similar exploration of the SWCNT device channel length effect on the defect-state emission properties, such as the broadness of emission peak as reported in pristine SWCNT devices[160,161], is also missing. These further investigations could lead to more robust electrical-driven single-photon emission, yet can be understandably challenging since the sp^3 defect number/density varied from nanotube to nanotube. To the best of our knowledge, direct visualization of sp^3 quantum defects on the sidewall has not yet been reported. Additionally, our work didn't resolve some open fundamental questions, for instance, whether the positive and negative trionic defect-state emission exhibit similar energy shifts from the excitonic defect-state emission. The observed likelihood of preferential probing of the lowest transition energy of neutral defect-state configuration in electroluminescence measurements may also be worth further validation, and potentially bring insight into the fundamental mechanism of defect-state emission via electrical or optical excitation.

Despite the observation of electrically driven single-photon emission from functionalized (7, 5) SWCNTs in Chapter 5, the unacceptable lengthy data acquisition time and the only acceptable signal-to-noise ratios of the coincidence histograms, imply the direction of future progress. Here, we discuss and demonstrate how to improve experimental and device performance for further advancing in an on-demand electrically driven room-temperature single-photon source. One of the approaches is to improve the emission stability. For instance, the suppression of potential spectral wandering due to the fluctuating environment[327] might have avoided the clear substantial photon count rate drop in **Figure 0.1** of the Appendix. Since the defect-state electroluminescence in our case mainly originates from radiative carrier recombination of excitons, operating the device under stable conditions for exciton formation would be critical. However, hysteresis is, for example, one of the notorious issues for device stability of low-dimensional carbon-based transistors. It is often attributed to the presence of water molecules[314,328] or capacitive charging of the filling and depleting traps in the surrounding dielectric by charge injection[329–331]. A demonstration was represented in **Figure 7.1** where 30 nm polytetrafluoroethylene (PTFE), Teflon, was coated on the SWCNT device via liquid-phase deposition[205], see Section 3.1.2. The electroluminescence spectrum and corresponding intensity correlation measurement histogram generated with 12 ps bin sizes at 77 K are shown with other supplementary results in **Figure 7.2**.

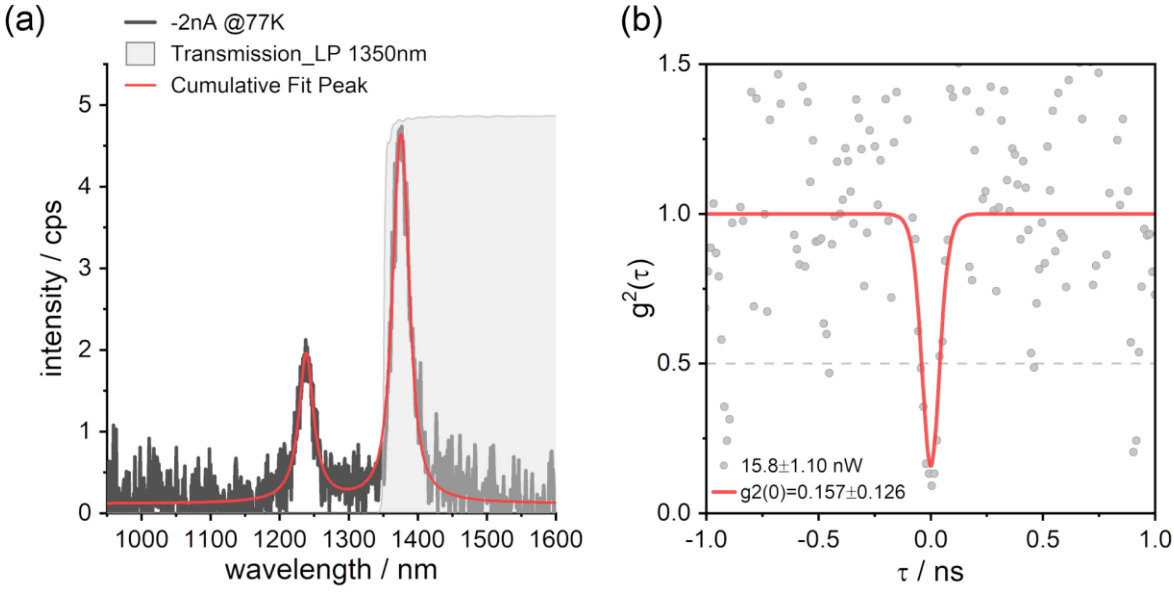

Figure 7.1: Intensity correlation measurement with polytetrafluoroethylene (PTFE) coating (a) The electroluminescence spectrum of a functionalized (7, 5) SWCNT device coated with 30 nm Teflon measured at 77 K under constant source-drain current -2 nA. The spectrum was fitted with Voigt functions and overlapped with the transmission spectra (grey area) of the spectral filter. The filtered light emission was then coupled into the HBT setup for the intensity correlation measurement (b) The coincidence histogram measured at 77 K by collecting spectrally filtered electroluminescence. The histogram was built with a 12 ps time resolution. The fitting curve is presented showing photon antibunching. The dashed grey lines served as a guide for the eye for the second-order correlation function at zero-time delay equals 0.5.

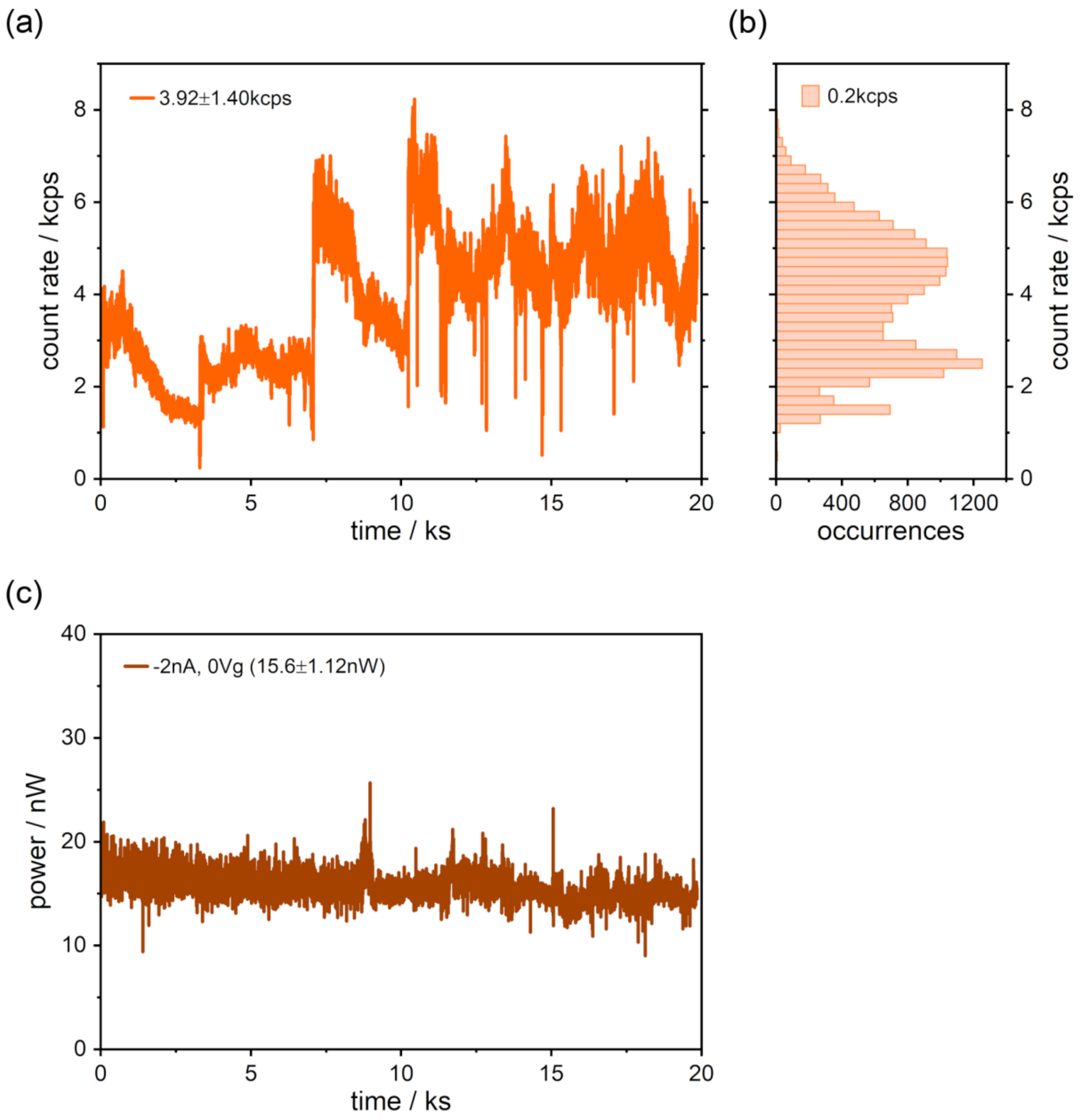

Figure 7.2: Photon count rate and electrical excitation time trace with Teflon coating (a) The collected photon count rates, 3.92±1.40 kcps, over 20 ks for the intensity correlation measurement under constant source-drain bias -2 nA of a functionalized (7, 5) device coated with 30 nm Teflon. (b) The accumulated histogram of the acquired photon count rates plotted with a bin size of 200 cps. (c) The time trace of dissipated electrical power for the intensity correlation measurement.

Although still far from ideal, some improvements could be noticed, such as reduced electrical noise. A comparison between the simultaneously recorded electrical noise time trace of functionalized SWCNT devices with or without a PTFE layer is in **Figure 7.3**. As the ultimate goal of passivation was to operate the device reliably at room temperature, room-temperature transconductance curves, and electroluminescence spectra can be seen in **Figure 7.4**. With Teflon coating, clear suppression of hysteresis in the transconductance curves could be observed within the same gate-voltage sweep range. Room-temperature electroluminescence with narrow emission lines was also achievable. The emission intensity and stability were, however, still not comparable to results at cryogenic temperature. Device/substrate treatment[332,333] or device measuring/triggering technique[334] to decouple SWCNT/surrounding dielectric interaction may be necessary for further enhancing the device/emission stability.

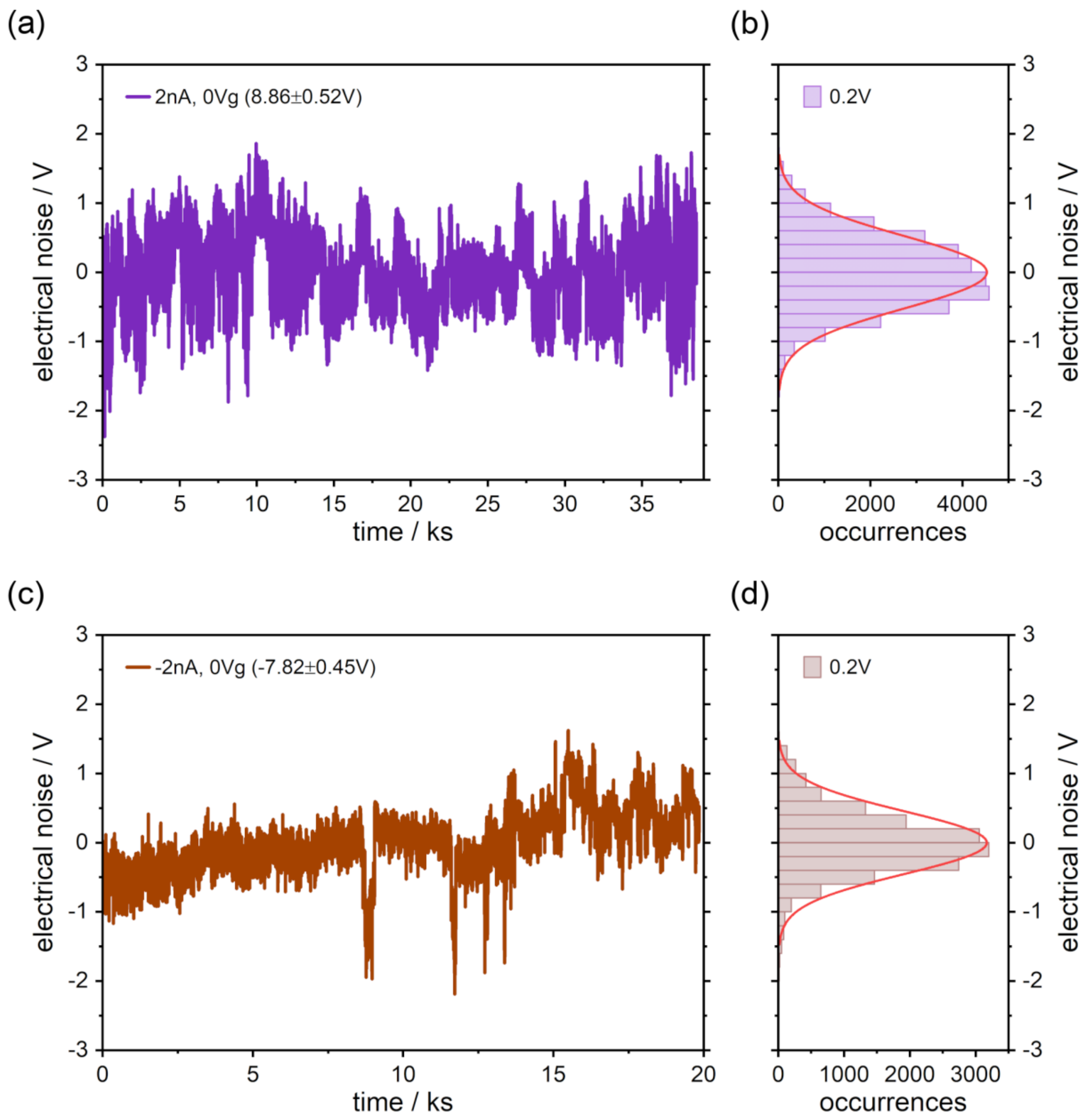

Figure 7.3: Electrical noise of the recorded source-drain voltage (a) The electrical noise (standard deviation of the recorded source-drain voltage) time trace of a functionalized (7, 5) SWCNT device shown in Figure 5.19 derived by subtracting the mean value of the DC bias and (c) for a SWCNT device with 30 nm Teflon deposition as demonstrated in Figure 7.2. The applied constant source-drain current and the mean value with the standard deviation of the DC bias were noted in the figures. (b), (d) Histograms of the electrical noise time trace plotted with a bin size of 0.2 V. Fitting curves with a normal distribution were overlaid.

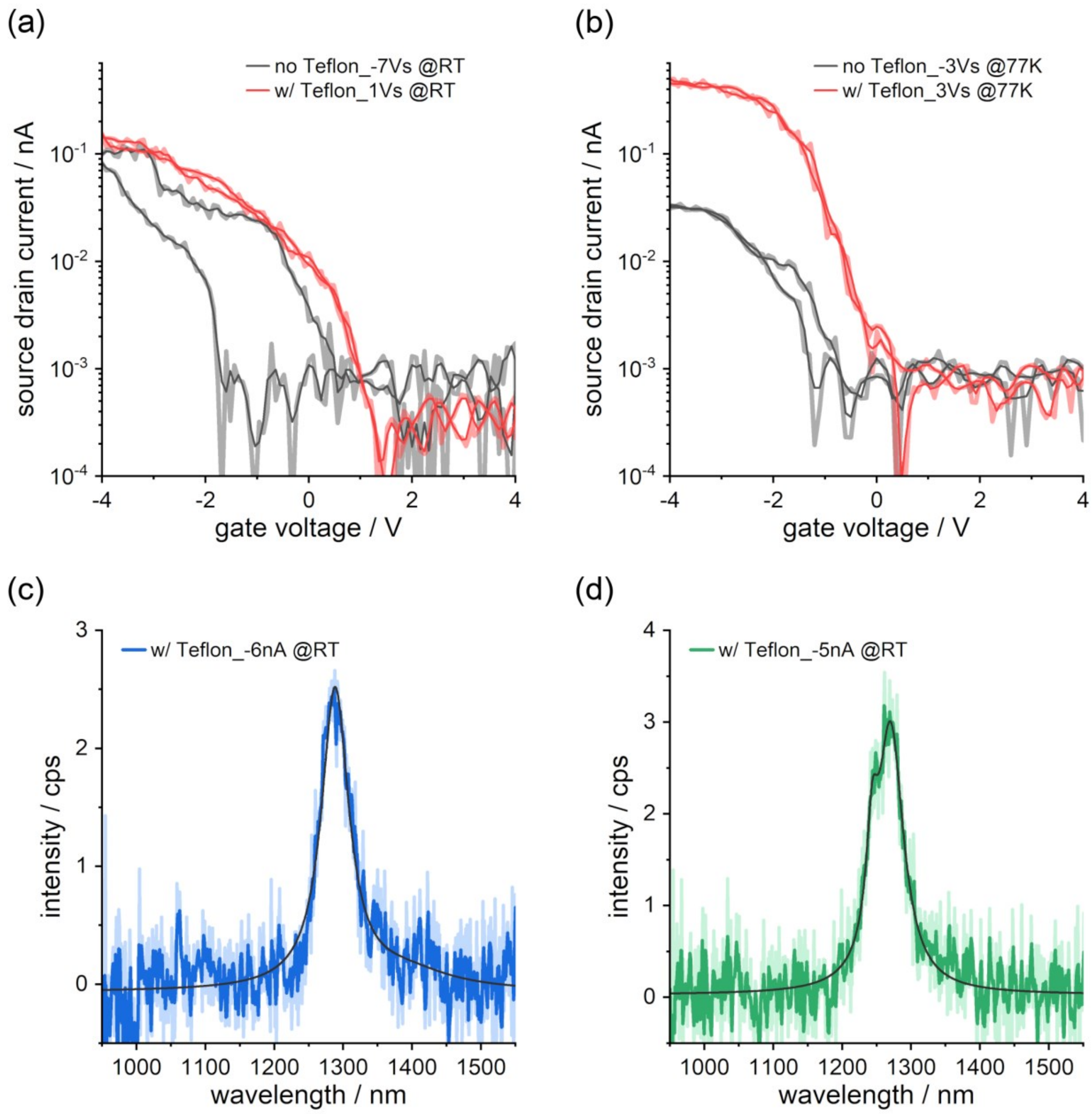

Figure 7.4: Room temperature measurement of devices with Teflon coating (a) Transconductance characteristics of functionalized (7, 5) SWCNT devices measured at room temperature and (b) at 77 K with or without 30 nm Teflon deposition for improving device stability by suppressing hysteresis[205]. Constant source-drain voltage with a gate voltage sweep of ±4 V was applied. The source-drain bias was -7 V at RT and -3 V at 77 K for device without Teflon, and 1 V at RT and 3 V at 77 K for Teflon coated device. (c), (d) Room temperature electroluminescence spectra from devices with Teflon layer coated. The devices were excited by constant source-drain currents of -6 nA and -5 nA respectively. Spectra were fitted with Voigt functions.

Another approach may be attempted as an extension work of Chapter 6 to improve the data quality of second-order correlation function measurement of electrically driven single-photon emission, is to shorten the long acquisition time by focusing on boosting the light-collecting efficiency and/or the emission brightness without worrying too much about the spectral purity and emission stability. For instance, we have demonstrated that integrating SWCNTs into cross-bar Si_3N_4 photonic crystal cavity devices with NCG electrodes, in which 3D couplers[324] were printed at the end of the nanowaveguides for emission outcoupling, not only increases the radiative emission rate but reduces the collection loss in a free-space microscopic system. In our previous work, we estimated around 20 % of emitted photon collection for 1400 – 1600 nm emission wavelength in free space with an objective (NA = 0.6)[70]. On the other hand, the coupling efficiency of waveguide-integrated light emission[11,256] was reported around 60 % and even above 98 % for on-resonance coupling efficiency[21] in the thesis. An additional advantage of integrating into photonic cavities is that they also act as a built-in on-chip filter of the photonic device for spectral cleaning[88]. Although according to the Purcell effect[322], the emission rate enhancement (accelerated decay rate) in the cavity would indicate lifetime reduction as well, in principle, it should not be an issue providing the usage of low-jitter superconducting single-photon detectors.

– this page left intentionally blank –

Appendix

Calculations of normal-mode frequencies

The normal-mode frequencies simulation in **Figure 4.16** was kindly done by our collaborator, Prof. Dr. Karin Fink, from Karlsruhe Institute of Technology as described in the following:

Density functional theory (DFT) calculations using the PBE functional and the def2-SVP basis set[335] were performed applying the program package TURBOMOLE,[336] with the following settings: grid 4, scfconv 7. The resolution of the identity approximation was used to accelerate the calculations of the Coulomb interactions. As a model system for 3,5-dichlorobenzene-functionalization, a $C_{54}H_{18}$ flake was used as a substrate. For the adsorption, three different situations were considered. a) adsorption of a 3,5-dichlorophenyl anion, b) the same in presence of hydrogen close by, and c) adsorption of a 3,5-dichlorophenyl radical. The structure of the flake was optimized under the assumption of C_{6h} symmetry, the structures with adsorbates in C_1 symmetry. For all optimized structures, analytical vibrational frequencies were calculated. In none of the cases, negative force constants were observed proving that all structures are local minima.

Redox-chemical doping of SWCNT suspensions

The redox-chemical doping measurement in **Figure 4.18** was kindly performed in collaboration with Martina Wederhake and valuable input from Dr. Friedrich Schöppler and Prof. Dr. Tobias Hertel, from Julius Maximilian Universität Würzburg as described in the following:

Redox-chemical doping (p-doped) of the SWCNT suspensions was performed by titration with gold(III) chloride solution (Sigma-Aldrich, ≥ 99.99 %) using 10:1 (v/v) toluene to acetonitrile solvent mixture for both SWCNT suspensions and redox solutions. The addition of acetonitrile is required to improve gold(III) chloride solubility. The PL spectra were recorded using a custom-built setup, with a supercontinuum light source (SuperK Extreme EXR-15, NKT Photonics), equipped with a variable band-pass filter (SuperK Varia, NKT Photonics). 650 nm (640 – 660 nm) laser light was used for the excitation of the SWCNTs in the visible region. A cuvette with a 10 mm path length, containing the SWCNT suspension ($OD(E_{11}) = 0.2$, 500 µL starting volume) was placed in the focus of the excitation laser. Near-infrared PL was collected at 90° off-axis. Scattered excitation light was blocked from entering the spectrograph by a 900 nm long-pass filter. After spectrally dispersing the emitted fluorescence using an F/4, 303 mm focal length Shamrock (SR-303i, Andor) grating spectrograph with a 150 lines/mm grating, the PL was detected by a thermo-electrically cooled InGaAs array (iDus PDA DU49-1.7, Andor). Spectra were corrected for dilution induced by the addition of gold chloride solution, as well as for grating and detector sensitivities.

Supplementary results of the photon correlation measurement at 77 K

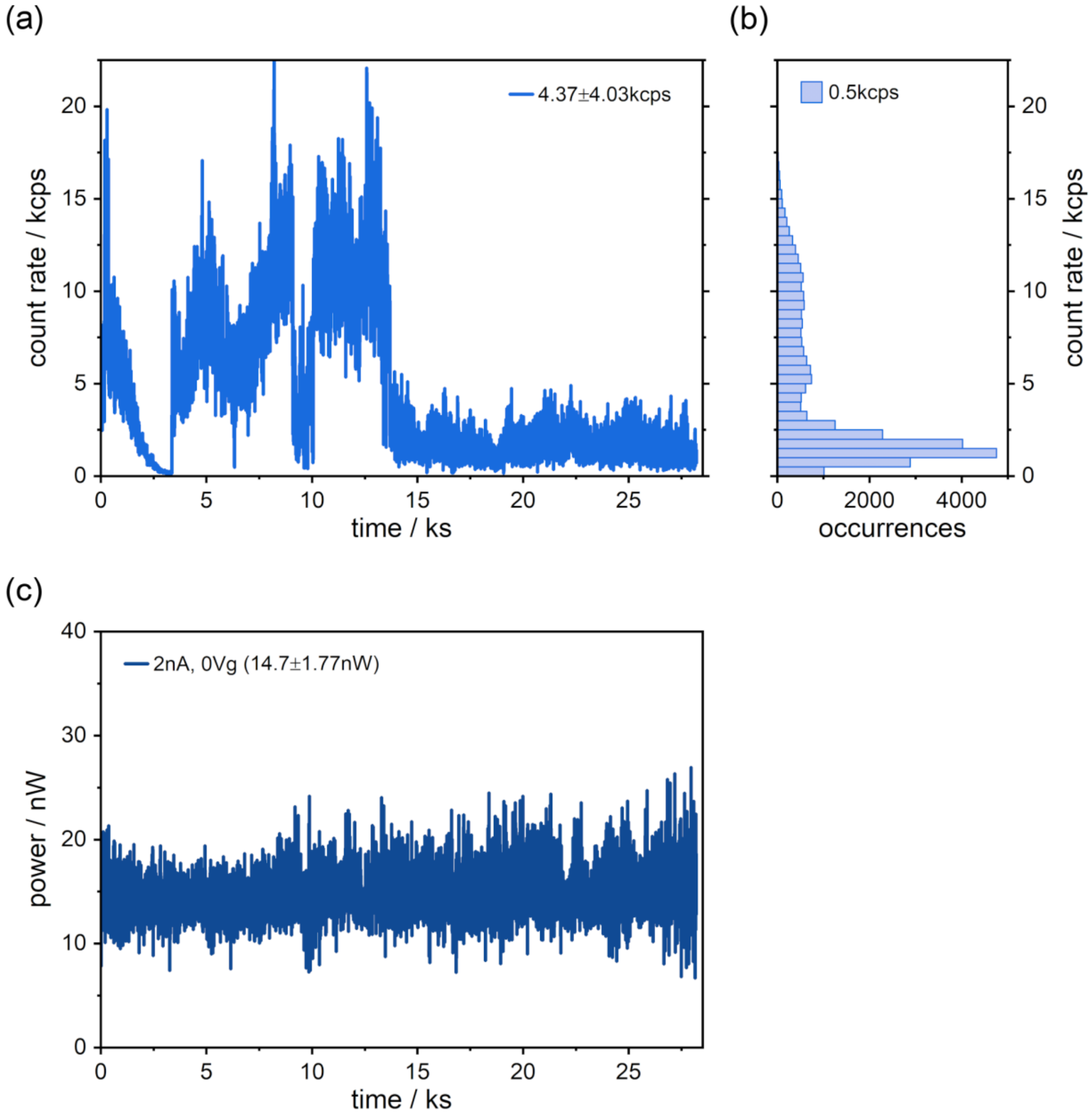

Figure 0.1: Photon count rate and excitation power time traces with 1300 nm band-pass (BP) filter (a) The collected photon count rates over the period of intensity correlation measurement under a constant 2 nA source-drain bias of a functionalized (7, 5) device at 77 K with a 1300 nm band-pass filter (FBH1300-12, Thorlabs), as shown in Figure 5.15a,b. The average count rate and the standard deviation are 4.37±4.03 kcps over 28 ks. The clear constant drop of count rate after around 14 ks may relate to spectral wandering due to the fluctuating environment[327]. (b) The accumulated histogram of the acquired photon count rates plotted with a bin size of 500 cps. (c) The simultaneously recorded excitation power time trace for the intensity correlation measurement.

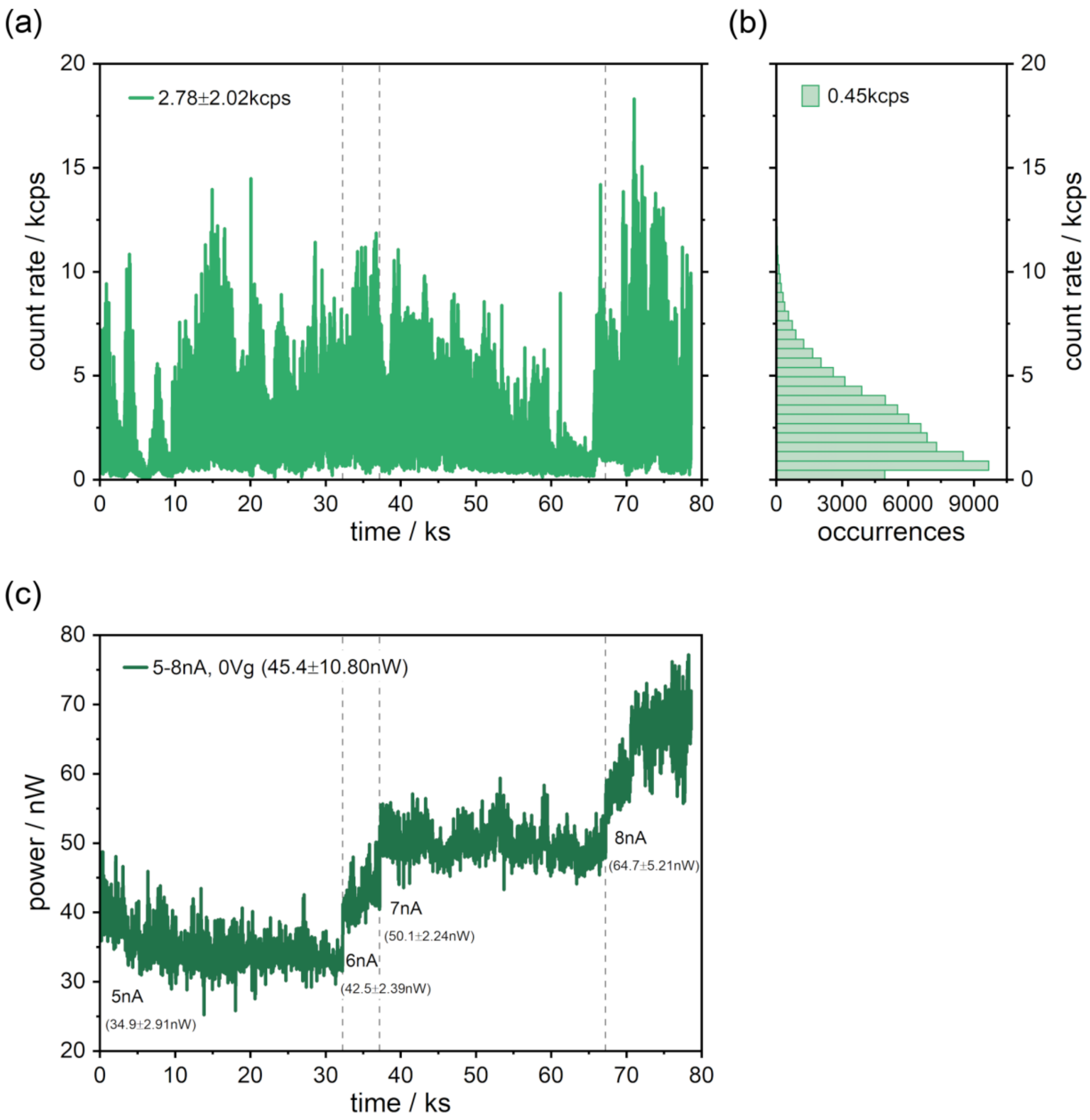

Figure 0.2: Photon count rate and excitation power time traces with 1200 nm band-pass (BP) filter (a) The collected photon count rates over the period of correlation measurement under constant source-drain bias between 5 to 8 nA of a functionalized (7, 5) device at 77 K with a 1200 nm band-pass filter (FBH1200-10, Thorlabs), as shown in Figure 5.15c,d. The average count rate and the standard deviation are 2.78±2.02 kcps over 78.5 ks. (b) The accumulated histogram of the acquired photon count rates plotted with a bin size of 450 cps. (c) The simultaneously recorded excitation power time trace for the intensity correlation measurement. Constant source-drain bias from 5 to 8 nA was applied and the grey dashed lines separate different current bias regions.

Low-loss cavity-compatible nanocrystalline graphene electrodes

The experiments were kindly performed in collaboration with Dr. Anna Ovvyan.

A key ingredient to our approach consists of the engineered NCG-SWCNT heterojunction atop the cross-bar cavity region. Since the electrodes are required to reach closely into the center of the cavity to drive the SWCNT (**Figure 6.1d**) and can potentially affect the resonance modes, we replaced conventional metallic electrodes with NCG electrodes atop the cavity. The benefit of using NCG electrodes compared to gold electrodes is shown in **Figure 0.3**. The insertion loss characterized via transmission measurements of the cross-bar structure increases with increasing cross-bar width as shown in **Figure 0.3a**. While insertion losses at junctions without electrodes are as low as 0.046 ± 0.006 dB/cross (red data points), they reach 0.084 ± 0.007 dB/cross for NCG electrodes and 1.050 ± 0.021 dB/cross for gold electrodes for a cross-bar width of 200 nm at a wavelength of 1550 nm. We note that insertion losses at a wavelength of 1490 nm show a similar trend. The effect of the electrode material on the Q-factor of a cross-bar PhC cavity is shown in **Figure 0.3c**. We find that the influence of NCG electrodes on the Q-factor is negligible, which can be seen by comparing the green and red curves, corresponding to similar cavities with NCG and without deposited electrodes, respectively. In contrast, gold electrodes decrease the Q-factor of the III-order resonance mode by more than 4.9 - 7.8 times, depending on the cross width. Increasing the width of the cross-bar w_{cr} leads to a decrease in the Q-factor for all considered cases. We note that the measured Q-factor was limited by the resolution of the spectrometer as well as the coherence length of the employed supercontinuum light source.

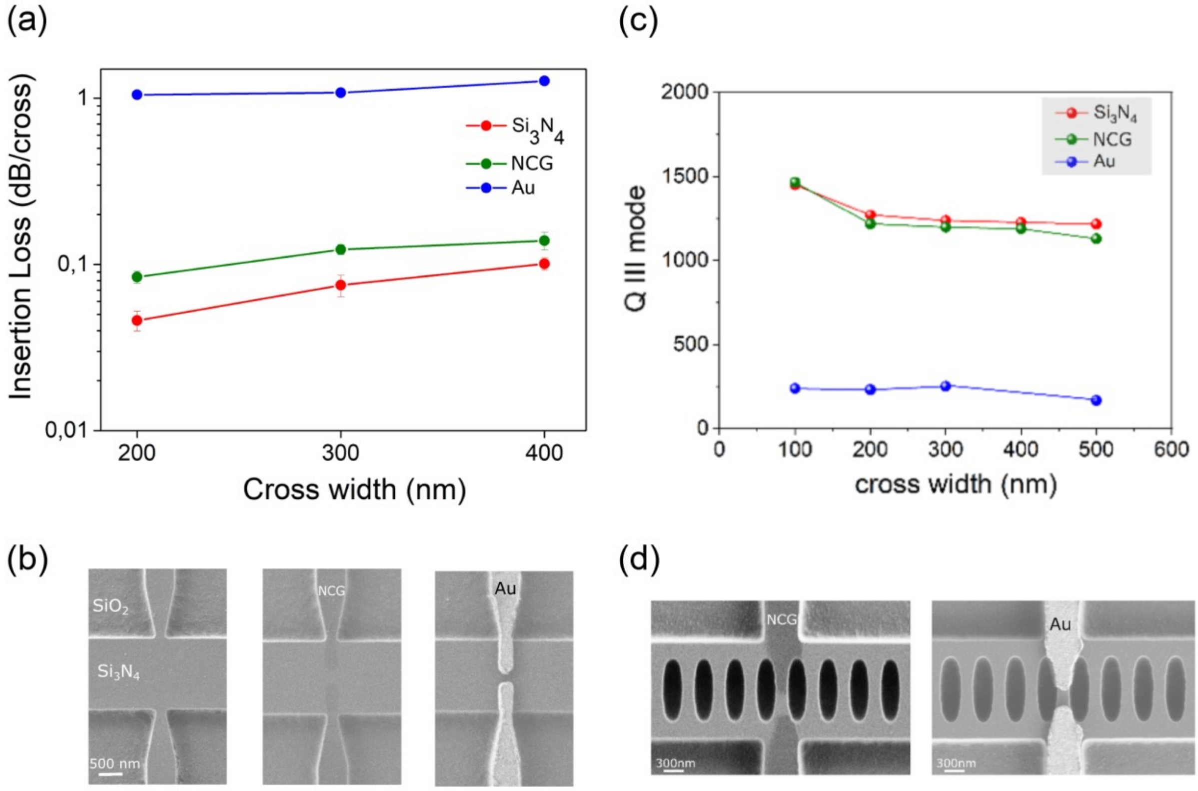

Figure 0.3: Low-loss NCG electrodes embedded within a photonic crystal (PhC) cavity (a) Measured insertion loss of cavity cross-bar structures without electrodes (red), with integrated NCG electrodes (green), and with gold electrodes (blue). The error bar was calculated by measuring the total loss through a device with multiple electrodes in dependence on the number of electrodes and fitting the result by linear regression. (b) SEM images of cavity cross-bars (from the left) without electrodes, with 5 nm thick NCG electrodes, and with 120 nm thick gold electrodes. (c) Dependence of the Q-factor of the III-order resonance mode of a cross-bar PhC cavity on the width of the cross-bar without electrodes (red), with NCG (green), and gold (blue) electrodes. (d) SEM image of the cavity region of a cross-bar PhC device equipped with NCG (left) and gold (right) electrodes.

Electron temperature of a NCG-based incandescent nanoemitter

We experimentally measured the free-space incandescent emission spectrum of an electrically biased NCG strip placed on a Si_3N_4 waveguide (similar device design as shown in **Figure 6.3c**, but without a PhC cavity). The detected monotonic thermal spectrum (red curve) is shown in **Figure 0.4**. Importantly, in our experiments, the utilized NCG strip (thickness 5 nm) is placed on a Si_3N_4 cavity or waveguide (the NCG strip is not suspended). These findings allow us to assess that NCG strip infrared emission results from an electronic temperature since there is no significant non-equilibrium phonon distribution present[326,337].

Thus, we fit the incandescent emission of the biased NCG strip at an applied electrical power of 2.87 mW (red curve in Supplementary Fig. 8a) with a grey-body theory (Planck's law, modified by an emissivity), and determine the electron temperature of NCG – T_e of ~ 1000 K, as indicated by the dashed blue curve in **Figure 0.4**.

$$I(\lambda, \mathrm{T}) = \varepsilon \left(\frac{2\pi hc^2}{\lambda^5}\right) \frac{1}{\exp\left(\frac{hc}{\lambda k_B T} - 1\right)}$$

Here we use the spectral energy density of thermal radiation from NCG strip $I(\lambda, \mathrm{T})$, Planck constant h =6.626x10^{-34} (J·s), Boltzmann constant k_B =1.38x10^{-23} (J/K), electron temperature of NCG strip T (K), wavelength of the emitted photons λ, speed of light c, emissivity of NCG strip ε (≈ 0.25)[326,338].

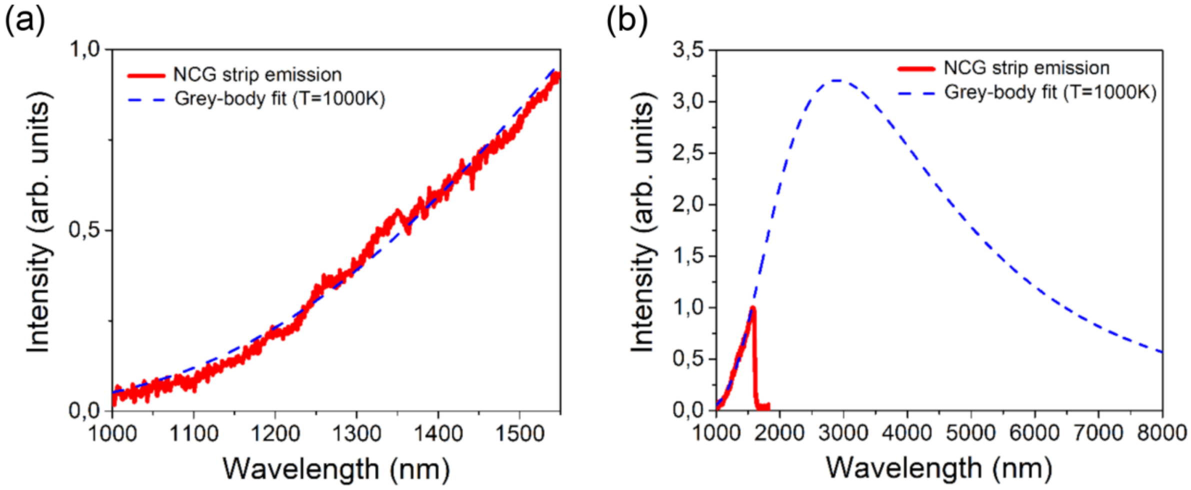

Figure 0.4: Emission spectrum of a NCG strip nanoemitter on a Si_3N_4 waveguide (a) Recorded free-space thermal emission spectrum of an electrically biased NCG strip using a source-drain current of 70 uA. The spectrum from the NCG strip was acquired with the polarizer parallel to the TE mode of the waveguide. The waist of the NCG strip is 250 nm in width. The drop of the detected intensity around λ = 1600 nm is due to the cut-off of sensitivity of the InGaAs photodiode. The blue dashed curve refers to the greybody fit to the spectrum at the extracted temperature T = 1000 K according to equation, where the fully fitted spectrum is shown in (b).

– this page left intentionally blank –

List of Figures

Figure 2.1: The honeycomb atomic structure and the Brillouin zone of graphene 6

Figure 2.2: Electronic band structure of graphene 7

Figure 2.3: Transmission electron microscopy images and schematic models of carbon nanotubes 8

Figure 2.4: Graphene sheet roll-up and various types of SWCNTs 9

Figure 2.5: A map of metallic and semiconducting SWCNTs categorized based on chiral indices 10

Figure 2.6: Illustrations of the mechanism of carbon nanotube growth process 12

Figure 2.7: Carbon nanotube sorting techniques..........14

Figure 2.8: Luminescent defects of carbon nanotubes by covalent functionalization 15

Figure 2.9: Quantized 1D wave vectors of SWCNTs 17

Figure 2.10: SWCNT band structures and density of states 18

Figure 2.11: Optical transition schematic and Kataura plot..........19

Figure 2.12: Schematic of photoluminescence process and photoluminescence excitation map 20

Figure 2.13: Raman spectroscopy of SWCNTs..........22

Figure 2.14: The defect-induced emission characteristics and relaxation processes 23

Figure 2.15: The diverse defect-induced red-shifted emission spectra 24

Figure 2.16: The roles of electrical contact in SWCNT field-effect transistors..........27

Figure 2.17: Electroluminescence mechanism and comparison between PL and EL of SWCNTs..........29

Figure 2.18: Defect-state electroluminescence from carrier recombination 31

Figure 2.19: Photon correlation measurement and the class of light sources 34

Figure 2.20: Single-photon emission of SWCNTs via pulsed optical excitation 35

Figure 2.21: Integration of functionalized SWCNTs into microcavities..........37

Figure 3.1: Schematic illustrations of SWCNT device fabrication process flow 42

Figure 3.2: Electroluminescence (EL) spectroscopy measurement setup..........46

Figure 3.3: A schematic illustration of the HBT experimental setup..........48

Figure 3.4: Incandescent light emission of graphene stripe for setup alignment 49

Figure 3.5: Data processing of $g^2(\tau)$ measurement for time offset adjustment 50

Figure 4.1: 3D model illustration of light emission from an electrically-biased graphene-contacted single-walled carbon nanotube with a quantum defect. 51

Figure 4.2: Optical properties of pristine and functionalized SWCNT suspensions 54

Figure 4.3: Photoluminescence excitation maps in logarithmic intensity scaling 55

Figure 4.4: Length distribution of SWCNT suspension and images with single-tube devices 56

Figure 4.5: Electroluminescence excitation maps 57

Figure 4.6: Integrated defect-state emission intensity maps 58

Figure 4.7: Contour maps of source-drain voltage and electrical power dissipation 59

Figure 4.8: Gate-voltage dependence of EL spectra 60

Figure 4.9: Peak positions and linewidths from functionalized (7, 5) EL spectra 61

Figure 4.10: Additional EL data of functionalized (7, 5) SWCNTs 62

Figure 4.11: Correlation between gate-voltage dependent emission and transport data 63

Figure 4.12: Electroluminescence data of functionalized (6, 5) SWCNTs at 4 K 64

Figure 4.13: Temperature-dependent EL spectra of functionalized (6, 5) SWCNTs 65

Figure 4.14: Additional emission lines at very low-temperature 66

Figure 4.15: Energy spacing of starred peaks 67

Figure 4.16: Simulation of normal mode frequencies of 3,5-dichlorophenyl-graphene(19) 68

Figure 4.17: Hot-exciton electroluminescence via phonon-mediated relaxation 69

Figure 4.18: Electroluminescence of electrostatic gating and photoluminescence of redox doping 73

Figure 4.19: PL spectra of (7, 5) SWCNT suspensions with different optical densities 73

Figure 5.1: 3D model illustration of single-photon emission from an electrically-biased quantum defect in graphene-contacted single-walled carbon nanotube device arrays. 76

Figure 5.2: Control Unit photos and an overview schematic of connecting configuration (1) 83

Figure 5.3: Crosstalk and schematics of configuration (2) 84

Figure 5.4: Current-voltage characteristics curves of configuration (1) and (2) at mK temperatures 86

Figure 5.5: Temperature-dependent current-voltage characteristics curves of configuration (1)..................88

Figure 5.6: Count rates and generated electrical pulses in dark or under illumination..................................90

Figure 5.7: Temperature-dependent dark count rate measurements...91

Figure 5.8: Photoresponse and detection efficiency..92

Figure 5.9: Photon number resolution of SSPDs 93

Figure 5.10: Determine system jitter by using a picosecond 1064 nm seed laser..94

Figure 5.11: Photon bunching effect from sub-threshold laser diode 96

Figure 5.12: Images of single-tube device and properties of carbon nanotube suspensions..........................98

Figure 5.13: Transconductance characteristics of functionalized (7, 5) SWCNT devices.................................99

Figure 5.14: Electroluminescence spectroscopy and coincidence histogram..100

Figure 5.15: Intensity correlation measurement with band-pass (BP) filters 101

Figure 5.16: Comparison of time offsets recorded with a nanotube emitter and a laser diode 102

Figure 5.17: Electrical power dissipation *versus* the $g^2(0)$ value and FWHM..103

Figure 5.18: Intensity correlation measurement of functionalized (7, 5) without spectral filter 104

Figure 5.19: Photon count rate and electrical excitation time trace 106

Figure 5.20: Electrical noise of the recorded source-drain voltage 107

Figure 6.1: Electrically controlled cross-bar PhC cavity with integrated SWCNT emitter..............................112

Figure 6.2: Simulated on-resonance LDOS enhancement spatial map and electric field distribution...........113

Figure 6.3: Nanocrystalline graphene-based nanoemitter 114

Figure 6.4: NCG-based incandescent nanoemitter at room temperature..115

Figure 6.5: Simulated on-resonance LDOS enhancement spatial map and polarization map.......................117

Figure 6.6: Dynamic control of electroluminescence (EL) from cavity-integrated SWCNT............................118

Figure 6.7: EL spectra of SWCNT coupled to a cross-bar PhC cavity at room temperature...........................119

Figure 6.8: Dynamic control of EL from another cavity-integrated SWCNT device 120

Figure 6.9: Fabricated hybrid devices on-chip 121

Figure 7.1: Intensity correlation measurement with polytetrafluoroethylene (PTFE) coating.......................125

Figure 7.2: Photon count rate and electrical excitation time trace with Teflon coating 126

Figure 7.3: Electrical noise of the recorded source-drain voltage 127

Figure 7.4: Room temperature measurement of devices with Teflon coating 128

Figure 0.1: Photon count rate and excitation power time traces with 1300 nm band-pass (BP) filter 132

Figure 0.2: Photon count rate and excitation power time traces with 1200 nm band-pass (BP) filter 133

Figure 0.3: Low-loss NCG electrodes embedded within a photonic crystal (PhC) cavity 134

Figure 0.4: Emission spectrum of a NCG strip nanoemitter on a Si_3N_4 waveguide 135

List of Abbreviations

BP	band-pass
CoMoCAT	Cobalt Molybdenum Catalyst process
CVD	chemical vapor deposition
DC	direct current
DCR	dark count rate
DEP	Dielectrophoresis
DOS	density of state
EL	electroluminescence
EHT	electron high tension
FDTD	Finite Difference Time Domain
FWHM	full width at half maximum
HBT	Hanbury Brown and Twiss
IMF	intermediate frequency mode
InGaAs	indium gallium arsenide
LDOS	Local Density of States
LP	long-pass
m-SWCNT	metallic single-walled carbon nanotube
NbN	niobium nitride
NCG	nanocrystalline graphene
NPLC	number of power line cycles
PhC	photonic crystal
PL	photoluminescence
PLE	photoluminescence excitation
PLC	power line cycles

PLQY	photoluminescence quantum yield
PMMA	Poly(methyl methacrylate)
PMT	photomultiplier tube
PNR	photon number resolution
PTFE	polytetrafluoroethylene
RF	Radio frequency
rpm	revolutions per minute
sc-SWCNT	semiconducting single-walled carbon nanotube
SE1	type I secondary electron
SEM	Scanning electron microscopy
SPD	single-photon detector
SSPD	superconducting single-photon detector
SPAD	single-photon avalanche diode
SNSPD	superconducting nanowire single-photon detector
SWCNT	single-walled carbon nanotube
T2	time-tagged
TCSPC	time-correlated single photon counting
TE	transverse electric
TEM	Transmission electron microscopy
vHs	van Hove singularities
VLSI	very large-scale integration

Bibliography

[1] M. J. O'Mahony, C. Politi, D. Klonidis, R. Nejabati, D. Simeonidou, *Journal of Lightwave Technology* **2006**, *24*, 4684.

[2] A. Shacham, K. Bergman, L. P. Carloni, *IEEE Transactions on Computers* **2008**, *57*, 1246.

[3] J. L. O'Brien, A. Furusawa, J. Vučković, *Nat Photonics* **2009**, *3*, 687.

[4] J. L. O'Brien, *Science* **2007**, *318*, 1567.

[5] A. Beveratos, R. Brouri, T. Gacoin, A. Villing, J.-P. Poizat, P. Grangier, *Phys Rev Lett* **2002**, *89*, 187901.

[6] E. Knill, R. Laflamme, G. J. Milburn, *Nature* **2001**, *409*, 46.

[7] P. Avouris, M. Freitag, V. Perebeinos, *Nat Photonics* **2008**, *2*, 341.

[8] X. He, H. Htoon, S. K. Doorn, W. H. P. Pernice, F. Pyatkov, R. Krupke, A. Jeantet, Y. Chassagneux, C. Voisin, *Nat Mater* **2018**, *17*, 663.

[9] M. Zheng, *Top Curr Chem* **2017**, *375*, 13.

[10] A. Högele, C. Galland, M. Winger, A. Imamoğlu, *Phys Rev Lett* **2008**, *100*, 217401.

[11] S. Khasminskaya, F. Pyatkov, K. Słowik, S. Ferrari, O. Kahl, V. Kovalyuk, P. Rath, A. Vetter, F. Hennrich, M. M. Kappes, G. Gol'tsman, A. Korneev, C. Rockstuhl, R. Krupke, W. H. P. Pernice, *Nat Photonics* **2016**, *10*, 727.

[12] F. Pyatkov, V. Fütterling, S. Khasminskaya, B. S. Flavel, F. Hennrich, M. M. Kappes, R. Krupke, W. H. P. Pernice, *Nat Photonics* **2016**, *10*, 420.

[13] Y. Luo, E. D. Ahmadi, K. Shayan, Y. Ma, K. S. Mistry, C. Zhang, J. Hone, J. L. Blackburn, S. Strauf, *Nat Commun* **2017**, *8*, 1413.

[14] A. Jeantet, Y. Chassagneux, C. Raynaud, Ph. Roussignol, J. S. Lauret, B. Besga, J. Estève, J. Reichel, C. Voisin, *Phys Rev Lett* **2016**, *116*, 247402.

[15] S. Ghosh, S. M. Bachilo, R. A. Simonette, K. M. Beckingham, R. B. Weisman, *Science* **2010**, *330*, 1656.

[16] Y. Piao, B. Meany, L. R. Powell, N. Valley, H. Kwon, G. C. Schatz, Y. Wang, *Nat Chem* **2013**, *5*, 840.

[17] X. Ma, N. F. Hartmann, J. K. S. Baldwin, S. K. Doorn, H. Htoon, *Nat Nanotechnol* **2015**, *10*, 671.

[18] X. He, N. F. Hartmann, X. Ma, Y. Kim, R. Ihly, J. L. Blackburn, W. Gao, J. Kono, Y. Yomogida, A. Hirano, T. Tanaka, H. Kataura, H. Htoon, S. K. Doorn, *Nat Photonics* **2017**, *11*, 577.

[19] M.-K. Li, A. Riaz, M. Wederhake, K. Fink, A. Saha, S. Dehm, X. He, F. Schöppler, M. M. Kappes, H. Htoon, V. N. Popov, S. K. Doorn, T. Hertel, F. Hennrich, R. Krupke, *ACS Nano* **2022**, *16*, 11742.

[20] M.-K. Li, S. Dehm, M. M. Kappes, F. Hennrich, R. Krupke, *ACS Nano* **2024**, *18*, 9525.

[21] A. P. Ovvyan, M.-K. Li, H. Gehring, F. Beutel, S. Kumar, F. Hennrich, L. Wei, Y. Chen, F. Pyatkov, R. Krupke, W. H. P. Pernice, *Nat Commun* **2023**, *14*, 3933.

[22] H. W. Kroto, J. R. Heath, S. C. O'Brien, R. F. Curl, R. E. Smalley, *Nature* **1985**, *318*, 162.

[23] K. S. Novoselov, A. K. Geim, S. V. Morozov, D. Jiang, Y. Zhang, S. V. Dubonos, I. V. Grigorieva, A. A. Firsov, *Science* **2004**, *306*, 666.

[24] A. H. Castro Neto, F. Guinea, N. M. R. Peres, K. S. Novoselov, A. K. Geim, *Rev Mod Phys* **2009**, *81*, 109.

[25] J.-C. Charlier, P. C. Eklund, J. Zhu, A. C. Ferrari, *Carbon Nanotubes*, published by Springer, **2007**, pp. 673–709, https://doi.org/10.1007/978-3-540-72865-8_21.

[26] F. Bonaccorso, Z. Sun, T. Hasan, A. C. Ferrari, *Nat Photonics* **2010**, *4*, 611.

[27] S. Iijima, *Nature* **1991**, *354*, 56.

[28] S. Iijima, T. Ichihashi, *Nature* **1993**, *363*, 603.

[29] D. S. Bethune, C. H. Kiang, M. S. de Vries, G. Gorman, R. Savoy, J. Vazquez, R. Beyers, *Nature* **1993**, *363*, 605.

[30] J. M. Schnorr, T. M. Swager, *Chemistry of Materials* **2011**, *23*, 646.

[31] M. S. Dresselhaus, G. Dresselhaus, R. Saito, *Carbon N Y* **1995**, *33*, 883.

[32] J.-C. Charlier, X. Blase, S. Roche, *Rev Mod Phys* **2007**, *79*, 677.

[33] W. Gao, J. Kono, *R Soc Open Sci* **2019**, *6*, 181605.

[34] R. Byron Pipes, S. J. V. Frankland, P. Hubert, E. Saether, *Compos Sci Technol* **2003**, *63*, 1349.

[35] M. Ouyang, J.-L. Huang, C. M. Lieber, *Acc Chem Res* **2002**, *35*, 1018.

[36] N. Grobert, *Materials Today* **2007**, *10*, 28.

[37] S. A. Hodge, M. K. Bayazit, K. S. Coleman, M. S. P. Shaffer, *Chem Soc Rev* **2012**, *41*, 4409.

[38] A. Thess, R. Lee, P. Nikolaev, H. Dai, P. Petit, J. Robert, C. Xu, Y. H. Lee, S. G. Kim, A. G. Rinzler, D. T. Colbert, G. E. Scuseria, D. Tománek, J. E. Fischer, R. E. Smalley, *Science* **1996**, *273*, 483.

[39] T. Guo, P. Nikolaev, A. Thess, D. T. Colbert, R. E. Smalley, *Chem Phys Lett* **1995**, *243*, 49.

[40] P. Nikolaev, M. J. Bronikowski, R. K. Bradley, F. Rohmund, D. T. Colbert, K. A. Smith, R. E. Smalley, *Chem Phys Lett* **1999**, *313*, 91.

[41] S. Maruyama, R. Kojima, Y. Miyauchi, S. Chiashi, M. Kohno, *Chem Phys Lett* **2002**, *360*, 229.

[42] D. E. Resasco, W. E. Alvarez, F. Pompeo, L. Balzano, J. E. Herrera, B. Kitiyanan, A. Borgna, *Journal of Nanoparticle Research* **2002**, *4*, 131.

[43] W. Krätschmer, L. D. Lamb, K. Fostiropoulos, D. R. Huffman, *Nature* **1990**, *347*, 354.

[44] M. Yudasaka, Y. Kasuya, F. Kokai, K. Takahashi, M. Takizawa, S. Bandow, S. Iijima, *Appl Phys A Mater Sci Process* **2002**, *74*, 377.

[45] C. Journet, W. K. Maser, P. Bernier, A. Loiseau, M. L. de la Chapelle, S. Lefrant, P. Deniard, R. Lee, J. E. Fischer, *Nature* **1997**, *388*, 756.

[46] M. Yudasaka, R. Yamada, N. Sensui, T. Wilkins, T. Ichihashi, S. Iijima, *J Phys Chem B* **1999**, *103*, 6224.

[47] S. Bandow, S. Asaka, Y. Saito, A. M. Rao, L. Grigorian, E. Richter, P. C. Eklund, *Phys Rev Lett* **1998**, *80*, 3779.

[48] R. Sen, Y. Ohtsuka, T. Ishigaki, D. Kasuya, S. Suzuki, H. Kataura, Y. Achiba, *Chem Phys Lett* **2000**, *332*, 467.

[49] T. W. Ebbesen, P. M. Ajayan, H. Hiura, K. Tanigaki, *Nature* **1994**, *367*, 519.

[50] S. Bandow, A. M. Rao, K. A. Williams, A. Thess, R. E. Smalley, P. C. Eklund, *J Phys Chem B* **1997**, *101*, 8839.

[51] R. T. K. Baker, M. A. Barber, P. S. Harris, F. S. Feates, R. J. Waite, *J Catal* **1972**, *26*, 51.

[52] R. T. K. Baker, R. J. Waite, *J Catal* **1975**, *37*, 101.

[53] Y. Yan, J. Miao, Z. Yang, F.-X. Xiao, H. Bin Yang, B. Liu, Y. Yang, *Chem Soc Rev* **2015**, *44*, 3295.

[54] M. J. Bronikowski, P. A. Willis, D. T. Colbert, K. A. Smith, R. E. Smalley, *Journal of Vacuum Science & Technology A: Vacuum, Surfaces, and Films* **2001**, *19*, 1800.

[55] B. Kitiyanan, W. E. Alvarez, J. H. Harwell, D. E. Resasco, *Chem Phys Lett* **2000**, *317*, 497.

[56] R. Krupke, F. Hennrich, H. v. Löhneysen, M. M. Kappes, *Science* **2003**, *301*, 344.

[57] M. S. Arnold, A. A. Green, J. F. Hulvat, S. I. Stupp, M. C. Hersam, *Nat Nanotechnol* **2006**, *1*, 60.

[58] J. A. Fagan, M. L. Becker, J. Chun, E. K. Hobbie, *Advanced Materials* **2008**, *20*, 1609.

[59] S. Ghosh, S. M. Bachilo, R. B. Weisman, *Nat Nanotechnol* **2010**, *5*, 443.

[60] H. Liu, D. Nishide, T. Tanaka, H. Kataura, *Nat Commun* **2011**, *2*, 309.

[61] C. Y. Khripin, J. A. Fagan, M. Zheng, *J Am Chem Soc* **2013**, *135*, 6822.

[62] H. Li, G. Gordeev, O. Garrity, S. Reich, B. S. Flavel, *ACS Nano* **2019**, *13*, 2567.

[63] M. Zheng, A. Jagota, M. S. Strano, A. P. Santos, P. Barone, S. G. Chou, B. A. Diner, M. S. Dresselhaus, R. S. Mclean, G. B. Onoa, G. G. Samsonidze, E. D. Semke, M. Usrey, D. J. Walls, *Science* **2003**, *302*, 1545.

[64] M. Zheng, A. Jagota, E. D. Semke, B. A. Diner, R. S. Mclean, S. R. Lustig, R. E. Richardson, N. G. Tassi, *Nat Mater* **2003**, *2*, 338.

[65] X. Tu, S. Manohar, A. Jagota, M. Zheng, *Nature* **2009**, *460*, 250.

[66] F. Chen, B. Wang, Y. Chen, L.-J. Li, *Nano Lett* **2007**, *7*, 3013.

[67] A. Nish, J.-Y. Hwang, J. Doig, R. J. Nicholas, *Nat Nanotechnol* **2007**, *2*, 640.

[68] J.-Y. Hwang, A. Nish, J. Doig, S. Douven, C.-W. Chen, L.-C. Chen, R. J. Nicholas, *J Am Chem Soc* **2008**, *130*, 3543.

[69] F. Hennrich, W. Li, R. Fischer, S. Lebedkin, R. Krupke, M. M. Kappes, *ACS Nano* **2016**, *10*, 1888.

[70] M. Gaulke, A. Janissek, N. A. Peyyety, I. Alamgir, A. Riaz, S. Dehm, H. Li, U. Lemmer, B. S. Flavel, M. M. Kappes, F. Hennrich, L. Wei, Y. Chen, F. Pyatkov, R. Krupke, *ACS Nano* **2020**, *14*, 2709.

[71] H. Ozawa, N. Ide, T. Fujigaya, Y. Niidome, N. Nakashima, *Chem Lett* **2011**, *40*, 239.

[72] N. F. Hartmann, R. Pramanik, A.-M. Dowgiallo, R. Ihly, J. L. Blackburn, S. K. Doorn, *ACS Nano* **2016**, *10*, 11449.

[73] T. Fujigaya, N. Nakashima, *Sci Technol Adv Mater* **2015**, *16*, 024802.

[74] L. Cognet, D. A. Tsyboulski, J.-D. R. Rocha, C. D. Doyle, J. M. Tour, R. B. Weisman, *Science* **2007**, *316*, 1465.

[75] N. W. S. Kam, H. Dai, *J Am Chem Soc* **2005**, *127*, 6021.

[76] Y. Miyauchi, M. Iwamura, S. Mouri, T. Kawazoe, M. Ohtsu, K. Matsuda, *Nat Photonics* **2013**, *7*, 715.

[77] X. Ma, L. Adamska, H. Yamaguchi, S. E. Yalcin, S. Tretiak, S. K. Doorn, H. Htoon, *ACS Nano* **2014**, *8*, 10782.

[78] H. Kwon, A. Furmanchuk, M. Kim, B. Meany, Y. Guo, G. C. Schatz, Y. Wang, *J Am Chem Soc* **2016**, *138*, 6878.

[79] S. Kilina, J. Ramirez, S. Tretiak, *Nano Lett* **2012**, *12*, 2306.

[80] J. Ramirez, M. L. Mayo, S. Kilina, S. Tretiak, *Chem Phys* **2013**, *413*, 89.

[81] X. He, B. J. Gifford, N. F. Hartmann, R. Ihly, X. Ma, S. V. Kilina, Y. Luo, K. Shayan, S. Strauf, J. L. Blackburn, S. Tretiak, S. K. Doorn, H. Htoon, *ACS Nano* **2017**, *11*, 10785.

[82] X. He, K. A. Velizhanin, G. Bullard, Y. Bai, J.-H. Olivier, N. F. Hartmann, B. J. Gifford, S. Kilina, S. Tretiak, H. Htoon, M. J. Therien, S. K. Doorn, *ACS Nano* **2018**, *12*, 8060.

[83] S. Settele, F. J. Berger, S. Lindenthal, S. Zhao, A. A. El Yumin, N. F. Zorn, A. Asyuda, M. Zharnikov, A. Högele, J. Zaumseil, *Nat Commun* **2021**, *12*, 2119.

[84] A. Saha, B. J. Gifford, X. He, G. Ao, M. Zheng, H. Kataura, H. Htoon, S. Kilina, S. Tretiak, S. K. Doorn, *Nat Chem* **2018**, *10*, 1089.

[85] N. F. Zorn, S. Settele, F. L. Sebastian, S. Lindenthal, J. Zaumseil, *ACS Applied Optical Materials* **2023**, *1*, 1706.

[86] P. Wang, J. Fortner, H. Luo, J. Kłos, X. Wu, H. Qu, F. Chen, Y. Li, Y. Wang, *J Am Chem Soc* **2022**, *144*, 13234.

[87] H. Qu, X. Wu, J. Fortner, M. Kim, P. Wang, Y. Wang, *ACS Nano* **2022**, *16*, 2077.

[88] A. Borel, T. Habrant-Claude, F. Rapisarda, J. Reichel, S. K. Doorn, C. Voisin, Y. Chassagneux, *ACS Photonics* **2023**, *10*, 2839.

[89] Y. Zheng, Y. Kim, A. C. Jones, G. Olinger, E. R. Bittner, S. M. Bachilo, S. K. Doorn, R. B. Weisman, A. Piryatinski, H. Htoon, *ACS Nano* **2021**, *15*, 10406.

[90] M. Nutz, J. Zhang, M. Kim, H. Kwon, X. Wu, Y. Wang, A. Högele, *Nano Lett* **2019**, *19*, 7078.

[91] Y. Luo, X. He, Y. Kim, J. L. Blackburn, S. K. Doorn, H. Htoon, S. Strauf, *Nano Lett* **2019**, *19*, 9037.

[92] A. K. Mandal, X. Wu, J. S. Ferreira, M. Kim, L. R. Powell, H. Kwon, L. Groc, Y. Wang, L. Cognet, *Sci Rep* **2020**, *10*, 5286.

[93] F. A. Mann, N. Herrmann, F. Opazo, S. Kruss, *Angewandte Chemie International Edition* **2020**, *59*, 17732.

[94] J. Ackermann, J. T. Metternich, S. Herbertz, S. Kruss, *Angewandte Chemie International Edition* **2022**, *61*, e202112372.

[95] N. Soltani, Y. Zheng, S. M. Bachilo, R. B. Weisman, *J Phys Chem Lett* **2023**, *14*, 7960.

[96] C. Ma, C. A. Schrage, J. Gretz, A. Akhtar, L. Sistemich, L. Schnitzler, H. Li, K. Tschulik, B. S. Flavel, S. Kruss, *ACS Nano* **2023**, *17*, 15989.

[97] F. L. Sebastian, N. F. Zorn, S. Settele, S. Lindenthal, F. J. Berger, C. Bendel, H. Li, B. S. Flavel, J. Zaumseil, *J Phys Chem Lett* **2022**, *13*, 3542.

[98] R. Saito, G. Dresselhaus, M. S. Dresselhaus, *Physical Properties of Carbon Nanotubes*, published by Imperial College Press, **1998**.

[99] R. Saito, G. Dresselhaus, M. S. Dresselhaus, *Phys Rev B* **2000**, *61*, 2981.

[100] M. V. Kharlamova, *Prog Mater Sci* **2016**, *77*, 125.

[101] A. G. Marinopoulos, L. Reining, A. Rubio, N. Vast, *Phys Rev Lett* **2003**, *91*, 046402.

[102] L. X. Benedict, S. G. Louie, M. L. Cohen, *Phys Rev B* **1995**, *52*, 8541.

[103] C. L. Kane, E. J. Mele, *Phys Rev Lett* **1997**, *78*, 1932.

[104] M. Ouyang, J.-L. Huang, C. L. Cheung, C. M. Lieber, *Science* **2001**, *292*, 702.

[105] H. Ajiki, T. Ando, *Physica B Condens Matter* **1994**, *201*, 349.

[106] H. Kataura, Y. Kumazawa, Y. Maniwa, I. Umezu, S. Suzuki, Y. Ohtsuka, Y. Achiba, *Synth Met* **1999**, *103*, 2555.

[107] R. B. Weisman, S. M. Bachilo, *Nano Lett* **2003**, *3*, 1235.

[108] M. E. Itkis, D. E. Perea, R. Jung, S. Niyogi, R. C. Haddon, *J Am Chem Soc* **2005**, *127*, 3439.

[109] M. Pfohl, D. D. Tune, A. Graf, J. Zaumseil, R. Krupke, B. S. Flavel, *ACS Omega* **2017**, *2*, 1163.

[110] M. J. O'Connell, S. M. Bachilo, C. B. Huffman, V. C. Moore, M. S. Strano, E. H. Haroz, K. L. Rialon, P. J. Boul, W. H. Noon, C. Kittrell, J. Ma, R. H. Hauge, R. B. Weisman, R. E. Smalley, *Science* **2002**, *297*, 593.

[111] S. M. Bachilo, M. S. Strano, C. Kittrell, R. H. Hauge, R. E. Smalley, R. B. Weisman, *Science* **2002**, *298*, 2361.

[112] C. D. Spataru, S. Ismail-Beigi, L. X. Benedict, S. G. Louie, *Phys Rev Lett* **2004**, *92*, 077402.

[113] F. Wang, G. Dukovic, L. E. Brus, T. F. Heinz, *Science* **2005**, *308*, 838.

[114] J. Maultzsch, R. Pomraenke, S. Reich, E. Chang, D. Prezzi, A. Ruini, E. Molinari, M. S. Strano, C. Thomsen, C. Lienau, *Phys Rev B* **2005**, *72*, 241402.

[115] M. S. Dresselhaus, G. Dresselhaus, R. Saito, A. Jorio, *Annu Rev Phys Chem* **2007**, *58*, 719.

[116] T. Ando, *J Physical Soc Japan* **2006**, *75*, 024707.

[117] H. Zhao, S. Mazumdar, *Phys Rev Lett* **2004**, *93*, 157402.

[118] A. Hartschuh, H. N. Pedrosa, L. Novotny, T. D. Krauss, *Science* **2003**, *301*, 1354.

[119] T. Hertel, S. Himmelein, T. Ackermann, D. Stich, J. Crochet, *ACS Nano* **2010**, *4*, 7161.

[120] V. Perebeinos, J. Tersoff, P. Avouris, *Nano Lett* **2005**, *5*, 2495.

[121] A. Hagen, M. Steiner, M. B. Raschke, C. Lienau, T. Hertel, H. Qian, A. J. Meixner, A. Hartschuh, *Phys Rev Lett* **2005**, *95*, 197401.

[122] S. Reich, M. Dworzak, A. Hoffmann, C. Thomsen, M. S. Strano, *Phys Rev B* **2005**, *71*, 033402.

[123] J. S. Park, Y. Hirana, S. Mouri, Y. Miyauchi, N. Nakashima, K. Matsuda, *J Am Chem Soc* **2012**, *134*, 14461.

[124] R. Matsunaga, K. Matsuda, Y. Kanemitsu, *Phys Rev Lett* **2011**, *106*, 037404.

[125] M. S. Dresselhaus, G. Dresselhaus, R. Saito, A. Jorio, *Phys Rep* **2005**, *409*, 47.

[126] A. Jorio, R. Saito, *J Appl Phys* **2021**, *129*, 021102.

[127] J. Maultzsch, H. Telg, S. Reich, C. Thomsen, *Phys Rev B* **2005**, *72*, 205438.

[128] A. Jorio, R. Saito, G. Dresselhaus, M. S. Dresselhaus, *Philosophical Transactions of the Royal Society of London. Series A: Mathematical, Physical and Engineering Sciences* **2004**, *362*, 2311.

[129] F. Hennrich, R. Krupke, S. Lebedkin, K. Arnold, R. Fischer, D. E. Resasco, M. M. Kappes, *J Phys Chem B* **2005**, *109*, 10567.

[130] P. T. Araujo, P. B. C. Pesce, M. S. Dresselhaus, K. Sato, R. Saito, A. Jorio, *Physica E Low Dimens Syst Nanostruct* **2010**, *42*, 1251.

[131] N. F. Hartmann, K. A. Velizhanin, E. H. Haroz, M. Kim, X. Ma, Y. Wang, H. Htoon, S. K. Doorn, *ACS Nano* **2016**, *10*, 8355.

[132] L. Lüer, S. Hoseinkhani, D. Polli, J. Crochet, T. Hertel, G. Lanzani, *Nat Phys* **2009**, *5*, 54.

[133] A. Ishii, M. Yoshida, Y. K. Kato, *Phys Rev B* **2015**, *91*, 125427.

[134] M. E. Sykes, M. Kim, X. Wu, G. P. Wiederrecht, L. Peng, Y. Wang, D. J. Gosztola, X. Ma, *ACS Nano* **2019**, *13*, 13264.

[135] M. Kim, X. Wu, G. Ao, X. He, H. Kwon, N. F. Hartmann, M. Zheng, S. K. Doorn, Y. Wang, *Chem* **2018**, *4*, 2180.

[136] T. Shiraki, S. Uchimura, T. Shiraishi, H. Onitsuka, N. Nakashima, *Chemical Communications* **2017**, *53*, 12544.

[137] B. M. Weight, B. J. Gifford, S. Tretiak, S. Kilina, *The Journal of Physical Chemistry C* **2021**, *125*, 4785.

[138] M. Kim, L. Adamska, N. F. Hartmann, H. Kwon, J. Liu, K. A. Velizhanin, Y. Piao, L. R. Powell, B. Meany, S. K. Doorn, S. Tretiak, Y. Wang, *The Journal of Physical Chemistry C* **2016**, *120*, 11268.

[139] B. Yu, S. Naka, H. Aoki, K. Kato, D. Yamashita, S. Fujii, Y. K. Kato, T. Fujigaya, T. Shiraki, *ACS Nano* **2022**, *16*, 21452.

[140] Corwin. Hansch, A. Leo, R. W. Taft, *Chem Rev* **1991**, *91*, 165.

[141] Y. Zhang, N. Valley, A. H. Brozena, Y. Piao, X. Song, G. C. Schatz, Y. Wang, *J Phys Chem Lett* **2013**, *4*, 826.

[142] H.-B. Luo, P. Wang, X. Wu, H. Qu, X. Ren, Y. Wang, *ACS Nano* **2019**, *13*, 8417.

[143] F. J. Berger, J. Lüttgens, T. Nowack, T. Kutsch, S. Lindenthal, L. Kistner, C. C. Müller, L. M. Bongartz, V. A. Lumsargis, Y. Zakharko, J. Zaumseil, *ACS Nano* **2019**, *13*, 9259.

[144] G. Gordeev, T. Rosenkranz, F. Hennrich, S. Reich, R. Krupke, *The Journal of Physical Chemistry C* **2022**, *126*, 9803.

[145] Z. Huang, L. R. Powell, X. Wu, M. Kim, H. Qu, P. Wang, J. L. Fortner, B. Xu, A. L. Ng, Y. Wang, *Advanced Materials* **2020**, *32*, 1906517.

[146] L. R. Powell, Y. Piao, Y. Wang, *J Phys Chem Lett* **2016**, *7*, 3690.

[147] D. Kozawa, X. Wu, A. Ishii, J. Fortner, K. Otsuka, R. Xiang, T. Inoue, S. Maruyama, Y. Wang, Y. K. Kato, *Nat Commun* **2022**, *13*, 2814.

[148] Y. Lee, S. M. Trocchia, S. B. Warren, E. F. Young, S. Vernick, K. L. Shepard, *ACS Nano* **2018**, *12*, 9922.

[149] H. Wilson, S. Ripp, L. Prisbrey, M. A. Brown, T. Sharf, D. J. T. Myles, K. G. Blank, E. D. Minot, *The Journal of Physical Chemistry C* **2016**, *120*, 1971.

[150] J. Laudenbach, D. Schmid, F. Herziger, F. Hennrich, M. Kappes, M. Muoth, M. Haluska, F. Hof, C. Backes, F. Hauke, A. Hirsch, J. Maultzsch, *Carbon N Y* **2017**, *112*, 1.

[151] F. L. Sebastian, F. Becker, Y. Yomogida, Y. Hosokawa, S. Settele, S. Lindenthal, K. Yanagi, J. Zaumseil, *ACS Nano* **2023**, *17*, 21771.

[152] N. Soltani, Y. Zheng, S. M. Bachilo, R. B. Weisman, *J Phys Chem Lett* **2023**, *14*, 7960.

[153] B. M. Weight, M. Zheng, S. Tretiak, *J Phys Chem Lett* **2023**, *14*, 1182.

[154] D. Mann, A. Javey, J. Kong, Q. Wang, H. Dai, *Nano Lett* **2003**, *3*, 1541.

[155] Z. Chen, J. Appenzeller, J. Knoch, Y. Lin, P. Avouris, *Nano Lett* **2005**, *5*, 1497.

[156] N. Nemec, D. Tománek, G. Cuniberti, *Phys Rev Lett* **2006**, *96*, 076802.

[157] M. Engel, D. B. Farmer, J. T. Azpiroz, J.-W. T. Seo, J. Kang, P. Avouris, M. C. Hersam, R. Krupke, M. Steiner, *Nat Commun* **2018**, *9*, 4095.

[158] A. D. Özdemir, P. Barua, F. Pyatkov, F. Hennrich, Y. Chen, W. Wenzel, R. Krupke, A. Fediai, *Commun Phys* **2021**, *4*, 246.

[159] J. A. Misewich, R. Martel, Ph. Avouris, J. C. Tsang, S. Heinze, J. Tersoff, *Science* **2003**, *300*, 783.

[160] M. Freitag, J. Chen, J. Tersoff, J. Tsang, Q. Fu, J. Liu, P. Avouris, *Phys Rev Lett* **2004**, *93*, 076803.

[161] M. Freitag, V. Perebeinos, J. Chen, A. Stein, J. C. Tsang, J. A. Misewich, R. Martel, P. Avouris, *Nano Lett* **2004**, *4*, 1063.

[162] T. Mueller, M. Kinoshita, M. Steiner, V. Perebeinos, A. A. Bol, D. B. Farmer, P. Avouris, *Nat Nanotechnol* **2010**, *5*, 27.

[163] S. Wang, Q. Zeng, L. Yang, Z. Zhang, Z. Wang, T. Pei, L. Ding, X. Liang, M. Gao, Y. Li, L.-M. Peng, *Nano Lett* **2011**, *11*, 23.

[164] X. Xie, A. E. Islam, M. A. Wahab, L. Ye, X. Ho, M. A. Alam, J. A. Rogers, *ACS Nano* **2012**, *6*, 7981.

[165] N. Higashide, M. Yoshida, T. Uda, A. Ishii, Y. K. Kato, *Appl Phys Lett* **2017**, *110*, 191101.

[166] J. Chen, V. Perebeinos, M. Freitag, J. Tsang, Q. Fu, J. Liu, P. Avouris, *Science* **2005**, *310*, 1171.

[167] V. Perebeinos, P. Avouris, *Phys Rev B* **2006**, *74*, 121410.

[168] M. Freitag, J. C. Tsang, J. Kirtley, A. Carlsen, J. Chen, A. Troeman, H. Hilgenkamp, P. Avouris, *Nano Lett* **2006**, *6*, 1425.

[169] M. Freitag, M. Steiner, A. Naumov, J. P. Small, A. A. Bol, V. Perebeinos, P. Avouris, *ACS Nano* **2009**, *3*, 3744.

[170] L. Marty, E. Adam, L. Albert, R. Doyon, D. Ménard, R. Martel, *Phys Rev Lett* **2006**, *96*, 136803.

[171] X. Wang, L. Zhang, Y. Lu, H. Dai, Y. K. Kato, E. Pop, *Appl Phys Lett* **2007**, *91*, 261102.

[172] D. Mann, Y. K. Kato, A. Kinkhabwala, E. Pop, J. Cao, X. Wang, L. Zhang, Q. Wang, J. Guo, H. Dai, *Nat Nanotechnol* **2007**, *2*, 33.

[173] Z. Liu, A. Bushmaker, M. Aykol, S. B. Cronin, *ACS Nano* **2011**, *5*, 4634.

[174] F. Pyatkov, S. Khasminskaya, V. Kovalyuk, F. Hennrich, M. M. Kappes, G. N. Goltsman, W. H. P. Pernice, R. Krupke, *Beilstein Journal of Nanotechnology* **2017**, *8*, 38.

[175] B. Wang, F. Rezaeifar, J. Chen, S. Yang, R. Kapadia, S. B. Cronin, *ACS Photonics* **2017**, *4*, 2706.

[176] T. Mori, Y. Yamauchi, S. Honda, H. Maki, *Nano Lett* **2014**, *14*, 3277.

[177] N. Hibino, S. Suzuki, H. Wakahara, Y. Kobayashi, T. Sato, H. Maki, *ACS Nano* **2011**, *5*, 1215.

[178] J. Lefebvre, J. M. Fraser, P. Finnie, Y. Homma, *Phys Rev B* **2004**, *69*, 075403.

[179] F. Jakubka, S. B. Grimm, Y. Zakharko, F. Gannott, J. Zaumseil, *ACS Nano* **2014**, *8*, 8477.

[180] E. Pop, D. Mann, J. Cao, Q. Wang, K. Goodson, H. Dai, *Phys Rev Lett* **2005**, *95*, 155505.

[181] K. Yoshikawa, R. Matsunaga, K. Matsuda, Y. Kanemitsu, *Appl Phys Lett* **2009**, *94*, 093109.

[182] Ph. Avouris, J. Chen, M. Freitag, V. Perebeinos, J. C. Tsang, *physica status solidi (b)* **2006**, *243*, 3197.

[183] J. Crochet, M. Clemens, T. Hertel, *J Am Chem Soc* **2007**, *129*, 8058.

[184] L. J. Carlson, S. E. Maccagnano, M. Zheng, J. Silcox, T. D. Krauss, *Nano Lett* **2007**, *7*, 3698.

[185] S. Liang, N. Wei, Z. Ma, F. Wang, H. Liu, S. Wang, L.-M. Peng, *ACS Photonics* **2017**, *4*, 435.

[186] J. Lefebvre, D. G. Austing, J. Bond, P. Finnie, *Nano Lett* **2006**, *6*, 1603.

[187] M. Steiner, M. Freitag, V. Perebeinos, A. Naumov, J. P. Small, A. A. Bol, P. Avouris, *Nano Lett* **2009**, *9*, 3477.

[188] M. Schweiger, Y. Zakharko, F. Gannott, S. B. Grimm, J. Zaumseil, *Nanoscale* **2015**, *7*, 16715.

[189] N. F. Zorn, F. J. Berger, J. Zaumseil, *ACS Nano* **2021**, *15*, 10451.

[190] B. Xu, X. Wu, M. Kim, P. Wang, Y. Wang, *J Appl Phys* **2021**, *129*, 044305.

[191] N. F. Zorn, S. Settele, F. L. Sebastian, S. Lindenthal, J. Zaumseil, *ACS Applied Optical Materials* **2023**, *1*, 1706.

[192] M. S. Hofmann, J. Noé, A. Kneer, J. J. Crochet, A. Högele, *Nano Lett* **2016**, *16*, 2958.

[193] T. Endo, J. Ishi-Hayase, H. Maki, *Appl Phys Lett* **2015**, *106*, 113106.

[194] X. Ma, O. Roslyak, J. G. Duque, X. Pang, S. K. Doorn, A. Piryatinski, D. H. Dunlap, H. Htoon, *Phys Rev Lett* **2015**, *115*, 017401.

[195] A. Ishii, T. Uda, Y. K. Kato, *Phys Rev Appl* **2017**, *8*, 054039.

[196] M. S. Hofmann, J. T. Glückert, J. Noé, C. Bourjau, R. Dehmel, A. Högele, *Nat Nanotechnol* **2013**, *8*, 502.

[197] W. Walden-Newman, I. Sarpkaya, S. Strauf, *Nano Lett* **2012**, *12*, 1934.

[198] R. Watahiki, T. Shimada, P. Zhao, S. Chiashi, S. Iwamoto, Y. Arakawa, S. Maruyama, Y. K. Kato, *Appl Phys Lett* **2012**, *101*, 141124.

[199] A. Jeantet, Y. Chassagneux, T. Claude, P. Roussignol, J. S. Lauret, J. Reichel, C. Voisin, *Nano Lett* **2017**, *17*, 4184.

[200] A. Ishii, X. He, N. F. Hartmann, H. Machiya, H. Htoon, S. K. Doorn, Y. K. Kato, *Nano Lett* **2018**, *18*, 3873.

[201] S. Lebedkin, F. Hennrich, O. Kiowski, M. M. Kappes, *Phys Rev B* **2008**, *77*, 165429.

[202] I. Haller, M. Hatzakis, R. Srinivasan, *IBM J Res Dev* **1968**, *12*, 251.

[203] M. Hatzakis, *J Electrochem Soc* **1969**, *116*, 1033.

[204] L. Anzi, A. Mansouri, P. Pedrinazzi, E. Guerriero, M. Fiocco, A. Pesquera, A. Centeno, A. Zurutuza, A. Behnam, E. A. Carrion, E. Pop, R. Sordan, *2D Mater* **2018**, *5*, 025014.

[205] S. Kumar, D. Dagli, S. Dehm, C. Das, L. Wei, Y. Chen, F. Hennrich, R. Krupke, *physica status solidi (RRL) – Rapid Research Letters* **2020**, *14*, 2000193.

[206] V. Karre, P. D. Keathley, Jing Guo, J. T. Hastings, *IEEE Trans Nanotechnol* **2009**, *8*, 139.

[207] R. Krupke, F. Hennrich, M. M. Kappes, H. v. Löhneysen, *Nano Lett* **2004**, *4*, 1395.

[208] W. Li, F. Hennrich, B. S. Flavel, S. Dehm, M. Kappes, R. Krupke, *Nano Res* **2021**, *14*, 2188.

[209] N. Klein, *IEEE Trans Electron Devices* **1966**, *ED-13*, 788.

[210] M. Engel, M. Steiner, A. Lombardo, A. C. Ferrari, H. v. Löhneysen, P. Avouris, R. Krupke, *Nat Commun* **2012**, *3*, 906.

[211] M. D. Eisaman, J. Fan, A. Migdall, S. V. Polyakov, *Review of Scientific Instruments* **2011**, *82*, 071101.

[212] I. Aharonovich, D. Englund, M. Toth, *Nat Photonics* **2016**, *10*, 631.

[213] C. Kurtsiefer, S. Mayer, P. Zarda, H. Weinfurter, *Phys Rev Lett* **2000**, *85*, 290.

[214] P. Michler, A. Kiraz, C. Becher, W. V. Schoenfeld, P. M. Petroff, L. Zhang, E. Hu, A. Imamoglu, *Science* **2000**, *290*, 2282.

[215] B. Lounis, W. E. Moerner, *Nature* **2000**, *407*, 491.

[216] Y. Maeda, S. Minami, Y. Takehana, J.-S. Dang, S. Aota, K. Matsuda, Y. Miyauchi, M. Yamada, M. Suzuki, R.-S. Zhao, X. Zhao, S. Nagase, *Nanoscale* **2016**, *8*, 16916.

[217] D. Janas, *Mater Horiz* **2020**, *7*, 2860.

[218] A. Spreinat, M. M. Dohmen, J. Lüttgens, N. Herrmann, L. F. Klepzig, R. Nißler, S. Weber, F. A. Mann, J. Lauth, S. Kruss, *The Journal of Physical Chemistry C* **2021**, *125*, 18341.

[219] Y. Zheng, S. M. Bachilo, R. B. Weisman, *ACS Nano* **2020**, *14*, 715.

[220] H. Kwon, M. Kim, M. Nutz, N. F. Hartmann, V. Perrin, B. Meany, M. S. Hofmann, C. W. Clark, H. Htoon, S. K. Doorn, A. Högele, Y. Wang, *ACS Cent Sci* **2019**, *5*, 1786.

[221] A. Högele, C. Galland, M. Winger, A. Imamoğlu, *Phys Rev Lett* **2008**, *100*,217401.

[222] S. Moritsubo, T. Murai, T. Shimada, Y. Murakami, S. Chiashi, S. Maruyama, Y. K. Kato, *Phys Rev Lett* **2010**, *104*, 247402.

[223] A. Vijayaraghavan, F. Hennrich, N. Stürzl, M. Engel, M. Ganzhorn, M. Oron-Carl, C. W. Marquardt, S. Dehm, S. Lebedkin, M. M. Kappes, R. Krupke, *ACS Nano* **2010**, *4*, 2748.

[224] X. Yi, H. Ozawa, G. Nakagawa, T. Fujigaya, N. Nakashima, T. Asano, *Jpn J Appl Phys* **2011**, *50*, 070207.

[225] J. R. Simpson, O. Roslyak, J. G. Duque, E. H. Hároz, J. J. Crochet, H. Telg, A. Piryatinski, A. R. H. Walker, S. K. Doorn, *Nat Commun* **2018**, *9*, 637.

[226] S. Grimm, S. P. Schießl, Y. Zakharko, M. Rother, M. Brohmann, J. Zaumseil, *Carbon N Y* **2017**, *118*, 261.

[227] J. Lefebvre, P. Finnie, Y. Homma, *Phys Rev B* **2004**, *70*, 045419.

[228] C. Galland, A. Högele, H. E. Türeci, A. Imamoğlu, *Phys Rev Lett* **2008**, *101*, 067402.

[229] F. Vialla, Y. Chassagneux, R. Ferreira, C. Roquelet, C. Diederichs, G. Cassabois, Ph. Roussignol, J. S. Lauret, C. Voisin, *Phys Rev Lett* **2014**, *113*, 057402.

[230] I. Sarpkaya, E. D. Ahmadi, G. D. Shepard, K. S. Mistry, J. L. Blackburn, S. Strauf, *ACS Nano* **2015**, *9*, 6383.

[231] M. Nutz, Signatures of Correlations and Interactions in the Optical Spectra of Localized Excitons in Carbon Nanotubes, **2020**.

[232] H. Tachikawa, H. Kawabata, *Jpn J Appl Phys* **2016**, *55*, 06GK05.

[233] E. Gross, S. Permogorov, Ya. Morozenko, B. Kharlamov, *Physica Status Solidi (b)* **1973**, *59*, 551.

[234] N. Pelekanos, J. Ding, Q. Fu, A. V. Nurmikko, S. M. Durbin, M. Kobayashi, R. L. Gunshor, *Phys Rev B* **1991**, *43*, 9354.

[235] C.-H. Cho, C. O. Aspetti, M. E. Turk, J. M. Kikkawa, S.-W. Nam, R. Agarwal, *Nat Mater* **2011**, *10*, 669.

[236] Q. Zhang, X. Liu, M. I. B. Utama, J. Zhang, M. de la Mata, J. Arbiol, Y. Lu, T. C. Sum, Q. Xiong, *Nano Lett* **2012**, *12*, 6420.

[237] S. Permogorov, *physica status solidi (b)* **1975**, *68*, 9.

[238] A. N. Vamivakas, Y. Yin, A. G. Walsh, M. S. Unlu, B. B. Goldberg, A. K. Swan, **2006**, https://doi.org/10.48550/arXiv.cond-mat/0609197 (accessed 2023/08/09).

[239] V. N. Popov, *Phys Rev B* **2018**, *98*, 085413.

[240] A. M. Kelley, *J Chem Phys* **2019**, *151*, 140901.

[241] R. C. C. Leite, J. F. Scott, T. C. Damen, *Phys Rev Lett* **1969**, *22*, 780.

[242] K. H. Eckstein, F. Oberndorfer, M. M. Achsnich, F. Schöppler, T. Hertel, *The Journal of Physical Chemistry C* **2019**, *123*, 30001.

[243] K. H. Eckstein, H. Hartleb, M. M. Achsnich, F. Schöppler, T. Hertel, *ACS Nano* **2017**, *11*, 10401.

[244] I. Namal, Fabrication and Optical and Electronic Characterization of Conjugated Polymer-Stabilized Semiconducting Single-Wall Carbon Nanotubes in Dispersions and Thin Films, **2018**.

[245] X. Wei, T. Tanaka, S. Li, M. Tsuzuki, G. Wang, Z. Yao, L. Li, Y. Yomogida, A. Hirano, H. Liu, H. Kataura, *Nano Lett* **2020**, *20*, 410.

[246] K. J. Trerayapiwat, S. Lohmann, X. Ma, S. Sharifzadeh, *J Appl Phys* **2021**, *129*, 014309.

[247] S.-H. Lohmann, K. J. Trerayapiwat, J. Niklas, O. G. Poluektov, S. Sharifzadeh, X. Ma, *ACS Nano* **2020**, *14*, 17675.

[248] Y. Maeda, H. Murakoshi, H. Tambo, P. Zhao, K. Kuroda, M. Yamada, X. Zhao, S. Nagase, M. Ehara, *Chemical Communications* **2019**, *55*, 13757.

[249] B. J. Gifford, X. He, M. Kim, H. Kwon, A. Saha, A. E. Sifain, Y. Wang, H. Htoon, S. Kilina, S. K. Doorn, S. Tretiak, *Chemistry of Materials* **2019**, *31*, 6950.

[250] S. Deshpande, J. Heo, A. Das, P. Bhattacharya, *Nat Commun* **2013**, *4*, 1675.

[251] T. Heindel, C. Schneider, M. Lermer, S. H. Kwon, T. Braun, S. Reitzenstein, S. Höfling, M. Kamp, A. Forchel, *Appl Phys Lett* **2010**, *96*, 011107.

[252] A. Lohrmann, S. Pezzagna, I. Dobrinets, P. Spinicelli, V. Jacques, J.-F. Roch, J. Meijer, A. M. Zaitsev, *Appl Phys Lett* **2011**, *99*, 251106.

[253] N. Mizuochi, T. Makino, H. Kato, D. Takeuchi, M. Ogura, H. Okushi, M. Nothaft, P. Neumann, A. Gali, F. Jelezko, J. Wrachtrup, S. Yamasaki, *Nat Photonics* **2012**, *6*, 299.

[254] C. Palacios-Berraquero, M. Barbone, D. M. Kara, X. Chen, I. Goykhman, D. Yoon, A. K. Ott, J. Beitner, K. Watanabe, T. Taniguchi, A. C. Ferrari, M. Atatüre, *Nat Commun* **2016**, *7*, 12978.

[255] C. Chakraborty, L. Kinnischtzke, K. M. Goodfellow, R. Beams, A. N. Vamivakas, *Nat Nanotechnol* **2015**, *10*, 507.

[256] S. Khasminskaya, F. Pyatkov, B. S. Flavel, W. H. Pernice, R. Krupke, *Advanced Materials* **2014**, *26*, 3465.

[257] S. Imamura, R. Watahiki, R. Miura, T. Shimada, Y. K. Kato, *Appl Phys Lett* **2013**, *102*, 161102.

[258] M. Ganzhorn, A. Vijayaraghavan, A. A. Green, S. Dehm, A. Voigt, M. Rapp, M. C. Hersam, R. Krupke, *Advanced Materials* **2011**, *23*, 1734.

[259] A. Vijayaraghavan, S. Blatt, D. Weissenberger, M. Oron-Carl, F. Hennrich, D. Gerthsen, H. Hahn, R. Krupke, *Nano Lett* **2007**, *7*, 1556.

[260] G. Hills, C. Lau, A. Wright, S. Fuller, M. D. Bishop, T. Srimani, P. Kanhaiya, R. Ho, A. Amer, Y. Stein, D. Murphy, Arvind, A. Chandrakasan, M. M. Shulaker, *Nature* **2019**, *572*, 595.

[261] T. Shiraki, Y. Miyauchi, K. Matsuda, N. Nakashima, *Acc Chem Res* **2020**, *53*, 1846.

[262] R. H. Hadfield, *Nat Photonics* **2009**, *3*, 696.

[263] A. W. Elshaari, W. Pernice, K. Srinivasan, O. Benson, V. Zwiller, *Nat Photonics* **2020**, *14*, 285.

[264] R. Sobolewski, A. Verevkin, G. N. Gol'tsman, A. Lipatov, K. Wilsher, *IEEE Transactions on Appiled Superconductivity* **2003**, *13*, 1151.

[265] R. H. BROWN, R. Q. TWISS, *Nature* **1956**, *177*, 27.

[266] S. Berciaud, L. Cognet, B. Lounis, *Phys Rev Lett* **2008**, *101*, 077402.

[267] Y. Miyauchi, H. Hirori, K. Matsuda, Y. Kanemitsu, *Phys Rev B* **2009**, *80*, 081410.

[268] H. Harutyunyan, T. Gokus, A. A. Green, M. C. Hersam, M. Allegrini, A. Hartschuh, *Nano Lett* **2009**, *9*, 2010.

[269] J. S. Allen, *Physical Review* **1939**, *55*, 966.

[270] D. Renker, *Nucl Instrum Methods Phys Res A* **2006**, *567*, 48.

[271] G. N. Gol'tsman, O. Okunev, G. Chulkova, A. Lipatov, A. Semenov, K. Smirnov, B. Voronov, A. Dzardanov, C. Williams, R. Sobolewski, *Appl Phys Lett* **2001**, *79*, 705.

[272] Jin Zhang, W. Slysz, A. Verevkin, O. Okunev, G. Chulkova, A. Korneev, A. Lipatov, G. N. Gol'tsman, R. Sobolewski, *IEEE Transactions on Appiled Superconductivity* **2003**, *13*, 180.

[273] A. Peacock, P. Verhoeve, N. Rando, A. van Dordrecht, B. G. Taylor, C. Erd, M. A. C. Perryman, R. Venn, J. Howlett, D. J. Goldie, J. Lumley, M. Wallis, *Nature* **1996**, *381*, 135.

[274] A. Peacock, P. Verhoeve, N. Rando, A. van Dordrecht, B. G. Taylor, C. Erd, M. A. C. Perryman, R. Venn, J. Howlett, D. J. Goldie, J. Lumley, M. Wallis, *J Appl Phys* **1997**, *81*, 7641.

[275] B. Cabrera, R. M. Clarke, P. Colling, A. J. Miller, S. Nam, R. W. Romani, *Appl Phys Lett* **1998**, *73*, 735.

[276] G. N. Gol'tsman, K. Smirnov, P. Kouminov, B. Voronov, N. Kaurova, V. Drakinsky, J. Zhang, A. Verevkin, R. Sobolewski, *IEEE Transactions on Appiled Superconductivity* **2003**, *13*, 192.

[277] A. J. Miller, A. E. Lita, B. Calkins, I. Vayshenker, S. M. Gruber, S. W. Nam, *Opt Express* **2011**, *19*, 9102.

[278] Y. Ivry, C.-S. Kim, A. E. Dane, D. De Fazio, A. N. McCaughan, K. A. Sunter, Q. Zhao, K. K. Berggren, *Phys Rev B* **2014**, *90*, 214515.

[279] R. H. Hadfield, G. Johansson, *Superconducting Devices in Quantum Optics*, Springer International Publishing, Cham, **2016**.

[280] S. Ferrari, C. Schuck, W. Pernice, *Nanophotonics* **2018**, *7*, 1725.

[281] O. Kahl, S. Ferrari, V. Kovalyuk, G. N. Goltsman, A. Korneev, W. H. P. Pernice, *Sci Rep* **2015**, *5*, 10941.

[282] H. Shibata, K. Fukao, N. Kirigane, S. Karimoto, H. Yamamoto, *IEEE Transactions on Applied Superconductivity* **2017**, *27*, 1.

[283] H. Shibata, K. Shimizu, H. Takesue, Y. Tokura, *Opt Lett* **2015**, *40*, 3428.

[284] J. R. Clem, K. K. Berggren, *Phys Rev B* **2011**, *84*, 174510.

[285] T. Yamashita, S. Miki, K. Makise, W. Qiu, H. Terai, M. Fujiwara, M. Sasaki, Z. Wang, *Appl Phys Lett* **2011**, *99*, 88.

[286] I. Charaev, A. Semenov, S. Doerner, G. Gomard, K. Ilin, M. Siegel, *Supercond Sci Technol* **2017**, *30*, 025016.

[287] A. Bahgat Shehata, A. Ruggeri, F. Stellari, A. J. Weger, P. Song, K. Sunter, F. Najafi, K. K. Berggren, V. Anant, in *Proc. of SPIE*, **2015**, 95550C, http://doi.org/10.1117/12.2188234 (accessed 2021/08/09.

[288] N. Calandri, Q.-Y. Zhao, D. Zhu, A. Dane, K. K. Berggren, *Appl Phys Lett* **2016**, *109*, 152601.

[289] L. You, X. Yang, Y. He, W. Zhang, D. Liu, W. Zhang, L. Zhang, L. Zhang, X. Liu, S. Chen, Z. Wang, X. Xie, *AIP Adv* **2013**, *3*, 072135.

[290] M. Sidorova, A. Semenov, H.-W. Hübers, I. Charaev, A. Kuzmin, S. Doerner, M. Siegel, *Phys Rev B* **2017**, *96*, 184504.

[291] F. Marsili, F. Bellei, F. Najafi, A. E. Dane, E. A. Dauler, R. J. Molnar, K. K. Berggren, *Nano Lett* **2012**, *12*, 4799.

[292] E. E. Wollman, V. B. Verma, A. D. Beyer, R. M. Briggs, B. Korzh, J. P. Allmaras, F. Marsili, A. E. Lita, R. P. Mirin, S. W. Nam, M. D. Shaw, *Opt Express* **2017**, *25*, 26792.

[293] R. Lusche, A. Semenov, K. Ilin, M. Siegel, Y. Korneeva, A. Trifonov, A. Korneev, G. Goltsman, D. Vodolazov, H.-W. Hübers, *J Appl Phys* **2014**, *116*, 043906.

[294] J. J. Renema, G. Frucci, Z. Zhou, F. Mattioli, A. Gaggero, R. Leoni, M. J. A. de Dood, A. Fiore, M. P. van Exter, *Opt Express* **2012**, *20*, 2806.

[295] M. S. Elezov, A. V. Semenov, P. P. An, M. A. Tarkhov, G. N. Goltsman, A. I. Kardakova, A. Yu. Kazakov, *Journal of Optical Technology* **2013**, *80*, 435.

[296] S. Ferrari, O. Kahl, V. Kovalyuk, G. N. Goltsman, A. Korneev, W. H. P. Pernice, *Appl Phys Lett* **2015**, *106*, 151101.

[297] F. Mattioli, R. Leoni, A. Gaggero, M. G. Castellano, P. Carelli, F. Marsili, A. Fiore, *J Appl Phys* **2007**, *101*, 054302.

[298] W. J. Skocpol, M. R. Beasley, M. Tinkham, *J Appl Phys* **1974**, *45*, 4054.

[299] A. Engel, H. Bartolf, A. Schilling, K. Il'in, M. Siegel, A. Semenov, H.-W. Hübers, *J Phys Conf Ser* **2008**, *97*, 012152.

[300] J. Kitaygorsky, S. Dorenbos, E. Reiger, R. Schouten, V. Zwiller, R. Sobolewski, *IEEE Transactions on Applied Superconductivity* **2009**, *19*, 346.

[301] B. L. Morgan, L. Mandel, *Phys Rev Lett* **1966**, *16*, 1012.

[302] P. K. Tan, G. H. Yeo, H. S. Poh, A. H. Chan, C. Kurtsiefer, *Astrophys J* **2014**, *789*, L10.

[303] P. K. Tan, X. J. Yeo, A. Z. W. Leow, L. Shen, C. Kurtsiefer, *Phys Rev Appl* **2023**, *20*, 014060.

[304] D. Scarl, *Physical Review* **1968**, *175*, 1661.

[305] P. K. Tan, X. J. Yeo, L. J. Shen, C. Kurtsiefer, in *Quantum Communications and Quantum Imaging XIX*, SPIE, **2021**, 118350C, https://doi.org/10.1117/12.2592964 (accessed 2022/04/21).

[306] T. Weig, T. Hager, G. Brüderl, U. Strauss, U. T. Schwarz, *Opt Express* **2014**, *22*, 27489.

[307] T. Lettau, H. A. M. Leymann, B. Melcher, J. Wiersig, *Phys Rev A (Coll Park)* **2018**, *97*, 053835.

[308] J. Piprek, P. Abraham, J. E. Bowers, *IEEE J Quantum Electron* **2000**, *36*, 366.

[309] R. Ulrich, S. C. Rashleigh, W. Eickhoff, *Opt Lett* **1980**, *5*, 273.

[310] K. Ogawa, *IEEE J Quantum Electron* **1982**, *18*, 849.

[311] Y. Kadria-Vili, S. M. Bachilo, J. L. Blackburn, R. B. Weisman, *The Journal of Physical Chemistry C* **2016**, *120*, 23898.

[312] S. Cambré, S. M. Santos, W. Wenseleers, A. R. T. Nugraha, R. Saito, L. Cognet, B. Lounis, *ACS Nano* **2012**, *6*, 2649.

[313] J. L. Blackburn, J. M. Holt, V. M. Irurzun, D. E. Resasco, G. Rumbles, *Nano Lett* **2012**, *12*, 1398.

[314] Y. Pascal-Levy, E. Shifman, M. Pal-Chowdhury, I. Kalifa, T. Rabkin, O. Shtempluck, A. Razin, V. Kochetkov, Y. E. Yaish, *Phys Rev B* **2012**, *86*, 115444.

[315] C. Georgi, N. Hartmann, T. Gokus, A. A. Green, M. C. Hersam, A. Hartschuh, *ChemPhysChem* **2008**, *9*, 1460.

[316] P. Frantsuzov, M. Kuno, B. Jankó, R. A. Marcus, *Nat Phys* **2008**, *4*, 519.

[317] N. F. Hartmann, S. E. Yalcin, L. Adamska, E. H. Hároz, X. Ma, S. Tretiak, H. Htoon, S. K. Doorn, *Nanoscale* **2015**, *7*, 20521.

[318] A. Riaz, F. Pyatkov, A. Alam, S. Dehm, A. Felten, V. S. K. Chakravadhanula, B. S. Flavel, C. Kübel, U. Lemmer, R. Krupke, *Nanotechnology* **2015**, *26*, 325202.

[319] R. Yekani, E. Rusak, A. Riaz, A. Felten, B. Breitung, S. Dehm, D. Perera, J. Rohrer, C. Rockstuhl, R. Krupke, *Nanoscale* **2018**, *10*, 12156.

[320] N. A. Peyyety, S. Kumar, M.-K. Li, S. Dehm, R. Krupke, *ACS Appl Mater Interfaces* **2022**, *14*, 9525.

[321] A. Graf, Y. Zakharko, S. P. Schießl, C. Backes, M. Pfohl, B. S. Flavel, J. Zaumseil, *Carbon N Y* **2016**, *105*, 593.

[322] E. M. Purcell, H. C. Torrey, R. V. Pound, *Physical Review* **1946**, *69*, 37.

[323] D. Yamashita, H. Machiya, K. Otsuka, A. Ishii, Y. K. Kato, *APL Photonics* **2021**, *6*, 031302.

[324] H. Gehring, A. Eich, C. Schuck, W. H. P. Pernice, *Opt Lett* **2019**, *44*, 5089.

[325] R.-J. Shiue, Y. Gao, C. Tan, C. Peng, J. Zheng, D. K. Efetov, Y. D. Kim, J. Hone, D. Englund, *Nat Commun* **2019**, *10*, 109.

[326] Y. D. Kim, H. Kim, Y. Cho, J. H. Ryoo, C.-H. Park, P. Kim, Y. S. Kim, S. Lee, Y. Li, S.-N. Park, Y. Shim Yoo, D. Yoon, V. E. Dorgan, E. Pop, T. F. Heinz, J. Hone, S.-H. Chun, H. Cheong, S. W. Lee, M.-H. Bae, Y. D. Park, *Nat Nanotechnol* **2015**, *10*, 676.

[327] H. Htoon, M. J. O'Connell, P. J. Cox, S. K. Doorn, V. I. Klimov, *Phys Rev Lett* **2004**, *93*, 027401.

[328] W. Kim, A. Javey, O. Vermesh, Q. Wang, Y. Li, H. Dai, *Nano Lett* **2003**, *3*, 193.

[329] A. Vijayaraghavan, C. W. Marquardt, S. Dehm, F. Hennrich, R. Krupke, *Carbon N Y* **2010**, *48*, 494.

[330] S. Kar, A. Vijayaraghavan, C. Soldano, S. Talapatra, R. Vajtai, O. Nalamasu, P. M. Ajayan, *Appl Phys Lett* **2006**, *89*, 132118.

[331] A. Vijayaraghavan, S. Kar, C. Soldano, S. Talapatra, O. Nalamasu, P. M. Ajayan, *Appl Phys Lett* **2006**, *89*, 162108.

[332] N. F. Zorn, S. Settele, S. Zhao, S. Lindenthal, A. A. El Yumin, T. Wedl, H. Li, B. S. Flavel, A. Högele, J. Zaumseil, *Adv Opt Mater* **2023**, *11*, 2300236.

[333] N. Ai, W. Walden-Newman, Q. Song, S. Kalliakos, S. Strauf, *ACS Nano* **2011**, *5*, 2664.

[334] D. Estrada, S. Dutta, A. Liao, E. Pop, *Nanotechnology* **2010**, *21*, 085702.

[335] A. Schäfer, H. Horn, R. Ahlrichs, *J Chem Phys* **1992**, *97*, 2571.

[336] TURBOMOLE (TURBOMOLE GmbH) V7.2, **2017**.

[337] M. Freitag, H.-Y. Chiu, M. Steiner, V. Perebeinos, P. Avouris, *Nat Nanotechnol* **2010**, *5*, 497.

[338] S.-E. Zhu, S. Yuan, G. C. A. M. Janssen, *EPL (Europhysics Letters)* **2014**, *108*, 17007.

Acknowledgements

First and foremost, I would like to express my sincere gratitude to my supervisor, Prof. Dr. Ralph Krupke, for his consideration and for offering me the opportunity to work at KIT and TU Darmstadt. I'm grateful for all the fruitful scientific and non-scientific discussions, as well as his thoughtful support inside and outside of work. Thank you, Ralph!

I would also like to extend my appreciation to Prof. Dr. Wolfram Pernice for being the co-referee, and I am thankful to Prof. Dr. Wolfgang Ensinger and Prof. Dr. Jan Philipp Hofmann for examining my doctoral thesis.

My special acknowledgment goes to Simone Dehm for her kind assistance with device fabrication and resolving numerous challenges during lab work. I also thank Dr. Frank Hennrich for the preparation of nanotube suspensions and the scientific insights. I appreciate Dr. Benjamin S. Flavel, Dr. Romain Danneau, and other group members for fostering a supportive working environment.

I acknowledge the courtesy of Prof. Dr. Karin Fink for the computational simulation of normal mode frequencies, as well as Martina, Dr. Friedrich Schöppler, and Prof. Dr. Tobias Hertel from Universität Würzburg for the redox-chemical doping measurements. The completion of this thesis would not be the same without the intense yet joyful collaboration with Dr. Anna Ovvyan from the group of Prof. Dr. Wolfram Pernice at Universität Heidelberg and Universität Münster for the hybrid photonic crystal cavity device project. I also appreciate the initial support from Dr. Felix Pyatkov and Dr. Marco Gaulke for a smooth start to the research project and into the group.

I am grateful for the friendly and supportive atmosphere of the Krupke Unit. The time spent working with Sandeep, Anirudh, and Devang in the lab, along with their consistent inspiration, will be cherished. I am thankful to Chris, Martin, Paul, Alisa, Jana, Shivani, Ayvaz, and Sonu, with whom I create memorable moments, especially during coffee breaks. Many thanks to my previous colleagues, Adnan, Pranauv, Rainer, Preeti, Han, Laura, and all the others with whom I have shared time at INT.

The support received during the final phase of my PhD, for both myself and my family, from our good friends in Karlsruhe, Yin-Ting, Chien-Yu, and Ting-Chen, will remain in my mind. Finally, I wish to express my eternal gratitude to my beloved wife, Yu-Han, our sons, my parents, sisters, and parents-in-law for their unwavering support and for allowing me to pursue a PhD abroad without concern. This journey would not have been possible without them.